

UNCLASSIFIED

AD NUMBER

AD914451

LIMITATION CHANGES

TO:

Approved for public release; distribution is unlimited.

FROM:

Distribution authorized to U.S. Gov't. agencies only; Test and Evaluation; SEP 1973. Other requests shall be referred to Army Materials and Mechanics Research Center, Attn: AMXMR-PL, Watertown, MA 02172.

AUTHORITY

DARPA ltr, 19 dec 1974

THIS PAGE IS UNCLASSIFIED

**Best Available  
Copy  
for all Pictures**

THIS REPORT HAS BEEN DELIMITED  
AND CLEARED FOR PUBLIC RELEASE  
UNDER DOD DIRECTIVE 5200.20 AND  
NO RESTRICTIONS ARE IMPOSED UPON  
ITS USE AND DISCLOSURE.

DISTRIBUTION STATEMENT A

APPROVED FOR PUBLIC RELEASE;  
DISTRIBUTION UNLIMITED.

AD 914451



AD

AMMRC CTR 73-32

BRITTLE MATERIALS DESIGN, HIGH TEMPERATURE GAS TURBINE

D D C  
REF ID: A6515  
NOV 15 1973  
C

Technical Report By:

Arthur F. McLean, Ford Motor Company, Dearborn, Michigan 48121

Eugene A. Fisher, Ford Motor Company, Dearborn, Michigan 48121

Raymond J. Bratton, Westinghouse Electric Corporation, Pittsburgh, Pennsylvania 15235

September 1973

Interim Report, January 1, 1973 to June 30, 1973

Contract Number DAAG 46-71-C-0162

Sponsored by the Advanced Research Projects Agency

ARPA Order Number 1849

Project Code Number 1D10

Agency Accession Number DA OD 4733

Distribution limited to U.S. Government agencies only: Test and Evaluation data; September 1973. Other requests for this document must be referred to the Director, Army, Materials and Mechanics Research Center, ATTN: AMXMR-PL, Watertown, Massachusetts 02172

Prepared for:

ARMY MATERIALS AND MECHANICS RESEARCH CENTER  
Watertown, Massachusetts 02172

The findings in this report are not to be construed as an official Advanced Research Projects Agency, Department of the Army, or U.S. Government position, either expressed or implied, unless so designated by other authorized documents.

Mention of any trade names or manufacturers in this report shall not be construed as advertising nor as an official endorsement or approval of such products or companies by the United States Government

#### DISPOSITION INSTRUCTIONS

Destroy this report when it is no longer needed. Do not return it to the originator.

AMMRC CTR 73-32

BRITTLE MATERIALS DESIGN, HIGH TEMPERATURE GAS TURBINE

Technical Report By:

Arthur F. McLean, Ford Motor Company, Dearborn, Michigan 48121  
Eugene A. Fisher, Ford Motor Company, Dearborn, Michigan 48121  
Raymond J. Bratton, Westinghouse Electric Corporation, Pittsburgh, Pennsylvania 15235

September 1973

Interim Report, January 1, 1973 to June 30, 1973

Contract Number DAAG 46-71-C-0162

Sponsored by the Advanced Research Projects Agency

ARPA Order Number 1849

Project Code Number 1D10

Agency Accession Number DA OD 4733

Distribution limited to U.S. Government agencies only: Test and Evaluation data; September 1973. Other requests for this document must be referred to the Director, Army, Materials and Mechanics Research Center, ATTN: AMXMR-PL, Watertown, Massachusetts 02172

Prepared for:

ARMY MATERIALS AND MECHANICS RESEARCH CENTER  
Watertown, Massachusetts 02172

## ABSTRACT

The "Brittle Materials Design, High Temperature Gas Turbine" program is to demonstrate successful use of brittle materials in demanding high temperature structural applications. A small vehicular gas turbine and a large stationary gas turbine, each utilizing uncooled ceramic components, will be used in this iterative design and materials development program. Both the contractor, Ford Motor Company, and the subcontractor, Westinghouse Electric Corporation, have had in-house research programs in this area prior to this contract.

In the vehicular turbine project, a more refined heat transfer and stress analysis was performed for the monolithic hot-pressed silicon nitride rotor. Methods of fabricating duo-density silicon nitride rotors were evaluated, with several rotors being made; the best of these failed at 50,500 rpm during spin testing. Revised design stators demonstrated improved durability, although cracking has not been completely eliminated. Creep resistance of reaction-sintered silicon nitride has been considerably improved by decreasing calcium-containing impurities. The strength of reaction-sintered silicon nitride has been increased by the use of small amounts of hydrogen added to the nitrogen atmosphere.

In the stationary turbine project, stress and heat transfer analyses were completed for the stator vane assembly system. The three dimensional stress analysis program has been expanded to include steady state and transient heat transfer capability. Installation of the static test rig for evaluating stator-vanes under turbine conditions has been completed. Additional information about the properties of hot-pressed silicon nitride and silicon carbide has been determined, and the microstructure of hot-pressed silicon carbide was studied in detail.

## FOREWARD

This report is the fourth semi-annual technical report of the "Brittle Materials Design, High Temperature Gas Turbine" program initiated by the Advanced Research Projects Agency, ARPA Order Number 1849, and monitored by the Army Materials and Mechanics Research Center, under Contract Number DAAG-46-71-C-0162. This is an incrementally-funded five year program.

Since this is an iterative design and materials development program, design concepts and materials selection and/or properties presented in this report will probably not be those finally utilized. Thus all design and property data contained in the semi-annual reports must be considered tentative, and the reports should be considered to be illustrative of the design, materials, processing, and NDT techniques being developed for brittle materials.

The principal investigator of this program is Mr. A. F. McLean, Ford Motor Company, and the technical monitor is Dr. A. E. Gorum, AMMRC. The authors would like to acknowledge the valuable contributions in the performance of this work by the following people:

### Ford Motor Company

D. Alexander, R. R. Baker, P. Beardmore, D. J. Cassidy, J. C. Caverly, J. J. Charneski, D. A. Davis, G. C. DeBell, A. Ezis, W. A. Fate, M. U. Goodyear, D. L. Hartsock, P. H. Havstad, D. W. Huser, R. A. Jeryan, C. F. Johnson, K. H. Kinsman, J. T. Kovach, J. A. Mangels, S. V. McGrath, W. E. Meyer, J. J. Mittman, T. G. Mohr, P. F. Nicholls, A. Paluszny, J. J. Schuldies, J. M. Scofield, K. H. Styhr, W. Trella, N. F. Waugh, T. J. Whalen.

### Westinghouse Electric Corporation

G. W. Bauserman, D. Boes, C. R. Booher, Jr., J. DeKlerk, E. S. Diaz, D. M. Fantozzi, W. C. Frazier, A. N. Holden, D. D. Lawthers, R. Kossowsky, F. F. Lange, S. Y. Lee, W. Malchman, D. G. Miller, S. Mumford, T. J. Rahaim, J. D. Roughgarden, A. Sagar, R. J. Schaller, S. C. Singhal, S. Twiss, C. Visser, J. H. White

### Army Material and Mechanics Research Center

E. M. Lenoe, R. N. Katz, D. R. Messier, H. Priest

## TABLE OF CONTENTS

	<u>Page No.</u>
Title Page	i
Abstract	ii
Foreward	iii
Table of Contents	iv
List of Illustrations	v
List of Tables	xvi
 1. Introduction	 1
2. Summary of Progress	9
2.1 Vehicular Turbine Project	9
2.2 Stationary Turbine Project	10
2.3 Materials Technology - Vehicular & Stationary Turbine Projects	11
 3. Progress on the Vehicular Turbine Project	 13
3.1 Ceramic Rotor Development	13
3.1.1 Design and Analysis	15
3.1.2 Materials and Fabrication	44
3.1.3 Testing	61
3.2 Metal Rotor Development	67
3.2.1 Materials Investigation	67
3.2.2 Testing	68
3.3 Ceramic Stators, Shrouds, and Nose Cones	71
3.3.1 Material and Fabrication	72
3.3.2 Testing	77
 4. Progress on the Stationary Turbine Project	 87
4.1 Stator Vane Development	87
4.1.1 Design	90
4.1.2 Stress Analysis	94
4.1.3 Vane Fabrication	111
4.1.4 Static Rig Testing	117
4.2 Rotor Blade Development	121
4.2.1 Three-Dimensional Finite Element Stress Analysis	122
4.2.2 Stress Analysis of Blades	124
 5. Progress on Materials Technology - Vehicular and Stationary Turbine Projects	 137
5.1 Materials Engineering Data	137
5.1.1 Physical Properties of Hot-Pressed Materials	138
5.1.2 Physical Properties of Reaction-Sintered Silicon Nitride	178
5.2 Material Science	187
5.2.1 Microstructural Characteristics of Hot Pressed Silicon Carbide	188
5.2.2 Gas-Solid Reactions	193
5.2.3 Development of Injection Molded Silicon Nitride	200
5.3 Non Destructive Evaluation of Materials	203
5.3.1 Ultrasonic NDE	204
5.3.2 Acoustic Emission	208
5.3.3 X-Ray Radiography	223
 6. References	 225

## LIST OF ILLUSTRATIONS

Page No.

Figure 1.1	Flow Path Schematic of Vehicular Gas Turbine	2
Figure 1.2	30 Mw Test Turbine Flow Path	3
Figure 1.3	Brittle Material Design/High Temperature Gas Turbine - Breakdown of Major Elements Reported	4
Figure 1.4	Brittle Material Design/High Temperature Gas Turbine - Block Diagram Flow Chart of Iterative Development	6
Figure 3.1	Effect of Finite Element Mesh Size on Stresses in First Stage Rotor Neck Under Full Speed Steady State Conditions	16
Figure 3.2	Effect of Finite Element Mesh Size on Transient Stresses Near the Rotor Bore	17
Figure 3.3	Maximum Principle Stresses (psi) in First Stage Rotor at 55% Speed Centrifugal Loading	19
Figure 3.4	Maximum Principle Stresses (psi) in First Stage Rotor at 110% Speed Centrifugal Loading	20
Figure 3.5	Maximum Principle Stresses (psi) in Second Stage Rotor at 55% Speed Centrifugal Loading	21
Figure 3.6	Maximum Principle Stresses (psi) in Second Stage Rotor at 110% Speed Centrifugal Loading	22
Figure 3.7	Isotherms ( $^{\circ}$ F) in First Stage Rotor at 55% Steady State Speed Temperature Boundary Conditions	24
Figure 3.8	Maximum Principle Stresses (psi) in First Stage Rotor, Combining Thermal and Centrifugal Stresses at 55% Speed	25
Figure 3.9	Isotherms ( $^{\circ}$ F) in Second Stage Rotor at 55% Steady State Speed Temperature Boundary Conditions	26
Figure 3.10	Maximum Principle Stresses (psi) in Second Stage Rotor, Combining Thermal and Centrifugal Stresses at 55% Speed	27
Figure 3.11	Isotherms ( $^{\circ}$ F) in First Stage Rotor at 100% Steady State Speed Temperature Boundary Conditions	28
Figure 3.12	Maximum Principle Stresses (psi) in First Stage Rotor, Combining Thermal Stresses at 100% Speed and Centrifugal Stresses at 110% Speed	29
Figure 3.13:	Isotherms ( $^{\circ}$ F) in Second Stage Rotor at 100% Steady State Speed Temperature Boundary Conditions	30
Figure 3.14	Maximum Principle Stresses (psi) in Second Stage Rotor, Combining Thermal Stresses at 100% Speed and Centrifugal Stresses at 110% Speed	31
Figure 3.15	Isotherms ( $^{\circ}$ F) in First Stage Rotor at 40 Seconds From Light With 55% Speed Temperature Boundary Conditions	32
Figure 3.16	Maximum Principle Stresses (psi) in First Stage Rotor at 40 Seconds From Light with 55% Speed Temperature Boundary Conditions Combined With Centrifugal Stresses at 55% Speed	33
Figure 3.17	Isotherms ( $^{\circ}$ F) in Second Stage Rotor at 40 Seconds From Light With 55% Speed Temperature Boundary Conditions	34

Figure 3.18	Maximum Principle Stresses (psi) in Second Stage Rotor at 40 Seconds From Light at 55% Speed Temperature Boundary Conditions Combined With Centrifugal Stresses at 55% Speed	35
Figure 3.19	Isotherms ( $^{\circ}$ F) in First Stage Rotor at 55 Seconds From Light with 100% Speed Temperature Boundary Conditions	36
Figure 3.20	Maximum Principle Stresses (psi) in First Stage Rotor at 55 Seconds From Light at 100% Speed Temperature Boundary Conditions Combined With Centrifugal Stresses at 110% Speed	37
Figure 3.21	Isotherms ( $^{\circ}$ F) in Second Stage Rotor at 55 Seconds From Light With 100% Speed Temperature Boundary Conditions	38
Figure 3.22	Maximum Principle Stresses (psi) in Second Stage Rotor at 55 Seconds From Light at 100% Speed Temperature Boundary Conditions Combined with Centrifugal Stresses at 110% Speed	39
Figure 3.23	Maximum Principle Stresses (psi) in First Stage Rotor at 40 Seconds From Light at 55% Speed Temperature Boundary Conditions Combined with Centrifugal Stresses at 110% Speed	40
Figure 3.24	Maximum Principle Stresses (psi) in Second Stage Rotor at 40 Seconds From Light at 55% Speed Temperature Boundary Conditions Combined With Centrifugal Stresses at 110% Speed	41
Figure 3.25	Duo-Density Rotor Fabrication Showing Tapered Silicon Nitride Hub and Mating Blade Ring	45
Figure 3.26	Concept for Bonding Duo-Density Rotor Without Tapered Sections	46
Figure 3.27	Microstructure Showing Good Bonding (1250X)	47
Figure 3.28	Sandwich-Type Construction for Fabricating Duo-Density Rotor	47
Figure 3.29	Concept for Employing Graphite Wedges for Fabricating Duo-Density Rotor	48
Figure 3.30	Graphite Wedges for Fabricating Duo-Density Rotor	49
Figure 3.31	Completed Duo-Density Rotor	50
Figure 3.32	Microstructure Showing Poor Bonding (1250X)	50
Figure 3.33	Microstructure Showing Good Bonding (1250X)	51
Figure 3.34	Deformation of Molded Blade Ring When Unsupported During Bonding	52
Figure 3.35	Hot-Pressed Preformed Silicon Nitride Hub	52
Figure 3.36	Hot-Pressing System for Bonding Silicon Nitride Disks	54
Figure 3.37	First Order Interaction Factorial Analysis of Bond Strength Parameters	55

Figure 3.38	Second Order Interaction Factorial Analysis of Bond Strength Parameters	56
Figure 3.39	Microstructure of Bonding Sample With a Bond Strength of 30,000 psi (500X)	56
Figure 3.40	Microstructure of Bonding Sample With a Bond Strength of 60,000 psi (500X)	57
Figure 3.41	CVD Silicon Carbide Rotors	58
Figure 3.42	CVD Silicon Carbide Rotor Showing Spalling of Material After Spin Testing	58
Figure 3.43	Lucas Hot-Pressed Silicon Nitride Rotor	59
Figure 3.44	Surface of Norton Hot-Pressed Silicon Carbide After EDM Cutting (500X)	60
Figure 3.45	Turbine Rotor Test Rig Installed in Test Cell	62
Figure 3.46	Schematic Diagram of Mounting of CVD Silicon Carbide Rotors	63
Figure 3.47	Failure of a Single Blade During Spin Testing of CVD Silicon Carbide Rotor Number Two	63
Figure 3.48	Failure of the Rim During Spin Testing on CVD Silicon Carbide Rotor Number Three	64
Figure 3.49	Failure of the Rim During Spin Testing of a Duo-Density Silicon Nitride Rotor	65
Figure 3.50	Hologram of Second Stage Rotor, Two Diameter Mode Shape. 3452 Cycles/Per Second	69
Figure 3.51	Hologram of Second Stage Rotor, Two Diameter Plus One Radial Mode Shape. 5444 Cycles/Per Second	69
Figure 3.52	Flow Path Components (A) Design B Components (B) Design C Components	73
Figure 3.53	Vanes and Outer Shroud for Inverted Channel Second Stage Stator	74
Figure 3.54	Assembled Second Stage Inverted Channel Stator	75
Figure 3.55	First and Second Stage Rotor Shrouds	75
Figure 3.56	Rotor Shroud Gap Change versus Time at Temperature for Various Nitriding Additives	76
Figure 3.57	Vane Temperatures	78
Figure 3.58	Vane Temperature versus Time During Cooling Cycle	78

	<u>Page No.</u>
Figure 3.59 Time-Temperature Response for First Stage Stator Blades	79
Figure 3.60 Ceramic Combustor Tube	80
Figure 3.61 Second Stage Design B Stator Designs (A) U-Channel Design, (B) Inverted Channel Design	83
Figure 3.62 Comparison of Modified and Design B Nose Cones	85
Figure 4.1 Schematic of 30 Mw Test Turbine Flow Path	89
Figure 4.2 Static Rig Test Assembly Mounting Arrangement (Circumferential View from Combustor Transition)	91
Figure 4.3 Circumferential View of Ceramic Vane Static Rig Test Assembly	92
Figure 4.4 Ceramic Components of the First Stage Stator Vane Assembly	93
Figure 4.5 Second Generation Vane Assembly	93
Figure 4.6 One-Dimensional Force Equilibrium Diagram for Airfoil End Cap Interface	95
Figure 4.7 Vane-End Cap Interface Edge Loading Analysis	96
Figure 4.8 Start-Up Tensile Contact Stress at Vane-End Cap Interface Showing Effects of Parameter Variation	97
Figure 4.9 Shut-Down Tensile Contact Stress at Vane-End Cap Interface Showing Effects of Parameter Variation	97
Figure 4.10 Critical Axial Radius vs Start-Up Coefficient of Friction at End Cap Insulator Interface	98
Figure 4.11 Start-Up Tensile Contact Stress at End Cap-Insulator Interface Showing Effects of Parameter Variation	99
Figure 4.12 Shut-Down Tensile Contact Stress at End Cap-Insulator Interface Showing Effects of Parameter Variation	99
Figure 4.13 Circumferential Edge Loading Analysis Hertzian Contact Stresses (Tensile) at Thick-Thin-End Cap-Insulator Interlocks	101
Figure 4.14 Two-Dimensional Finite Element Mesh for Heat Transfer in the End Cap Sections AA, BB-CC-DD and EE.	103

Figure 4.15	Steady State Thermal Contour Representation Through End Cap Section AA	104
Figure 4.16	Steady State Thermal Contour Representation Through End Cap Section CC	105
Figure 4.17	Thermal Contour Representation Through End Cap Section AA 5 Seconds after Shut-Down	106
Figure 4.18	Thermal Contour Representation Through End Cap Section CC 5 Seconds after Shut-Down	107
Figure 4.19	Thermal Contour Representation Through End Cap Section AA 6 Seconds after Shut-Down	108
Figure 4.20	Thermal Contour Representation Through End Cap Section CC 60 Seconds after Shut-Down	109
Figure 4.21	Two Dimensional Finite Element Mesh for Thermal Stresses in Ceramic End Caps	110
Figure 4.22	Thermal Stress Distribution in Ceramic End Caps under Steady State Conditions	110
Figure 4.23	First Generation Stator Vane Assemblies as Supplied by Norton from HS-130 Silicon Nitride	111
Figure 4.24	"Xyglo" Photograph of Two Machined Airfoils - Note: Surface Scratches and Crack on the Trailing Edge of Airfoil #19	113
Figure 4.25	"Xyglo" Photograph of End Cap Showing Scratches Inside Cavity and Surface Irregularities	114
Figure 4.26	Ultrasonic Scan of End Cap Indicating Low Density Inclusions (Large Peaks are Reflections from Top and Bottom Surfaces)	114
Figure 4.27	The Static Rig for Testing Ceramic Stator Vanes at 2200 and 2500°F (Mitered Section is 42 Inches in Diameter)	118
Figure 4.28	Silicon Nitride Stator Vanes Assembled with Support Structure for Test at 2200°F	118
Figure 4.29	Mitered Section of Static Rig Showing Barrier Plate for the Installation of the Test Assembly	119

Figure 4.30	Static Rig - Schematic Representation	119
Figure 4.31	Flange Assembly Section	123
Figure 4.32	Finite Element Model of the Flange Assembly with Temperature Distribution at 0.01 Hours Superimposed Upon It	123
Figure 4.33	Exploded View of Three Dimensional Computer Model	125
Figure 4.34	Radial Stress Contours (psi) on Section 300 of Blade Model	126
Figure 4.35	Radial Stress Contours (psi) on Section 500 of Blade Model	127
Figure 4.36	Radial Stress Contours (psi) on Section 700 of Blade Model	128
Figure 4.37	Two-Dimensional Blade Root Model	130
Figure 4.38	Two-Dimensional Computer Model for a 30° Blade Root	130
Figure 4.39	Maximum Principal Stress Contours in a 30° Blade Root (No Shear, $\mu = 0$ )	131
Figure 4.40	Maximum Principal Stress Contours in a 30° Blade Root (With Shear, $\mu = 1.73$ )	132
Figure 4.41	Effect of Root Angle and Maximum Stress in a Blade Root	134
Figure 4.42	Effect of Friction Coefficient on Maximum Stress in a Blade Root	134
Figure 4.43	Effect of Contact Area on Maximum Stress in a Blade Root	135
Figure 4.44	Hollow Ceramic Rotor Blade	135
Figure 5.1	Room Temperature Strength of Hot Pressed $\text{Si}_3\text{N}_4$ (HS-130) as a Function of Test Mode (Weibull Analysis Based on Area and Volume)	139
Figure 5.2	Two Parameter Weibull Volume Prediction of Failure Stress in $\text{Si}_3\text{N}_4$ for Flexural and Tensile Test Modes	140

Figure 5.3 -- Two Parameter Weibull Area Prediction of Failure Stress in Si <sub>3</sub> N <sub>4</sub> at Elevated Temperature for Flexural and Tensile Test Modes	141
Figure 5.4 -- The Relationship Between Flexural Stress with Tensile Stress as Adjusted by 2-Parameter Weibull Statistics Based on Area	142
Figure 5.5 -- Tensile Test Specimens	142
Figure 5.6 -- Tensile Strength of Norton HS-130 Silicon Nitride	143
Figure 5.7 -- Failed Silicon Nitride Tensile Specimens	145
Figure 5.8 Tensile Specimen Configuration	145
Figure 5.9 Cutting Plan for Hot Pressed Si <sub>3</sub> N <sub>4</sub> Billets	146
Figure 5.10 Results of the Load Train Alignment Check (TIR)	147
Figure 5.11 Tensile Stress versus Axial Strain for Axial Tensile Specimens of Norton HS 130 Silicon Nitride	148
Figure 5.12 Tensile Stress versus Temperature for Axial Tensile Specimens of Norton HS 130 Silicon Nitride	148
Figure 5.13 Tensile Elastic Modulus versus Temperature for Axial Tensile Specimens of Norton HS 130 Silicon Nitride	149
Figure 5.14 Effect of Temperature on the Elastic Modulus of Norton HS-130 Silicon Nitride	149
Figure 5.15 The Tensile Strength of Norton Hot Pressed Silicon Carbide	150
Figure 5.16 Failed Silicon Carbide Tensile Specimens	151
Figure 5.17 The Effect of Temperature on the Elastic Modulus of Norton Hot Pressed Silicon Carbide	152
Figure 5.18 The Effect of Temperature and Strain Rate on the Flexural Strength of Norton HS-130 Silicon Nitride (Strong, Perpendicular to Hot Press, Direction)	153

Figure 5.19 -- The Effect of Temperature and Strain Rate on the Flexural Strength of Norton HS-130 Silicon Nitride (Weak, Normal to Hot Pressing, Direction)	153
Figure 5.20 Flexural Strength versus Temperature of Hot-Pressed and Reaction-Sintered Silicon Nitrides	154
Figure 5.21 -- The Effect of Temperature on the Flexural Strength of Norton Hot Pressed Silicon Carbide	155
Figure 5.22 -- The Effect of Stress Rate on the Flexural Strength of Norton Hot Pressed Silicon Carbide	156
Figure 5.23 Flexural Strength versus Temperature of Hot-Pressed and Refil Silicon Carbides	156
Figure 5.24 Compressive Strength versus Temperature of Hot-Pressed Silicon Carbide and Silicon Nitride	158
Figure 5.25 Battelle High Temperature Dilatometer for Direct View Expansion Measurements	158
Figure 5.26 Battelle Thermal Diffusivity Apparatus	159
Figure 5.27 Battelle Ice Calorimeter	159
Figure 5.28 Specific Heat of Norton Hot Pressed Silicon Carbide	161
Figure 5.29 Thermal Expansion of Norton Hot Pressed Silicon Carbide	163
Figure 5.30 Thermal Diffusivity of Norton Hot Pressed Silicon Carbide	163
Figure 5.31 Thermal Conductivity of Norton Hot Pressed Silicon Carbide	165
Figure 5.32 Creep Properties of Hot Pressed $\text{Si}_3\text{N}_4$ at 10,000 psi, 2300°F	167
Figure 5.33 Effect of Temperature on the Creep Properties of Norton HS-130 Silicon Nitride in Air	168
Figure 5.34 Compressive Creep of Norton Hot Pressed Silicon Nitride in Air at $1 \times 10^5$ psi, 2500°F	169

Figure 5.35 -- Surface Appearance of $\text{Si}_3\text{N}_4$ and SiC after 250 hours at 2000°F (Turbine Passage Test at 3 atm Using Exxon #2 Diesel Oil)	171
Figure 5.36 -- Corrosion-Erosion Behavior of Hot Pressed Silicon Nitride in Turbine Passage at 2000°F, 3 atm and 500 ft/sec Gas Velocity Using Exxon GT-2 Oil (Microscopic Measurement of Surface Recession)	171
Figure 5.37 -- Corrosion-Erosion Behavior of Hot Pressed Silicon Carbide in Turbine Passage at 2000°F, 3 atm Pressure and 500 ft/sec Gas Velocity Using Exxon No. GT-2 Oil (Microscopic Measurement of Surface Recession)	172
Figure 5.38 -- Effect of Corrosion-Erosion in Turbine Passage on the Flexural Strength of Hot Pressed $\text{Si}_3\text{N}_4$ and SiC	172
Figure 5.39 -- Gas Turbine Passage as Modified for 2500°F Testing	174
Figure 5.40 -- Stainless Steel Flange and Test Section for 2500°F Turbine Passage	175
Figure 5.41 -- Low Cycle Fatigue - 4 Pt. Bend Test, in Air for Norton HS-130 $\text{Si}_3\text{N}_4$	176
Figure 5.42 Shear Modulus versus Temperature for Norton HS-130 Hot-Pressed Silicon Nitride	177
Figure 5.43 Creep Test Rig	179
Figure 5.44 Total Strain Versus Time for Two Types of Reaction-Sintered Silicon Nitride	181
Figure 5.45 Steady State Strain Rate Versus Stress for Two Types of Reaction-Sintered Silicon Nitride	182
Figure 5.46 Specific Heat of Injection Molded Reaction-Sintered Silicon Nitride	182
Figure 5.47 Thermal Conductivity of Injection-Molded and Slip-Cast Silicon Nitride	184
Figure 5.48 Thermal Diffusivity of Injection-Molded and Slip-Cast Silicon Nitride	184
Figure 5.49 Strength Versus Temperature for Slip Cast Silicon Nitride	185

Figure 5.50	Secondary-Ion-Mass Spectrometer Micrographs of Major Impurities in SiC - A-Al, B-W, C-Ti, D-B and E-Fe	189
Figure 5.51	SEM Micrograph of Polished SiC Showing Impurities (2000 X)	190
Figure 5.52	SEM Micrograph, Thermally Etched, Hot Pressed SiC Creep Specimen, (Particles Show Si, W and Traces of Ti and Fe - No Al)	190
Figure 5.53	Transmission Electron Micrographs Showing Inclusions in Grain Boundaries of Hot Pressed SiC A - Bright Field; B - Dark Field (1000 KV)	191
Figure 5.54	Typical Microstructural Details in Hot Pressed SiC (1 $\mu$ m Scale Bar)	191
FIG. 5.55	Typical Parabolic Oxidation of Hot Pressed Silicon Nitride in $O_2 + N_2$ , $O_2 + Ar$ , and $O_2 + Ar + N_2$ Gas Mixtures at 2500°F 1 atm Total Pressure	194
Figure 5.56	The Oxidation of Hot Pressed $Si_3N_4$ in $O_2 + Ar$ Gas Mixture at 2500°F, 1 atm Total Pressure	195
Figure 5.57	The Oxidation of Hot Pressed $Si_3N_4$ in $O_2 + Ar + N_2$ Gas Mixture at 2500°F ( $P_{O_2} = 0.2$ atm, $P_{total} = 1$ atm)	195
Figure 5.58	The Parabolic Rate Constants for the Oxidation of Hot Pressed $Si_3N_4$ in Dry and Wet Oxygen as a Function of Temperature	197
Figure 5.59	The Parabolic Rate Constants for the Oxidation of Hot Pressed SiC in Dry and Wet Oxygen as a Function of Temperature	197
Figure 5.60	Ion Images from a Single Region of the Oxide Layer on a Hot Pressed SiC Specimen Oxidized for 24 hours at 2500°F in Pure, Dry Oxygen	198
Figure 5.61	Oxygen, Aluminum, and Tungsten Profiles Across the Oxide Layer on a Hot Pressed SiC Specimen Oxidized for 24 hours at 2500°F in Pure, Dry Oxygen	199
Figure 5.62	Particle Size Distribution of Silicon Metal Powder	201
Figure 5.63	Density and Strength of Injection-Molded Silicon Nitride as a Function of Particle Size Variation of Silicon Metal Powder	201

Figure 5.64	Microstructure Scattering of Ultrasonic Echoes in Hot-Pressed Silicon Nitride, A,B,C-Ford Material, D-Norton HS-130 Material	206
Figure 5.65	Digital Recordings of Electrical Noise and Ultrasonic Echoes From Flat-Bottomed Hole in Plastic Specimen.	207
A)	One Digital Sample per Waveform Position	
B)	Ten Digital Samples per Waveform Position	
C)	One Hundred Digital Samples per Waveform Position	
Figure 5.66	Program Plan For Thermal Stress Monitoring	209
Figure 5.67	Notch Sensitivity of Ford Hot-Pressed Silicon Nitride Shown as a Rapid Increase in AE with Decreasing Defocus Distance (Increasing Power Density).	210
Figure 5.68	Scanning Electron Micrographs of Ford Hot-Pressed Silicon Nitride Showing Surface Crack Severity and Orientation. AE Detected During Shocking: A) 1255 and B) 219 (80X)	212
Figure 5.69	Scanning Electron Micrograph of Ford Hot-Pressed Silicon Nitride Showing Pitting and Irregular Heat-Affected Area, Indicating Possible High Energy Concentrations During Laser Shocking. Total AE Detected Was 394. (80X)	213
Figure 5.70	Reduction in Flexural Strength vs AE Detected During Laser Shocking the Surface of Ford Dense Silicon Nitride Test Specimens.	214
Figure 5.71	Scanning Electron Micrographs of Fractured Flexure Test Ford Dense Silicon Nitride: A) View of Laser Shocked and Final Fracture Surfaces, (135X), B) View of Laser Induced Cracks and Final Fracture on Tensile Surface. (225X)	215
Figure 5.72	Crack Extension of Ford Hot-Pressed Silicon Nitride During Flexure Testing Shown as an Increase in AE Prior to Final Fracture.	
Figure 5.73	Laser Scanning to Detect Surface Flaws.	216
Figure 5.74	Experimental Setup Used For Study of Acoustic Emission From Samples Under Four-Point Bend Test.	217
Figure 5.75	Total Count vs Load For a $\text{Si}_3\text{N}_4$ Sample	219
Figure 5.76	Total Count vs Load For Another Portion of $\text{Si}_3\text{N}_4$ Sample Shown in Figure 5.82	220
Figure 5.77	Total Count vs Load For a $\text{Si}_3\text{N}_4$ Sample Pre-quenched in Air From 2552 $^{\circ}$ F.	221
Figure 5.78	Fractured Surface of The $\text{Si}_3\text{N}_4$ Sample For Which The Acoustic Emission Data is Shown in Figure 3a. (10X)	221
Figure 5.79	Total Count vs Load For SiC Sample Pre-quenched in Air From 2552 $^{\circ}$ F (1400 $^{\circ}$ C)	222
Figure 5.80	Total Count vs Load For a SiC Sample Not Subjected to Thermal Shock.	222

LIST OF TABLES

	<u>Page No.</u>
Table 3.1      Summary of Stress-Temperature Conditions for Design C Hot Pressed Silicon Nitride Turbine Rotors	42
Table 3.2      Bonding Study Parameters Considered Important For Bonding $\text{Si}_3\text{N}_4$ Component Parts Together With Investigated Parameters Underlined	53
Table 3.3      Summary of Flexural Strength Measurements of Bonds and Hot-Pressing Parameter for Bonded Discs	54
Table 3.4      Second Stage Turbine Rotor Natural Frequencies	68
Table 3.5      Summary of Testing of Ceramic Nose Cones, Stators and Shrouds	82
Table 3.6      Life Data For Design B and C First Stage Stators	83
Table 3.7      Life Data For Second Stage Design B Stators	83
Table 4.1      Properties of Norton Noralide HC-203 Silicon Carbide	116
Table 4.2      Effect of Critical Design Parameters on Maximum Tensile Stress	136
Table 5.1      Comparison of 2 and 3 Parameter Weibull Results	140
Table 5.2      Tensile Properties of Norton HS-130 Silicon Nitride	144
Table 5.3      Tensile Properties of Norton Hot Pressed Silicon Carbide	150
Table 5.4      Effect of Surface Preparation on Flexural Strength of Hot-Pressed SiC	155
Table 5.5      Specific Heat of Hot Pressed Silicon Carbide	161
Table 5.6      Thermal Expansion of Silicon Carbide	162
Table 5.7      Thermal Diffusivity of Norton SiC	164
Table 5.8      Thermal Conductivity of Norton SiC	166
Table 5.9      Effect of Atmosphere on Creep Parameters, Hot Pressed HS-130 $\text{Si}_3\text{N}_4$	168
Table 5.10     Impurity Analysis of Silicon Metal	179
Table 5.11     Test Sample History	179
Table 5.12     Creep Test Results	181

Page No.

Table 5.13	Nitriding Results	202
Table 5.14	Scanning Data in Terms of Detected Acoustic Emission	218
Table 5.15	Comparison of Quality Levels Obtained on the Hot-Pressed Silicon Nitride Radiographic Standard	224

## 1. INTRODUCTION

As stipulated by the Advanced Research Projects Agency of the Department of Defense, the major purpose of this program is to demonstrate that brittle materials can be successfully utilized in demanding high temperature structural applications. The gas turbine engine, utilizing uncooled ceramic components in the hot flow path, was chosen as the vehicle for this demonstration. Two hundred hours of operation over a representative duty cycle at ceramic temperatures up to 2500°F is required for the demonstration.

It is the further purpose of this program to develop design technology for ceramic materials on a systems basis requiring close integration of design, engineering, materials selection, materials processing and fabrication, testing and evaluation.

The progress of the gas turbine engine has been closely related to the development of materials capable of withstanding the engine's environment at high operating temperature. Since the early days of the jet engine, new metals have been developed which have allowed a gradual increase in operating temperatures. Today's nickel-chrome superalloys are in use without cooling at turbine inlet gas temperatures of 1800° to 1900°F. However, there is considerable incentive to further increase turbine inlet temperature to improve specific air and fuel consumptions. The use of ceramics in the gas turbine engine as a demonstration vehicle for this program promises to make a major step in increasing turbine inlet temperature. Success will offer significant advances in engine efficiency, power per unit weight, cost, pollution abatement, and fuel utilization.

This program will demonstrate the use of ceramics in two demanding gas turbine applications:

- (1) A small-vehicular type of engine (Ford). Such an engine would have a major impact on the technology of mobile field power units, military vehicles and craft. As a consequence of its significantly increased operating temperature it would not only provide more horsepower/unit weight than current engines, but would also provide improved fuel economy. In addition, the benefits of low emissions and multi-fuel capability are attained. A simplified schematic of the flow path of this regenerative type of engine is shown in Figure 1.1. A brief explanation of this flow path will be given to familiarize the reader with the various components considered for ceramics. Air is induced through an intake silencer and filter into a radial compressor, and then is compressed and ducted through one side of each of two rotary regenerators. The hot compressed air is then supplied to a combustion chamber where fuel is added and combustion takes place.

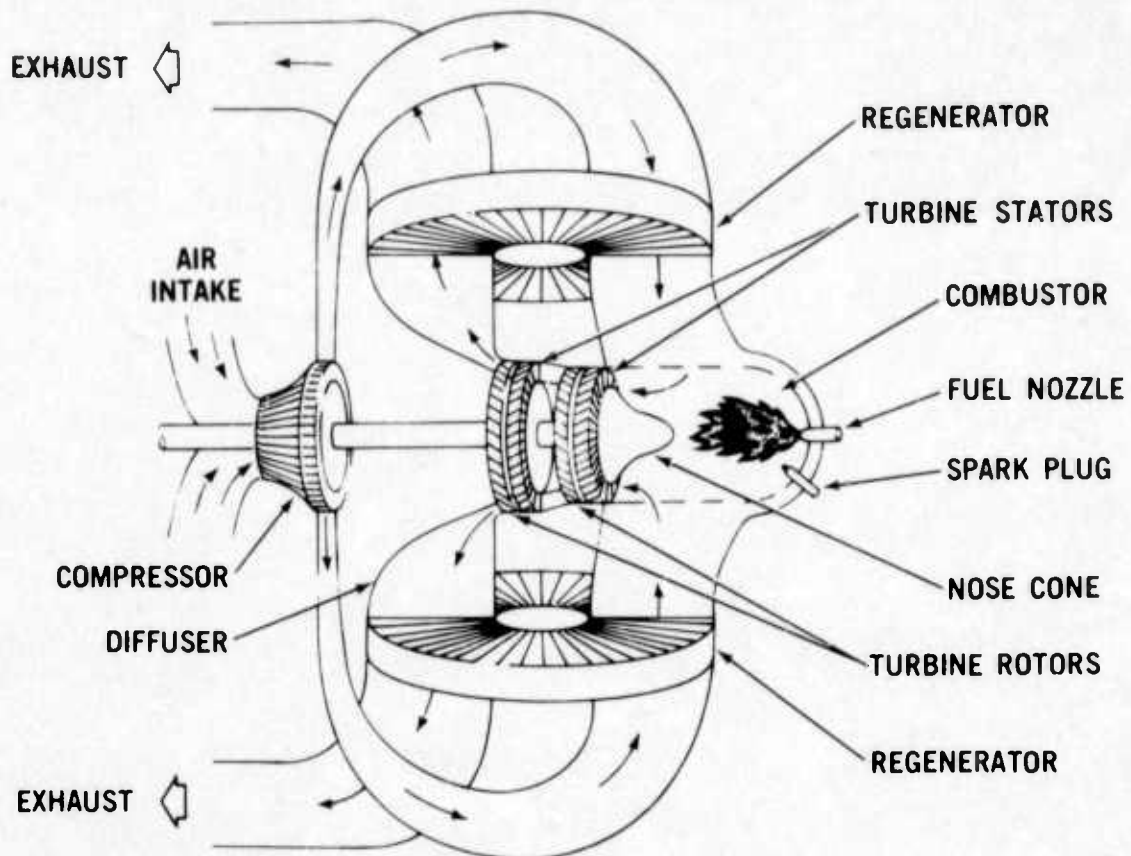


Figure 1.1 - Flow Path Schematic of Vehicular Gas Turbine

The hot gas discharging from the combustor is then directed into the turbine stages by a turbine inlet structure, in this case shown as a nose cone: The gas then passes through the turbine stages which comprise two turbine stators, each having stationary airfoil blades which direct the gas onto each corresponding turbine rotor. In passing through the turbine, the gas expands and generates work to drive the compressor and supply useful power. The expanded turbine exhaust gas is then ducted through the hot side of each of the two regenerators which, to conserve fuel consumption, transfer much of the exhaust heat back into the compressed air.

The parts which are subject to the peak cycle temperature and are made out of superalloys in today's gas turbine are the combustor, the turbine inlet nose cone, the turbine stators and the turbine rotors. These are areas where ceramics could be exploited to the fullest and have been selected for application in the vehicular turbine project.

- (2) A large-stationary gas turbine for electric power production (Westinghouse). Such an engine would be most desirable for DOD installations requiring on-site power generation. Not only will ceramics facilitate significantly increased operating temperatures with attendant improvement in power and fuel economy, but, because of their improved corrosion-erosion resistance they will also facilitate use of low cost residual fuel. In addition, the environmental benefits of low emissions and lack of cooling water (with its attendant thermal pollution problems) are attained. A simplified sketch of the hot flow path of the engine is shown in Figure 1.2. As with the vehicular turbine project, a brief explanation of the flow path of the stationary turbine will be given to help the reader understand the function of the components to be made from ceramic materials.

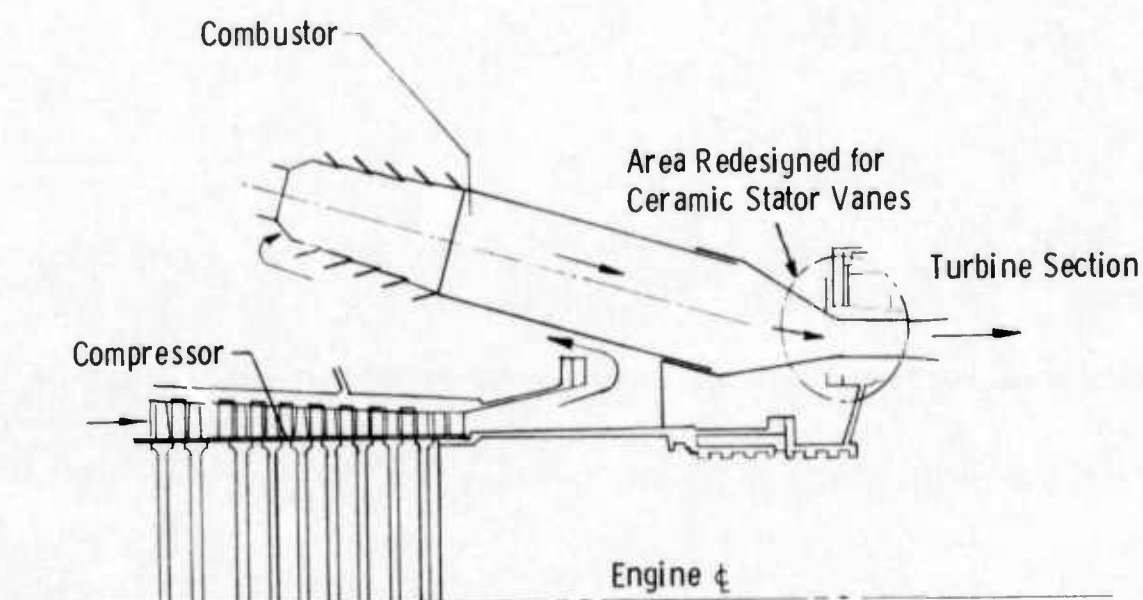


Figure 1.2 - 30 Mw Test Turbine Flow Path

Air is induced through a large intake silencer and filter into an 18 stage axial compressor where it is compressed before entering the combustor housing. The combustor housing supplies air at 650°F to combustion cans assembled in a circumferential array. Air is mixed with distillate fuel or natural gas and ignited in the primary combustion zone. The gas passes down stream through the combustors mixing with secondary air. Flow continues from the combustion section, through the transition zone, and enters the power turbine at a gas temperature of 2500°F. The hot gases expand through the three stage turbine section and are either exhausted through a stack or ducted into a reheat boiler as part of a combined cycle power generating unit.

The parts, where ceramics could be exploited to the fullest, selected for application in the stationary turbine project are the first stage turbine stator vanes and the first stage turbine rotor.

To maintain coherence, progress on the vehicular and stationary turbine projects are reported separately. Also reported separately is the common link between these two programs, materials technology. Information presented under materials technology is general, and does not specifically apply to one or the other of the gas turbine engines. On the other hand, items reported under the vehicular and stationary turbine projects are categorized by components and therefore relate directly to those projects (even these items, however, are indirectly related when it comes to such considerations as design techniques, etc.). Figure 1.3 has been prepared to help the reader understand the interrelationship between the major elements of the report.

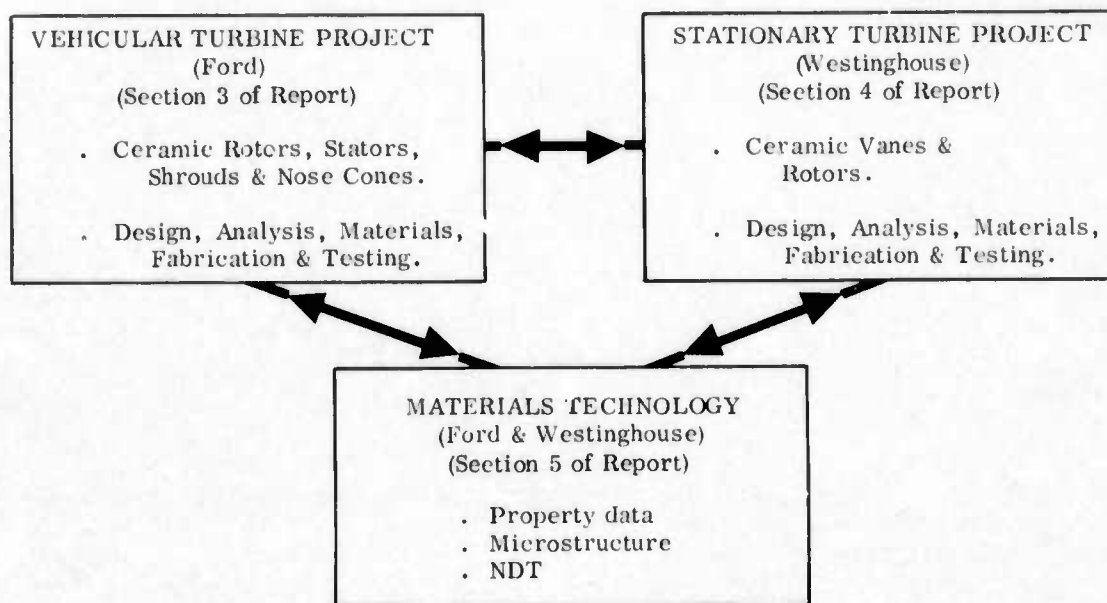


Figure 1.3 - Brittle Material Design/High Temperature Gas Turbine - Breakdown of Major Elements Reported

Successful demonstration of a high temperature gas turbine engine will involve a complex iterative development. One cannot divorce the development of ceramic materials from processes for making parts; no more so can one isolate the design of those parts from how they are made or from what they are made. Likewise, the design of mountings and attachments between metal and ceramic parts within the engine are equally important. Innovation in the control of the environment of critical engine components is another link in the chain. Each of these factors has a relationship with the others, and to obtain success in any one may involve compromises in the others. Testing plays an important role during the iterative development since it provides a positive, objective way of evaluating the various combinations of factors involved. If successful, the test forms the credibility to move on to the next link in the development chain. If unsuccessful, the test flags a warning and prompts feedback to earlier developments to seek out and solve the problem which has resulted in failure. Finally, all of the links in the chain are evaluated by a complete engine test, by which means the ultimate objective of the program will be demonstrated.

Figure 1.4 shows a block diagram flow chart of the major factors involved including the feedback loops, which serves to illustrate this complex and comprehensive iterative development program. The starting point is the concept of a design to use brittle materials. From this, a design layout is prepared and analyzed leading to the detailed design and analysis of the gas turbine engine components made of or involving ceramics. In parallel with the design phase, ceramic materials are developed and screened for application to the gas turbine engine. Process development of candidate ceramics then takes place and material science and property evaluation are used to improve materials and processes, and to feed information back into the design phase. Next with the first detail designs completed and with the process for the selected ceramics reasonably developed, tooling can be designed and fabrication development started to make actual ceramic turbine engine components. Non-destructive testing of these parts will be developed to form a feedback for improving material and fabrication methods. In conjunction with non-destructive evaluation, techniques will be developed for proof testing ceramic components prior to use in engines. In parallel with ceramic part fabrication, proof testing, and non-destructive evaluation, metal parts for the ceramic turbine engine and test rigs are made per the detail design requirements. The ceramic and metal parts are then dimensionally inspected and instrumented for engine testing. Assembly techniques for brittle materials are developed, and testing and durability developments in both test rigs and engines are performed. Failure analysis from test rig and engine testing forms the feedback loops for corrective action; almost all of the factors involved in the development could be affected by experience learned in the test phase of the program. Finally, when engine durability has reached a given level of development, the 200 hour demonstration test will be conducted to meet the program objective.

It should be noted that both the contractor and subcontractor had in-house research programs in this area prior to the initiation of this program. Many ceramic materials were extensively tested and screened leading to the selection of silicon nitride and silicon carbide. In the stationary turbine program, preliminary design concepts were in existence before the award of the contract. In the vehicular turbine program, development was fairly well along and at least one pass had been completed through all of the factors shown in Figure 1.4 prior to the initiation of this program. This one pass, involving many minor iterations led to a vehicular turbine hot flow path having all ceramic stationary components and designated Design A. Based on further experience gained during engine testing, a modified flow path was generated and designated Design B.

Since initiation of this program with AMMRC and ARPA, work on both the vehicular and stationary gas turbine projects was accelerated. Work accomplished during the first reporting period included, for the vehicular turbine project, initial fabrication development and successful preliminary testing of Design B turbine stators and nose cones made of reaction sintered silicon nitride. Design studies of ceramic turbine rotors showed that computed operating stresses can be withstood by dense silicon carbide and dense silicon nitride. Development programs were started to explore several approaches to fabricate rotors in these materials.

Accomplishments on the stationary turbine project during the first reporting period included obtaining physical property data of hot pressed silicon nitride ceramic and identifying microstructural details of this material. The initial design of ceramic stator vanes was completed and calculated vane stresses were reduced 40% by decreasing the stator vane chord.

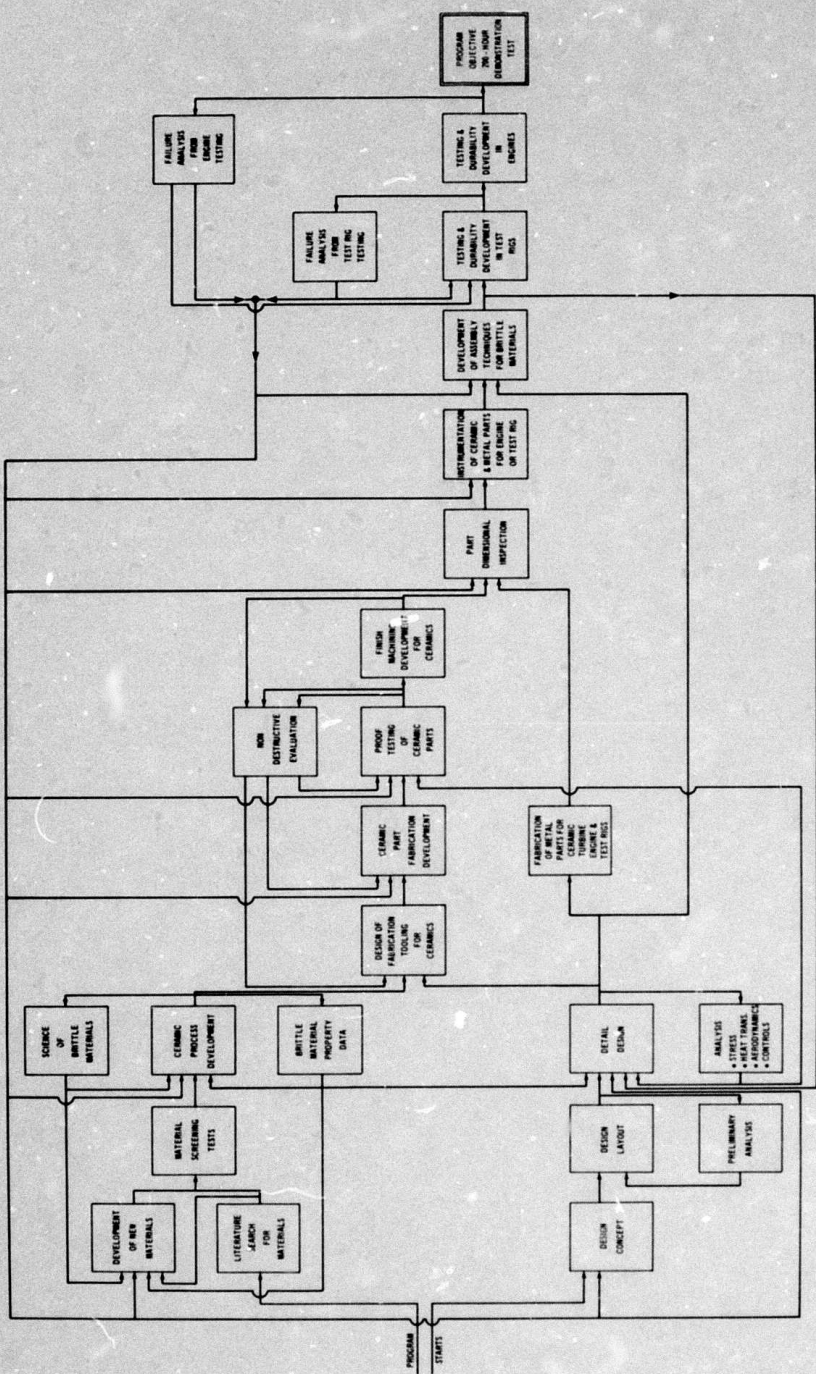


Figure 1.4 — Brittle Material Design/Hight Temperature Gas Turbine - Block Diagram Flow Chart of Iterative Development

The results of work accomplished during the second reporting period included, for the vehicular turbine project, continued fabrication development as well as rig and engine testing of the second generation design (Design B) turbine stators and inlet nose cones. Ceramic turbine rotor design studies were performed on an expanded two-dimensional heat transfer computer program to include rotor attachment designs. Progress was reported on the multi-approaches being explored to fabricate a one-piece, intricately-shaped turbine rotor from candidate high strength ceramic materials.

The results of work accomplished on the stationary turbine project included the stress analysis and design of first stage vanes as well as a preliminary report on the rig for statically testing the stator vanes. Progress on the development of a new three-dimensional, finite-element, stress analysis computer program for subsequent use in ceramic rotor blade design was also reported.

Development of materials technology for both the vehicular and stationary gas turbines was reported and includes continued compilation of material property data, continued characterization of material structure, and development of non-destructive evaluation techniques such as ultrasonics, radiography and acoustic emission.

The results of work accomplished during the third reporting period included, for the vehicular turbine project, considerable emphasis on the development of the ceramic turbine rotor. Development was started on a new concept for a silicon nitride rotor, termed "duo-density". Progress was made on the stress analysis and the development of machining techniques for fabricating monolithic rotors from high-strength hot-pressed materials. A cracking problem in the first stage stator blade appeared solved with the aid of a thermal shock test rig.

On the stationary turbine project, a full scale model of the first generation stator vane assembly showed that the design was functional when subjected to differential motions well in excess of design limits. Using improved physical property data, the transient thermal stresses in the first stage stator vane were recalculated. The three-dimensional stress analysis program was applied to a dense silicon nitride rotor blade.

Work on materials technology resulted in additional property data on candidate ceramic materials, and further relationships of microstructure to properties were uncovered. A number of processing parameters were examined for reaction-sintered silicon nitride.

The work accomplished during this fourth reporting period includes, for the vehicular turbine project, the continued development of methods for fabricating duo-density silicon nitride turbine rotors during which several rotors were made; the best of these was spin-tested to 50,500 rpm before failure. A refined stress analysis of a monolithic silicon nitride rotor was completed, and the effects of a severe flame-out transient on the duo-density rotor was analyzed. Design revisions have been made to both stator stages, which resulted in the elimination of most but not all cracking.

Work accomplished on the stationary turbine project includes stator vane design modifications with improvements to aerodynamics and methods of mounting. Additional stress analyses have been performed at critical interfaces. The static test rig, for evaluation of ceramic stator vanes under realistic gas turbine conditions, has been completed and installed. Design concepts and stress analyses of rotating turbine blades continue to be investigated.

Work on materials technology is continuing in both the vehicular and stationary turbine projects. Additional property data on candidate ceramic materials has been determined, and further relationships of microstructure to properties have been uncovered. A number of processing parameters have been examined for reaction-sintered silicon nitride.

This report covers the progress in the period January 1, 1973, thru June 30, 1973.

## 2. SUMMARY OF PROGRESS

### 2.1 VEHICULAR TURBINE PROJECT

The vehicular turbine project is composed of three primary sections -- design, materials, and testing. Within these primary areas there exist many tasks which must be accomplished in order to achieve the program goal of 200 hours of turbine engine operation over a representative duty cycle at ceramic temperatures up to 2500° F. Each semi-annual report is really a progress report detailing the results of work over a six month time increment, and reporting on the individual accomplishments on the tasks which will culminate in the final program objective.

Work is in progress concurrently in areas of turbine engine component design and analysis, ceramic material and process development, material and engine testing, materials technology, and nondestructive evaluation of ceramic engine components. Progress, made in several of these areas in this reporting period, is summarized in this section of the report.

- (1) Refined stress and heat transfer analyses of the monolithic  $\text{Si}_3\text{N}_4$  turbine rotors have been completed and the resulting data reported. The effects of engine flame-out at maximum speed and inlet temperature were analyzed, for the duo-density  $\text{Si}_3\text{N}_4$  rotors, and show that a maximum circumferential stress of 16,000 psi should be expected under these conditions. Refer to Section 3.1.1 for more details of this work.
- (2) Fabrication development of the duo-density  $\text{Si}_3\text{N}_4$  rotor has been primarily concerned with establishing good bonding between the molded blade ring and the hot-pressed hub. A parametric bonding study identified the time, temperature, and pressure required, and also indicated that no additive was needed to promote joining. A number of various techniques to accomplish pressure bonding were evaluated, and several rotors were fabricated. Refer to Section 3.1.2 for further information.
- (3) Additional work on forming chemically vapor deposited silicon carbide turbine rotors resulted in the delivery of seven rotors for evaluation. The troublesome cavity at the base of each blade was eliminated by the use of a two-step deposition. Refer to Section 3.1.2 for a more detailed account of this work.
- (4) The test rig for the evaluation of ceramic rotors under turbine conditions has been completed and initial shakedown tests were performed successfully. Refer to Section 3.1.3 for more information.
- (5) A number of ceramic turbine rotors have been spin tested to failure. The best duo-density rotor failed at 50,500 rpm; a duo-density hub of hot-pressed  $\text{Si}_3\text{N}_4$  did not fail at 80,000 rpm, which is well above the 64,200 rpm maximum design speed. The best of the CVD silicon carbide rotors failed at only 13,260 rpm, indicating the need for considerable material quality improvement. Refer to Section 3.1.3 for more details of this testing.
- (6) A revised design stator assembly, termed inverted channel, has been tested and found to greatly reduce but not completely eliminate second stage stator shroud cracking. Blade cracking of the first stage stator has been substantially reduced by design modifications. One of these stators has survived 104 hours of static testing in a turbine engine. Refer to Sections 3.3.1 and 3.3.2 for more information.

## 2.2 STATIONARY TURBINE PROJECT

The stationary turbine project is a design study of brittle materials in a high temperature gas turbine application, culminating with the demonstration of uncooled ceramic stator vanes in an advanced power turbine operating for 200 hours. This operation will consist of 100 sequences of peaking cycle service. A performance simulation of ceramic rotor blades will also be performed by computer. Work is currently in progress in areas of stator vane design and analysis, rotor blade design and analysis based on 3 dimensional finite element stress analysis codes, component fabrication, and material technology. Progress is summarized in this section of the report.

(1) The 3 piece ceramic stator vane of first generation design is discussed with respect to the static rig test assembly. Eight silicon nitride vanes, together with insulators and all other support structures will be subjected to actual turbine conditions at 2200° F. A second generation design is expected to improve the aerodynamic characteristics of the stator vane assembly and also lower the contact and thermal stresses, especially within the end caps. Refer to section 4.1.1 of this report for more detailed information.

(2) Two dimensional finite element stress and heat transfer analyses of the airfoil-end cap-insulator system were completed. A maximum contact stress of 6000 psi is expected to develop at the airfoil-end cap interface. Contact stresses at the major end cap-insulator interface should not exceed 500 psi. If edge loading should occur at the end cap-insulator interlocks, the contact stress may reach 10,000 psi. A thermal stress distribution of 6500 to 13,400 psi has been calculated for silicon nitride end caps under steady state conditions. Refer to section 4.1.2 of this report for more complete information.

(3) Norton delivered 20 stator vane assemblies machined from HS-130 silicon nitride. Defects in the form of surface scratches, cracks, and inclusions were documented by Xy glo, x-ray radiography, and ultrasonic scanning. Dimensions and surface finish were also checked. The results are discussed in section 4.1.3.

(4) The static rig for the test and evaluation of ceramic components at temperatures up to 2500° F has been installed at Westinghouse Gas Turbine Systems Division. Tests at 2200° F are scheduled to begin in July. The static rig is described in section 4.1.4 of this report.

(5) The Westinghouse Isoparametric Element Code (WISEC) for the three dimensional stress analysis of solids has been expanded to include steady state and transient heat transfer analysis. This additional capability is demonstrated by comparing a simple solution for heat transfer in a flange assembly with 2 dimensional finite element and finite difference results in section 4.2.1 of this report.

(6) The three dimensional finite element stress analysis codes have been used to determine stress distribution in a tentative rotor blade design under conditions of centrifugal loading. The effect of friction and contact angle at the dovetail attachment of the blade with the disc contribute to stresses as high as 38,000 psi in the root section. Refer to section 4.2.2 of this report for more detailed information.

## 2.3 MATERIALS TECHNOLOGY - VEHICULAR AND STATIONARY TURBINE PROJECTS

Complete property characterization of the ceramic materials for turbine engine use is an enormous task, which will proceed throughout the life span of the contract. This task is complicated by the fact that many of the materials being investigated are in the developmental stage. Improvements in properties are anticipated, which will require that some, if not all of the physical properties will be re-determined eventually. Progress in materials technology is summarized in this section of the report.

(1) Physical property data were obtained for various ceramic materials during this reporting period. Transverse strength measurements were used to compare Norton HS-130 hot pressed silicon nitride with Norton hot pressed silicon carbide and "Refel" reaction sintered silicon carbide. The compressive strength of hot pressed silicon carbide and silicon nitride are reported as a function of temperature. Additional data describe the shear modulus of silicon nitride. Refer to section 5.1.1 for more information.

(2) Weibull statistics were used to relate the flexural and tensile strength properties of Norton HS-130 silicon nitride. Tensile and flexural data for different areas under stress at 1800°F fall on the curve predicted by 2 parameter Weibull when  $m = 5.3$  and  $\sigma_0 = 58,800$  psi. Refer to section 5.1.1 for a further discussion of these results.

(3) The tensile strength of Norton HS-130 silicon nitride varies between 61,000 psi at room temperature and 20,000 psi at 2500°F. These results were verified by tests at Southern Research at RT and 2350°F. Ultimate tensile strength and elastic modulus of Norton hot pressed silicon carbide are also reported in section 5.1.1 of this report.

(4) The thermal properties of Norton hot pressed silicon carbide were measured by Battelle. Thermal expansion, diffusivity, conductivity and specific heat are reported for both directions of the material in section 5.1.1 of this report.

(5) Creep of Norton HS-130 silicon nitride in air is approximately three times greater than in an inert atmosphere. Creep strains exceeding 2% are reported. Stress rupture life in air is essentially the same as in helium. This phenomenon is discussed in section 5.1.1 of this report.

(6) Corrosion erosion tests at 2000°F using additive free diesel fuel indicate that silicon nitride and silicon carbide remain nominally unaffected. Preliminary data have been acquired at 2500°F. Evidence of oxidation was observed after 25 hours but the results were certainly not catastrophic. Refer to section 5.1.1 for more information.

(7) Creep testing in bending has been performed on reaction-sintered silicon nitride, which revealed that calcium has a substantial deleterious effect upon creep. Low calcium silicon nitride had a creep rate of  $3 \times 10^{-6}$  in/in/hr as compared with a creep rate of  $7.5 \times 10^{-4}$  in/in/hr for high calcium material when both materials were tested at 2210°F. and 5000 psi stress. Please refer to Section 5.1.2 for more information.

(8) Specific heat and thermal conductivity of reaction-sintered silicon nitride have been determined. Section 5.1.2 contains data from this work.

(9) The microstructure of Norton hot pressed silicon carbide was studied in detail. Aluminum and tungsten represent impurities in greatest concentration. Stacking faults and dislocations were identified within the microstructure. Refer to section 5.2.1 for more information.

(10) The static oxidation of silicon nitride and silicon carbide in wet oxygen is somewhat greater than that observed in dry oxygen. An oxide layer of aluminum silicate and cristobalite was identified on SiC. Refer to section 5.2.2 for complete details.

(11) Continued work in sintering parameters has shown that the strength of reaction-sintered silicon nitride can be substantially improved by the addition of small amounts of hydrogen to the nitrogen atmosphere used for nitriding. Please refer to Section 5.2.3 for more information.

(12) Activities in non-destructive material evaluation were primarily concern with defects in hot-pressed silicon nitride. A computer-aided ultrasonic defect detection system was evaluated as to its potential for locating small flaws; this work is described in Section 5.3.1. A novel method for locating surface cracks in hot-pressed silicon nitride, using a CO<sub>2</sub> laser in conjunction with acoustic emission measuring equipment, is described in Section 5.3.2.

### 3. PROGRESS ON VEHICULAR TURBINE PROJECT

#### 3.1 CERAMIC ROTOR DEVELOPMENT

##### SUMMARY

The ceramic rotor development program placed increased emphasis on the "duo-density" concept which combined injection-molded reaction-sintered silicon nitride blades with a hot-pressed silicon nitride hub.

During this reporting period, considerable work was done on developing bonding techniques between the reaction-bonded silicon nitride blade rings and the hot-pressed hubs. It was shown that a bond could be achieved between these components if total support is provided for the blades during the pressing stage of this process. This total blade support has not yet been achieved; however, partial support using segmented tapered graphite dies inside a tapered graphite ring has shown encouraging results. Repeatability in achieving good bonding is the most difficult unsolved problem with this technique.

In-depth processing studies have been initiated in conjunction with the duo-density bonding technique investigation. The effects on bond strength of varying pressure, temperature, time, and magnesium oxide bonding aid are presented from this study.

Analytical investigations of the effects of engine flame-out at full speed and maximum inlet temperature were performed on the duo-density design, and it was found that a maximum circumferential stress of 16,000 psi existed in the reaction-sintered silicon nitride rim. A detailed three-dimensional finite element analysis will be required to completely map the stress distribution in this region.

Fabrication difficulties have been encountered in the attempts to form a fully monolithic hot-pressed silicon nitride rotor by the conformable tool, pseudo-isostatic method. Apparently insurmountable problems of gross blade distortion and cracking resulted in discontinuation of this program.

Structural design analysis of the monolithic hot-pressed silicon nitride rotor concept continued during this reporting period with refinements to the basic two-dimensional analysis. Emphasis was placed on the cold-start and full-power acceleration transients. This basic design remains the most attractive candidate rotor concept under consideration based upon design stress considerations.

The chemically vapor deposited silicon carbide rotor program has produced seven rotors. Success was achieved in completely filling the blade cavity by the use of a two-step deposition technique. However, failure analysis of rotors which were spin tested indicated that excessive residual stresses are present in these rotors.

Work is continuing on electric discharge machining of a fully dense silicon carbide rotor. Attempts have been made to machine simulated rotor airfoils having flat tapered shapes. However, fracture occurred prior to complete machining of the entire length of these shapes. Scanning electron microscopic examination indicates rough irregular surfaces are being generated. Further machining studies are in progress in an attempt to reduce this surface damage.

Spin tests have been made on duo-density rotors, rotor components, and test specimens. It was concluded that the hot-pressed hubs, by themselves, are adequate for high speed applications. As was expected, the reaction-bonded blade ring failures occurred at less than design speed, indicating the need for support from the hot-pressed hub.

The Turbine Rotor Test Rig has been completely assembled and is undergoing shakedown. Room temperature tests to 70,000 RPM have been successfully achieved with metal rotors. An evaluation of simulated engine transient conditions is currently being conducted in this rig.

### 3.1.1 DESIGN AND ANALYSIS

#### Introduction

Finite element heat transfer and stress analysis results are presented for both monolithic Design C hot-pressed silicon nitride and duo-density silicon nitride ceramic rotor concepts. Comprehensive refinements have been made to the monolithic analyses presented in the previous reports. (1,2) The results of cold-start and idle-to-full power accelerations are discussed for the monolithic design. The analysis of the duo-density concept concentrated on the severe condition of engine flame-out at temperature. The results of these analyses, including isotherms and stress contour plots, are presented in this section.

#### Analysis of Design C Monolithic Hot-Pressed Silicon Nitride Rotors

The analysis of Design C hot-pressed  $\text{Si}_3\text{N}_4$  turbine rotors was continued during this reporting period for idle, full-speed, and transient engine operating conditions. Finite element computer models of the individual rotors were used with the thermal boundary conditions determined by the computer model of the rotor and attachment assembly presented in the last report. (1) This method follows the organization of the design process as presented in an earlier report. (2)

A model of a large section of the engine containing the rotors and the turbine shaft together with the rotor attachment was used initially. This model provided realistic thermal boundary conditions for a more refined model of the rotors and rotor attachment assembly. The rotor attachment assembly model was used to analyze the folded bolt rotor attachment concept. The assembly model also pinpointed the highly stressed regions in the rotors as well as supplying thermal boundary conditions for models of the individual turbine rotors. Although the stress data gathered from the rotor attachment assembly model reported earlier (1) was known to be a low estimate of the actual rotor stresses, the time of maximum transient stresses determined for each rotor was considered to be accurate.

Throughout this section, reference will be made to first and second transient conditions. The first transient condition assumed the rotors to be at room temperature and then suddenly exposed to idle turbine inlet temperature conditions while rotating at 55% of full speed. The stresses in the rotors were studied as a function of time to determine the time and magnitude of maximum rotor stress. The second transient condition assumed the rotors to have the temperature distribution corresponding to the time of maximum stress during the first transient and be suddenly subjected to full speed turbine inlet temperature conditions while rotating at 110% of full speed. These were the most severe thermal up-shock conditions possible in the engine.

Finite element models of the rotors were made with a mesh density approximately eight times that used for the rotor attachment assembly model. To determine if this refined mesh was sufficiently dense to produce satisfactory results, two additional mesh densities were used to analyze the stresses in the first stage rotor neck. These additional models had mesh densities

of one half and twice that of the model used to study the first stage rotor. The results of the model study are shown in Figure 3.1 along with the stress distribution across the first stage rotor neck determined from the rotor assembly model. It can be seen that doubling the mesh density increases the maximum stress at the surface very little (approximately 3%). This indicated that the mesh density used to model the first and second stage rotors was sufficient and that the effort required to increase the density was not warranted.

Figure 3.1 also indicated that not only was the coarse assembly model a poor mathematical model but it was a poor physical representation of the rotor. With the extremely coarse mesh the rotor geometry could not be represented satisfactorily. The coarse mesh caused the finite element analysis to indicate low stresses on the front face of the first stage rotor. Due to the poor representation of the rotor itself the stress distribution was distorted to the point of indicating rotor neck stresses that were high on the opposite side of the rotor neck compared to those indicated by the individual rotor models.

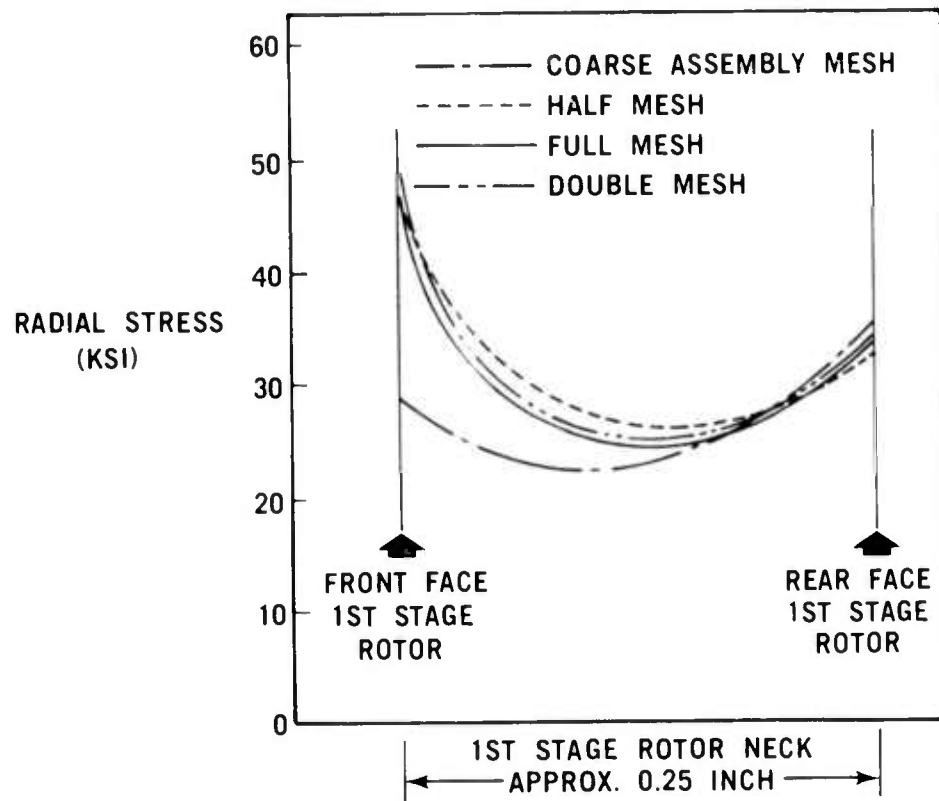


Figure 3.1 Effect of Finite Element Mesh Size on Stresses in First Stage Rotor Neck Under Full Speed Steady State Conditions

The effect of the finite element mesh size on transient stresses near the rotor bore is shown in Figure 3.2. Again, the coarse mesh model of the rotor assembly indicated stresses much lower than the fine mesh models of individual rotors. The largest variance in stresses between the coarse and fine mesh models occurred in the first stage rotor. The individual rotor model indicated stresses approximately 15% higher than indicated by the coarse assembly model for both idle and full speed steady state operating conditions. Both fine mesh models showed increases of approximately 15% over the coarse model for peak stresses during first and second transient conditions.

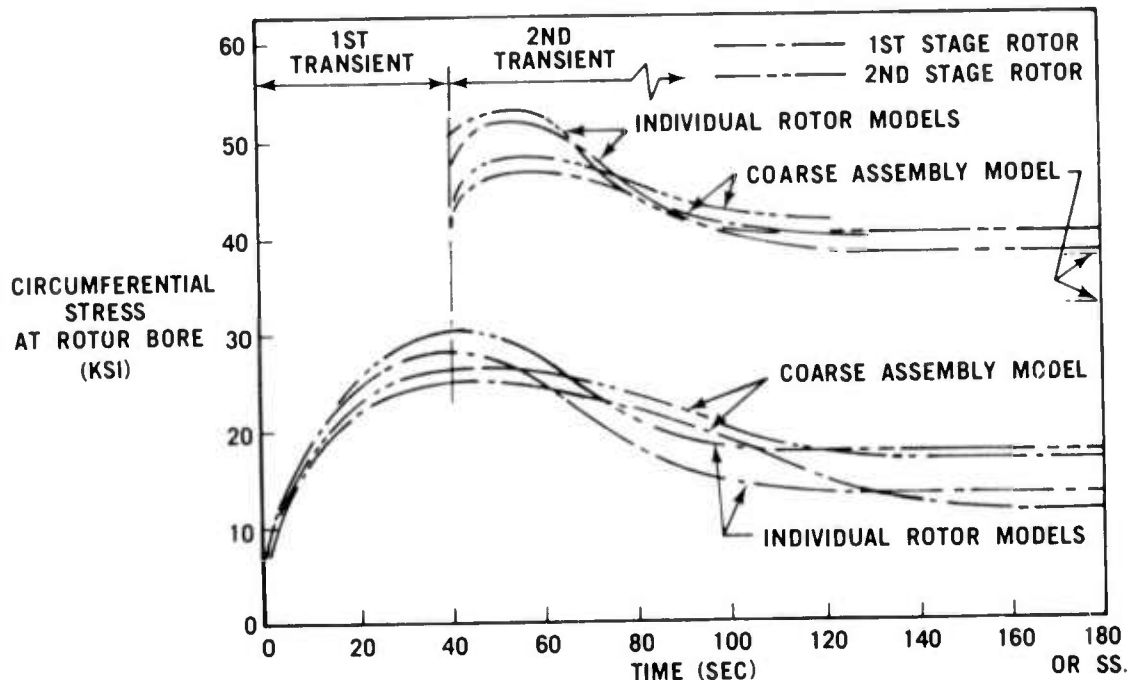


Figure 3.2 Effect of Finite Element Mesh Size on Transient Stresses Near the Rotor Bore

As indicated by Figure 3.1, the mesh density of the finite element models used to analyze each rotor produces acceptable mathematical models. Comparison of the individual rotor models and the assembly model to the actual rotor geometry in the area of the rotor hubs indicates that the physical profile of the rotors is well represented by either mesh density model. Therefore, the 15% increase in stresses indicated in Figure 3.2 were attributed directly to the increased accuracy of the mathematical modeling and independent of any geometry misrepresentation that occurred at or outside the rotor neck region.

From the results of the model comparisons shown in Figures 3.1 and 3.2 it was concluded that the finite element models used to analyze the first and second stage rotors were acceptable mathematical and geometrical representations of these components. Therefore, based on this assumption, the stress and temperature distributions represent the actual stresses and temperatures expected in the Design C hot-pressed silicon nitride rotors for the geometry and loading modes indicated.

The isotherm and isostress plots which follow were plotted on a Gerber drafting machine from magnetic tapes generated by in-house computer codes. These post-processing computer codes were written specifically to handle output data from the finite element two-dimensional axisymmetric heat transfer and stress analysis computer programs used to analyze the turbine rotors.

The turbine rotor blades are not shown in any of the plots. Since the computer codes used in the analysis were axisymmetric, pseudo material properties were used to represent the blades and the transfer of the blade load to the rotor.

Isotherms were plotted every 20° with bold isotherms every 100°. The isostress contours were plotted for the average element stress at each element centroid. Isostress contours were plotted for each 1000 psi with bold lines of constant stress plotted every 5000 psi. Where pseudo material properties were used (i.e., rotor couplings, rotor blades) the element stress was eliminated from the contouring algorithms to avoid distorting the stress contours. Idle condition is 55% speed while 110% speed provides a 10% safety factor to allow for control response lag.

The contouring code generated data to be plotted on a regular rectangular grid. In some instances, this contouring grid did not meet the boundary of the rotor, which causes a blank area near the perimeter of the rotor. The stress contours for this area can be approximated by continuing the last contouring density out to the rotor perimeter. It should be noted, however, that the stress gradient is not constant near the surface at any point. This can be seen in Figure 3.1.

The element stress used to produce the stress contours was the maximum principle stress in each element. This stress was deemed the most useful in showing trends and critical areas since ceramics are most susceptible to failure in tension. In the area of the rotor bore, the maximum principle stress in all elements is always in the circumferential direction. In the rotor neck region, the maximum principle stress is in the radial direction in all elements. Between the bore and the neck region, the maximum principle stress in some elements is radial while in others it is circumferential.

The strength of the hot-pressed silicon nitride material assumed for this component is a function of its temperature. For this reason not only the stress distribution but the corresponding temperature at that stressed point must be known. With the temperature-stress data known, a realistic evaluation of the design can be made.

Thermal stresses are very difficult to predict in a complex structure and even more difficult if the thermal boundary conditions vary with respect to time and/or distance. Stresses resulting from centrifugal loading alone, however, are predictable. Centrifugal or mechanical stresses are a function of the rotational speed squared, therefore when the speed is doubled, with no thermal gradients, the stress in the rotor should quadruple for any given radial dimension. This effect is shown for the first stage rotor in Figures 3.3 and 3.4 and the second stage rotors in Figures 3.5 and 3.6.

## HOT GAS FLOW

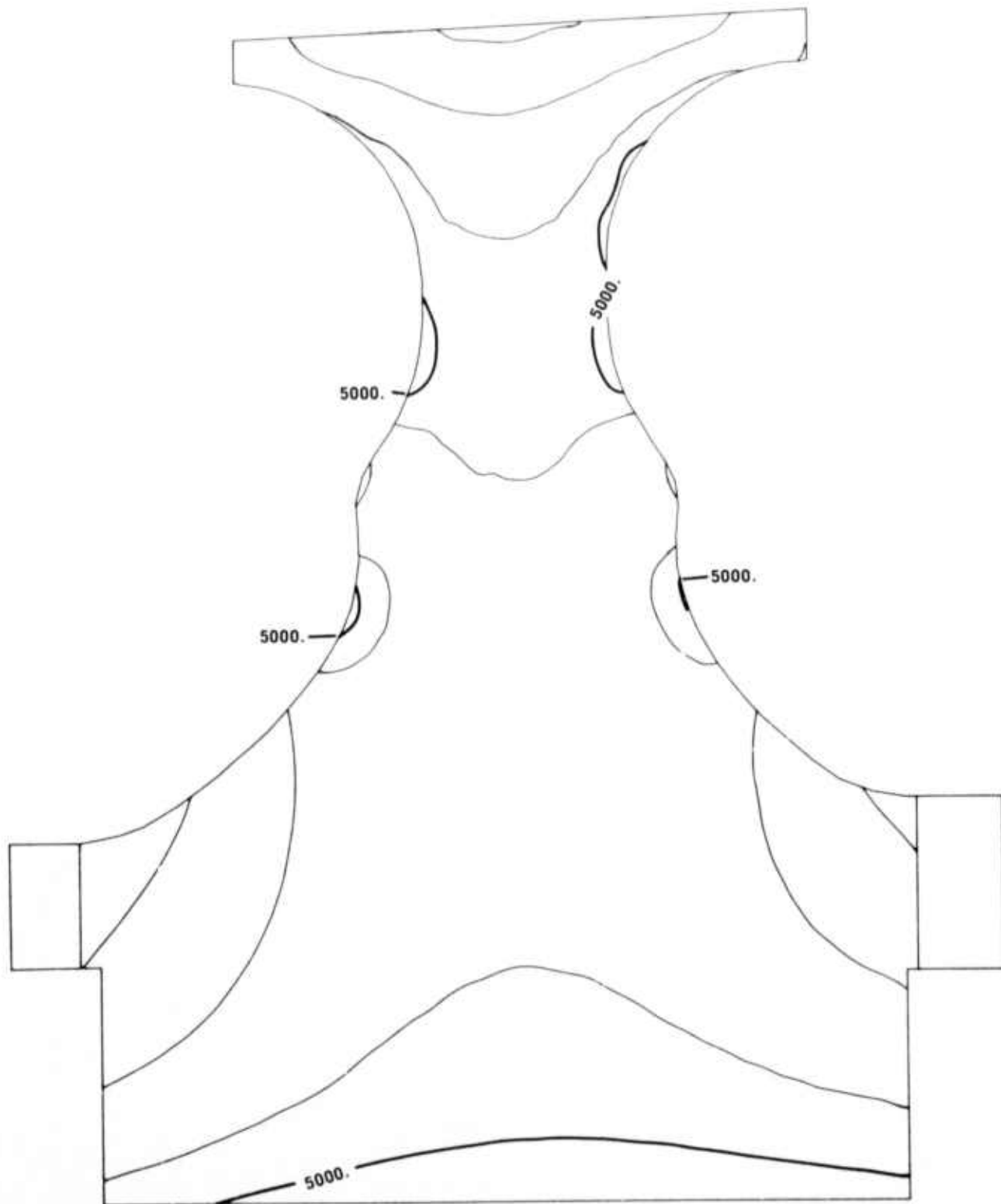


Figure 3.3 Maximum Principle Stresses (psi) in First Stage Rotor at 55% Speed Centrifugal Loading

## HOT GAS FLOW

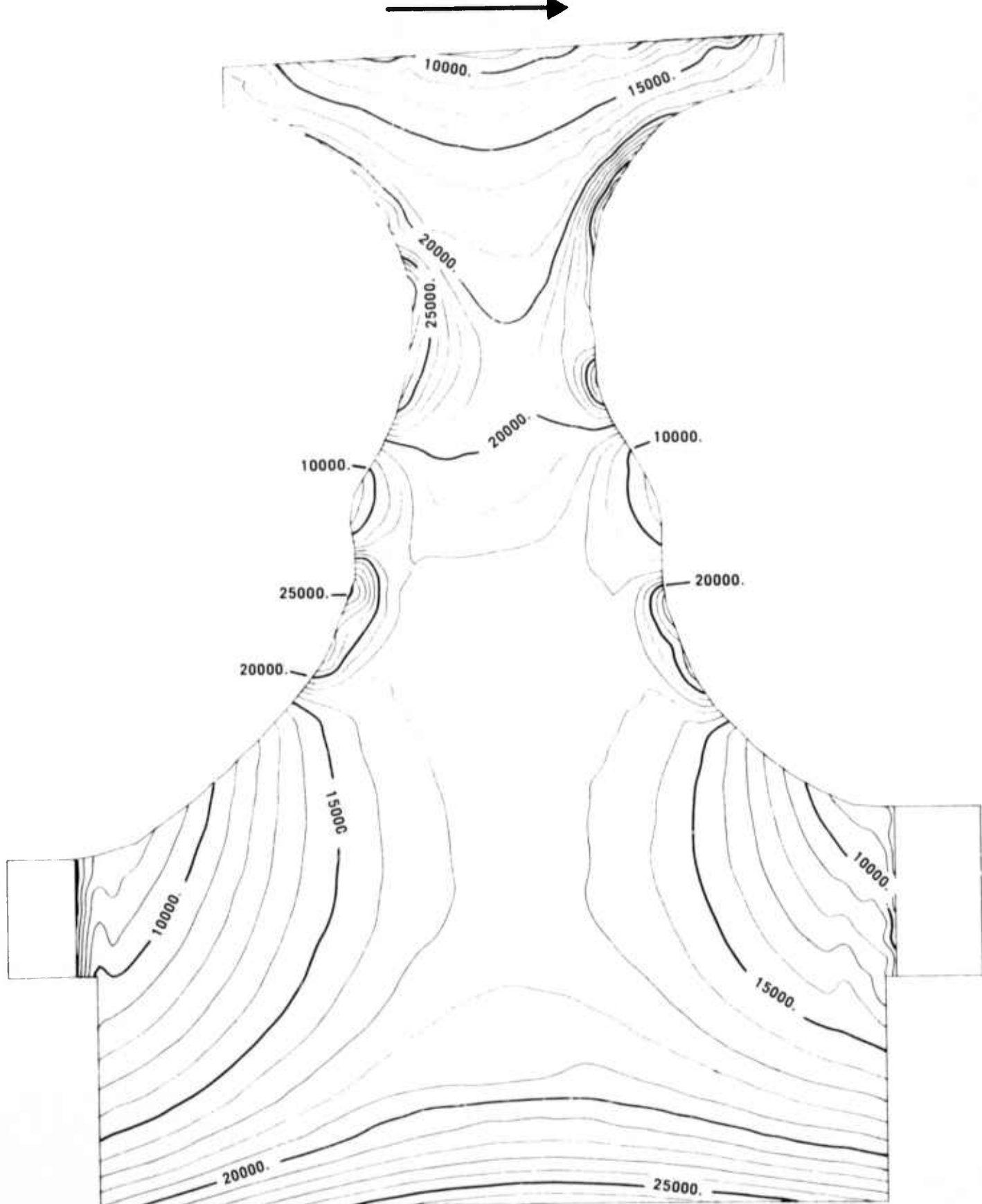


Figure 3.4 Maximum Principle Stresses (psi) in First Stage Rotor at  
110% Speed Centrifugal Loading

## HOT GAS FLOW

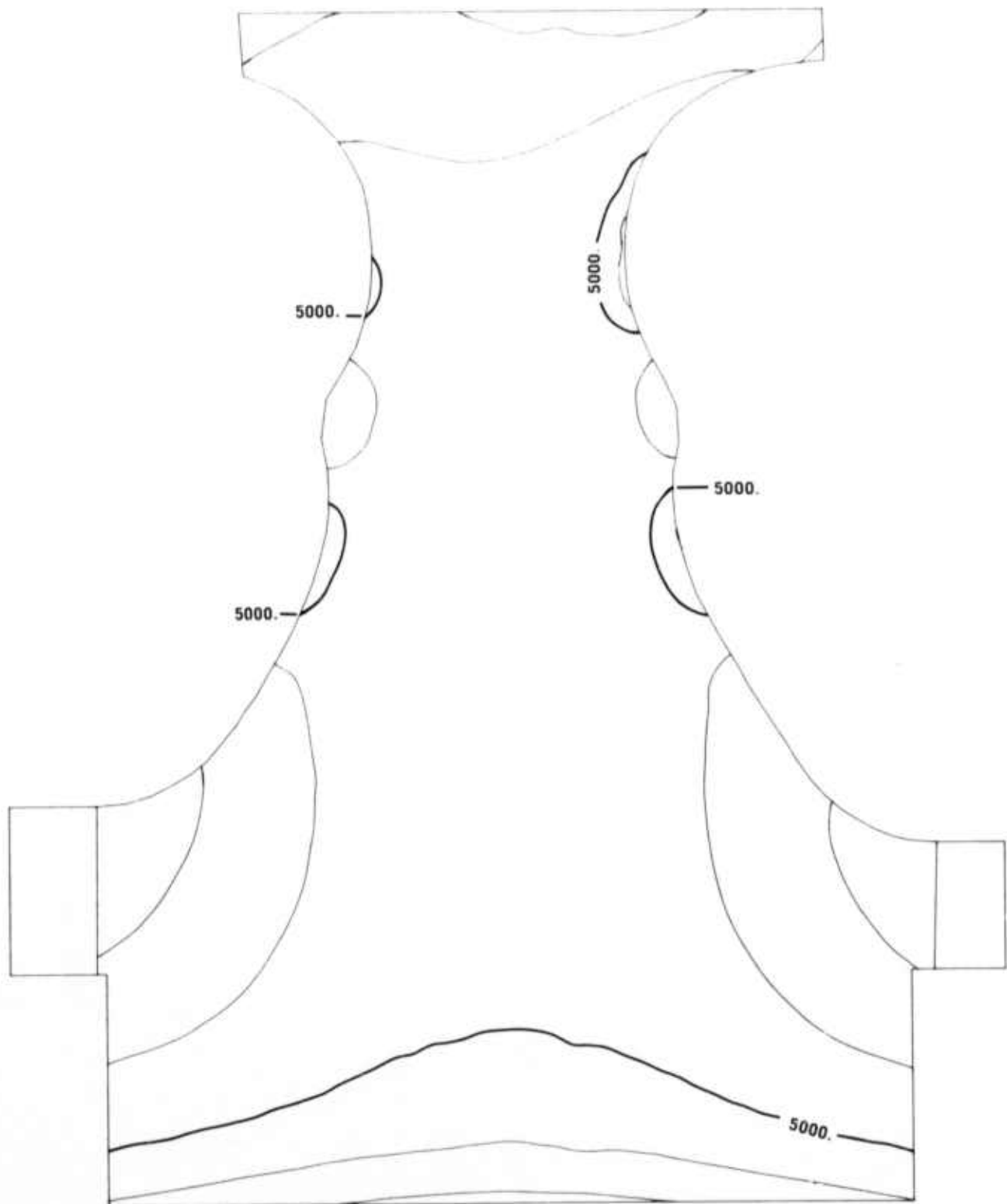


Figure 3.5 Maximum Principle Stresses (psi) in Second Stage Rotor at 55% Speed Centrifugal Loading

## HOT GAS FLOW

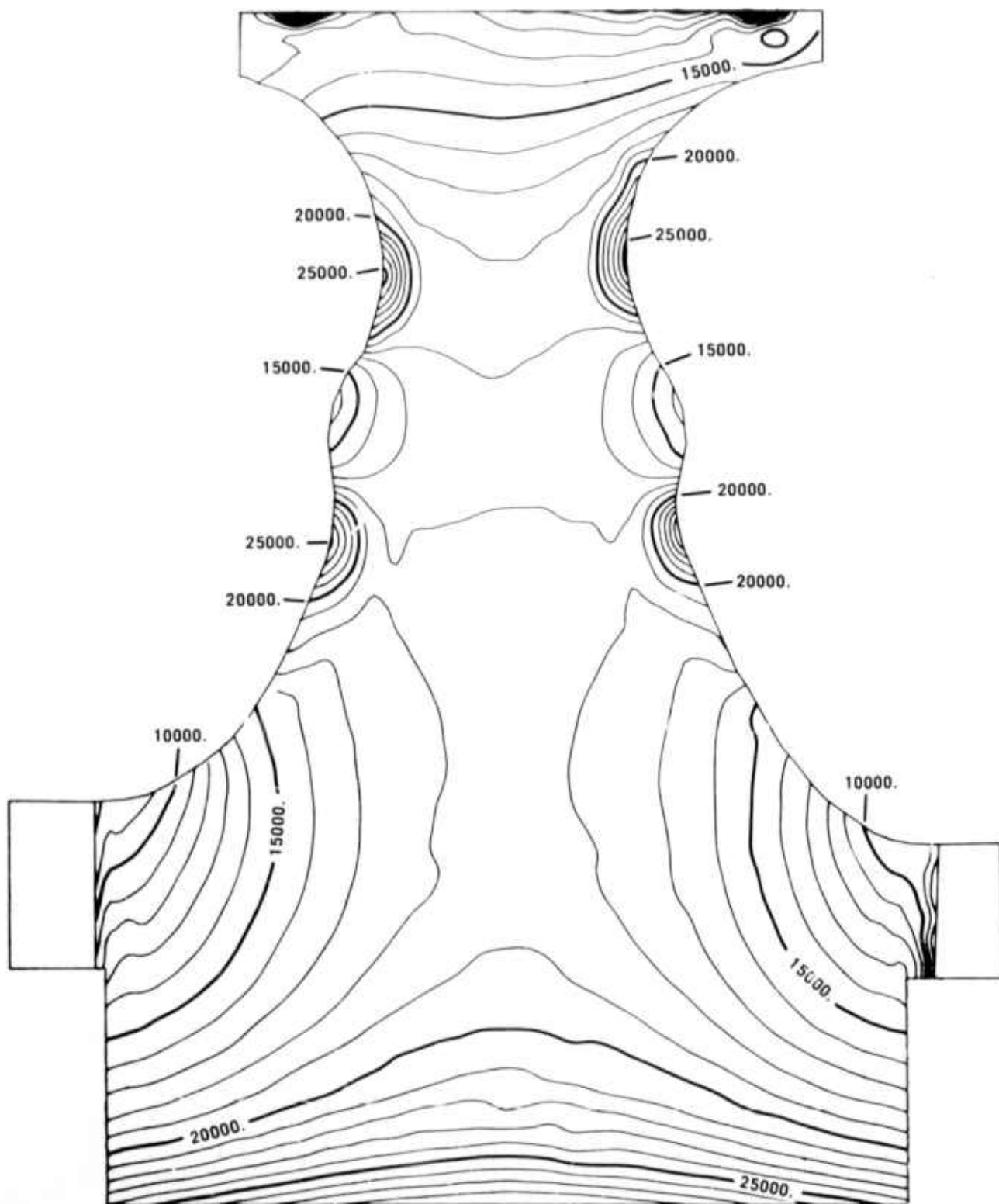


Figure 3.6 Maximum Principle Stresses (psi) in Second Stage Rotor at 110% Speed Centrifugal Loading

Figures 3.3 through 3.6 show that the centrifugal stresses are evenly distributed over the rotor cross sections, indicating a well balanced geometry in the plane of rotation. It must be emphasized, however, that these stress distributions are mechanical only; the addition of thermal stresses can alter the total stress distribution considerably.

The least severe steady state engine operating conditions occur at 55% speed. These minimum steady state operating conditions for the first and second stage rotors are shown in Figures 3.7 through 3.10. Note that the stress distributions are no longer symmetric as was the case for centrifugal loading only. Rotor bolt cooling air washes the front face of the first stage rotor while the turbine end labyrinth seal on the high speed shaft bleeds cool air up the rear face of the second stage. Due to the chilling effect of these cooling air streams the front face of the first stage and rear face of the second stage rotors have both increased stresses and stress gradients.

Figures 3.7 and 3.8 show a maximum idle steady state operating stress at the first stage rotor bore of 13,000 psi at a temperature of 1580°F while the maximum stress in the rotor neck is 13,000 psi at 1780°F on the front face. For the second stage rotor, Figures 3.9 and 3.10 show 18,000 psi at 1400°F at the bore and 17,000 psi at 1580°F for the rear face of the rotor neck under the same engine operating conditions.

The most severe steady state operating temperature and stress levels are shown in Figures 3.11 through 3.14 for the first and second stage rotors. Again, the stress distributions are distorted from a symmetric distribution due to the thermal gradients and cooling air streams. Figures 3.11 and 3.12 show a maximum bore stress of 39,000 psi at 1600°F and maximum neck stress of 43,000 psi at 1900°F for the first stage rotor. Maximum stresses for the second stage rotor, Figures 3.13 and 3.14, are 40,000 psi at 1320°F and 36,000 psi at 1580°F for the bore and neck regions respectively.

Figures 3.15 through 3.18 show the temperature and stress distributions in the first and second stage rotors at time of maximum stress during the first transient. This condition was found to exist 40 seconds after engine ignition took place.

The maximum stress in the rotors occurs 55 seconds after ignition during the second transient. The stress conditions existing at that time are shown in Figures 3.19 through 3.22. The first stage rotor bore is expected to experience 52,000 psi at 780°F while the neck region stress will go up to 53,000 psi at 1400°F. The second stage rotor will be subjected to 53,000 psi at 740°F at the bore and 45,000 psi at 1400°F at the neck region. Figures 3.23 and 3.24 indicate that very little of this second transient stress is a result of the thermal gradients. The rotor thermal gradients were maintained at the maximum stress point during the first transient and only the rotational speed was changed. With reference to Figures 3.3 through 3.6 it can be seen that the change in rotational speed contributed 21,000 psi of the 24,000 psi stress increase in the

## HOT GAS FLOW

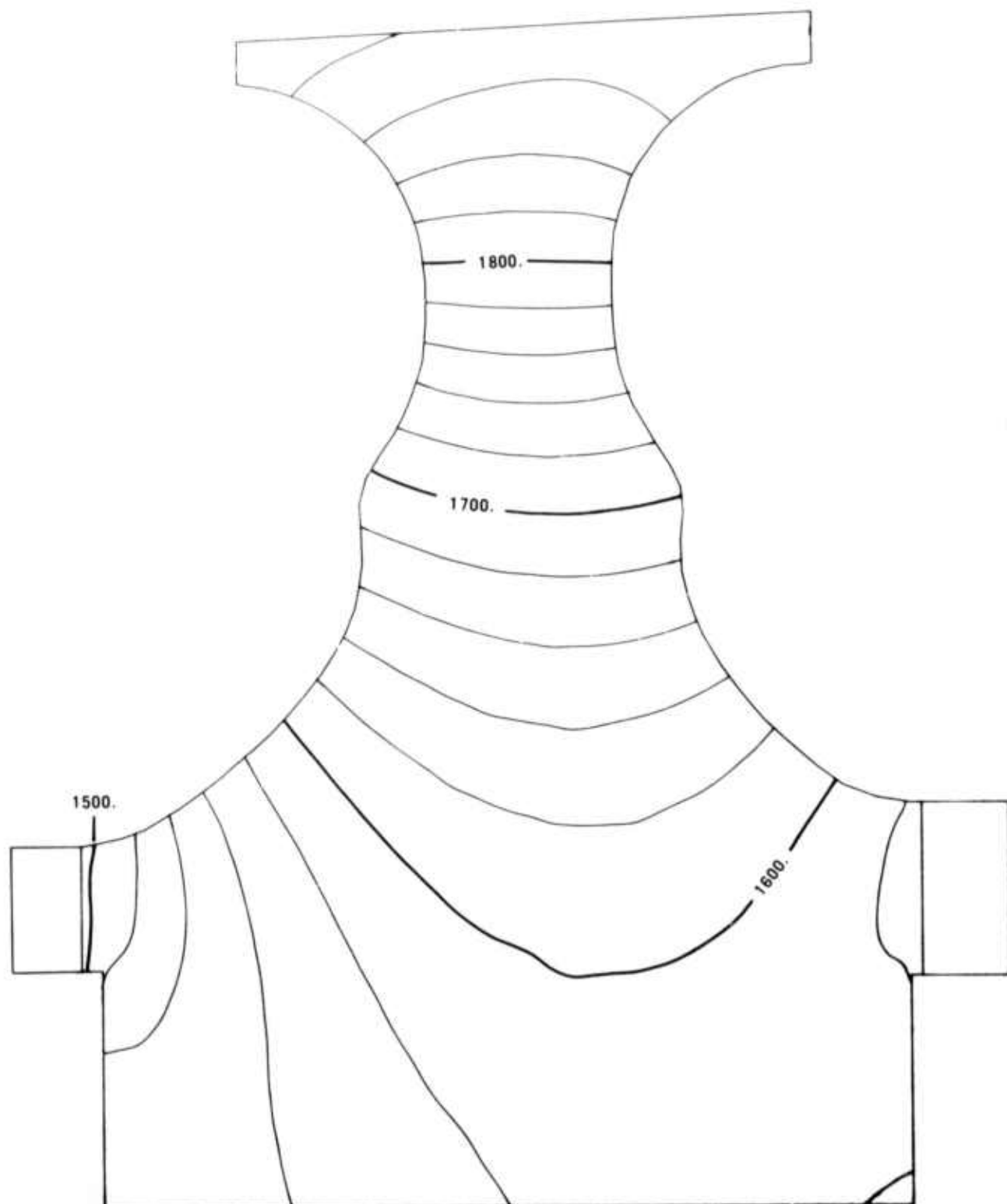


Figure 3.7 Isotherms ( $^{\circ}$ F) in First Stage Rotor at 55% Steady State Speed Temperature Boundary Conditions

## HOT GAS FLOW

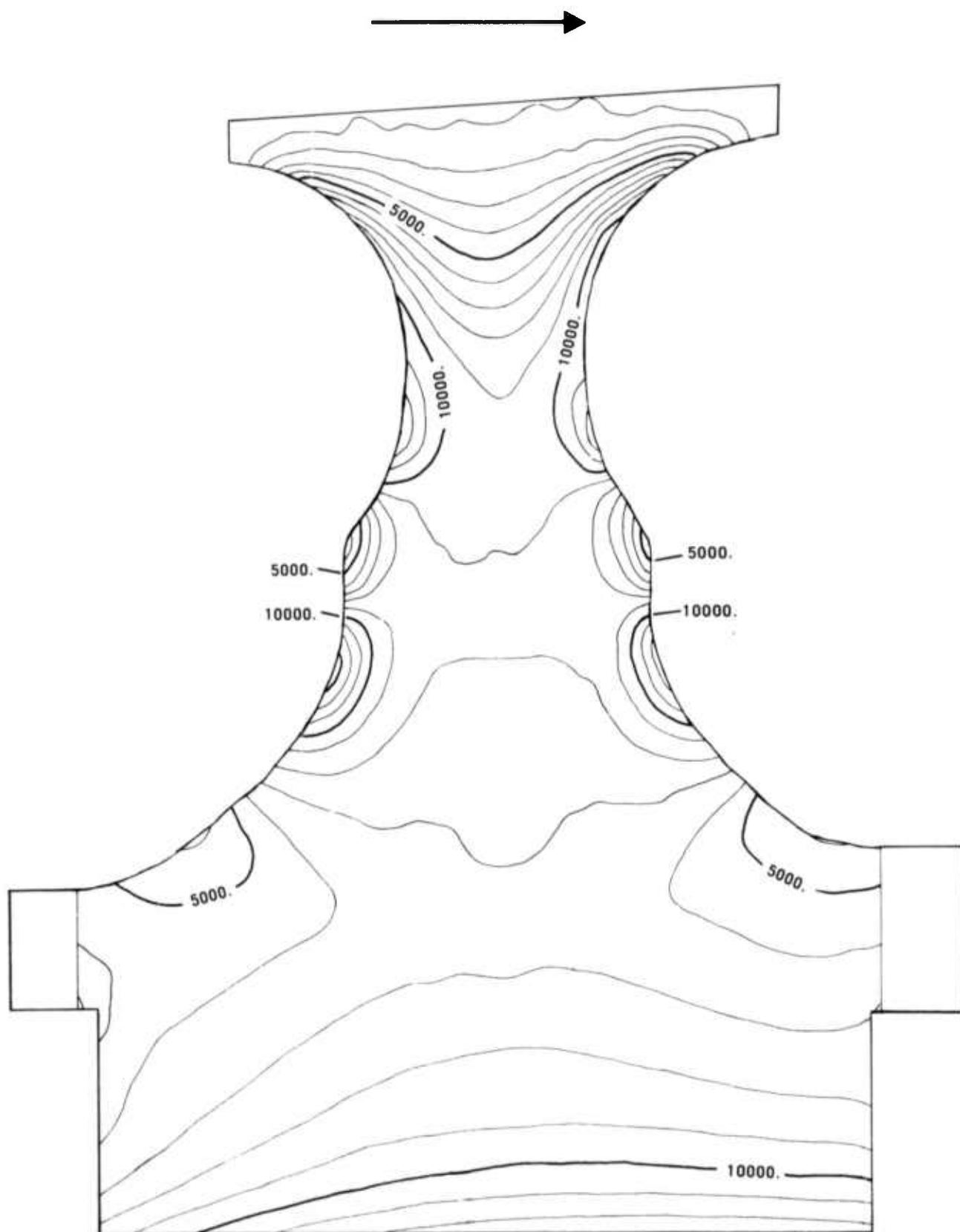


Figure 3.8 Maximum Principle Stresses (psi) in First Stage Rotor,  
Combining Thermal and Centrifugal Stresses at 55% Speed

## HOT GAS FLOW

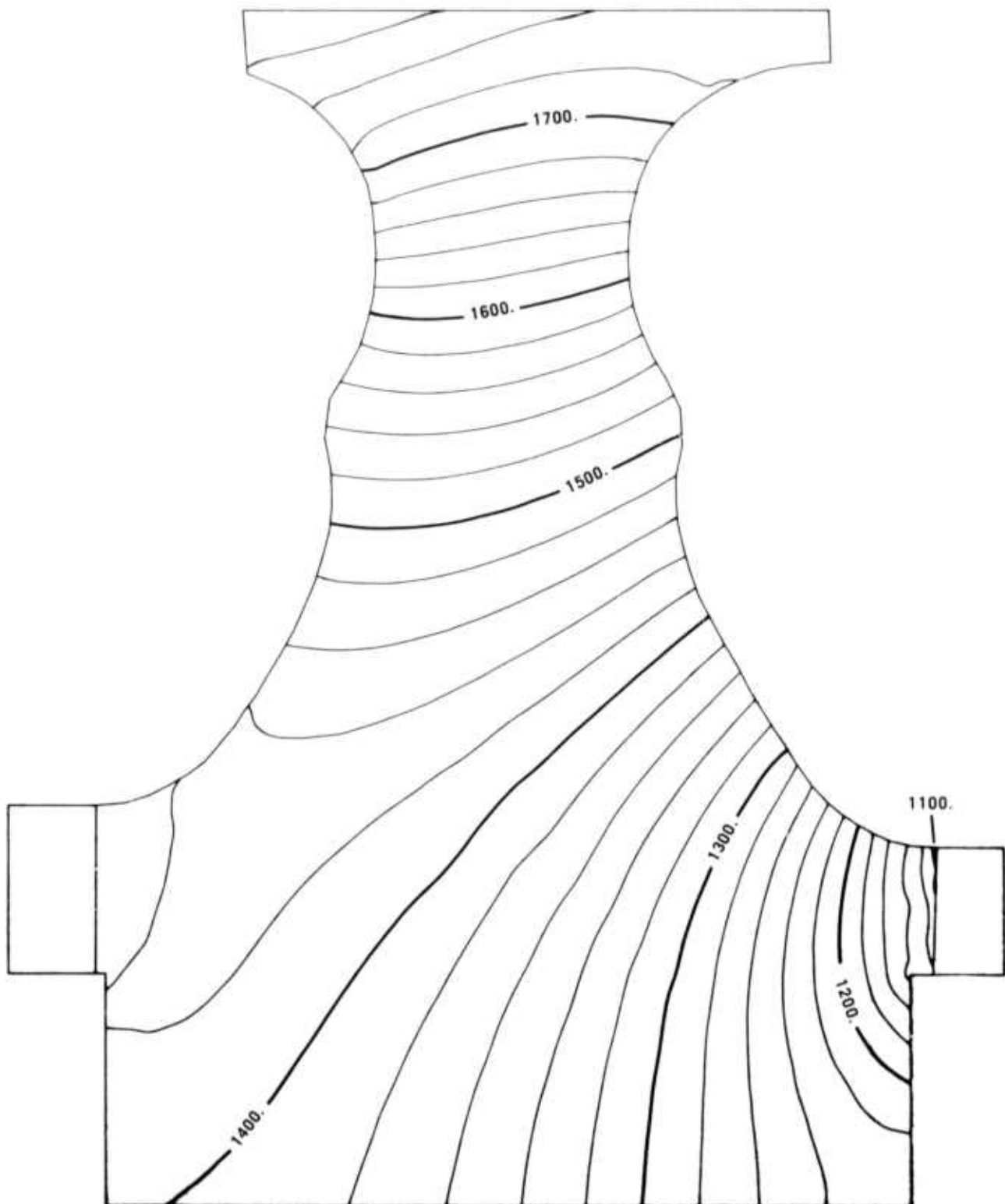


Figure 3.9 Isotherms ( $^{\circ}$ F) in Second Stage Rotor at 55% Steady State Speed Temperature Boundary Conditions

## HOT GAS FLOW

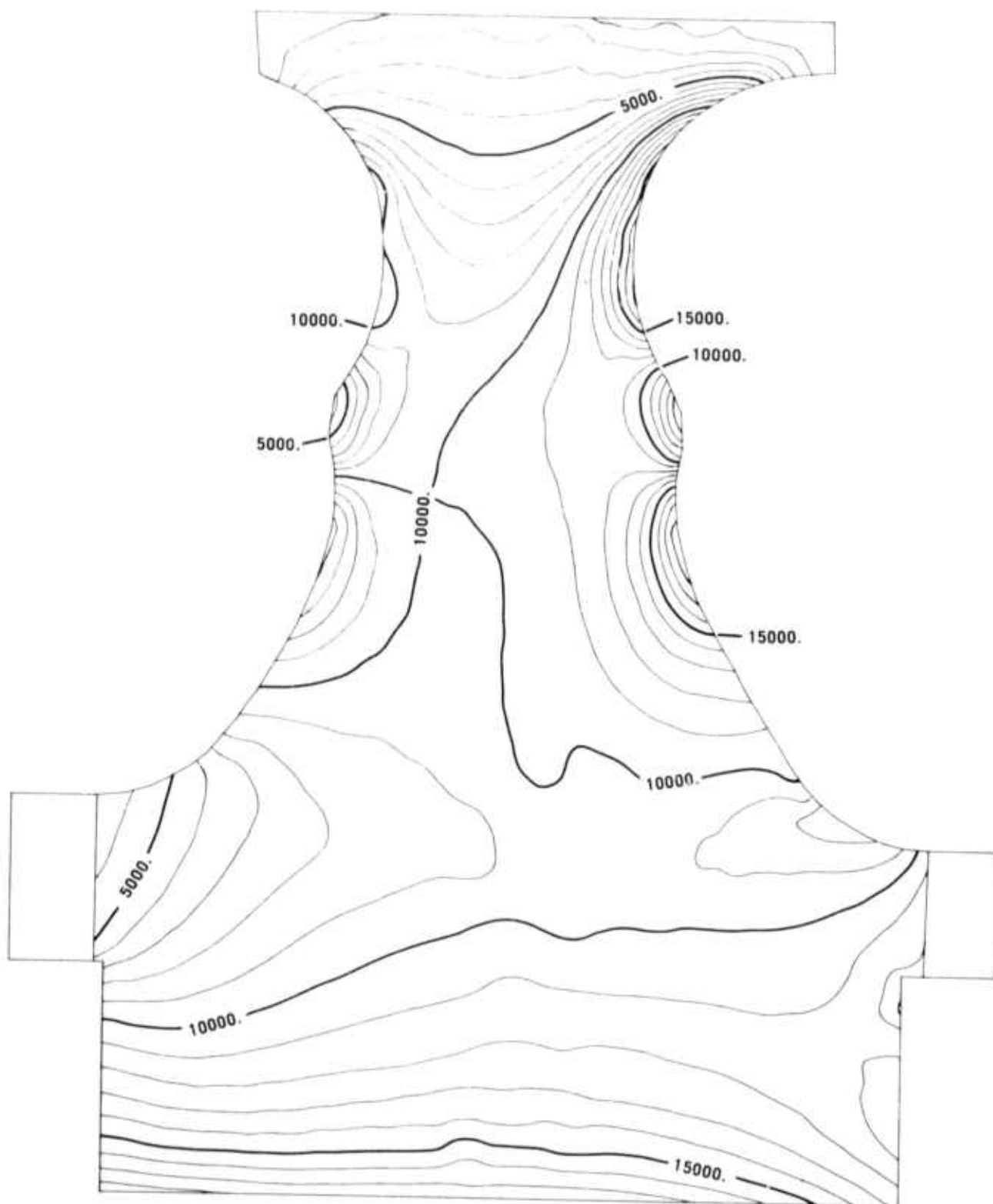


Figure 3.10 Maximum Principle Stresses (psi) in Second Stage Rotor, Combining Thermal and Centrifugal Stresses at 55% Speed

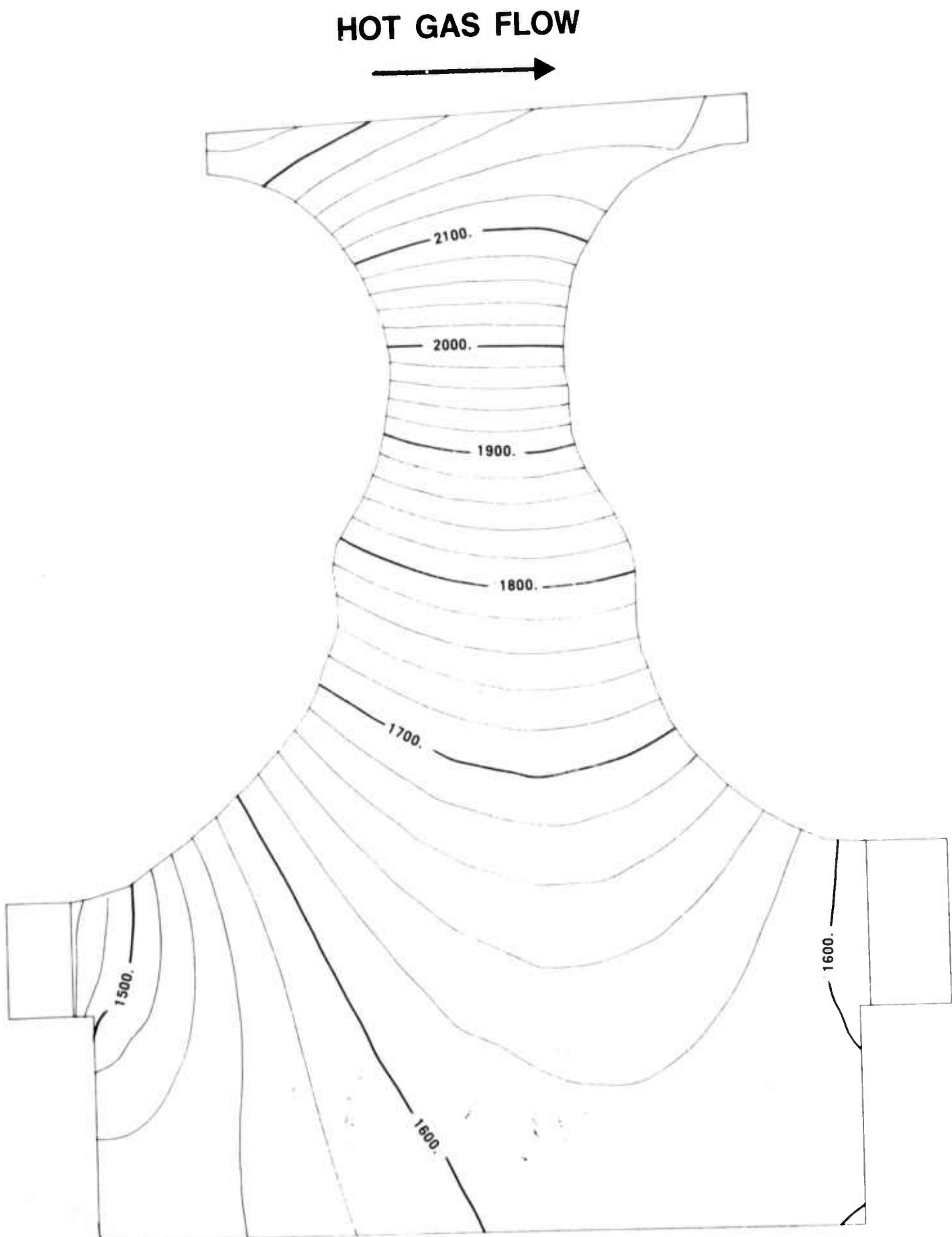


Figure 3.11      Isotherms ( $^{\circ}$ F) in First Stage Rotor at 100% Steady State Speed Temperature Boundary Conditions

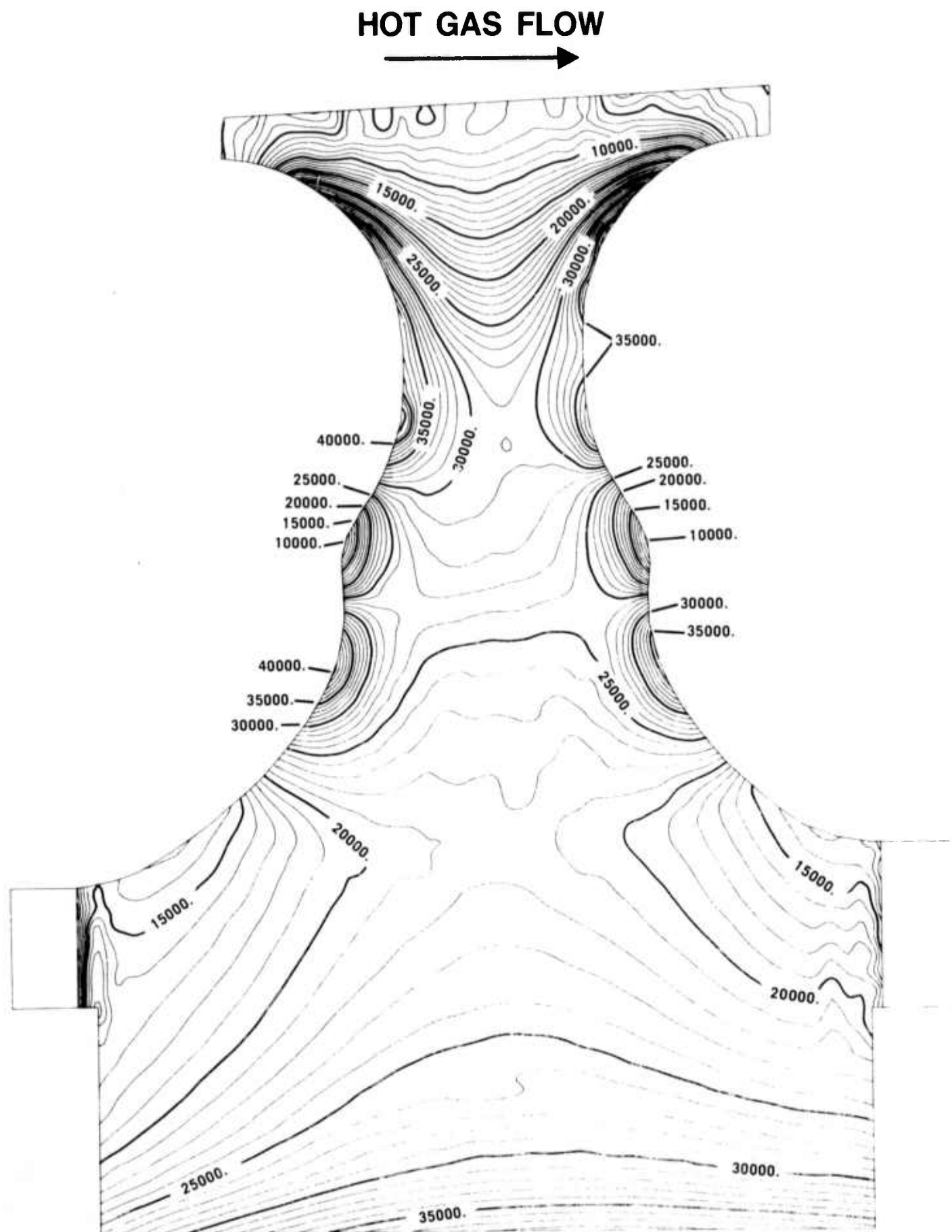


Figure 3.12 Maximum Principle Stresses (psi) in First Stage Rotor,  
Combining Thermal Stresses at 100% Speed and Centrifugal  
Stresses at 110% Speed

## HOT GAS FLOW

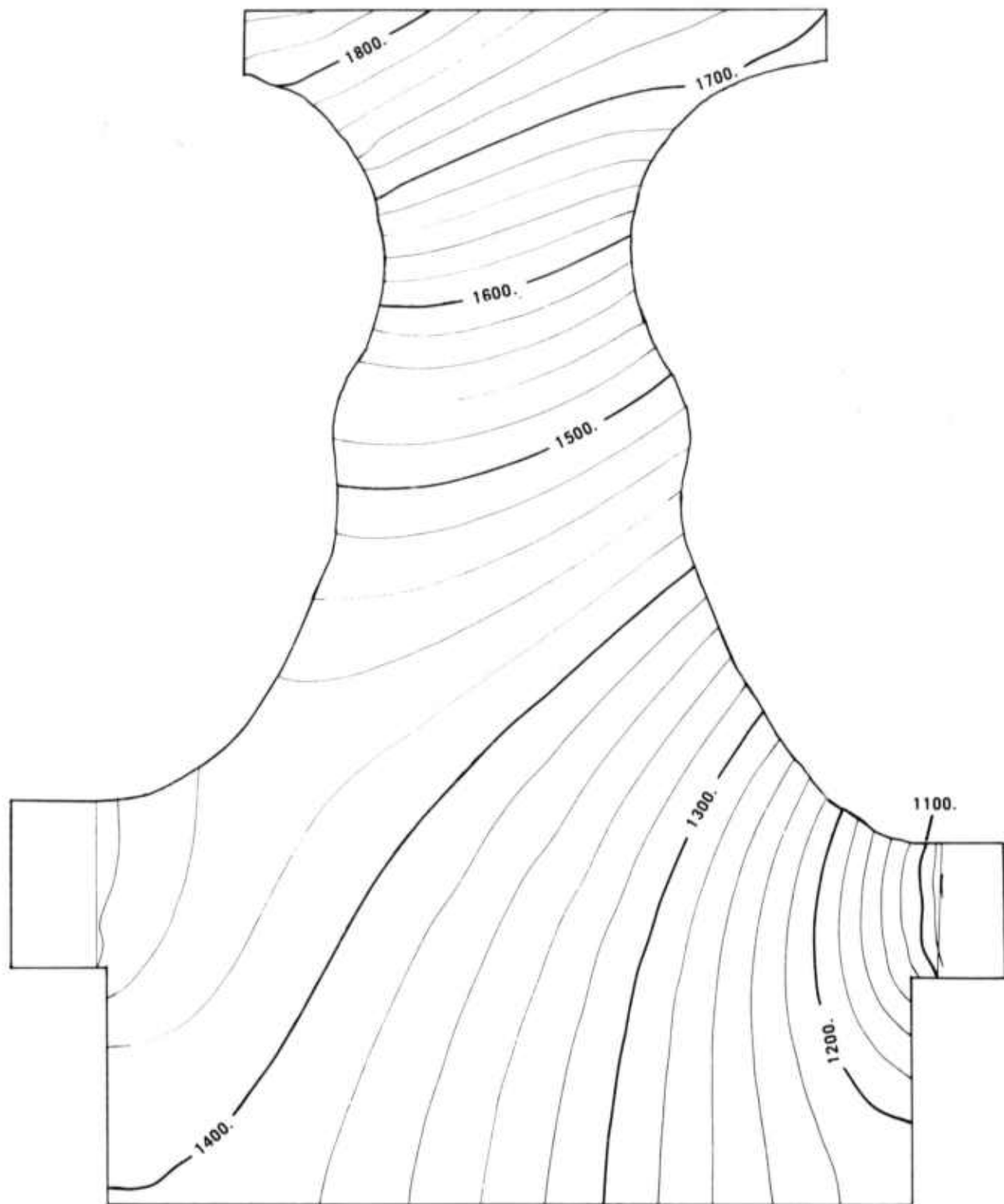


Figure 3.13: Isotherms ( $^{\circ}$ F) in Second Stage Rotor at 100% Steady State Speed Temperature Boundary Conditions

## HOT GAS FLOW

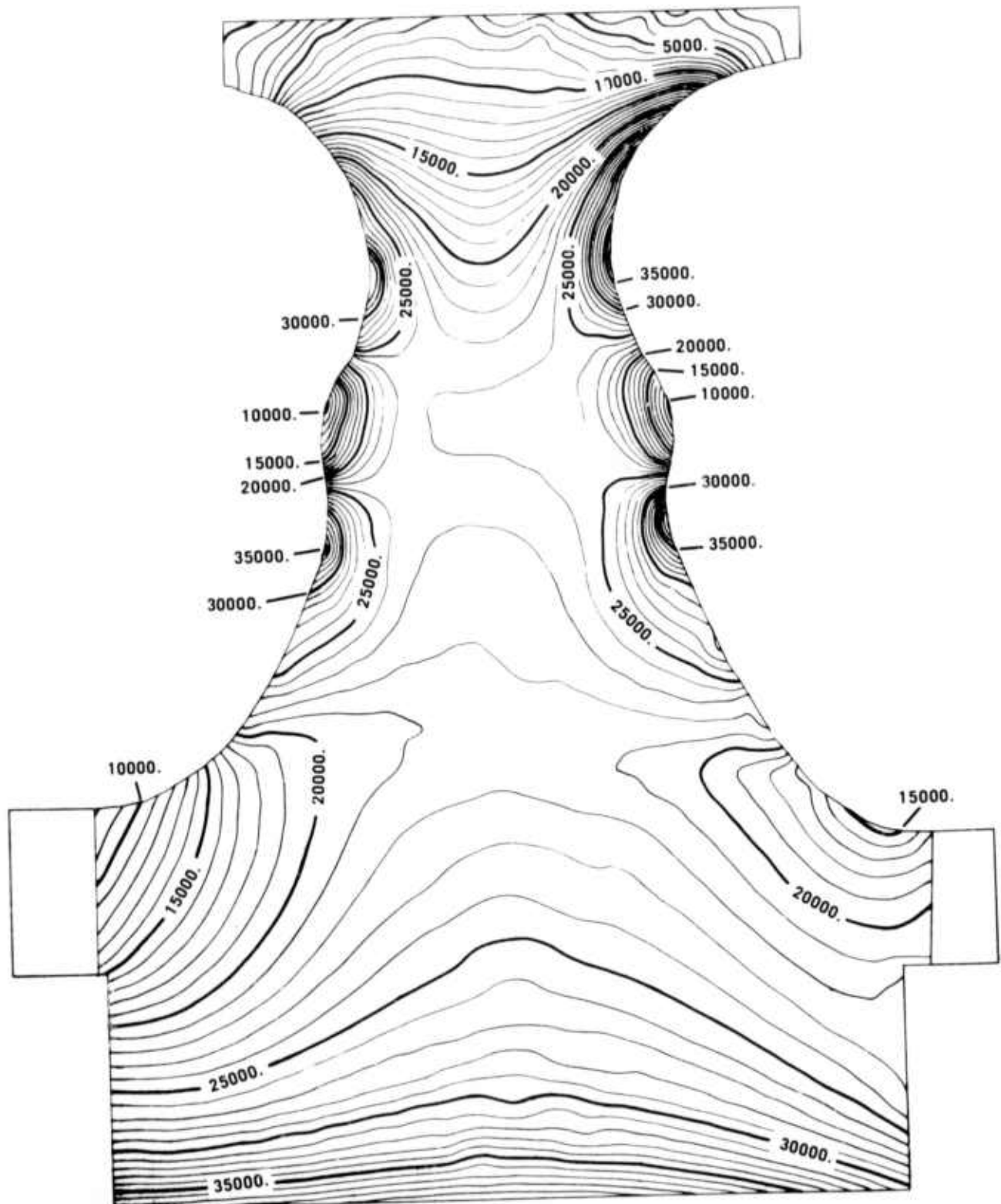


Figure 3.14 Maximum Principle Stresses (psi) in Second Stage Rotor,  
Combining Thermal Stresses at 100% Speed and Centrifugal  
Stresses at 110% Speed

## HOT GAS FLOW

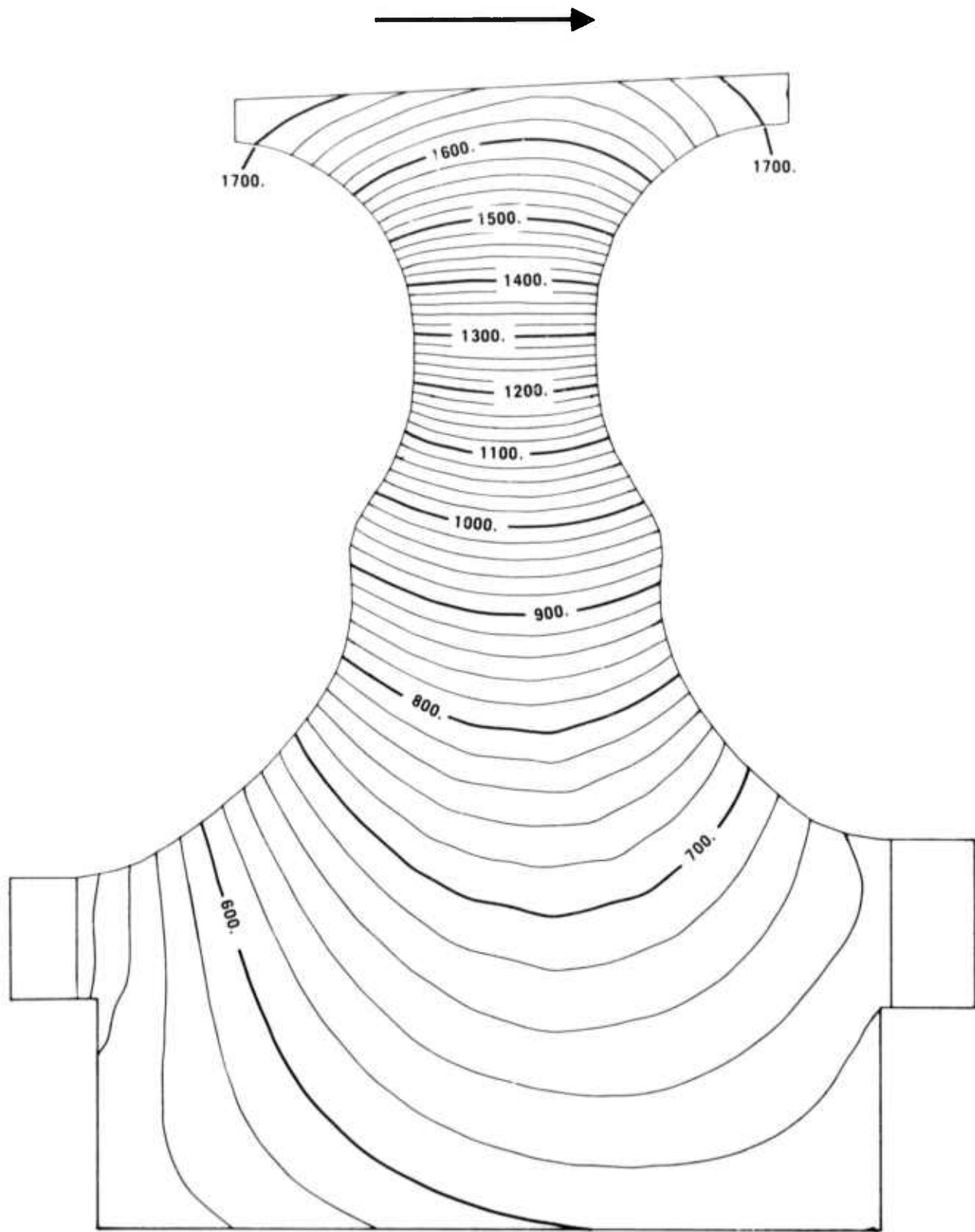


Figure 3.15      Isotherms ( $^{\circ}$ F) in First Stage Rotor at 40 Seconds From Light With 55% Speed Temperature Boundary Conditions

## HOT GAS FLOW

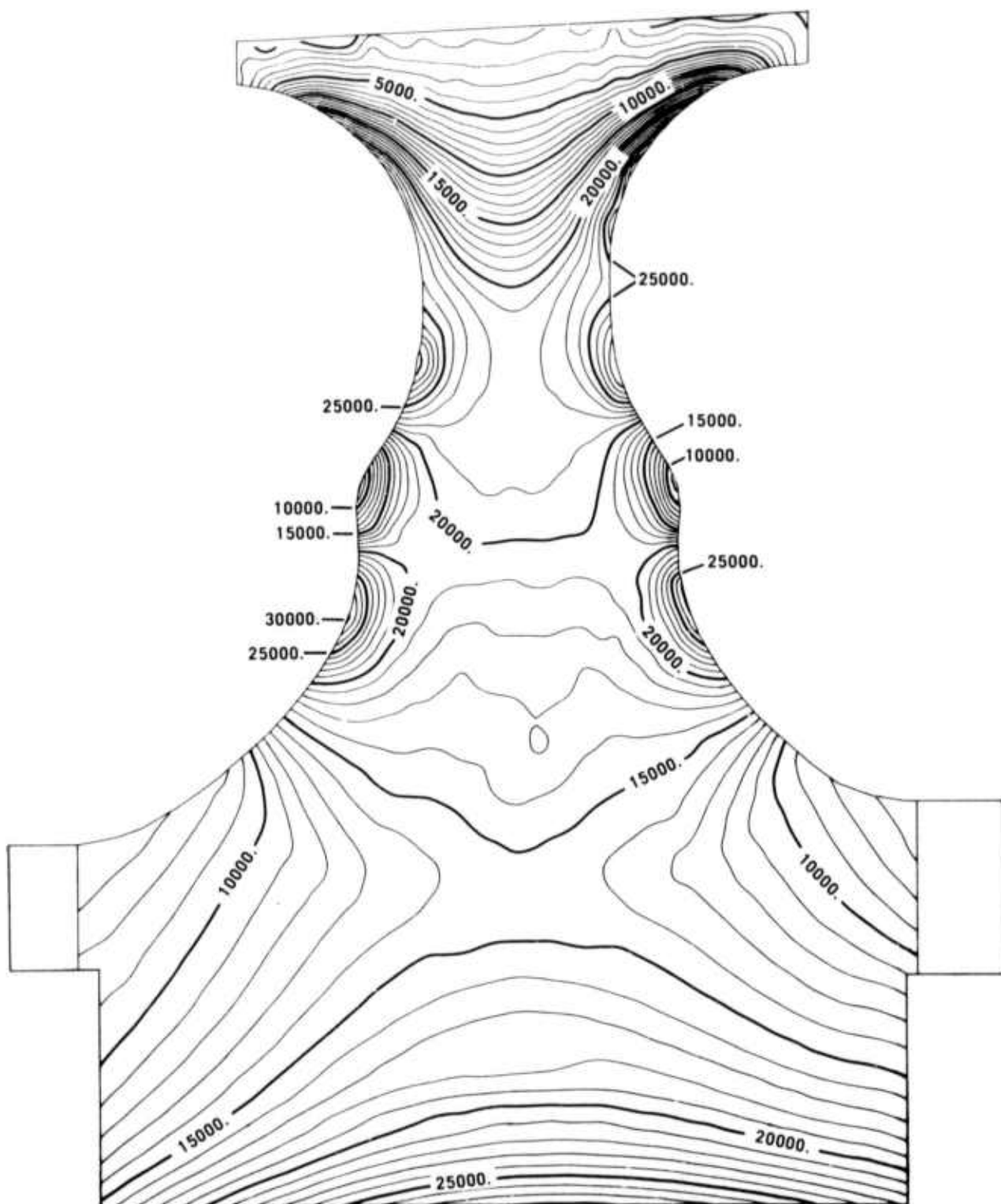


Figure 3.16 Maximum Principle Stresses (psi) in First Stage Rotor at 40 Seconds From Light with 55% Speed Temperature Boundary Conditions Combined With Centrifugal Stresses at 55% Speed

## HOT GAS FLOW

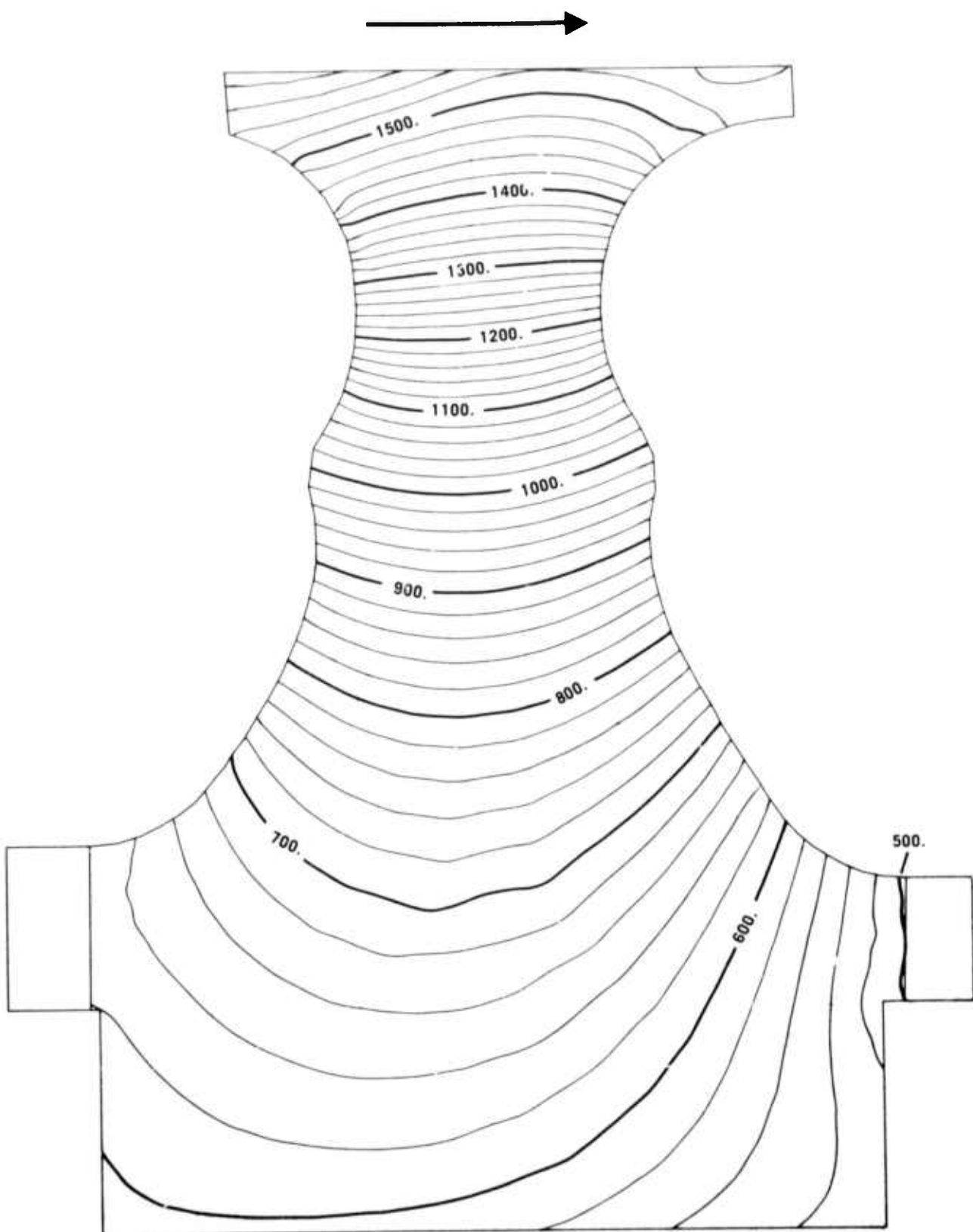


Figure 3.17 Isotherms ( $^{\circ}$ F) in Second Stage Rotor at 40 Seconds From Light With 55% Speed Temperature Boundary Conditions

## HOT GAS FLOW

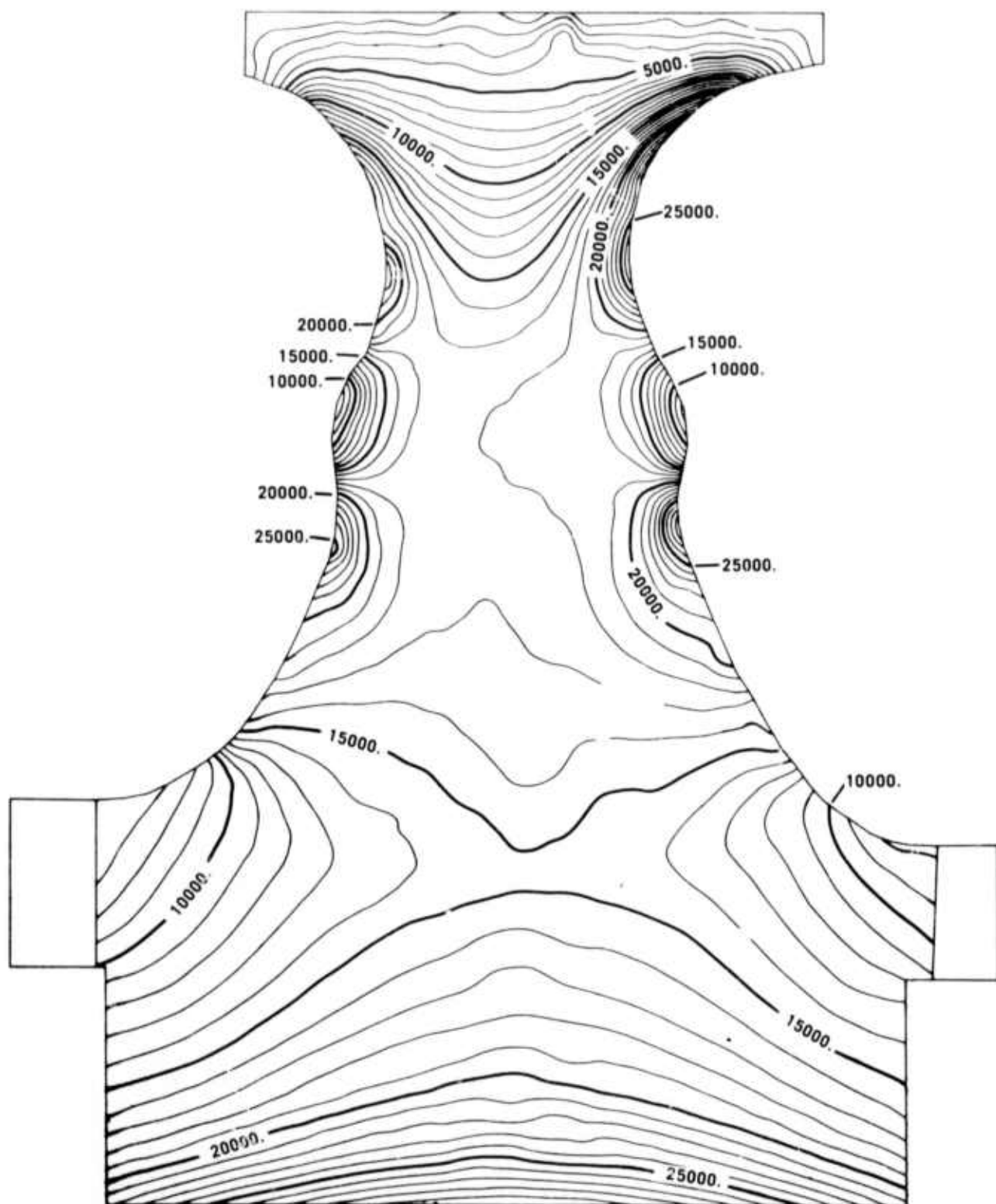


Figure 3.18 Maximum Principle Stresses (psi) in Second Stage Rotor at 40 Seconds From Light at 55% Speed Temperature Boundary Conditions Combined With Centrifugal Stresses at 55% Speed

## HOT GAS FLOW

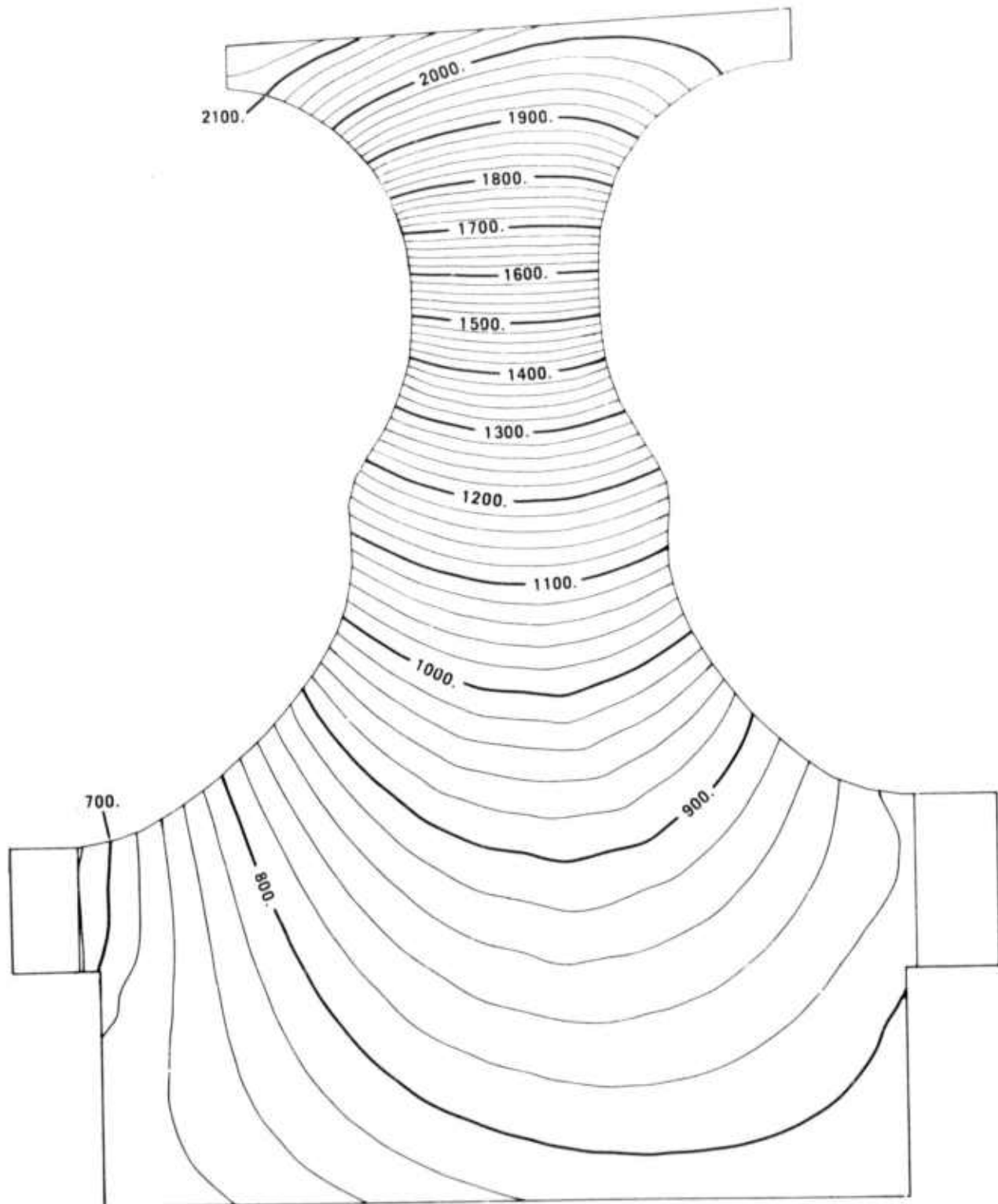


Figure 3.19 Isotherms ( $^{\circ}$ F) in First Stage Rotor at 55 Seconds From Light with 100% Speed Temperature Boundary Conditions

## HOT GAS FLOW

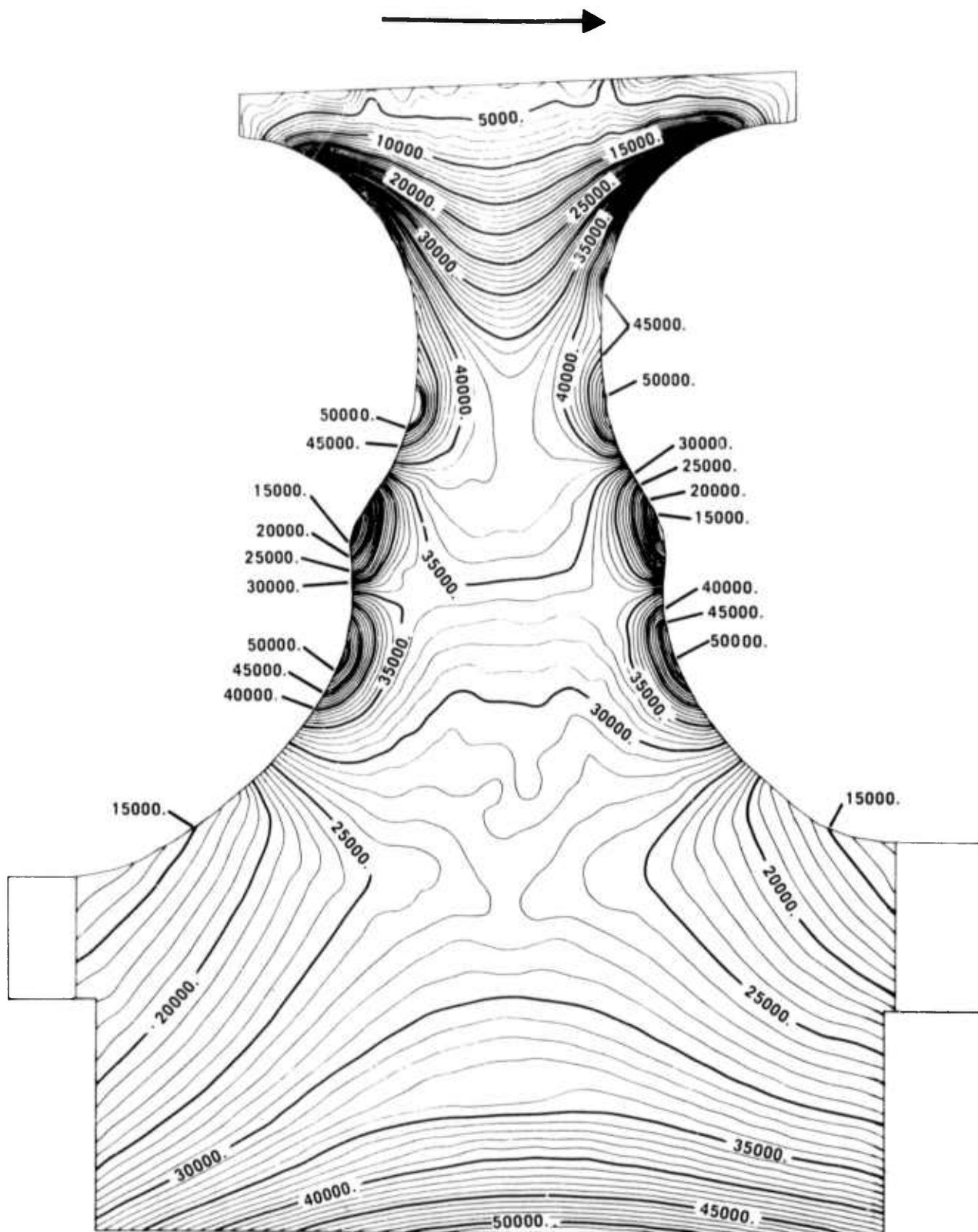


Figure 3.20 Maximum Principle Stresses (psi) in First Stage Rotor  
at 55 Seconds From Light at 100% Speed Temperature Boundary  
Conditions Combined With Centrifugal Stresses at 110% Speed

## HOT GAS FLOW

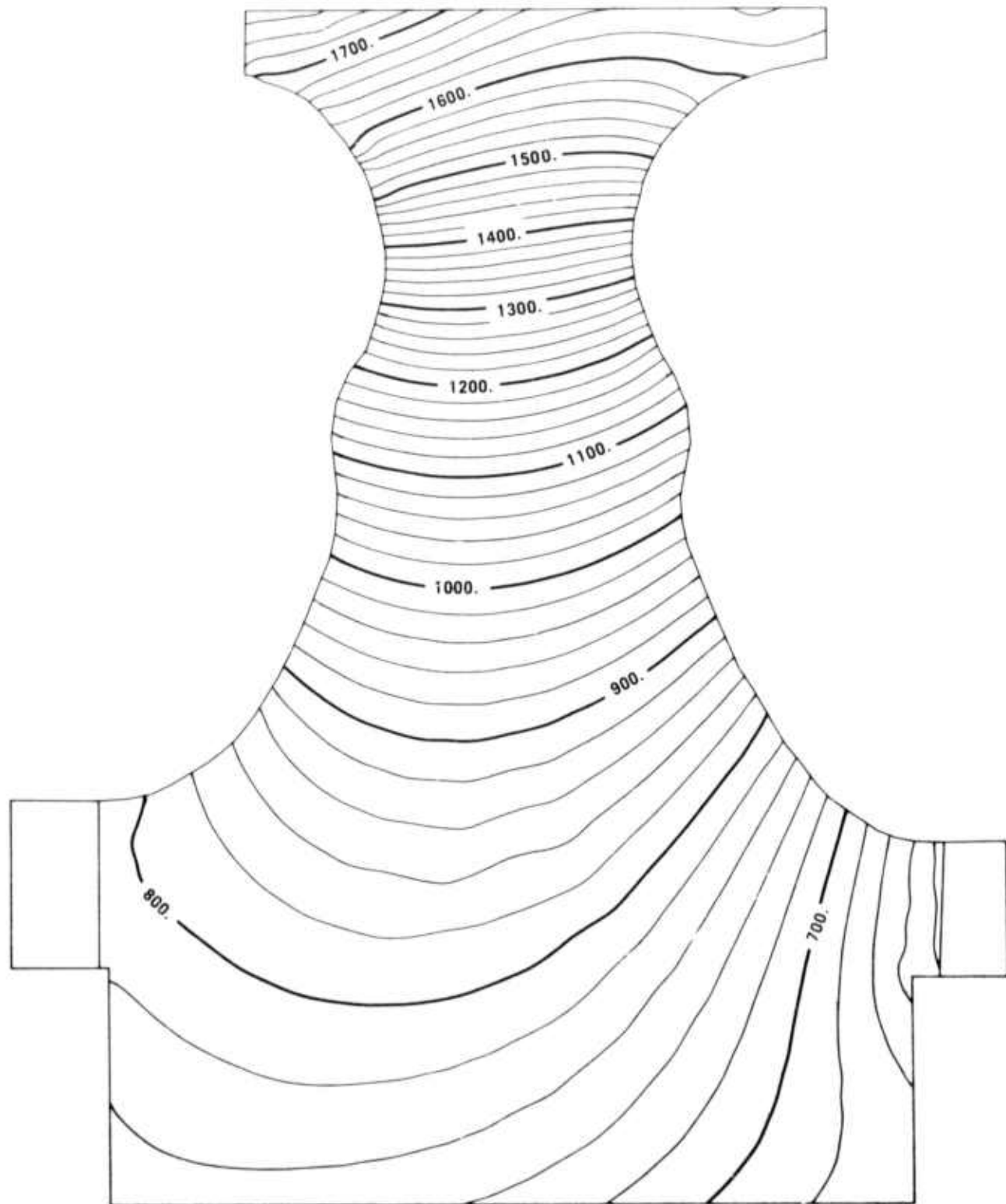


Figure 3.21 Isotherms ( $^{\circ}$ F) in Second Stage Rotor at 55 Seconds From Light With 100% Speed Temperature Boundary Conditions

## HOT GAS FLOW

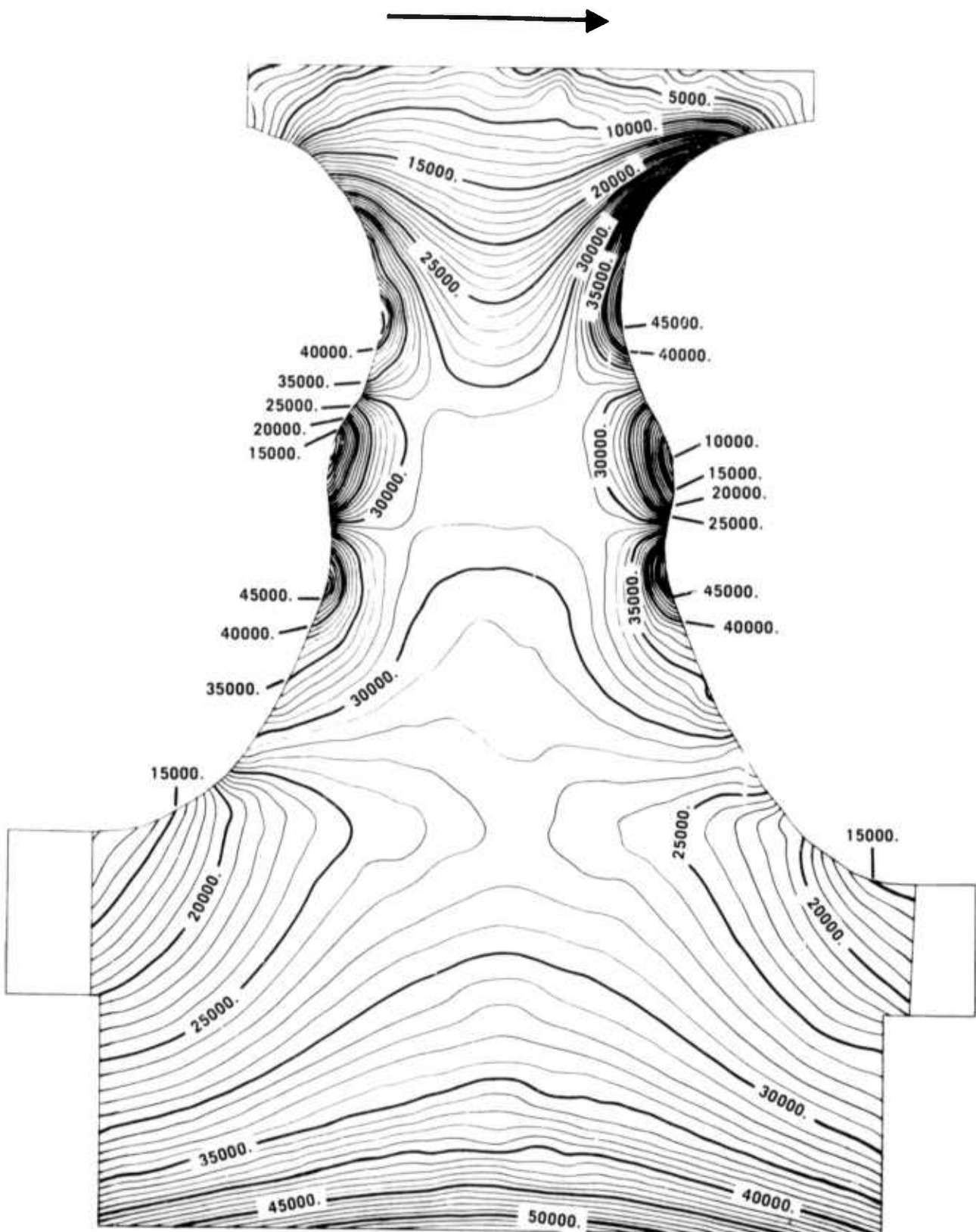


Figure 3.22 Maximum Principle Stresses (psi) in Second Stage Rotor at 55 Seconds From Light at 100% Speed Temperature Boundary Conditions Combined with Centrifugal Stresses at 110% Speed

## HOT GAS FLOW

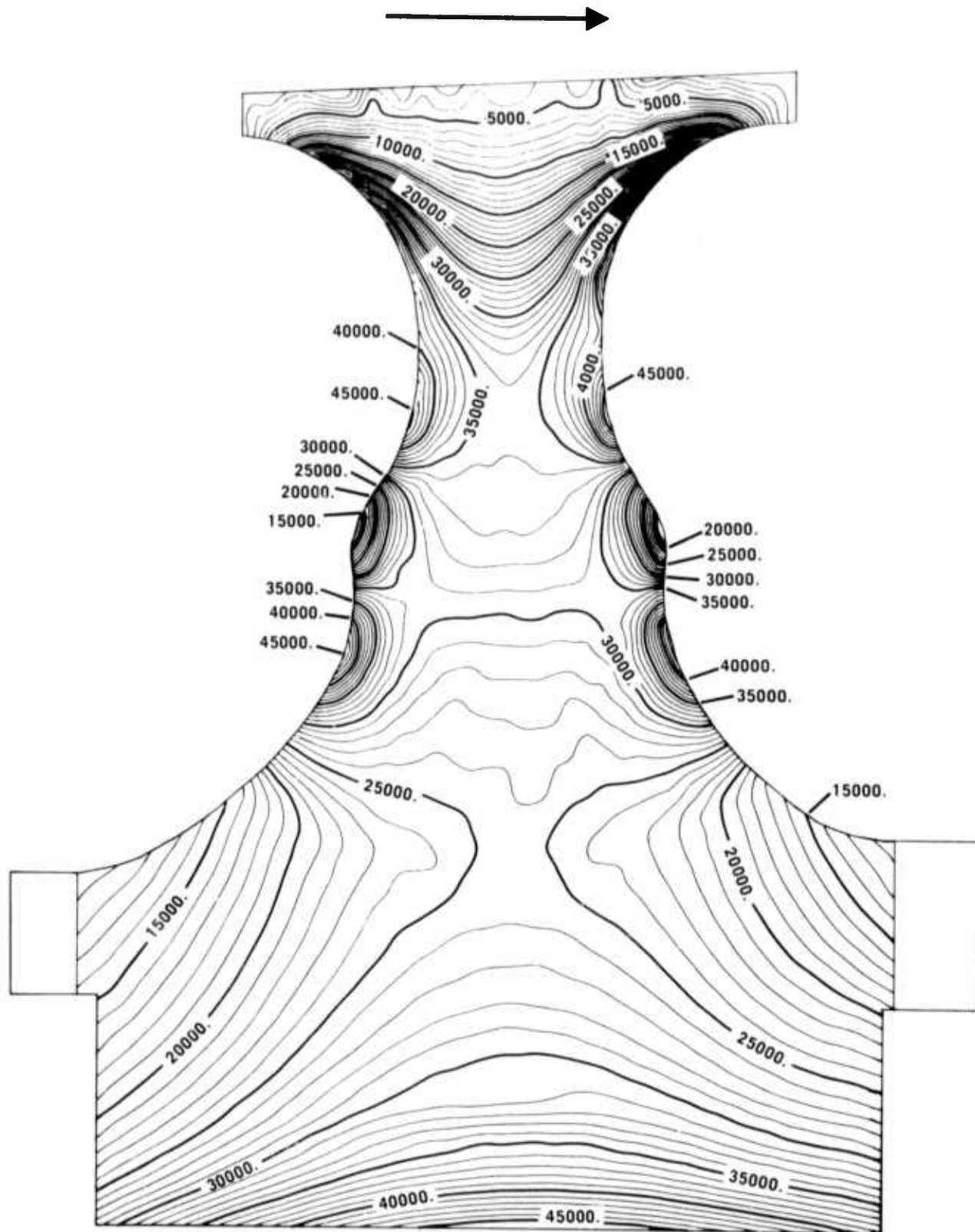


Figure 3.23 Maximum Principle Stresses (psi) in First Stage Rotor at 40 Seconds From Light at 55% Speed Temperature Boundary Conditions Combined with Centrifugal Stresses at 110% Speed

## HOT GAS FLOW

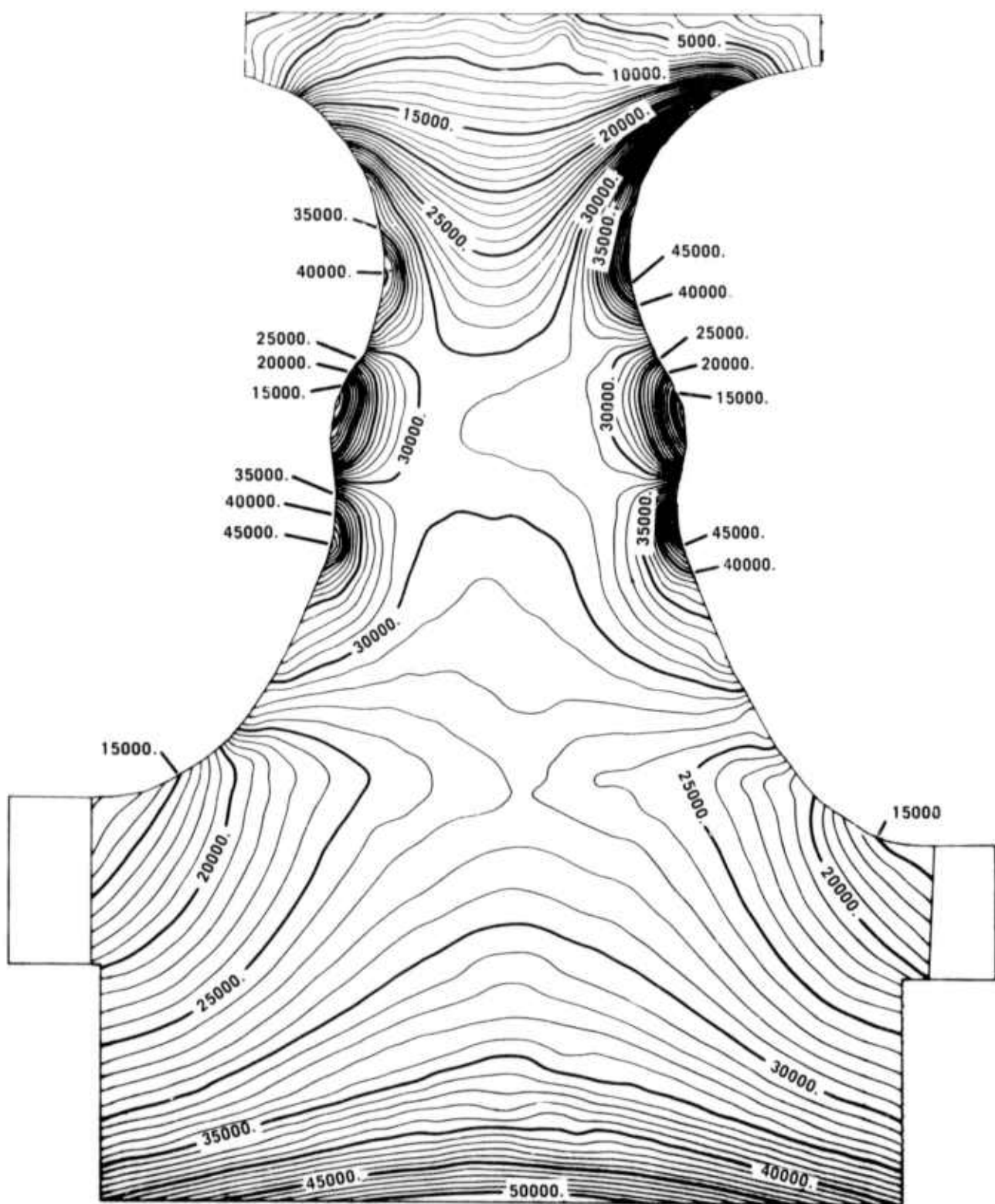


Figure 3.24 Maximum Principle Stresses (psi) in Second Stage Rotor at 40 Seconds From Light at 55% Speed Temperature Boundary Conditions Combined With Centrifugal Stresses at 110% Speed

first stage rotor bore between the first and second transient maximum stress conditions. Therefore, the centrifugal loading constitutes 88% of the stress increase between first and second transient maximum stress times for the first stage rotor bore. Centrifugal loading accounts for 95% of the increase in the second stage bore for the same change in conditions. The increased stress levels in both first and second stage rotor necks during the second transient is due entirely to centrifugal loading.

Table 3.1 summarizes the stress-temperature conditions for the Design C hot-pressed silicon nitride turbine rotors analyzed. Future analysis of these same basic rotors will include transient thermal stress analysis for shutdown conditions in the engine. Modifications in the rotor profiles will be analyzed also in an attempt to achieve more uniform stress gradients and stress distributions under operating conditions. Studies will also be conducted to determine the effect of material property variations on stress distributions.

Table 3.1 Summary of Stress-Temperature Conditions for Design C Hot Pressed Silicon Nitride Turbine Rotors

CONDITION		Idle Steady State	Full Speed Steady State	First Transient	Second Transient
<b>First Stage Rotor</b>					
Bore	Stress, psi Temp. °F	13,000 1580	39,000 1600	28,000 600	52,000 780
Neck	Stress, psi Temp. °F	13,000 1780	43,000 1900	30,000 1160	53,000 1400
<b>Second Stage Rotor</b>					
Bore	Stress, psi Temp. °F	18,000 1400	40,000 1320	30,000 580	53,000 740
Neck	Stress, psi Temp. °F	17,000 1380	36,000 1580	27,000 1220	45,000 1400

### Analysis of Design C Duo-Density Silicon Nitride Rotors

The duo-density rotor is composed of a ring of blades of molded reaction-sintered silicon nitride bonded to a disk of hot-pressed silicon nitride.

In the previous report,(1) results of temperature and stress analyses of the rotor disks for 55% and 110% speed steady state conditions were presented. The purpose of the analysis reported herein is to determine the transient stresses in the reaction-sintered ring.

Axisymmetric heat transfer and stress finite element programs were used in this analysis. The assumption of axial symmetry is violated by the blades, and since the region of interest is in the immediate vicinity of the blades, the calculated stresses will be lower than the true stresses due to the stress concentration around the blade root. Thus the results of this analysis cannot be used to establish final stresses in the ring.

The transient loading considered is the loss of flame from the 110% steady state thermal condition. Aero-thermal analysis indicates a temperature drop of 640°F in the gas temperature across the rotor platforms during a loss of flame from 110% steady state. The rotor heat transfer analysis assumes the temperature drop to occur instantaneously. The rotor velocity is assumed constant at 110% speed throughout the transient.

The maximum stress during the transient is 16,000 psi in a circumferential direction, occurring at 7 seconds after the loss of flame. The maximum stress is the same for the first and second stage rotors.

A more accurate three-dimensional analysis is required in order to define the true stress distribution. A three-dimensional finite element stress analysis program is now operational, and a three-dimensional finite element transient heat transfer program is currently being procured. When this program is ready, the complete analysis of combined stresses will be performed.

### Ceramic Rotor Attachment

A previous report (2) described progress on the development of a curvic coupling to provide transfer of torque from the first stage to the second stage rotor, and from the ceramic rotors to the metal turbine shaft.

Prototype curvics consisting of a metal and a ceramic (hot-pressed  $\text{Si}_3\text{N}_4$ ) member for the rotor-shaft coupling application were evaluated on a test fixture built to simulate thermal and mechanical loads expected during engine operation. A goal was established consisting of 200 cycles between room temperature and 600°F, with a maximum axial load of 9400 pounds.

Two sets of curvic test specimens were evaluated during this reporting period. The first set failed after three cycles at a loading of 8000 pounds, and the second set failed during the first cycle at a 5000 pound load. The failures occurred in the ceramic member at nearly every tooth at the center of the root. A redesign was initiated, changing the pressure angle from 30° to 45°, and specifying a better surface finish. This is expected to solve the cracking problem. Samples are being processed for further evaluation on the test fixture.

### 3.1.2 MATERIALS AND FABRICATION

#### Introduction

Development of materials and fabrication processes for ceramic turbine rotors continues to emphasize two materials, silicon nitride and silicon carbide. The primary in-house effort has been directed at the duo-density concept<sup>(1)</sup> which combines an injection molded ring of airfoil blades made from reaction-sintered silicon nitride, bonded onto a fully dense, hot-pressed silicon nitride disk. Experimental press-bonding trials have produced some duo-density rotors sufficiently sound to be evaluated by spin testing.

Further development of the ultrasonic machining of turbine rotors from hot-pressed  $\text{Si}_3\text{N}_4$  was delayed during this reporting period in order to complete modifications to the ultrasonic machine. The program to fabricate rotors from silicon carbide by the chemical vapor deposition process progressed sufficiently so that seven full size rotors were delivered. Feasibility has not been established for the conformable tool, psuedo-isostatic method<sup>(1,2)</sup> of fabricating a dense silicon nitride rotor. Because of the likelihood that too much time would be required to solve problems and complete development, work on this approach has been discontinued.

Machining of ceramic rotors from dense, hot-pressed silicon carbide blanks by the electric discharge machining method is being evaluated. The amount of surface damage caused by the EDM technique is a matter of concern, and will require further work on the basic machining and material parameters before attempting to fabricate a turbine rotor.

#### Duo-Density $\text{Si}_3\text{N}_4$ Rotors

The duo-density concept<sup>(1)</sup> is one of several techniques being investigated for fabricating a ceramic turbine rotor. In this concept, the high-strength of the hot-pressed  $\text{Si}_3\text{N}_4$  is utilized in the disk region where stresses are greatest but temperatures are moderate and therefore creep problems are minimized. Reaction-sintered  $\text{Si}_3\text{N}_4$  which can be readily formed into the complex airfoil blade shapes by injection-molding, is utilized for the blades which are exposed to the highest temperatures but lowest stress levels.

Work during this reporting period was directed toward developing fabrication techniques for bonding the reaction-sintered  $\text{Si}_3\text{N}_4$  ring of blades and the hot-pressed disk, or hub, together. The blade ring assembly was injection molded as one piece from silicon metal powder and subsequently nitrided to form  $\text{Si}_3\text{N}_4$  having a density of  $2.3 \text{ gm/cm}^3$ . The  $\text{Si}_3\text{N}_4$  hub component was prepared by hot-pressing alpha  $\text{Si}_3\text{N}_4$  powder (AME) containing 2 w/o  $\text{MgO}$  to theoretically dense discs. The bond surfaces of all component parts were machined to remove any oxide or reaction surface layers. Bonding studies were also made to determine the effect of the fabrication parameters on the degree of bonding.

Several potential assembly techniques were evaluated. One technique involved hot-pressing a tapered reaction-sintered blade ring onto a mating tapered hot-pressed hub as shown in Figure 3.25. The angle  $\phi$  was varied from  $1.5^\circ$  to  $10^\circ$ . The hot-pressing parameters varied from 1650 to 1750°C and 500 to 2000 psi for temperature and pressure, respectively. No circumferential support was given to the reaction-sintered  $\text{Si}_3\text{N}_4$  blade ring. It was anticipated that the applied force would be vertically transmitted to the tapered bond surface resulting in bonding. However, bonding did not result during any of the trials. The reaction-sintered blade ring fractured when the applied force was greater than 1000 psi due to the high tension forces in the rim. Pressures below 1000 psi were insufficient to affect bonding.

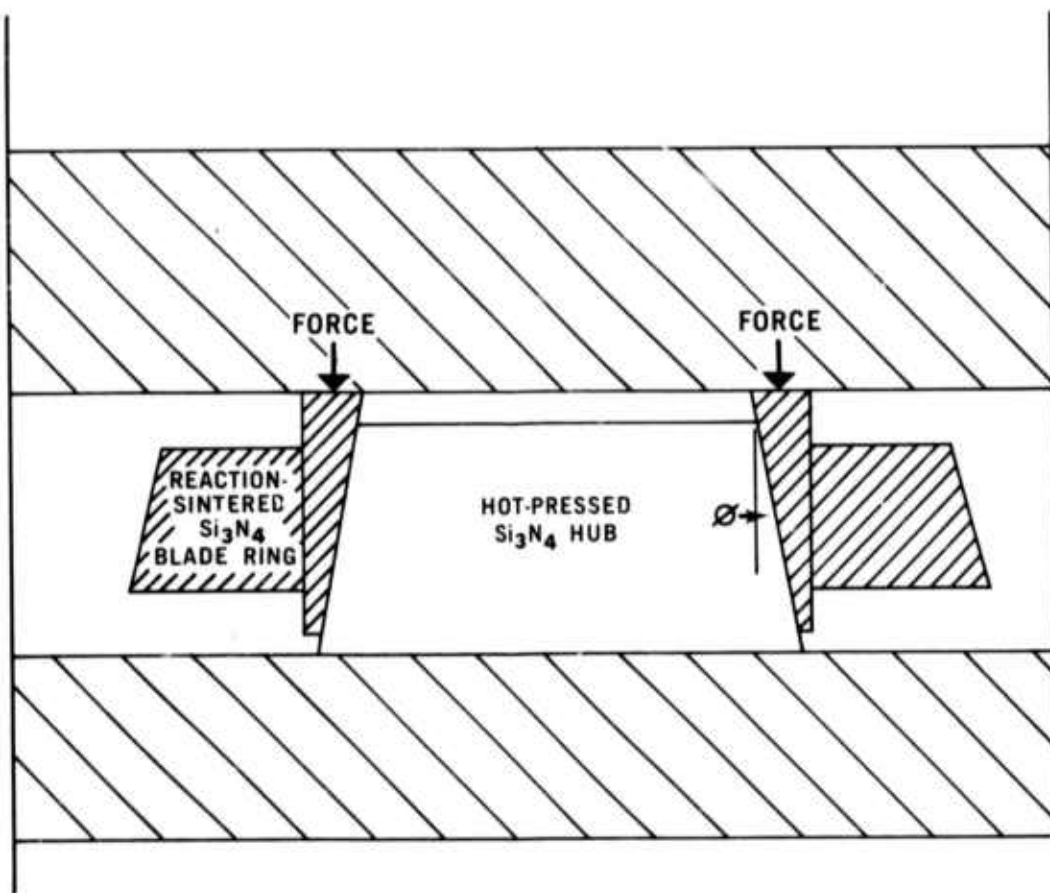


Figure 3.25 Duo-Density Rotor Fabrication Showing Tapered Silicon Nitride Hub and Mating Blade Ring

A second technique involved hot-pressing the  $\text{Si}_3\text{N}_4$  hub into the central cavity of the reaction-sintered blade ring. This technique is illustrated in Figure 3.26. The hot-pressed hub was machined to slip fit the inside diameter of the reaction-sintered blade ring. Graphite rings to circumferentially support the rim of the blade ring at both the top and bottom were machined to close tolerances. All graphite surfaces adjacent to the  $\text{Si}_3\text{N}_4$  components were covered with graphite foil and a boron nitride coating to prevent the formation of  $\text{SiC}$ . Boron nitride powder was also compacted around the  $\text{Si}_3\text{N}_4$  rotor blades. This entire assembly was hot-pressed by applying pressure uniaxially to the

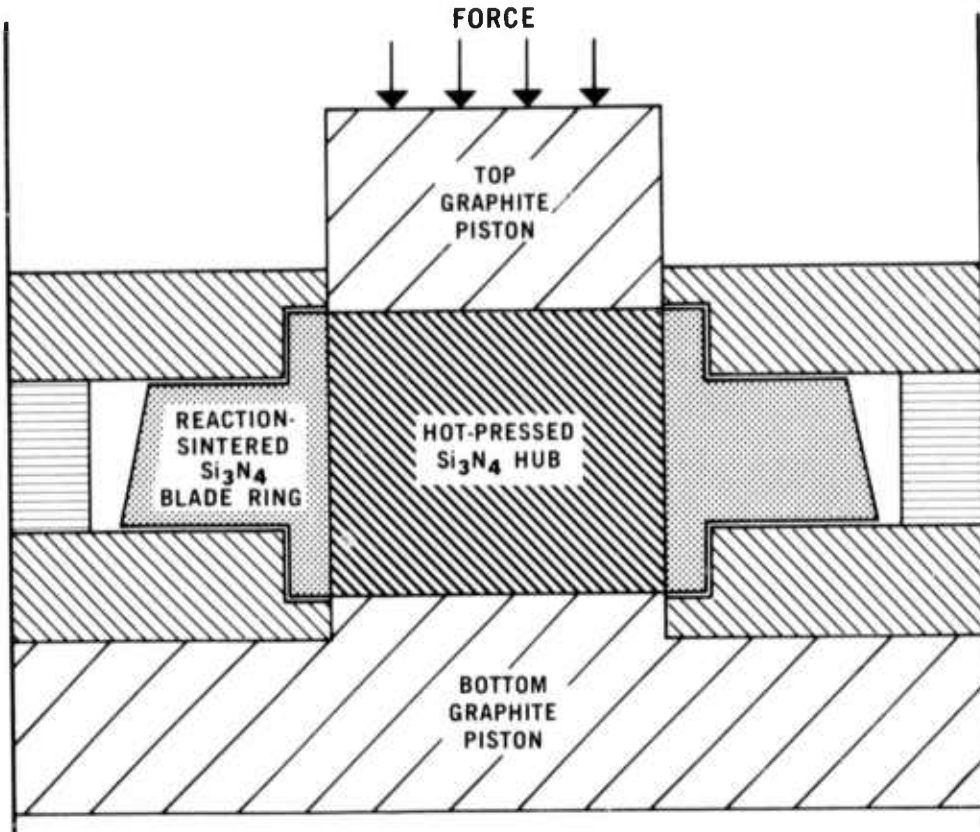


Figure 3.26 Concept for Bonding Duo-Density Rotor Without Tapered Sections

$\text{Si}_3\text{N}_4$  hub causing the hub to deform and exert pressure on the inside diameter of the blade ring. The main disadvantage of this technique is the inability to support the blade ring between the turbine blades. The hot-pressing parameters varied from 1650 to 1750°C and 1000 to 2000 psi for the temperature and applied pressure, respectively. Again, as in the previous technique, the rim of the blade ring fractured in most attempts due to the high tangential tension stresses developed in the rim. However, bonding resulted in several cases, as shown in Figure 3.27. There was also considerable cracking or tearing of the reaction-sintered  $\text{Si}_3\text{N}_4$  rim between the rotor blades due to lack of support in this area. Several attempts were made to support the rotor at the turbine blade ends; however this resulted in distorted and fractured turbine blades.

A third technique, termed the "sandwich" construction, is illustrated in Figure 3.28. This technique is similar to the one previously described in that a uniaxial pressure is applied to the  $\text{Si}_3\text{N}_4$  hub to effect bonding. This technique requires substantially more machining as three rather than one separate hot-pressed  $\text{Si}_3\text{N}_4$  component parts are required. Again, all graphite surfaces adjacent to  $\text{Si}_3\text{N}_4$  were covered with graphite foil and coated with BN. The turbine blade cavities were also filled with boron nitride powder. The rotors were hot-pressed at 1675°C and pressures varying from 1000 to 2000 psi. This technique proved unsuccessful as small tears or cracks resulted between the turbine blades in the reaction-sintered  $\text{Si}_3\text{N}_4$  material. Again, fracture is believed to be related to failure of the unsupported rotor blade ring to resist deformation.

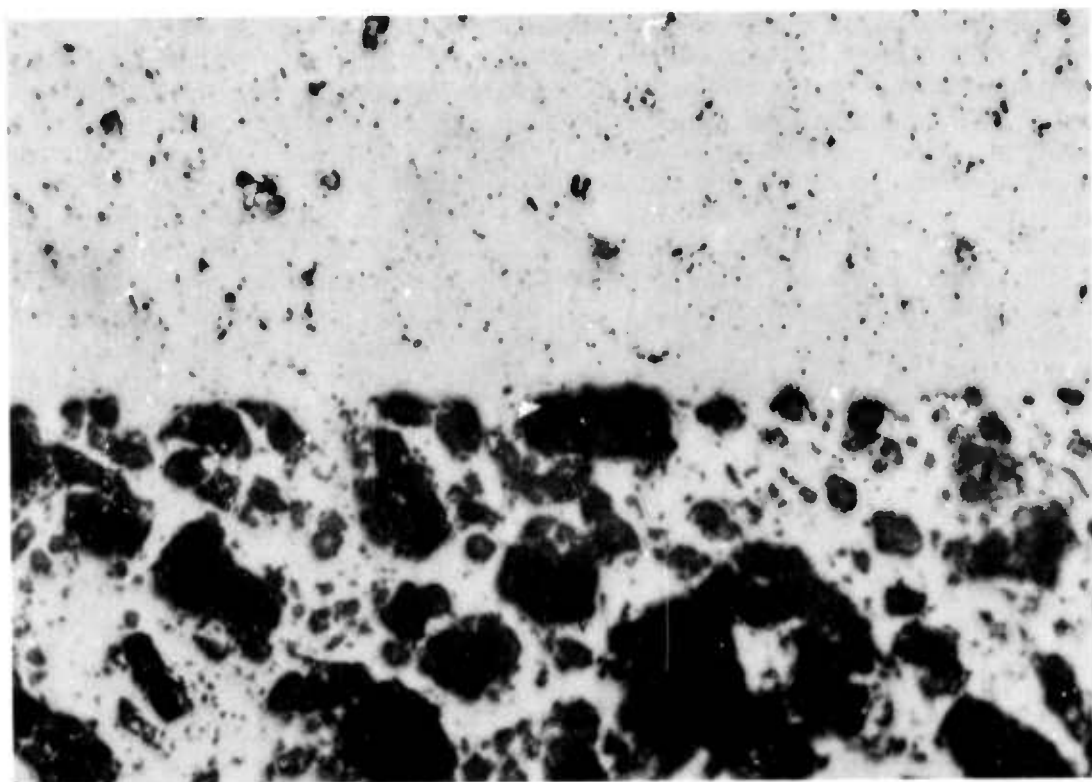


Figure 3.27 Microstructure Showing Good Bonding (1250X)

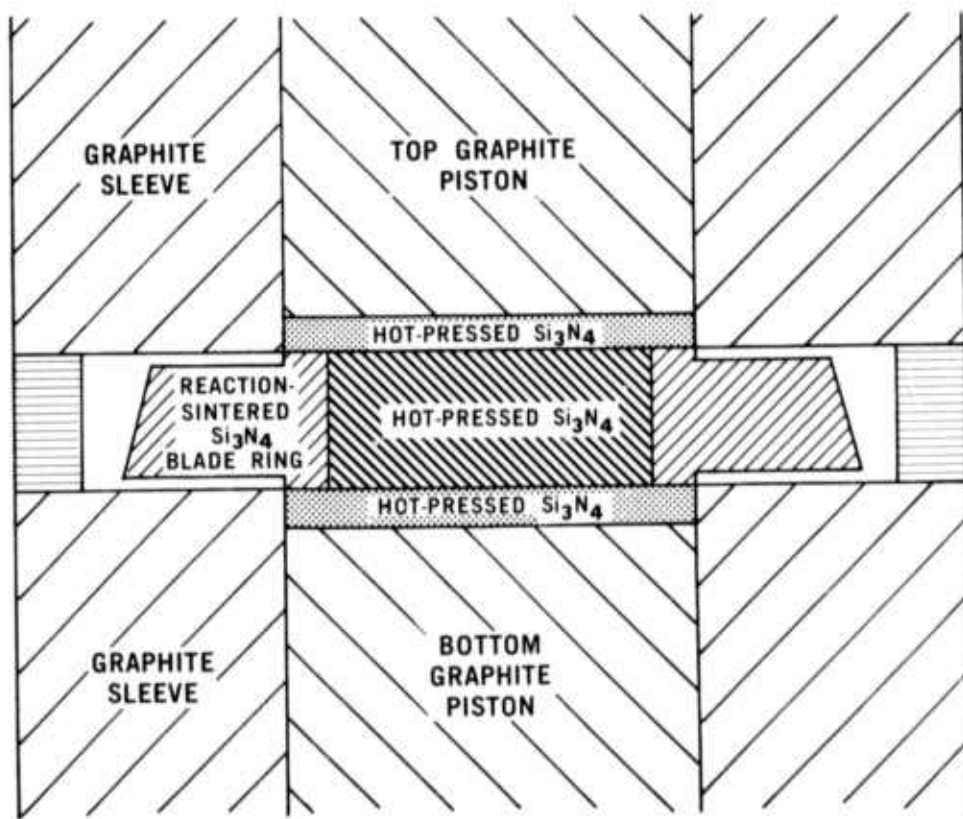


Figure 3.28 Sandwich-Type Construction for Fabricating Duo-Density Rotor

In all three cases, fracture of the reaction-sintered blade ring was the predominate cause of the inability to fabricate acceptable turbine rotors. Therefore, a system was designed to minimize or eliminate the high tangential tensile stresses developed in the rim during hot-press bonding. This technique involved hot-pressing the reaction-sintered  $\text{Si}_3\text{N}_4$  blade ring onto the hot-pressed  $\text{Si}_3\text{N}_4$  hub. This design is shown in Figure 3.29 and employs the use of graphite wedges to apply pressure to the blade and periphery, forcing the blade ring onto the hub. The  $10^\circ$  tapered graphite wedges (four bottom and four top wedges) are shown in Figure 3.30. A gap of approximately 0.100 in. between each wedge permitted inward movement of about 0.070 in. Graphite foil and boron nitride were used as barrier materials between the graphite parts and  $\text{Si}_3\text{N}_4$ . A one piece, outside tapered graphite ring was placed around the tapered graphite inserts. The uniaxial pressure exerted on this ring forced the inserts inward against the reaction-sintered blade ring. A graphite spacer was placed above the hot-pressed hub to prevent upward deformation of the hub. The hot pressing parameters varied from  $1650^\circ\text{C}$  to  $1750^\circ\text{C}$  and from 1000 to 2500 psi for temperature and pressure respectively.

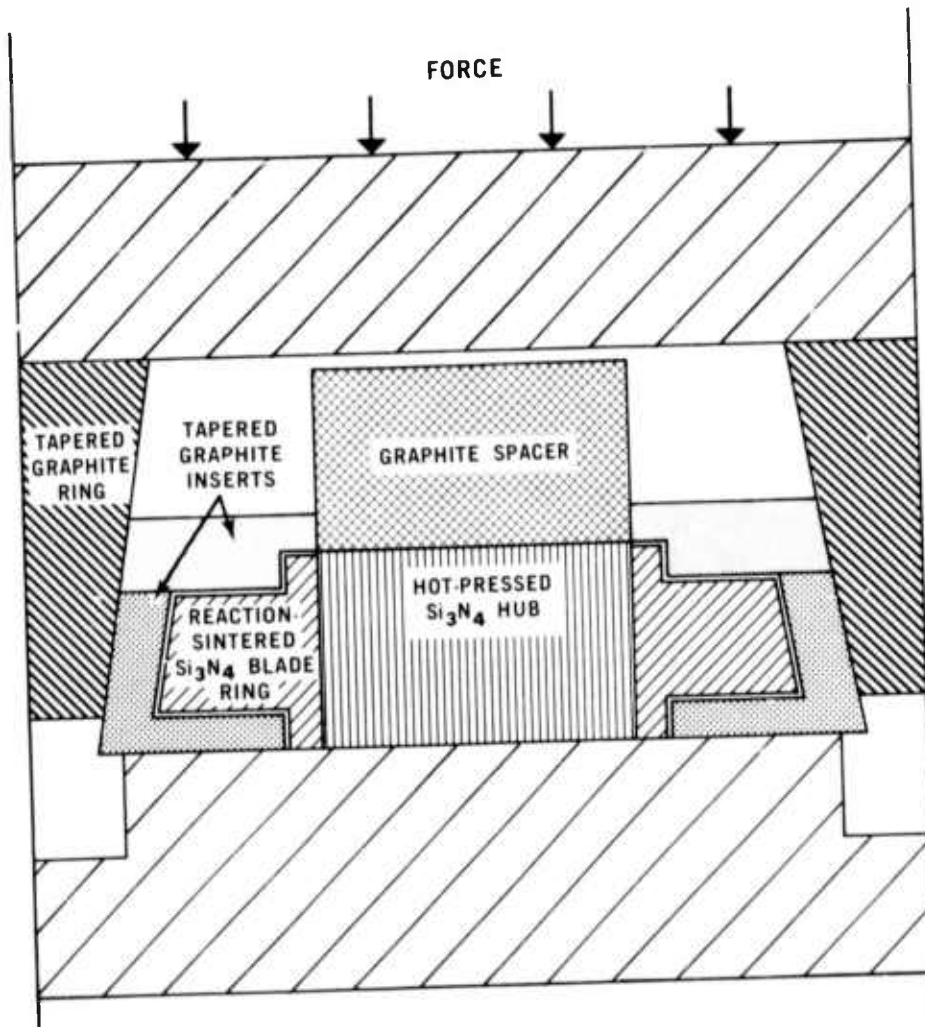


Figure 3.29 Concept for Employing Graphite Wedges for Fabricating Duo-Density Rotor

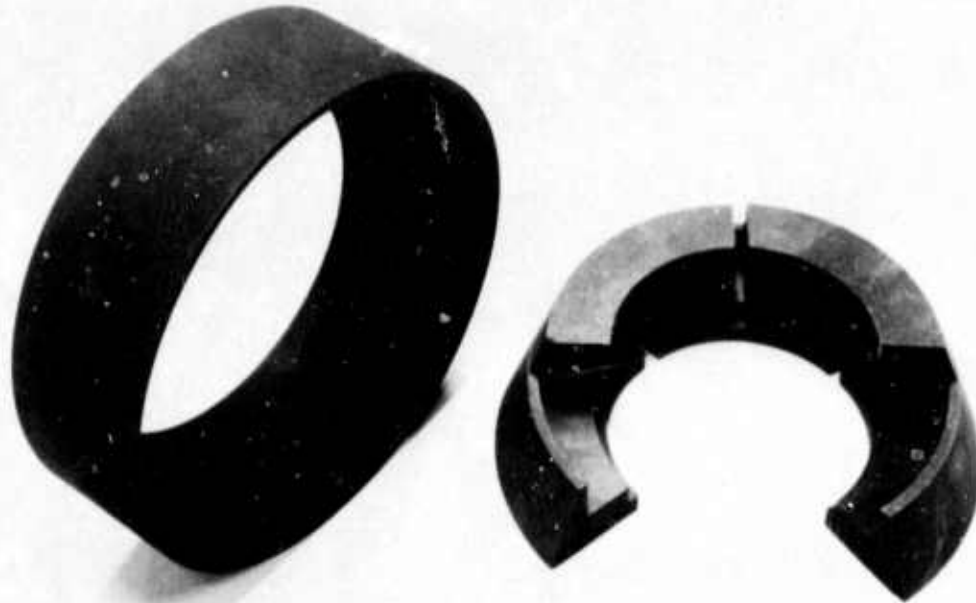


Figure 3.30 Graphite Wedges for Fabricating Duo-Density Rotor

A typical duo-density turbine rotor hot-pressed by this technique is shown in Figure 3.31. Metallographic examination of several of these rotors showed the bonding between the reaction-sintered blade ring and hot-pressed hub to be inconsistent under similar hot-pressing conditions, as illustrated in Figures 3.32 and 3.33. Several turbine rotors fabricated by this technique were spin-tested and results will be discussed in Section 3.1.3.

This inconsistent bonding is probably related to variations in the actual bonding pressure. Due to friction at the tapered surfaces, it is difficult to correlate the actual bonding pressure with the uniaxial applied pressure, making it difficult to reproduce pressure. The radial force exerted on the blade ring rim must be balanced by the vertical force on the hub portion in order to produce pressure at the bond surface. An unequal mismatch of either force will result in a weak bond or fracture of the blade ring; both conditions have been observed. Fracturing of the reaction-sintered blade ring usually resulted in small cracks or tears between the turbine blades and was always associated with an increase in the blade ring diameter. Since the rim was only supported above and below the turbine blades (Figure 3.29) with no support between the turbine blades to restrict deformation of the hot-pressed  $\text{Si}_3\text{N}_4$  hub, the reaction-sintered blade ring crept and fractured in this area.

A reaction-sintered  $\text{Si}_3\text{N}_4$  ring with no blades and a hot-pressed  $\text{Si}_3\text{N}_4$  hub were bonded together by this technique, allowing complete circumferential support of the reaction-sintered ring. Metallographic examination showed excellent bonding. There were no fractures or cracks in the reaction-sintered ring, demonstrating the importance of total support of the reaction-sintered  $\text{Si}_3\text{N}_4$  blade ring.

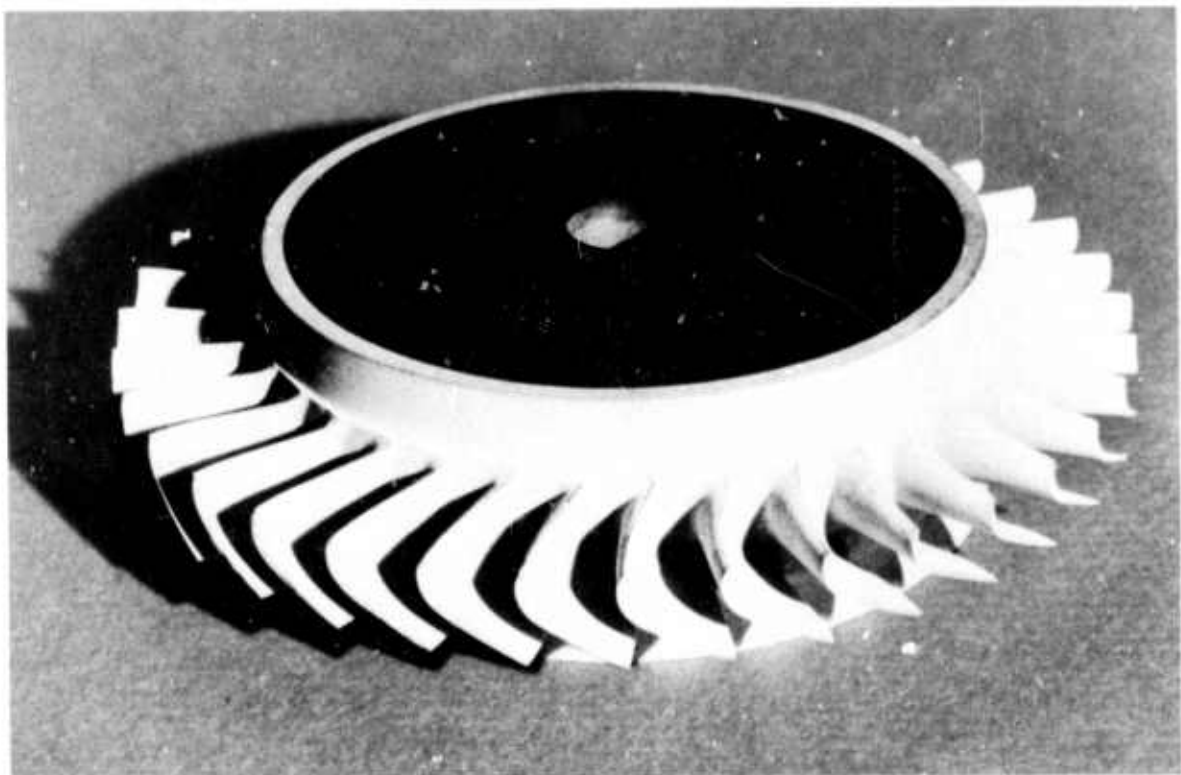


Figure 3.31 Completed Duo-Density Rotor

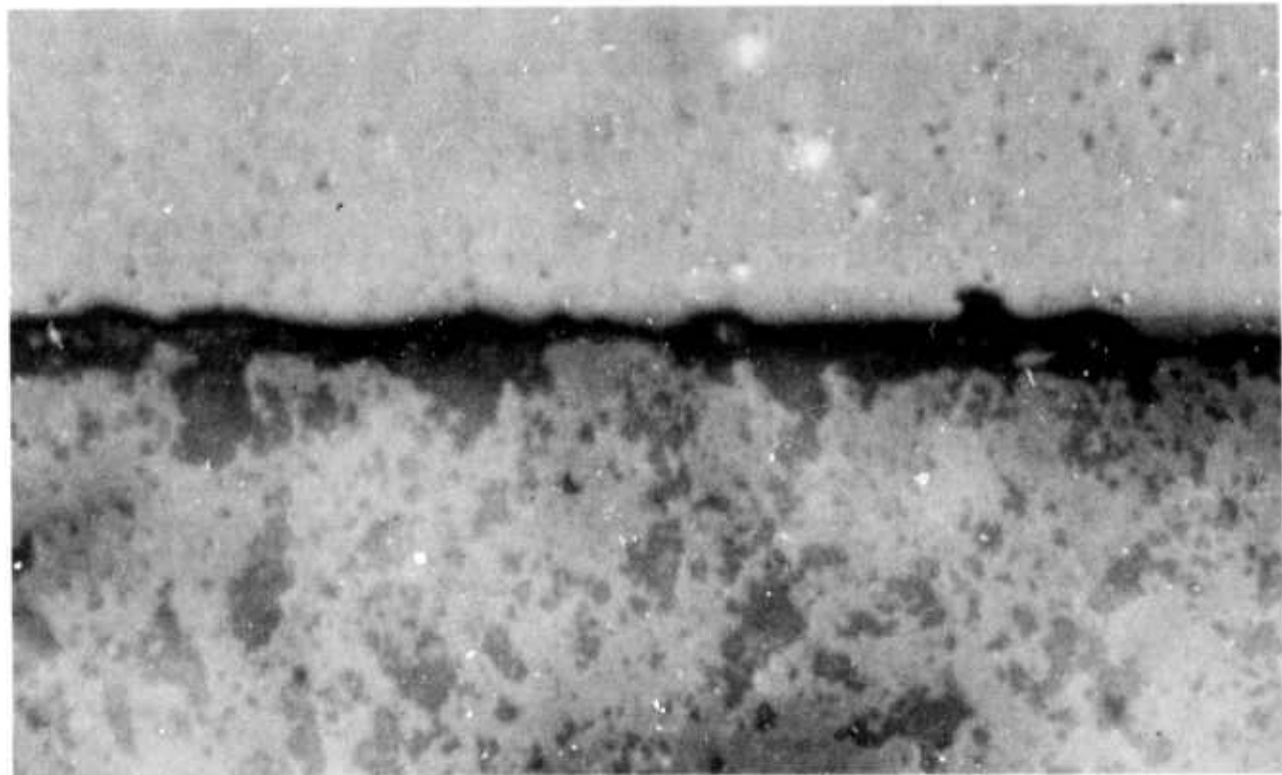


Figure 3.32 Microstructure Showing Poor Bonding (1250X)

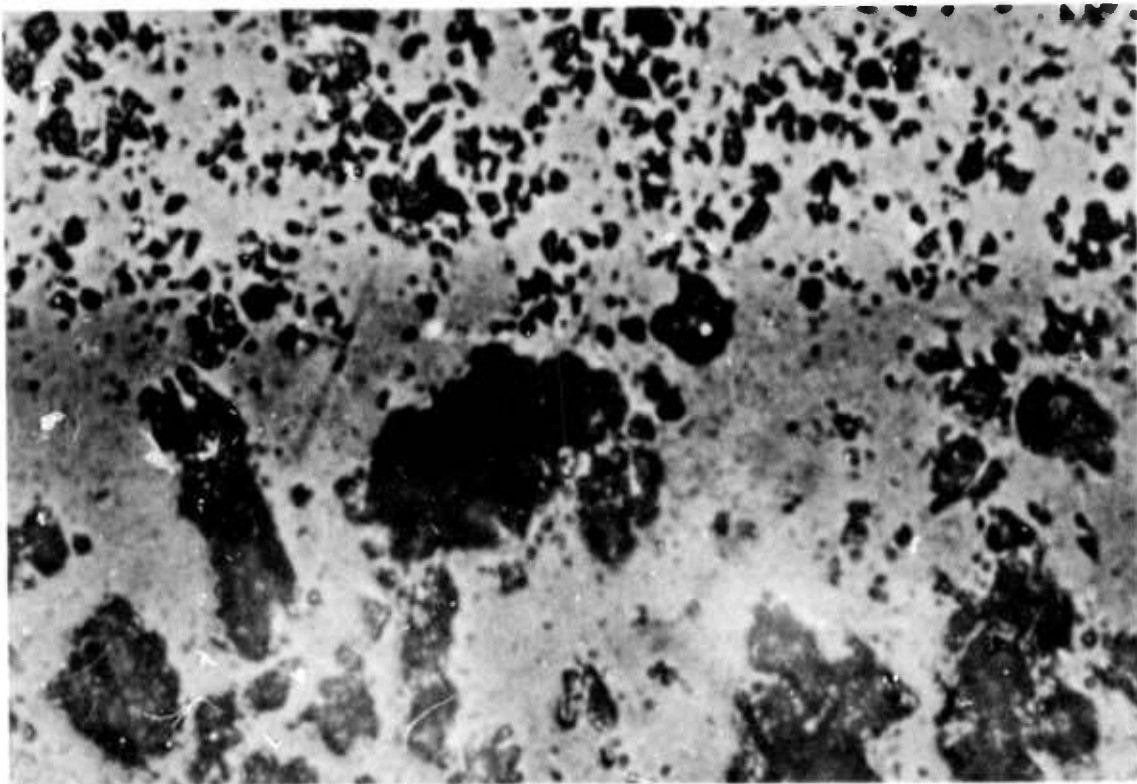


Figure 3.33 Microstructure Showing Good Bonding (1250X)

Figure 3.34 illustrates typical deformation of the reaction-sintered  $\text{Si}_3\text{N}_4$  blade ring when unsupported at the blade cavities for both a thick (0.250 in.) and thin (.100 in.) walled ring. The heavy walled ring offers some resistance toward deformation, although some bowing (0.050 in.) is observed at the blade region. However, note the deformation of the thin (0.100 in.) walled blade ring which resulted in fracture. These cases illustrate the deformation and fracture characteristics often observed in the hot-pressed duo-density turbine rotors fabricated by the various techniques. Therefore, once a total support system of the blade ring periphery has been developed, the likelihood of fabricating a high quality duo-density turbine rotor will be greatly enhanced.

In an effort to minimize final machining of the duo-density turbine rotors, some hub component parts were preformed to the approximate hub contour by hot-pressing in pre-shaped graphite dies. A preformed  $\text{Si}_3\text{N}_4$  hub is shown in Figure 3.35. Silicon nitride powder was wet ball milled in rubber mills using alumina balls with a 2 w/o  $\text{MgO}$  addition as a densification aid. After milling, the  $\text{Si}_3\text{N}_4$  powder was dried and hot-pressed at 1775°C and 4000 psi for 2 hours to theoretical density. After bonding the contoured hub to a reaction bonded ring, finish machining will only require removing approximately 0.050 in. from the contoured surface. These formed hubs will be utilized for fabrication of rotors in the future.

Since bonding of  $\text{Si}_3\text{N}_4$  component parts is critical to the success of the duo-density turbine rotor, studies were initiated to evaluate the effect of fabrication parameters on the degree of bonding.

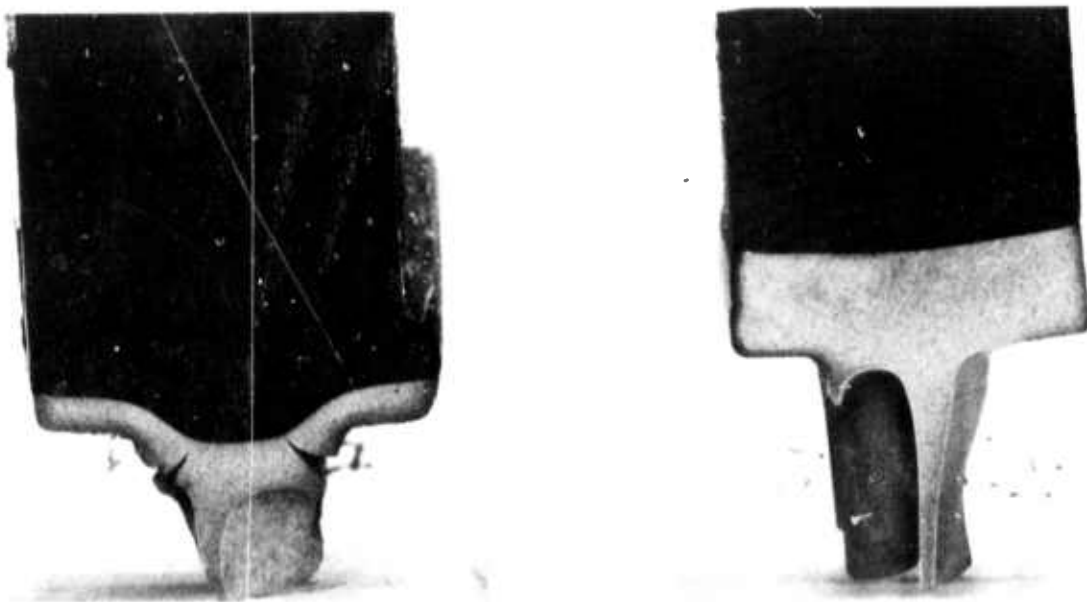


Figure 3.34 Deformation of Molded Blade Ring When Unsupported During Bonding



Figure 3.35 Hot-Pressed Preformed Silicon Nitride Hub

The hot-pressing parameters considered significant for bonding  $\text{Si}_3\text{N}_4$  parts are summarized in Table 3.2, along with a range of values for each parameter. Each of the first three, temperature, pressure, and time at temperature and pressure, may be varied over a fairly wide range while still achieving some degree of bonding. Four or five levels were arbitrarily selected for each parameter within their respective ranges for investigation. The  $\text{Si}_3\text{N}_4$  slip consisted of a slurry of  $\text{Si}_3\text{N}_4$  powder with various magnesium oxide concentrations, dispersed in lacquer, which is painted on the bond surfaces to act as a filler layer or bonding agent.

BONDING STUDY PARAMETERS						
TEMPERATURE, $^{\circ}\text{C}$	1550	<u>1600</u>	1650	1700	<u>1750</u>	1800
PRESSURE, p.s.i.	500	<u>1000</u>	1500	2000	<u>2500</u>	3000
TIME, HOURS	0.5	<u>1</u>	2	<u>3</u>	4	
$\text{Si}_3\text{N}_4$ SLIP, %MgO	NO <u>SLIP</u>	1	<u>2</u>	5		

Table 3.2 Bonding Study Parameters Considered Important For Bonding  $\text{Si}_3\text{N}_4$  Component Parts With Investigated Parameters Underlined

Since over 700 experiments would be required to evaluate all possible combinations, a statistically designed study was initiated to minimize the number of experimental runs. A factorial experiment test was made with each of the four assigned factors utilized at two levels, as indicated in Table 3.2. This means that only 16 experimental runs are required to evaluate the effect of each parameter on bond strength.

Initial experiments (1) on bonding reaction-sintered discs to hot-pressed discs yielded bonds greater than the strength of the reaction-sintered portion. Since the bond cannot be evaluated if failure occurs in the reaction bonded half, it was necessary to study the bond between two hot-pressed discs. The bonding study was critical since minimum temperature and pressure requirements are needed to minimize both the SiC reaction and fracture of the reaction-sintered component during hot-pressing.

These studies involved hot-press bonding two discs together as shown in Figure 3.36. This was repeated for the various processing conditions. Each bonded specimen was characterized with respect to microstructure and bond strength. Room temperature flexural strength measurements were made to evaluate the bond strength. The test samples were positioned such that the point of maximum tensile stress occurs at the bond area. The flexural strength results are summarized in Table 3.3 along with the hot-press bonding parameters. The flexural strength values are averages of ten values for each hot-press bonding condition.

A first order interaction factorial analysis of the data in Table 3.3 is summarized in Figure 3.37. For the first case, temperature is the main factor. The effect of the remaining three factors -- pressure, time, and slip -- cancel one another since all levels of each are present at both the upper and lower limits of temperature. This is also true for each remaining case where, in turn, pressure, time, and slip are the main factors.

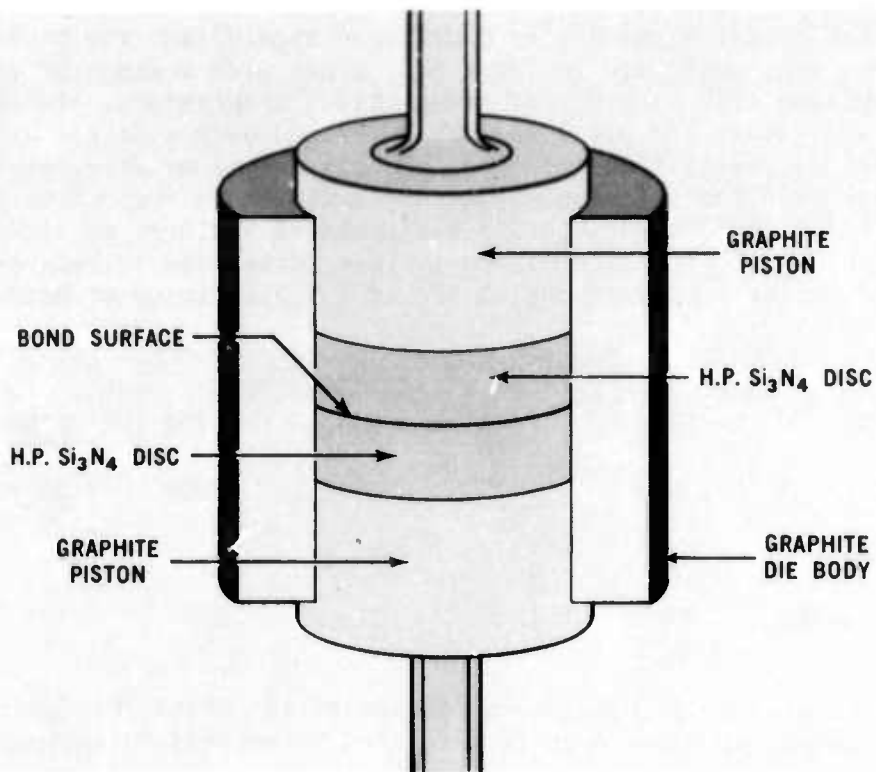


Figure 3.36 Hot-Pressing System for Bonding Silicon Nitride Disks

Table 3.3 Summary of Flexural Strength Measurements of the Bond for Various Hot Press Parameters

Hot-Press Run	Temperature °C	Pressure psi	Time Hr.	Slip %MgO	Flexural Strength Kpsi	Average	Std. Dev.
HP-225	1600	1000	1	None	18.5	7.31	
HP-250	1750	1000	1	None	31.9	5.91	
HP-235	1600	2500	1	None	31.8	6.83	
HP-241	1750	2500	1	None	58.0	7.97	
HP-226	1600	1000	3	None	50.8	4.66	
HP-229	1750	1000	3	None	54.4	6.76	
HP-231	1600	2500	3	None	45.8	7.54	
HP-240	1750	2500	3	None	61.0	6.21	
HP-227	1600	1000	1	2	11.5	6.32	
HP-230	1750	1000	1	2	48.7	4.22	
HP-228	1600	2500	1	2	40.4	5.98	
HP-255	1750	2500	1	2	58.4	7.50	
HP-248	1600	1000	3	2	22.7	7.74	
HP-252	1750	1000	3	2	43.4	8.12	
HP-247	1600	2500	3	2	22.7	4.18	
HP-253	1750	2500	3	2	67.6	2.17	

Samples tested in 4 point bonding.

Sample size 1/8 inch by 1/8 inch by 1-1/4 inch long.

Top span 0.375 inch, bottom span 1.125 inch.

Cross head speed was 0.1 inch per minute.

Strength values are average of 10 determinations.

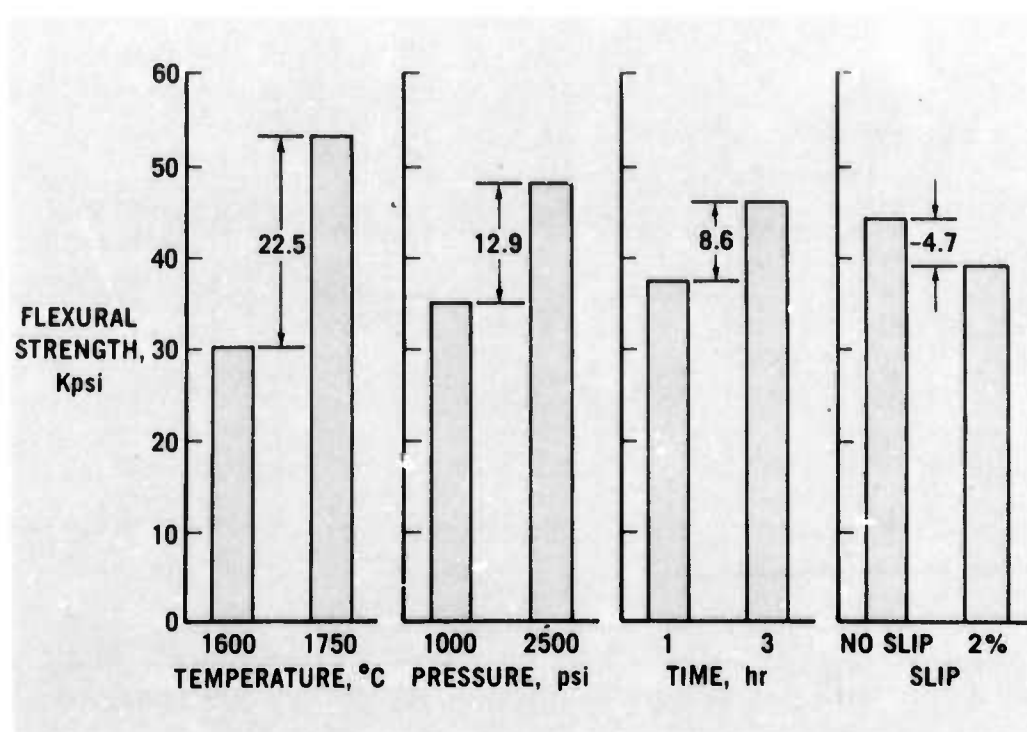


Figure 3.37 First Order Interaction Factorial Analysis of Bond Strength Parameters

The results show a 74% increase in bond strength, from 30.4 to 52.9 Kpsi, by increasing the temperature 150° from 1600 to 1750°C, which was the most effective factor on bonding. Similarly, a 37% (35.2 to 48.1 Kpsi) and 23% (37.4 to 46.0 Kpsi) increase in bond strength was exhibited by pressure and time respectively. Surprisingly, an 11% decrease in bond strength -- from 44.0 to 39.3 Kpsi -- resulted when a 2% MgO - Si<sub>3</sub>N<sub>4</sub> slip was used at the bond surface. It was anticipated that slips with higher MgO concentrations would enhance bonding and permit greater flexibility in the fabrication parameters without sacrificing the bond integrity.

A second order interaction factorial analysis of the data in Table 3.3 is summarized in Figure 3.38. The first two cases represent the difference in effect of temperature at the two levels of pressure and time, respectively, and indicate that the temperature increase has about the same effect on the bond strength at both levels of pressure and time. The third case represents the difference in effect of pressure at the two levels of time, indicating higher pressures are less effective on the bond strength at longer processing times.

Figures 3.39 and 3.40 show typical microstructures of the bond area for two hot-pressed bonded specimens having bond strengths of approximately 30 and 60 Kpsi, respectively. The poor quality bond of 30 Kpsi shown in Figure 3.39, is substantially stronger than reaction-bonded Si<sub>3</sub>N<sub>4</sub>, indicating perfect bonding need not be achieved for success of the duo-density turbine rotor.

These preliminary results indicate the effect of the hot-pressing parameters on the bond strength of cemented Si<sub>3</sub>N<sub>4</sub> component parts. These studies will be continued in more detail to generate information for fabricating the duo-density turbine rotors.

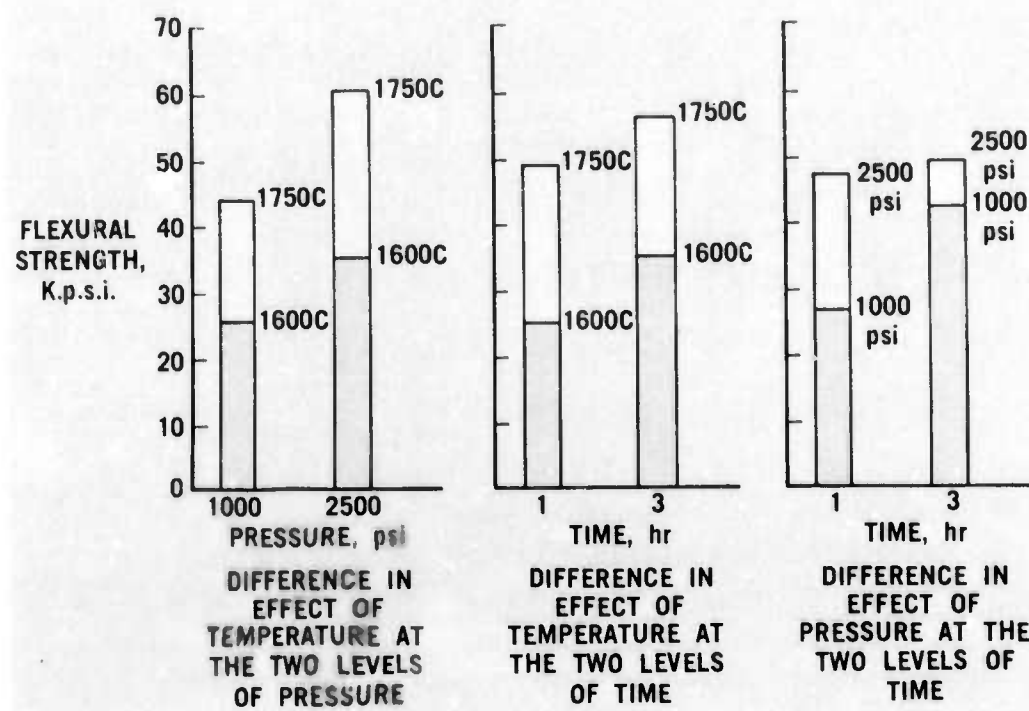


Figure 3.38 Second Order Interaction Factorial Analysis of Bond Strength Parameters

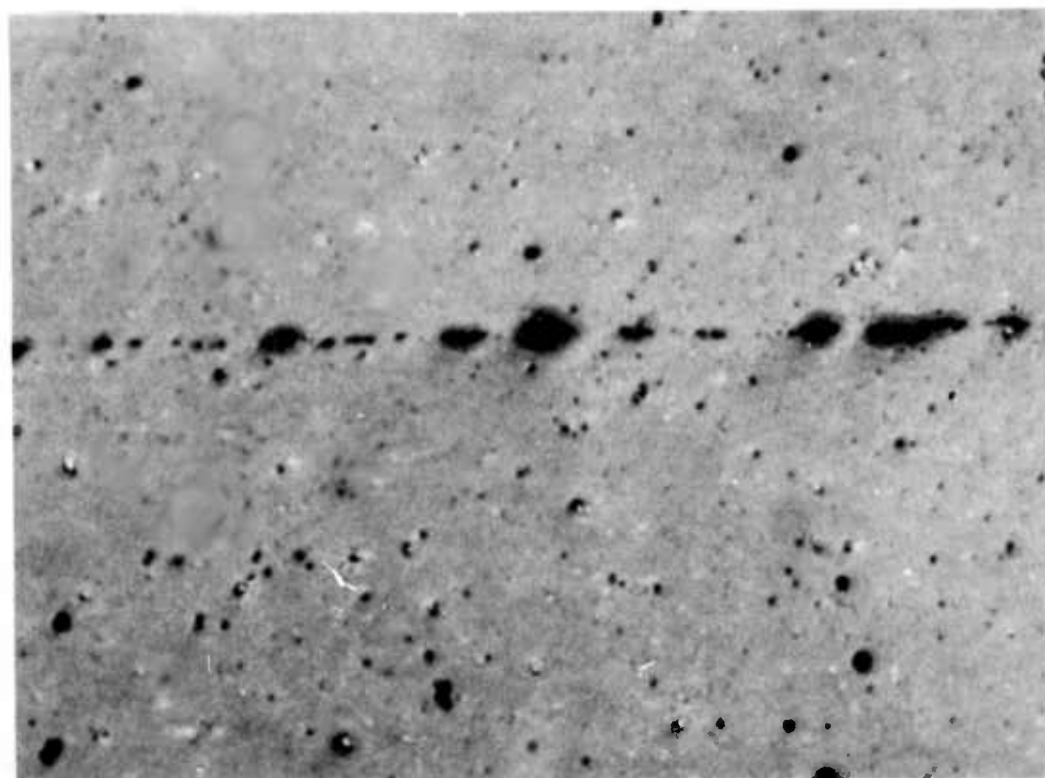


Figure 3.39 Microstructure of Bonding Sample With a Bond Strength of 30,000 psi (500X)

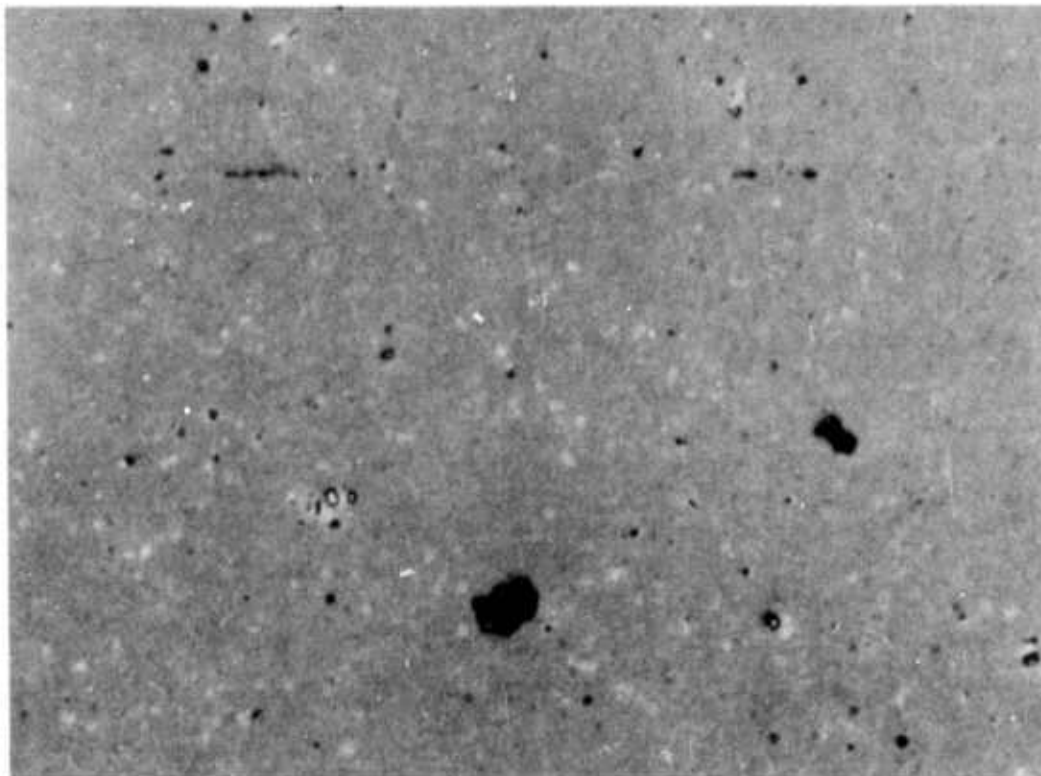


Figure 3.40 Microstructure of Bonding Sample With a Bond Strength of 60,000 psi (500X)

Ford/Energy Research CVD Silicon Carbide

It was previously demonstrated (1,2) that free standing, full rotor shapes could be produced by chemical vapor deposition (CVD) of silicon carbide. Deposition in a tungsten mold had produced one rotor with essentially complete blade fill. However, filling the cavity at the base of the blades and the formation of a homogeneous hoop had yet to be accomplished. (1)

During this reporting period, 11 rotor runs were made, resulting in delivery of 7 additional CVD SiC rotors. Four of these were made by a two step deposition process in which the blades and the rim with the hollow blade base regions were grown. The rotor was then removed from the apparatus and the internal diameter of the rim diamond ground to a flat uniform surface. The rotor was then put back into the apparatus and the rim deposition restarted on the ground surface, filling the hollow region at the base of each blade. These 4 rotors are shown in Figure 3.41. Two of these were spin tested; the results are discussed in Section 3.1.3. These rotors all showed evidence of severe residual stresses within the deposited silicon carbide. This evidence took the form of spalled chunks of material, and was especially prevalent in the thick rim areas. This spalling of chunks of SiC from the rim is visible in Figure 3.42, showing a rotor after spin testing. One of the 7 rotors delivered was deposited in a carbon mold. This rotor appeared to have less residual stress than rotors deposited in tungsten as evidenced by a lack of spalling near the edges of the rim. However, spin testing of the carbon-deposited rotor did not show any significant increase in hoop strength.



Figure 3.41 CVD Silicon Carbide Rotors

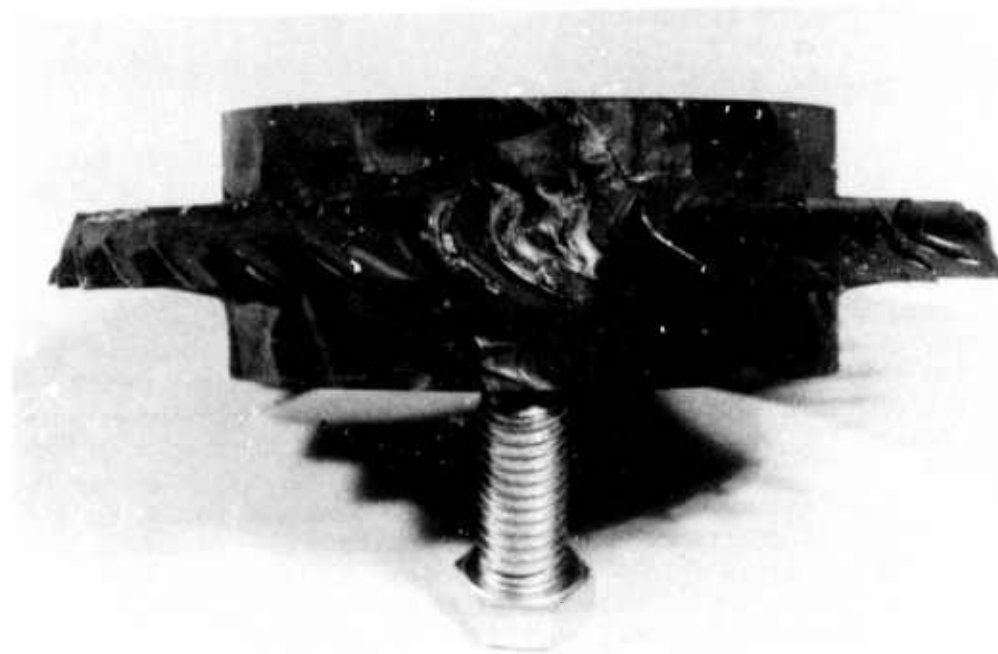


Figure 3.42 CVD Silicon Carbide Rotor Showing Spalling of Material After Spin Testing

### Ford/Lucas Silicon Nitride Program

The Joseph Lucas Company, under subcontract to the Ford Motor Company, has been endeavoring to fabricate ceramic turbine rotors from hot-pressed silicon nitride. (1,2) They begin with well characterized, high alpha phase silicon nitride powder which is incorporated into a binder system such that individual rotor blades may be molded sufficiently oversized so that when further processed to full density they will shrink to the desired volume.

As previously described (1) these complex airfoil-shaped preforms are assembled into a ring, and the rotor densified by hot-pressing in a conformable material serving as part of the die set. Figure 3.43 is a photograph of the best rotor made by this method. The preform densified to  $3.08 \text{ gm/cm}^3$  (97% of theoretical) accompanied by a decrease in volume of well over 2:1. However, as is apparent from the photograph, distortion was severe, including:

1. The diameter of the central hub increased by 0.25 in. and the hub depth was 0.325 in. less than print dimensions.
2. The length of blades were reduced by 0.125 in. due to a breaking and overlapping problem. The breaking and overlapping occurred at a relatively early stage in the cycle since in many cases the overlapped portions had press-bonded together.
3. The plane of the blades was dished indicating that they were not on the true neutral axis of compaction.

Due to the many problems encountered during the development of this process, it was decided to suspend work on this approach.

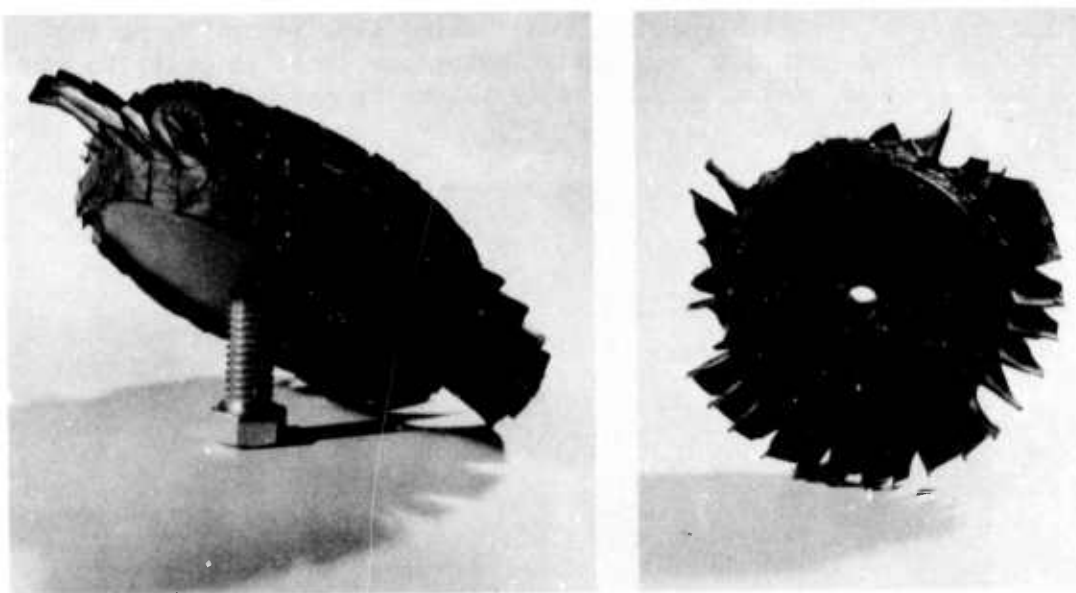


Figure 3.43 Lucas Hot-Pressed Silicon Nitride Rotor

### Electric Discharge Machining of Hot-Pressed Silicon Carbide

It was previously reported (1) that a feasibility study had been started to determine if Electric Discharge Machining (EDM) could be used to fabricate turbine rotors from hot-pressed silicon carbide. Four grades of silicon carbide had been evaluated, two of which could be machined at reasonable rates.

Two additional samples of hot-pressed silicon carbide have been examined and found suitable for EDM, one from the Norton Company and one from the Carborundum Company. Both samples were described by their suppliers only as hot-pressed silicon carbide with no specific code designation. Both companies reported active EDM programs in-house, so it appears that conductive SiC will be available from several sources.

A small copper EDM electrode was designed which allowed machining of simple straight-sided wedges simulating the thicknesses of both the leading and trailing edge of the rotor blade. This tool was used on two materials, Ceradyne 146A5 and the Norton hot-pressed silicon carbide. In initial cuts all wedges fractured in both materials before the full length of the blade had been achieved. The machined segments will be examined on the scanning electron microscope to determine the nature of damage caused by the EDM process. Preliminary results indicate the EDM surface is considerably rougher than a diamond ground surface and small cracks are apparent in the surface, as shown by the scanning electron micrograph in Figure 3.44. Further studies are required before definite conclusions may be drawn; therefore, fabrication of full size rotors has been postponed until a satisfactory combination of material properties and EDM parameters has been found.

### Ultrasonic Machining

Some progress in ultrasonic machining of airfoil-shaped blades was mentioned in the last report (1). However, due to lack of available machine time, very little work was done during this reporting period. A Cavitron machine was obtained and is being installed in order to continue this program, and should be ready to use in the near future.



Figure 3.44     Surface of Norton Hot-Pressed Silicon Carbide After EDM  
Cutting (500X)  
60

### 3.1.3 TESTING

#### Introduction

The Turbine Rotor Test Rig, designed specifically for high temperature testing of ceramic rotors, has been assembled and is being tested. The main function of the TRTR will be to evaluate ceramic rotors over the full range of expected engine operating conditions. The test rig has considerably fewer parts than a complete engine and can be quickly rebuilt after a rotor failure. All rotors will be fully tested in the test rig prior to engine use.

The results of fifteen room temperature ceramic rotor spin pit tests are also presented in this section. Three of these tests were performed on CVD silicon carbide rotors from Energy Research Corporation and the remainder were on duo-density rotors fabricated in-house or on components from which duo-density rotors are fabricated.

#### Turbine Rotor Test Rig

The Turbine Rotor Test Rig (TRTR), designed for ceramic rotor development is currently undergoing shakedown testing. Upon completion of the shakedown tests, the TRTR will be used to evaluate ceramic rotors over the full range of expected engine operating conditions. All rotors will be initially tested prior to engine use and the first complete set of ceramic rotors will be subjected to a 200 hour duty durability cycle which ranges up to 100% rotor speed (64,240 rpm) and 2500°F turbine inlet temperature. The TRTR design<sup>(1)</sup> is similar to an engine and employs much of the latest engine hardware but is simpler than the engine and can be rebuilt faster in the event of a rotor failure. Figure 3.45 shows the rig installed in the test cell.

Shakedown tests are currently being conducted utilizing metallic rotors with a simple bolt-on attachment mechanism. Mechanical rotor speeds up to 70,000 rpm have been successfully attained during cold tests. Hot tests now underway include evaluation of methods to simulate engine transient conditions. The TRTR will be ready for complete ceramic rotor evaluation at the completion of these tests.

#### Ceramic Rotor Spin Testing

The apparatus for spin testing rotors and test specimens has been described in a previous report.<sup>(2)</sup> Selected ceramic rotors available from the several hardware development programs described in Section 3.1.2 were subjected to destructive, room temperature spin testing.

#### CVD Silicon Carbide Rotors

Three of the 7 CVD SiC rotors received from Energy Research Corporation were spin-tested to failure. All three were mounted for testing in the same manner, i.e., supported on four rubber O-rings in contact with the internal diameter and both edges of the rim hoop as shown schematically

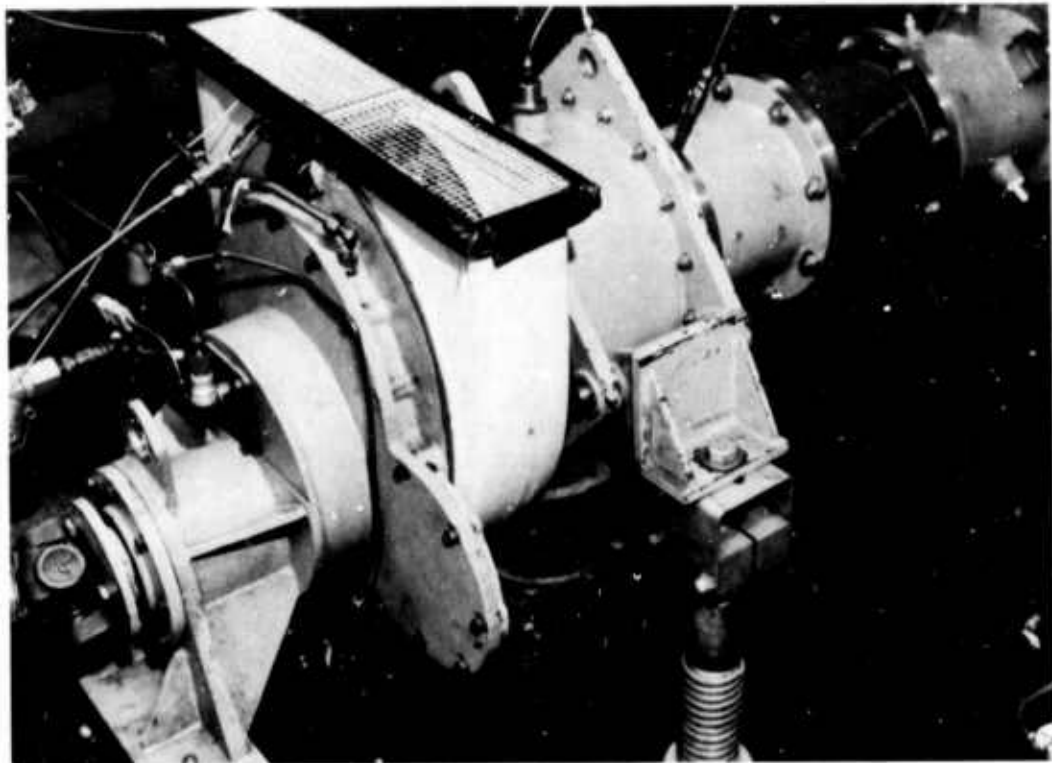


Figure 3.45      Turbine Rotor Test Rig Installed in Test Cell

in Figure 3.46. Two of the three rotors were deposited in tungsten molds, and failed in testing by losing individual blades at the junction with the hoop. Number one rotor lost two blades at 13,260 rpm while number two lost one blade at 11,360 rpm. These speeds are equivalent to low stress levels. Figure 3.47 is a photograph taken at the time of failure of CVD rotor number two, as the failed blade struck the surrounding strobe light triggering ring. Figure 3.42 shows the region of the hoop where the blades failed on rotor number one and the adjacent laminar chips.

The third rotor tested was deposited in a carbon mold. Weak blades were physically removed prior to the test and failure occurred in the hoop at 16,590 rpm. This failure, also at a low stress level (in the order of 2,000 to 3,000 psi) was also photographed and is shown in Figure 3.48.

#### Duo-Density Rotors

A total of 12 spin tests to failure were conducted on duo-density silicon nitride rotors, on rotor hubs, or on test samples which simulated duo-density rotors.

The hot-pressed silicon nitride hub components of a duo-density rotor, fabricated at Ford from AME powder, were spun to 80,000 rpm without failure. Since this is well in excess of the 64,200 rpm maximum design

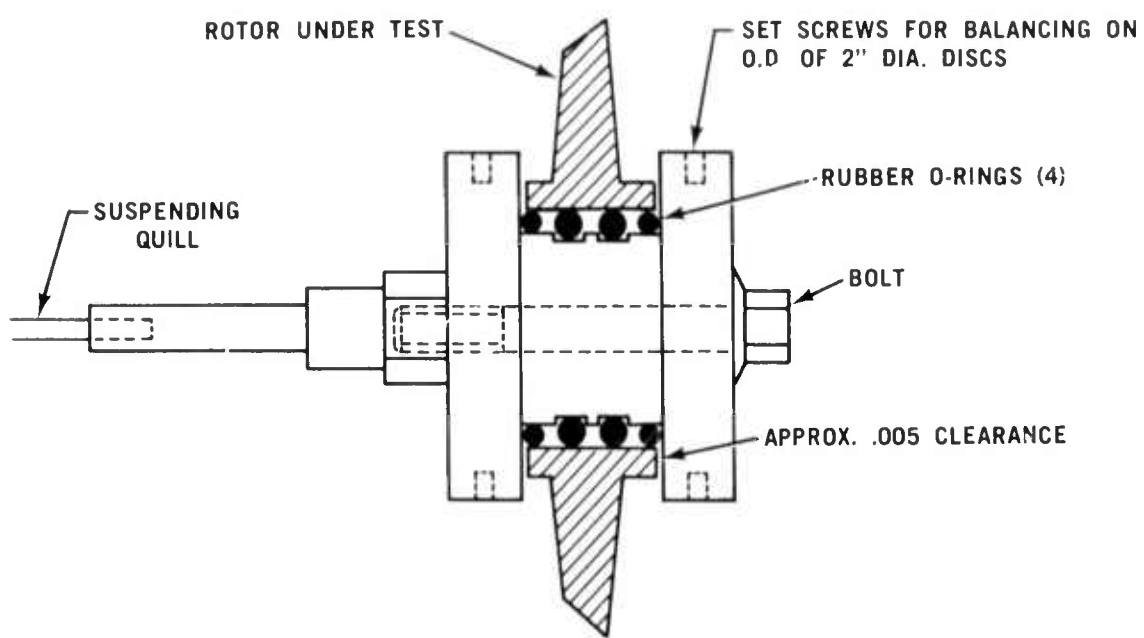


Figure 3.46 Schematic Diagram of Mounting of CVD Silicon Carbide Rotors

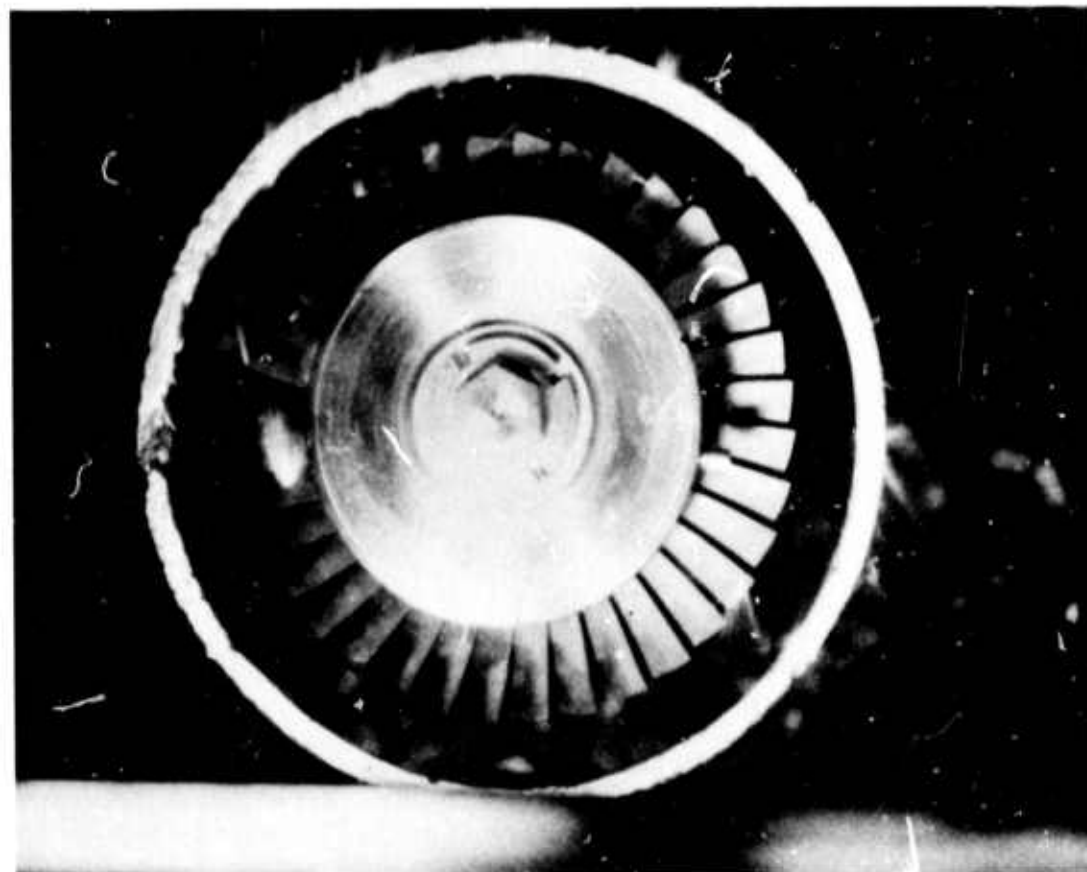


Figure 3.47 Failure of a Single Blade During Spin Testing of CVD Silicon Carbide Rotor Number Two

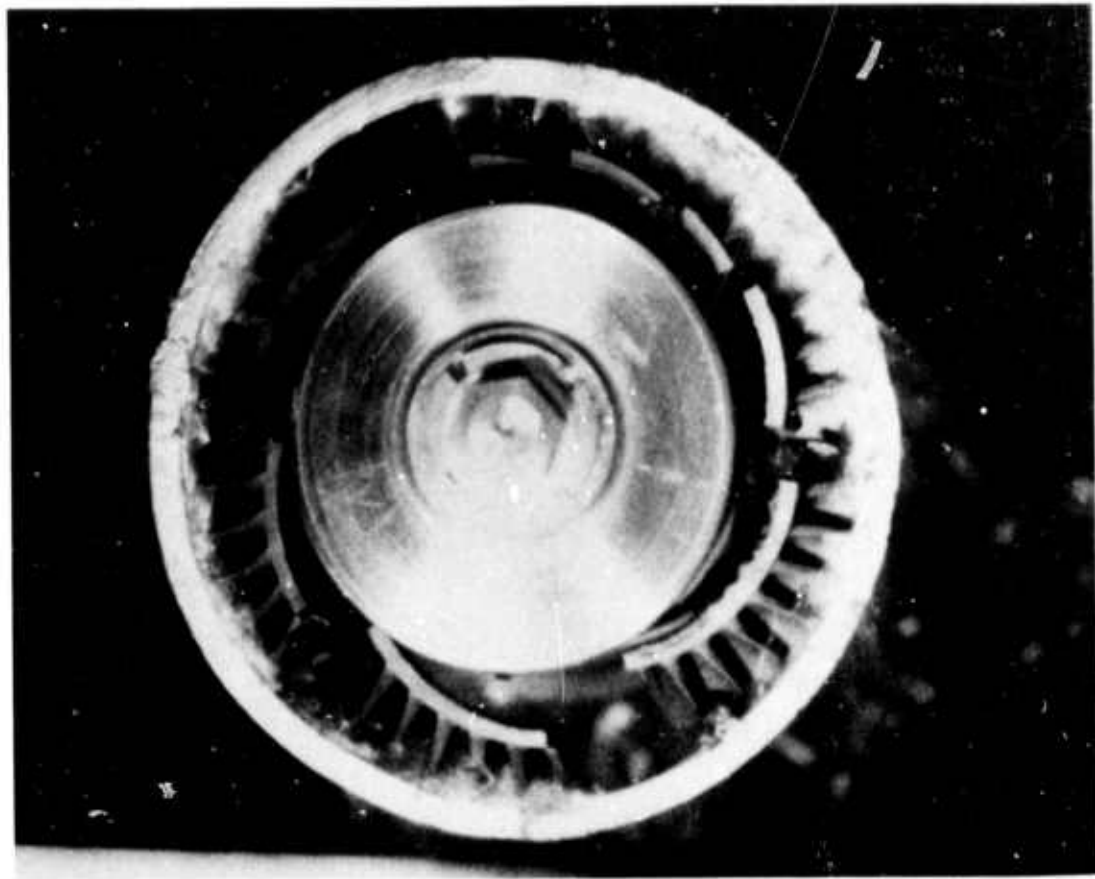


Figure 3.48 Failure of the Rim During Spin Testing on CVD Silicon Carbide Rotor Number Three

speed, it appears that the material will withstand the mechanical loads imposed by the application. Blade rims of Ford injection molded  $\text{Si}_3\text{N}_4$ , supported on rubber O-rings in a manner similar to the CVD SiC rotors (Figure 3.46), failed on the average at 30,000 rpm. These blade rims contained some voids. Improvement in blade rim quality is expected, based upon known molding technology.

Duo-Density rotors, made by the "wedge" technique described in Section 3.1.2, have been spun as high as 50,500 rpm, proving the existence of some bonding of the blade ring to the hub. This is equivalent to 18,700 psi stress in the bond region at failure. However, in this test the strobe misfired and no photograph was obtained. Since the hub, blade ring and the test fixture all were destroyed, it is not known which failed first. The test results on rotors exhibited a large spread in failure speeds indicating the bonding technique required further development. One rotor, for instance, failed at 30,000 rpm, similar to that expected for an unsupported blade rim. The failure, photographed as shown in Figure 3.49, was traced to the formation of a soft silicon carbide layer in the bond zone, essentially preventing bonding. This contamination has been substantially reduced in subsequent bonding runs and does not appear to limit the usefulness of the technique.

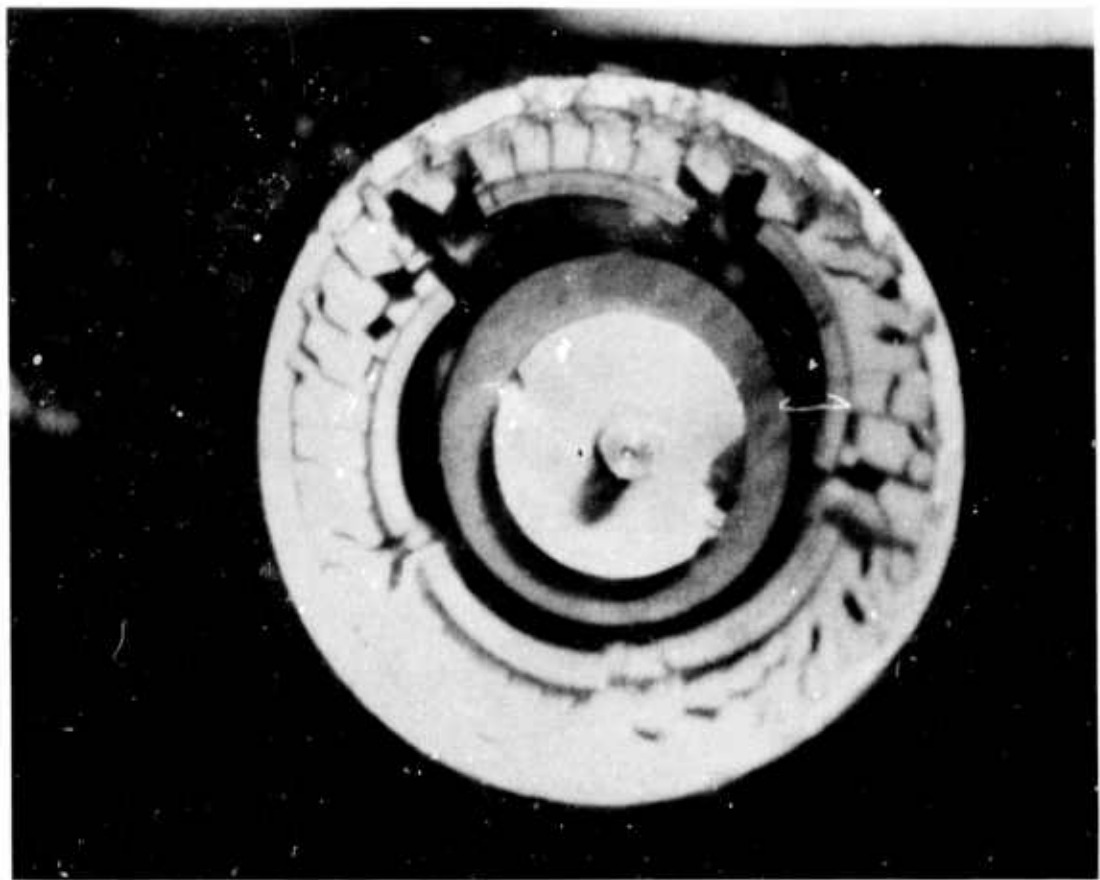


Figure 3.49 Failure of the Rim During Spin Testing of a Duo-Density Silicon Nitride Rotor

### 3.2 METAL ROTOR DEVELOPMENT

#### SUMMARY

A considerable amount of dynamic engine testing is being conducted with metal rotors, pending the development of ceramic rotors. While the use of metal rotors limits the turbine inlet temperature to 2000°F, much valuable information about stationary ceramic components is being obtained. However, failures of second stage metal rotors have limited the amount of testing. Several of these failures have been identified as having been caused by high cycle fatigue. The cause of these fatigue failures was poor quality castings combined with a resonant condition at 55% engine speed.

New casting have been received from one vendor and another casting vendor will be supplying turbine rotors in the near future. Meanwhile, test engines are accelerated through the resonant speed range in order to continue the development of ceramic turbine components. Over 70 hours of dynamic testing was accumulated by this procedure during this reporting period.

#### 3.2.1 MATERIALS INVESTIGATION

The ceramic turbine rotors present the most formidable task in the development of the small ceramic gas turbine engine, due to the high strength required plus the complex shape. In order that the development and testing of the other ceramic components are allowed to continue in parallel, metal turbine rotors are used for dynamic testing. While this limits the turbine inlet temperature to a maximum of 2000°F, a considerable amount of meaningful durability and performance testing can be done in order to confirm the design concepts of the other ceramic components. When ceramic rotors are available, they will replace the metal rotors.

Efforts to optimize the MTO-001 superalloy previously used for investment cast rotors did not result in obtaining mechanical properties, measured on test specimens machined from castings, deemed necessary for engine operation. Consequently, a different superalloy was selected to circumvent casting problems associated with the MTO-001 material. The alloy selected, primarily on the basis of improved castability and ductility, was MM-002, a Martin Metals nickel-base superalloy. Additional casting vendors were contacted to alleviate problems associated with obtaining castings from a single source. One additional vendor was selected as a second source for MM-002 rotor castings.

The efforts of the previous rotor casting vendor culminated in obtaining two acceptable rotors out of a casting lot of six. This lot had reported average properties of 139 Ksi (ultimate strength), 118 Ksi (.2% yield strength), and 9% elongation. However, a subsequent lot of castings had inadequate ultimate and yield strengths and were therefore rejected for engine use. This vendor was then redirected to reproduce castings with mechanical properties previously achieved, prior to shipment of any additional rotors.

The second casting vendor's endeavors proved successful, and castings with mechanical properties sufficient for engine operation were achieved after making adjustments to their initial casting parameters. Rotor castings exhibited little scatter in mechanical properties as shown by specimens machined from various regions and this consistency is a definite indication of casting homogeneity. This vendor is equipped with an experimental parts laboratory capable of mold preparation, alloy melting and casting, processing and nondestructive testing to assume quality hardware. Future investment cast components should reflect this capability.

### 3.2.2 TESTING

The lack of final machined new rotor castings conforming to the tighter materials specification has delayed the investigation into the possible sources of excitation. Over 70 hours of dynamic engine testing have been accumulated during this reporting period by accelerating the engines through the resonant speed area of 55% speed.

The Design C engine uses a different second stage turbine stator which has the inner diameter of the flowpath as an integral part of the stator. This requires that the platform on the second stage turbine disk be removed. A rotor was modified to this configuration and its natural frequencies determined by holographic techniques. The results for some of the critical frequencies are shown in Table 3.4 for both Designs B and C. Figures 3.50 and 3.51 show typical mode shapes for the Design C rotor.

It was noted in the last report (1) that Design B rotor failures in engines occurred as a result of operation at 55% engine speed. The critical natural frequency excitation mode appeared to be the two diameter plus one radial, which for Design C, has increased 10%. Therefore, the critical engine speed for Design C rotors will be 60%. Engine testing will be carried out to confirm this critical condition.

Table 3.4  
Second Stage Turbine Rotor Natural Frequencies

Mode Shape	Natural Frequency (cycles per second)		% Increase of Design "C"
	Design "B"	Design "C"	
Two diameter	3383	3462	2.3
One radial	4158	5947	43.
Two diameter plus one radial	4925	5444	10.
Four diameter plus one radial	9600	9753	1.5

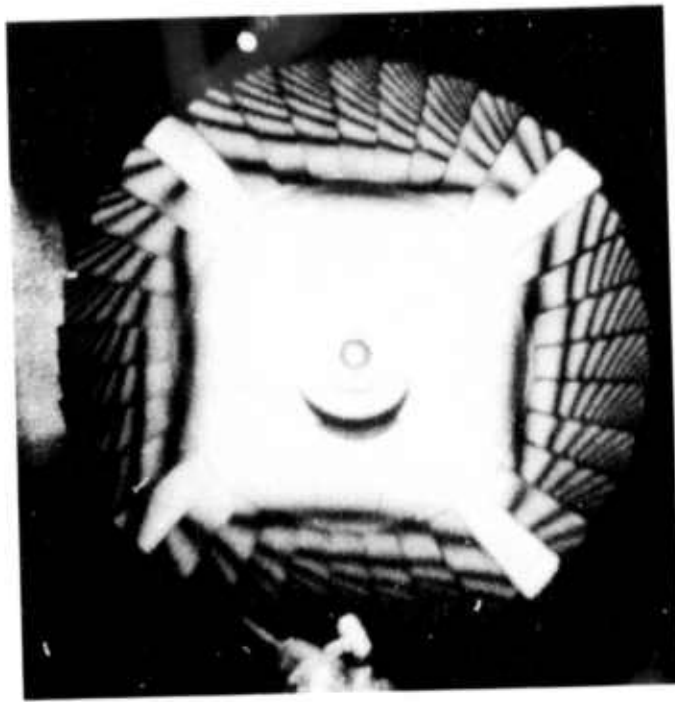


Figure 3.50      Hologram of Second Stage Rotor, Two Diameter Mode Shape.  
3452 Cycles/Per Second

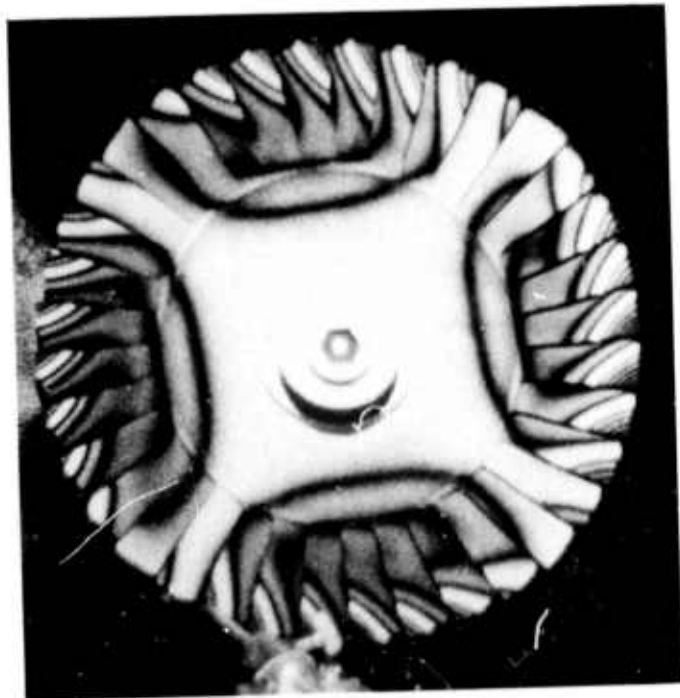


Figure 3.51      Hologram of Second Stage Rotor, Two Diameter Plus One  
Radial Mode Shape. 5444 Cycles/Per Second

### 3.3 CERAMIC STATORS, SHROUDS, NOSE CONES AND COMBUSTORS

#### SUMMARY

Stators incorporating a revised outer shroud design, intended to eliminate cracking of the shroud, were fabricated and evaluated. Hot static and dynamic testing of Design B second stage components of this configuration showed considerable reduction in, but not complete elimination of this shroud cracking.

The first stage stator blade geometry has been modified to provide a more uniform temperature response to transients. This was shown quantitatively on the thermal shock test rig, which was found to provide close correlation with calculated stator thermal response in the engine. Two stators were extensively tested and one survived 104 hours of hot static testing while the other withstood 272 light-off cycles, both remaining serviceable but with shroud cracks.

The thermal shock test rig was also utilized to evaluate the new Design C second stage stator with inner shroud and results indicated this design to have poor thermal shock resistance.

The use of rotor shrouds made of slip-cast reaction-sintered  $\text{Si}_3\text{N}_4$  eliminated past cracking problems experienced with shrouds made by a cold-pressing process. However, these shrouds exhibited plastic deformation under load. An evaluation of the effect of nitriding additives upon this deformation showed that the calcium containing material normally used caused considerable plastic deformation, while iron oxide was shown to be a good nitriding aid and did not contribute to deformation.

Slip cast  $\text{Si}_3\text{N}_4$ , Norton Crystar SiC and Carborundum KT SiC were evaluated as combustors in a turbine test rig. Preliminary results showed the KT SiC material to be the most promising.

Several redesigns in the nose cone have been made in an effort to eliminate axial cracking. This problem has not been eliminated, and design changes will continue along with hot static and dynamic testing of the redesigned nose cones.

PRECEDING PAGE BLANK-NOT FILMED

### 3.3.1 MATERIALS AND FABRICATION

#### Introduction

As previously reported (1), first stage stators had experienced both a vane cracking problem and an outer shroud cracking problem, and the second stage stators had also experienced outer shroud cracking. Stator material and fabrication development during this reporting period, addressed these problems and also was concerned with the second stage stator designed for ceramic turbine rotors and designated Design C.

Design B and Design C flow path components are shown in Figure 3.52, and the differences are noted.

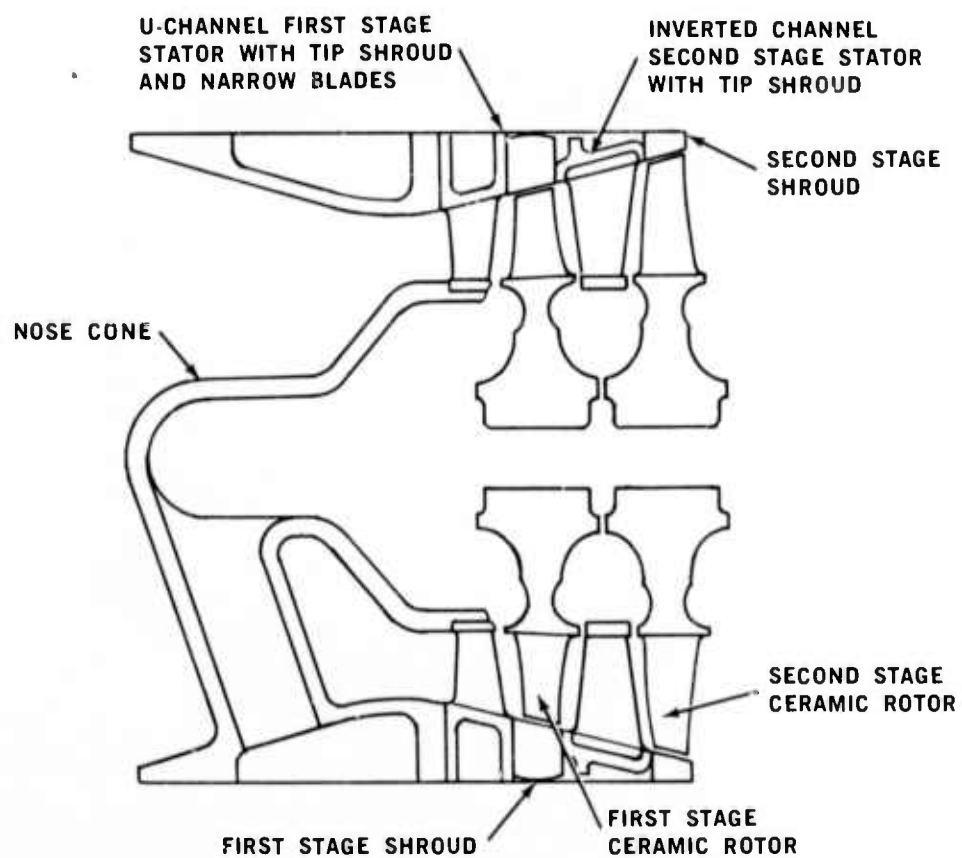
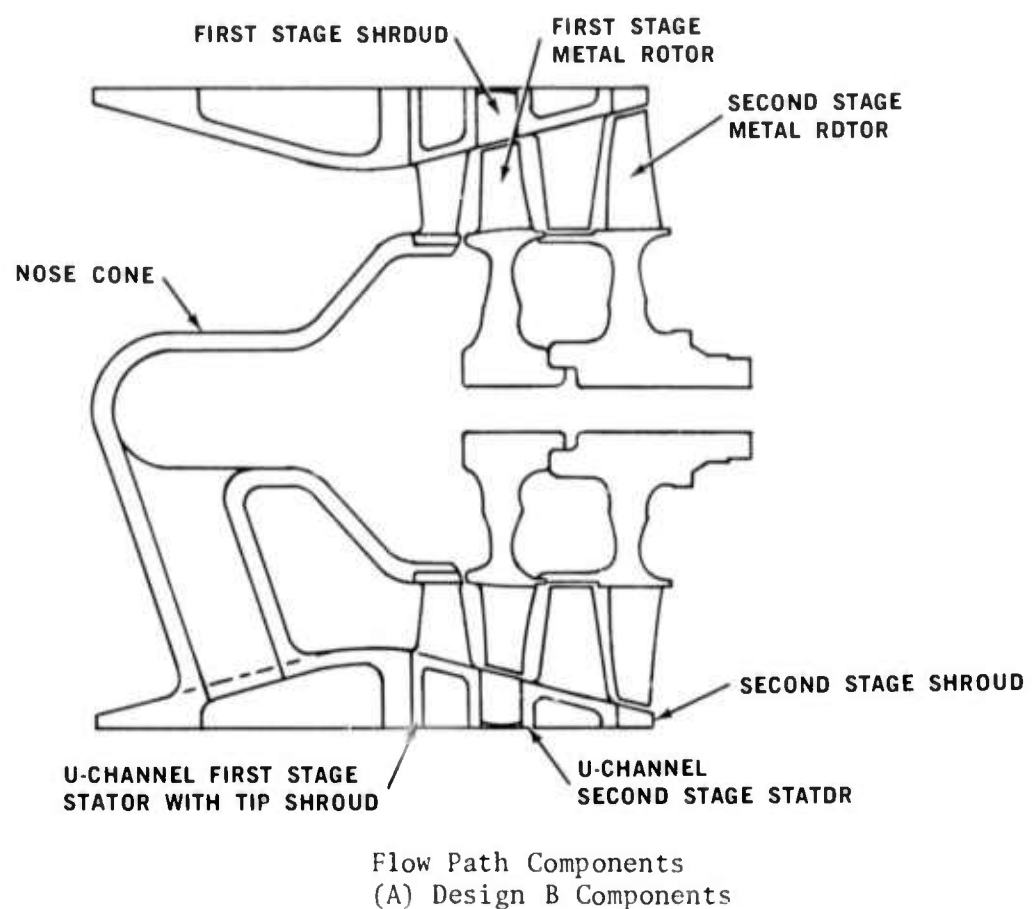
Engine and bench tests on slip cast reaction-sintered  $\text{Si}_3\text{N}_4$  rotor shrouds indicated a problem with plastic deformation. This deformation is related to nitriding additives and experiments are being conducted to determine the effect of various nitriding additives on this problem.

#### Stator Fabrication and Assembly

Previous testing of Design B first stage stator segments and assemblies with the trailing edge reduced by 0.140 in. demonstrated this modification would solve the vane cracking problem experienced on the first stage stator vanes. (1) The first stage vanes evaluated on the thermal shock test rig and under static and dynamic engine conditions were Design B vanes reduced by hand grinding 0.140 in. from the vane chord at the trailing edge. Design C vanes, as this Design B modification was designated, are now molded to shape and incorporate the positive assembly locating feature discussed in the previous report (1) to control inner shroud gaps. The molded vane is expected to have improved aerodynamic characteristics as compared to the more irregular hand-ground vanes.

Tooling to injection mold Design C second stage stators, with an inner shroud, has been procured and stator assemblies were fabricated. This inner shroud design resulted in reduced thermal shock resistance and vane cracking as determined by several series of tests on the thermal shock rig. Reduction in thickness of the inner shroud and reduction of vane trailing edges are being evaluated presently as a solution to this cracking problem.

During this reporting period, progress was made in several areas relative to improving the technique for assembly of Design B second stage stators. This assembly method was discussed in the previous report (1) and consisted of the bonding of pre-sintered silicon stator segments onto a pre-sintered slip cast backing ring. Although the incidence of outer shroud cracking was reduced during engine testing, some cracks still occurred. This cracking may have been caused by the inability to achieve complete bonding between adjacent segments and between segments and the backing ring. The regions that were incompletely bonded may have formed notches acting on the outer ring that decreased the intrinsic strength of this ring. To minimize this notch effect on the outer ring and to



(B) Design C Components  
Figure 3.52 Flow Path Components

minimize actual bonding surface area, the outer shroud ring and the injection molded blade segments were redesigned. In this design, referred to as "inverted channel", the blade segments consisted of an airfoil and a relatively thin platform. A slip cast outer shroud was channeled on the inside diameter to accomodate the blades as shown in Figure 3.53. Bonding of the slip cast ring and stator segments was accomplished by application of a silicon metal slip onto the mating parts, followed by sintering in nitrogen to convert the entire assembly into silicon nitride as shown in Figure 3.54. Please refer to Section 3.3.2 for engine testing results of these assemblies.

#### Rotor Shroud Development

Rotor shroud rings, shown in Figure 3.55, are located directly downstream from each stator stage in the engine assembly and form the outer tip shroud. A gap is cut into the shrouds during final machining, making in effect a split ring which allows the shroud to move as it expands relative to its housing. Cracking of these rings, made by cold pressing and sintering, during engine operation demonstrated the need for a stronger reaction-sintered  $\text{Si}_3\text{N}_4$ . Consequently, a slip cast technique was developed to yield higher density and higher strength materials. Rotor shroud rings fabricated by slip casting have not cracked during engine testing. These shroud rings, however, have changed dimensions during engine operation, which may be creep phenomenon. Both the first and second stage shroud rings decreased in diameter as a function of hot time in the engine.

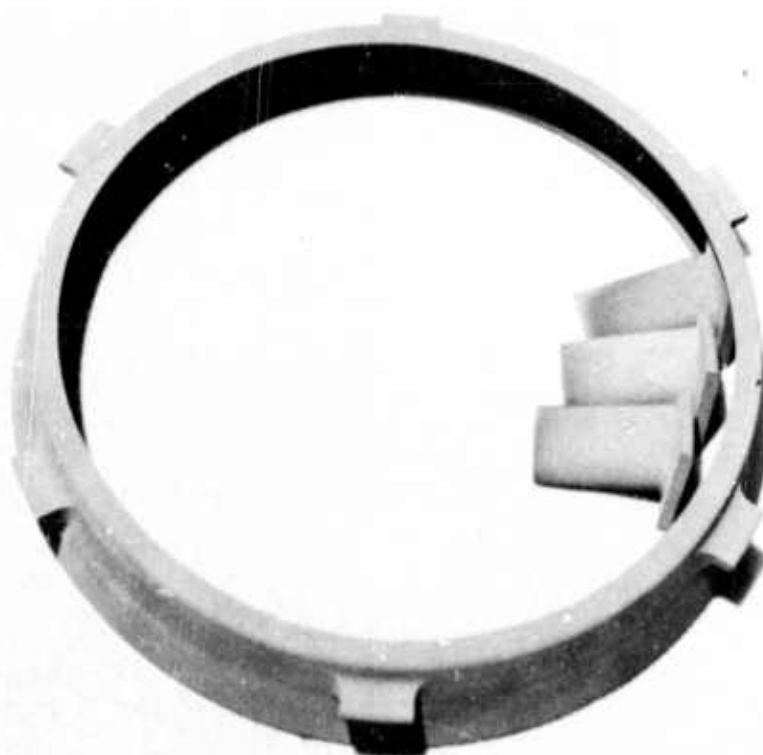


Figure 3.53 Vanes and Outer Shroud for Inverted Channel Second Stage Stator

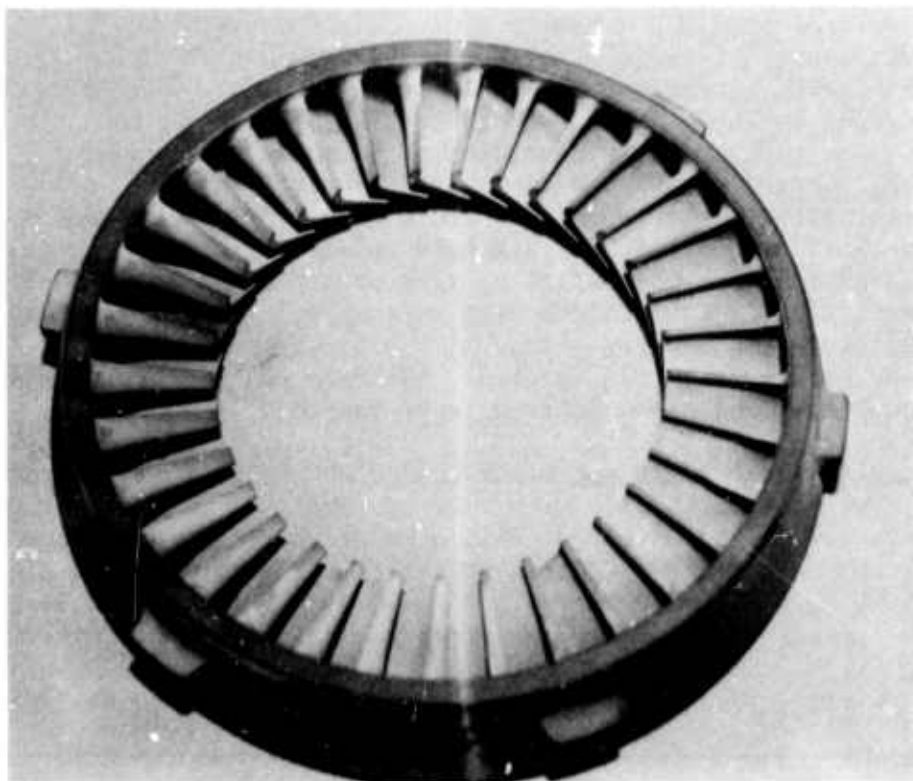


Figure 3.54 Assembled Second Stage Inverted Channel Stator

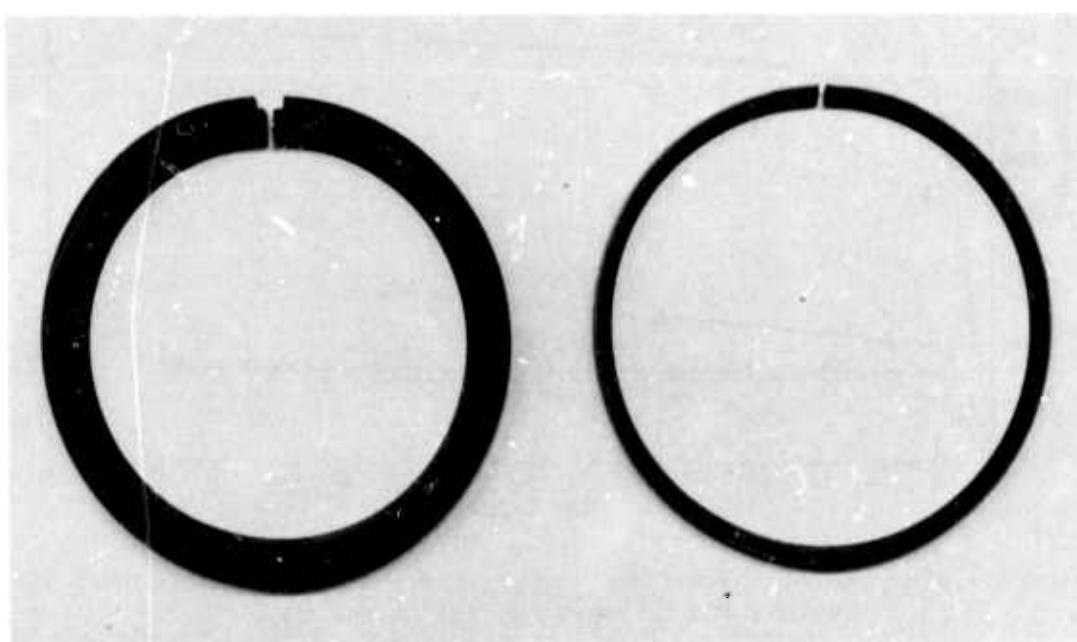


Figure 3.55 First and Second Stage Rotor Shrouds

A test program was formulated to identify the possible causes for this dimensional change. A number of formulations were tested, with the impurity level of the silicon powder being the principle variable. Impurities deliberately added were iron and calcium. The Fe impurity was introduced as  $\text{Fe}_2\text{O}_3$  and Ca was added as  $\text{CaF}_2$ .  $\text{Fe}_2\text{O}_3$  and  $\text{CaF}_2$  are nitriding aids that promote conversion of Si metal to  $\text{Si}_3\text{N}_4$  in a nitrogen atmosphere. Shroud rings were fabricated by drain casting hollow cylinders. After pre-sintering, the tubes are sliced into rings, nitrided and diamond ground to final dimensions. To simulate actual engine conditions, each ring was placed inside of a close-fitting ring of lithium-aluminum-silicate material, and heated at 1900°F for various time intervals. The relative expansions of the two materials applied a load as the expansion of the  $\text{Si}_3\text{N}_4$  was restrained. After each time interval, the free gap width of the shroud was measured and dimensional changes were recorded.

Figure 3.56 shows the gap width change at given time intervals for slip cast silicon nitride with varying levels of nitriding aids. This shows that the stability of slip cast silicon nitride without a nitriding aid is relatively poor. Stability improved with the use of nitriding aids with the best results provided by additions of  $\text{Fe}_2\text{O}_3$ . There are several factors which may lead to increased stability with nitriding aid additions, including the probability that conversion of Si metal to  $\text{Si}_3\text{N}_4$  may be more complete. X-ray diffraction analysis

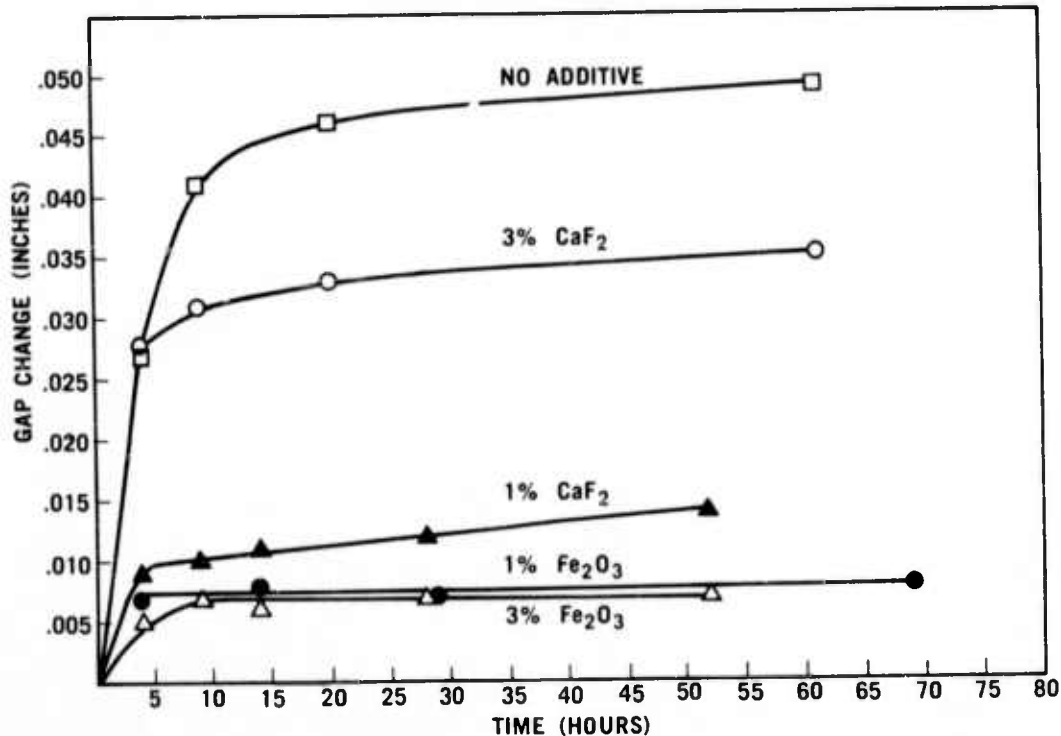


Figure 3.56 Rotor Shroud Gap Change versus Time at Temperature for Various Nitriding Additives

Showed no residual silicon metal in any of the systems, however, x-ray analysis cannot detect silicon metal concentrations less than 3%. Subsequent photomicrographs did reveal some unreacted silicon metal in the  $\text{Si}_3\text{N}_4$  without additives, and its poor stability may be due to the small amount of unreacted silicon.

Figure 3.56 also shows that the greater the concentration of calcium the greater the instability of  $\text{Si}_3\text{N}_4$ . These results parallel those obtained with creep measurements on hot-pressed(1) and reaction-sintered silicon nitride (Section 5.1.2).

### 3.3.2 TESTING

#### Introduction

The combustor, inlet nose cone, stators, and shrouds are classified as the hot gas flow path stationary components. These components must be developed to withstand (a) thermal shock upon start up and shutdown, (b) aerodynamic loading at engine operating conditions, and (c) mechanical and vibratory loads transmitted from the surrounding structure. Testing of some of these ceramic components was also carried out using a thermal shock rig in the search for solutions to stator blade cracking problems, because experimental components could be evaluated quickly with repeatable and easily observable test conditions.

#### Thermal Shock Rig Testing

The thermal shock rig and its use to simulate stator vane cracking was discussed in the last report. (1) The basic rig has since been modified by adding an infrared sensing pyrometer and temperature recorder.

An Ircon Model 300L infrared sensing pyrometer was used to determine the temperature response of various areas of the stator vanes when heated and cooled by the thermal shock test rig. Temperatures from  $170^{\circ}\text{F}$  to  $3000^{\circ}\text{F}$  can be measured with an accuracy of  $\pm 2\%$  of temperature with a repeatability of  $0.5\%$  of temperature at various spots  $1/8$  in. in diameter. Response time is 0.1 seconds for 95% of scale reading and output is a nonlinear 0-10 mv.

A Varian Associates X-Y plotter with an integral time base was coupled with the pyrometer output to provide a record of temperature and temperature versus time. Figure 3.57 shows the vane temperature 45 seconds after entering a  $3000^{\circ}\text{F}$  flame, for designs B and C. The design C vane has a thinner cross-section and is approximately 0.140 inches shorter along its chord than the B design. These modifications lowered the trailing edge temperature and resulted in a more uniform temperature distribution in the vane.

Utilizing the Ircon plotter, combination heating and cooling rates of vanes were determined. Comparative cooling curves for design B and design C vanes are shown in Figure 3.58. These curves show that the Design C vane has a somewhat slower cooling rate and therefore should be superior in thermal downshock resistance to design B vanes.

This technique of plotting temperature versus time was used to compare calculated temperature response in the engine to measured temperature response in the thermal shock rig. Figure 3.59 shows the vane temperature rise is slightly more severe on the thermal shock rig while the temperature of the shrouds vary above and below calculated data due to limitations of heating and cooling capabilities of the present shock rig. The close approximation of vane temperatures supports the correlation experienced between thermal shock test rig results and engine test results.

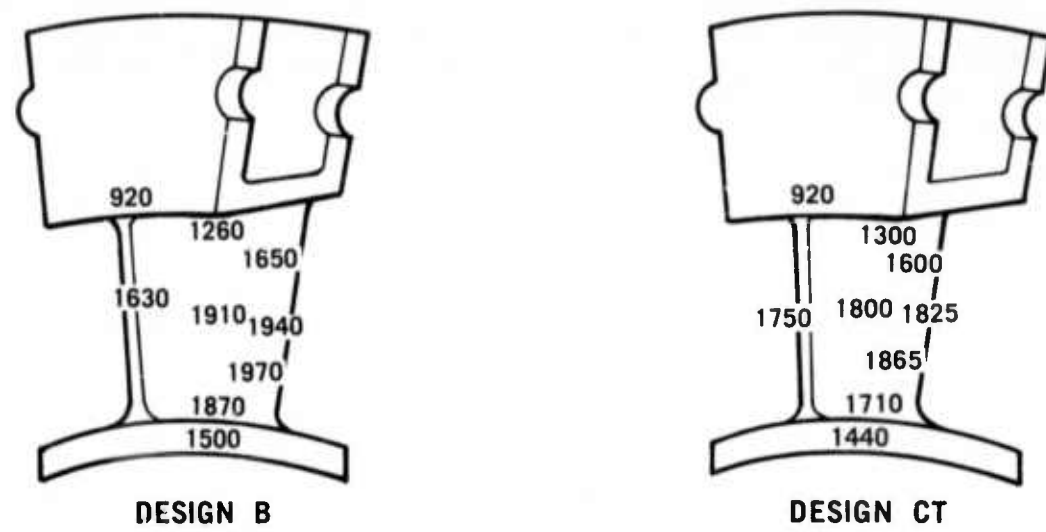


Figure 3.57 Vane Temperatures

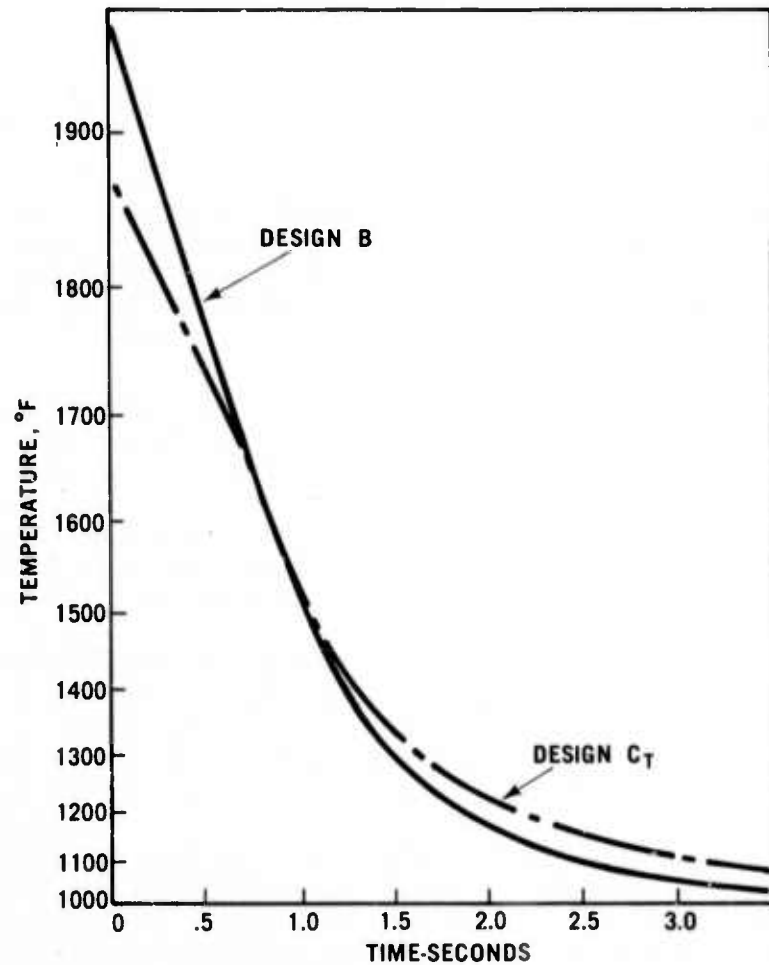


Figure 3.58 Vane Temperature versus Time During Cooling Cycle

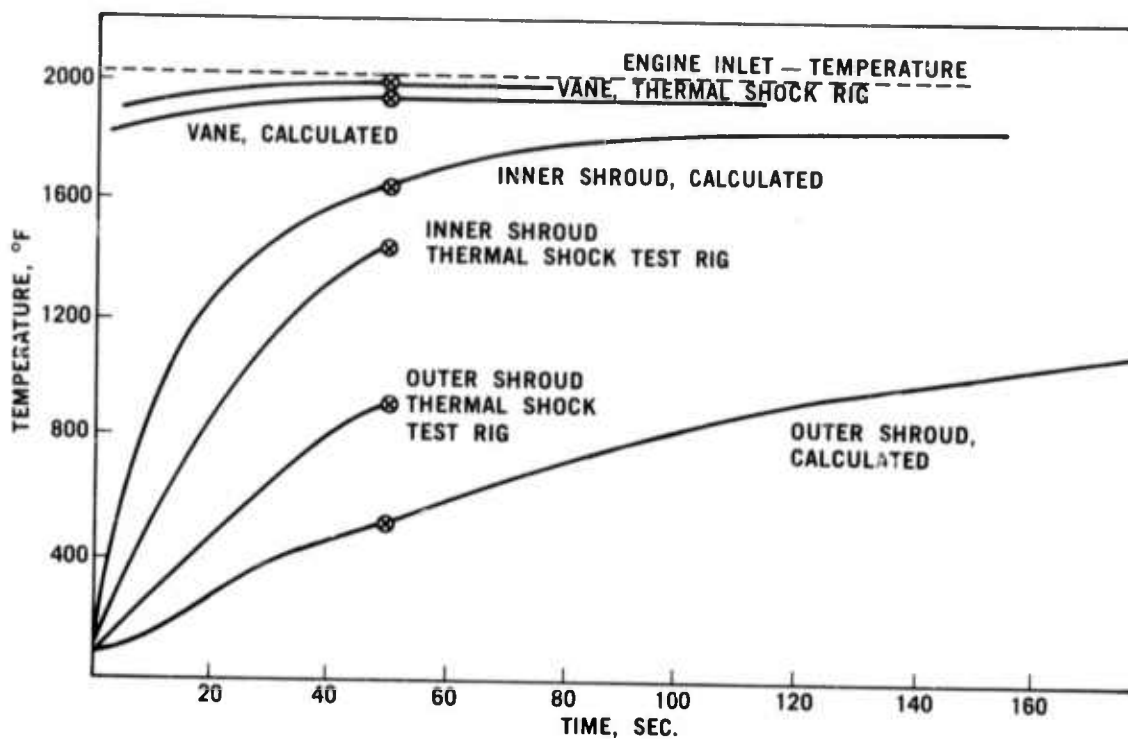


Figure 3.59 Time-Temperature Response for First Stage Stator Blades

Design C first stage stator vanes were tested for 1000 cycles at  $3000^{\circ}\text{F}$  flame temperature with no failures in the 24 vane segments evaluated. Vane temperatures of  $2400^{\circ}\text{F}$  have been run intermittently with no failures in approximately 200 cycles.

Second stage Design C stator vanes were also evaluated on the thermal shock test rig and failed approximately 1/4 in. above the inner shroud. The trailing edge temperatures were more concentrated in this vane than in those of the unshrouded Design "B" vane. Reducing the thickness of the inner shroud and reducing the vane chord are being investigated with the aim of achieving a more uniform cross-sectional temperature distribution.

#### Combustor Testing

The ceramic combustor testing program has subjected ceramic candidate materials to a series of tests simulating engine conditions. A preliminary screening sequence was developed in which a ceramic combustor tube (Figure 360) was installed in a test engine replacing the metal combustor can. The engine was then run for approximately 5 minutes at  $1900^{\circ}\text{F}$  turbine inlet temperature. The engine was shut off and when the temperature of the combustor had reached  $100^{\circ}\text{F}$ , the test was repeated. A set of 10 lights and cooldowns comprise a test set. This procedure was used on each candidate combustor.

Ford slip cast reaction-sintered  $\text{Si}_3\text{N}_4$  was the first material evaluated. All components which were tested cracked severely, indicating poor thermal shock resistance of  $\text{Si}_3\text{N}_4$  in this design configuration.

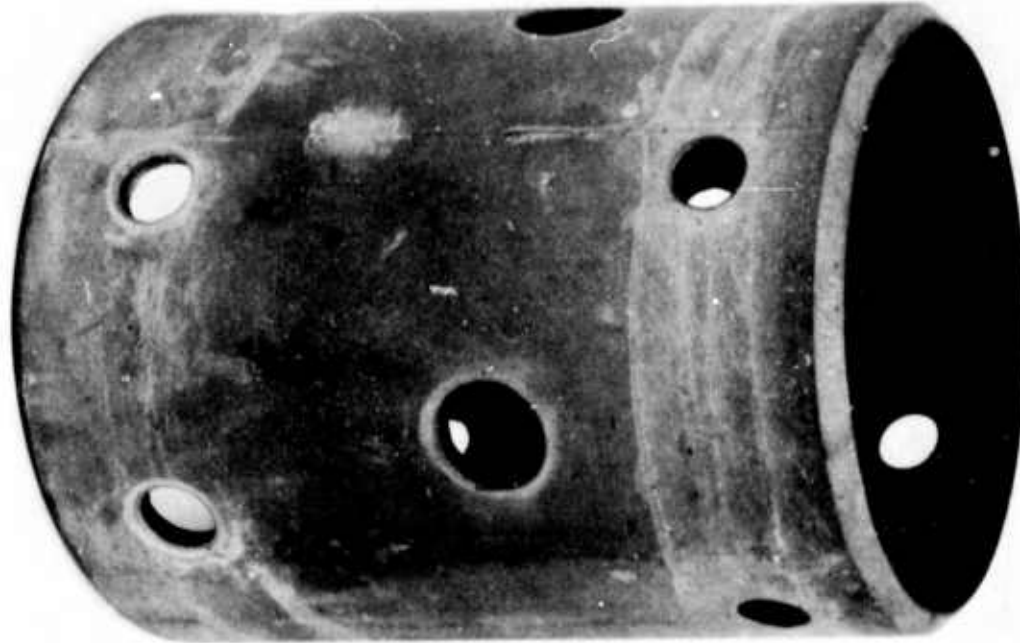


Figure 3.60 Ceramic Combustor Tube

Norton Crystar SiC of various compositions was also tested in this configuration. Several combustors were each made from three grades of Crystar, designated by Norton as CS-101, CS-201 and CS-411. Performance was erratic for all types of Crystar tested with at least one failure in each type of material.

A KT silicon carbide combustor tube supplied by the Carborundum Company was tested and did not fail. Due to limited testing hours available, it was decided that more extensive testing should be done on the KT silicon carbide tube. Norton Crystar combustors will be more fully evaluated as time permits.

#### Hot Static and Dynamic Testing of Stators, Shrouds and Nose Cones

The ceramic stators, shrouds and nose cones were qualified in an engine test rig prior to incorporation in a complete engine for continued testing and development.

Component qualification consisted of the following:

- (1) 25 static light cycles
- (2) 3 hours of static testing, and
- (3) 25 hours of dynamic testing

Testing without rotors was referred to as static testing whereas testing with rotors was referred to as dynamic testing. The various test conditions under which the ceramic stators, nose cones, and shrouds were qualified was as follows:

Static testing - 55% engine speed with turbine inlet temperature limited to 1800°F.

- . Dynamic testing - 60% speed with turbine inlet temperature limited to 2000° F.
- . Cyclic testing (static) - a sequence of (1) light-off and acceleration to 55% speed, and (2) shutdown (zero fuel) and speed reduction back to light-off condition. This condition is held until the turbine inlet temperature falls to 1000° F, whereupon the sequence is repeated for the desired number of cycles. One of these cycles is termed the one light test.

The evaluation of Design B and C nose cones, stators and shrouds was accomplished in engine test rigs, and the results are summarized in Table 3.5 which gives the total time on all components which underwent any testing during this reporting period. Most of the components listed were manufactured from reaction-sintered silicon nitride except those with the superscript 5 which were made from lithium-aluminum-silicate.

Earlier testing of first stage stators indicated that there was a severe vane cracking problem. Subsequent evaluation of several different vane configurations on the thermal shock test rig revealed that cracking was reduced when the chord of the vane was reduced by removing material from the trailing edge. Stators with this vane design were designated as Design C and seven of these have been evaluated. Failure occurred in five of these stator assemblies. One stator, serial number 260, suffered a collapsed shroud and vane cracks were encountered in the other four. Although five out of seven is a high failure rate, three of these failures were caused by errors. The collapsed shroud occurred when the stator was improperly installed in the engine, causing a very high localized stress. Two of the four stators with vane cracks were found to have no gap between the segments of the inner shroud, a condition known to cause high stresses and vane cracking. The two surviving stators exhibited improved life. One stator survived 104 hours of hot static testing and another one endured 272 light-off cycles. Both of these stators are still in good condition. The life per crack rate in these Design C stators was also significantly higher than in Design B. Table 3.6 shows that the hours per crack and lights per crack of Design C was an order of magnitude greater than for Design B components. As the quality control of these parts improves, the life should increase further.

In addition to evaluating Design C stators, three parts with a thinner but more uniform vane cross-section were tested. All three of these stators failed during light-off tests. This configuration was abandoned.

Table 3.5 shows that no second stage stators failed as a result of cracked or broken vanes. The only cause of failure of the second stage stator was axial cracking of the outer shroud. The original Design B configuration referred to as the "U" channel, shown in Figure 3.61A was very prone to cracking between the blade segments. In order to eliminate the segment joints on the outside diameter which underwent a thermal tensile stress during light-off, a new outer shroud design incorporating a solid outer ring was tried. This configuration is shown in Figure 3.61B and was referred to as the "inverted channel" design. This new design, although not failure free, did exhibit much better life than the original design. The improvement in life is presented in Table 3.7.

TABLE 3.5  
SUMMARY OF TESTING OF CERAMIC NOSE CONES, STATORS AND SHROUDS

COMPONENT	COMPONENT SERIAL NUMBER										TOTALS
First Stage Stator	260 <sup>4</sup>	322	331 <sup>4</sup>	351 <sup>2</sup>	354 <sup>2</sup>	355 <sup>2</sup>	359 <sup>4</sup>	360 <sup>4</sup>	361 <sup>4</sup>	363 <sup>4</sup>	366 <sup>4</sup>
.Hot Static Hrs.	10	2	8.5	3	0	0	0	.5	10.5	104.5	1
.Hot Dynamic Hrs.	29.5	0	26	0	0	0	0	0	18	0	8
Total Hot Hrs.	39.5	2	34.5	3	0	0	0	.5	28.5	104.5	9
Total Lights	109	3	69	54	25	25	38	169	63	272	852
Status	F,C	F,V	F,V	F,V	F,V	F,V	F,V	F,V	S,C	S,C	
Second Stage Stator	305	309	317	324	1 <sup>3</sup>	2 <sup>3</sup>	3 <sup>3</sup>	4 <sup>3</sup>	5 <sup>3</sup>	7 <sup>3</sup>	9 <sup>3</sup>
.Hot Static Hrs.	4.5	3.5	4.5	3	7.5	3.5	6	3	32	75.5	.5
.Hot Dynamic Hrs.	28.5	8	8	5	16	2.5	1.8	.5	0	5	0
Total Hot Hrs.	33	11.5	12.5	8	23.5	6	24	3.5	32	75.5	8.5
Total Lights	42	29	43	33	38	29	38	45	5	47	25
Status	F,C	F,C	F,C	F,C	F,C	F,C	F,C	F,C	S	S	573
First Stage Shroud	8B	9	10B	11	21	22	23	1 <sup>5</sup>	5	5	5
.Hot Static Hrs.	22	42.5	4.5	16	42	1	42.5	110.5	11	.5	.5
.Hot Dynamic Hrs.	6	28.5	13	42	0	0	0	18	0	5	8
Total Hot Hrs.	28	71	17.5	58	42	1	42.5	128.5	11	5.5	8.5
Total Lights	109	492	49	209	269	1	91	223	417	113	61
Status	F,K	F,K	F,C	F,K	F,K	F,C	F,K	S,C	S,C	S	S
Second Stage Shroud	10	16	17	18	20	21	22	27	2 <sup>5</sup>	5	5
.Hot Static Hrs.	16	34.5	34.5	0	46	0	8	0	3	104	.5
.Hot Dynamic Hrs.	37	4.5	1	9.5	0	11.5	0	0	18	0	.5
Total Hot Hrs.	53	48	35.5	9.5	46	11.5	8	0	21	104	8
Total Lights	759	31	47	83	146	5	31	57	111	113	30
Status	F,K	F,K	F,K	F,H	F,K	F,K	F,K	F,X	S	S	S
Nose Cone	35	36	37	38	40	42	52	54	55	58 <sup>6</sup>	59 <sup>6</sup>
.Hot Static Hrs.	113.5	31	1	23	3	7.5	.5	68	0	2.5	.5
.Hot Dynamic Hrs.	3	0	0	28	10.5	13.5	0	0	12	0	0
Total Hot Hrs.	116.5	31	1	51	13.5	21	.5	68	12	2.5	8.5
Total Lights	252	122	220	80	34	91	38	130	6	2	89
Status	S,C	F,C	S,C	S,C	F,C	F,C	F,C	S,C	S,C	S,C	F,C

<sup>1</sup>Status Legend

C - Cracked Shroud

F - Failed

H - Broken during handling

K - Part failed due to creep

S - Serviceable; at present nose cones are considered serviceable if outer shroud has only axial cracks. First stage stators are considered serviceable if outer shroud is cracked.

V - Cracked or broken vane(s)

X - Result of other component failure

2 Experimental Thin Blade Design

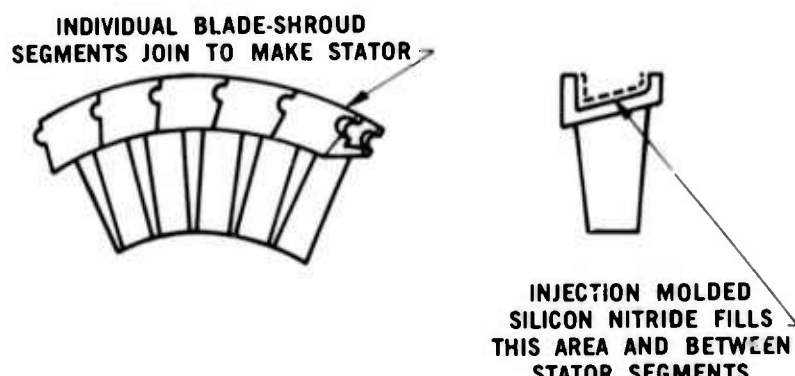
3 Inverted Channel Design

4 Design "C"

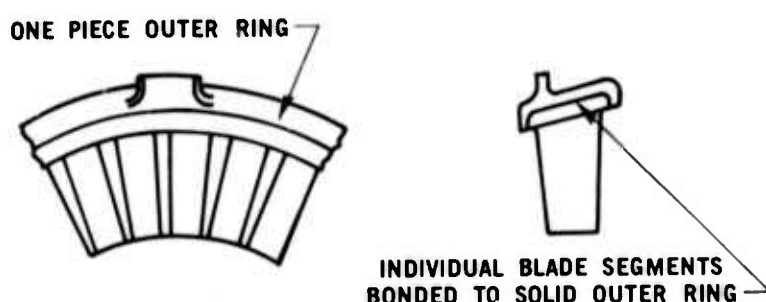
5 Lithium-Aluminum-Silicate Material  
6 "Scalloped" Nose Cone Design

Table 3.6 LIFE DATA FOR DESIGN B AND C FIRST STAGE STATORS

Design	Number of Stators Tested	Total Hours	Total Lights	Total Number of Broken or Cracked Blades	Average Hrs. Per Failure	Average Lights Per Failure
B	9	151	356	60	2.5	5.9
C	7	212	611	7	30.3	87.3



(A) U-Channel Design,



(B) Inverted Channel Design  
Figure 3.61 Second Stage Design B Stator Designs

Table 3.7 LIFE DATA FOR SECOND STAGE DESIGN B STATORS

Design	Number of Stators Tested	Total Hours	Total Lights	Total Number of Shroud Failures	Average Hrs. Per Failure	Average Lights Per Failure
"U" Channel	9	29	204	27	1.1	7.5
Inverted	9	179	425	6	29.8	71

Extensive testing of silicon nitride first and second stage shrouds indicated that these shrouds were deforming plastically after a few hours of hot running. This phenomenon was verified in other tests, and the problem is presently being studied (see Section 3.3.1). Due to the reduction in rotor tip clearance caused by the deformation of the shrouds, it was not possible to run these shrouds in an engine with rotors. Therefore, in order to continue engine testing, an interim shroud design was incorporated. This shroud was a solid ring made from lithium-aluminum-silicate. These shrouds survived over 150 hours of testing and are still performing satisfactorily. This material is only acceptable for engines with a turbine inlet temperature limited to 2000°F, due to its low melting temperature.

The evaluation of nose cones showed that these parts consistently developed an axial crack in the outer shroud that often went completely across this section. These cracks usually passed through the rear flange midway between the struts and through the thermocouple holes near the front flange. Usually there would not be more than one of these axial cracks between any two struts and thus they did not endanger the integrity of the part. However, occasionally an axial crack would not go completely across the part, but would turn in a circumferential direction. This type of crack would jeopardize the part and was thus considered a critical failure. An early attempt to cure the problem was to groove the nose cone along the outer shroud and thus encourage the crack to propagate completely across the shroud along this low resistance path. It was believed that once the part was thus stress relieved, it would be stable. However, testing of these parts revealed that after cracking along the groove the component would occasionally develop an additional crack, branching from the first one. This indicated that there were still high thermal stresses being developed in the part.

Modifications to the nose cone were then incorporated to reduce these stresses. These modifications were basically two-fold. First, the rear flange was scalloped to reduce the high tensile stresses which design analysis showed existed during transient conditions. Second, the thermocouple holes were eliminated from the front flange, and the cross-sectional area was made more uniform. These modifications are shown in figure 3.62. Three nose cones of this "scalloped" configuration received limited testing and two have developed an axial crack completely across the shroud. The location of these failures was beside a strut, however, instead of midway between two struts as had been observed on the previous configuration. Since the location of the maximum stress of a hoop loaded radially at three points is at the load, the failure seemed likely to have been caused by loading through the strut resulting from differential expansion rates of the shroud and struts during transient heating. In order to alleviate this stress, the nose cone will be pre-cut through the outer shroud midway between the struts. Two nose cones of this configuration have been constructed and will shortly be evaluated.

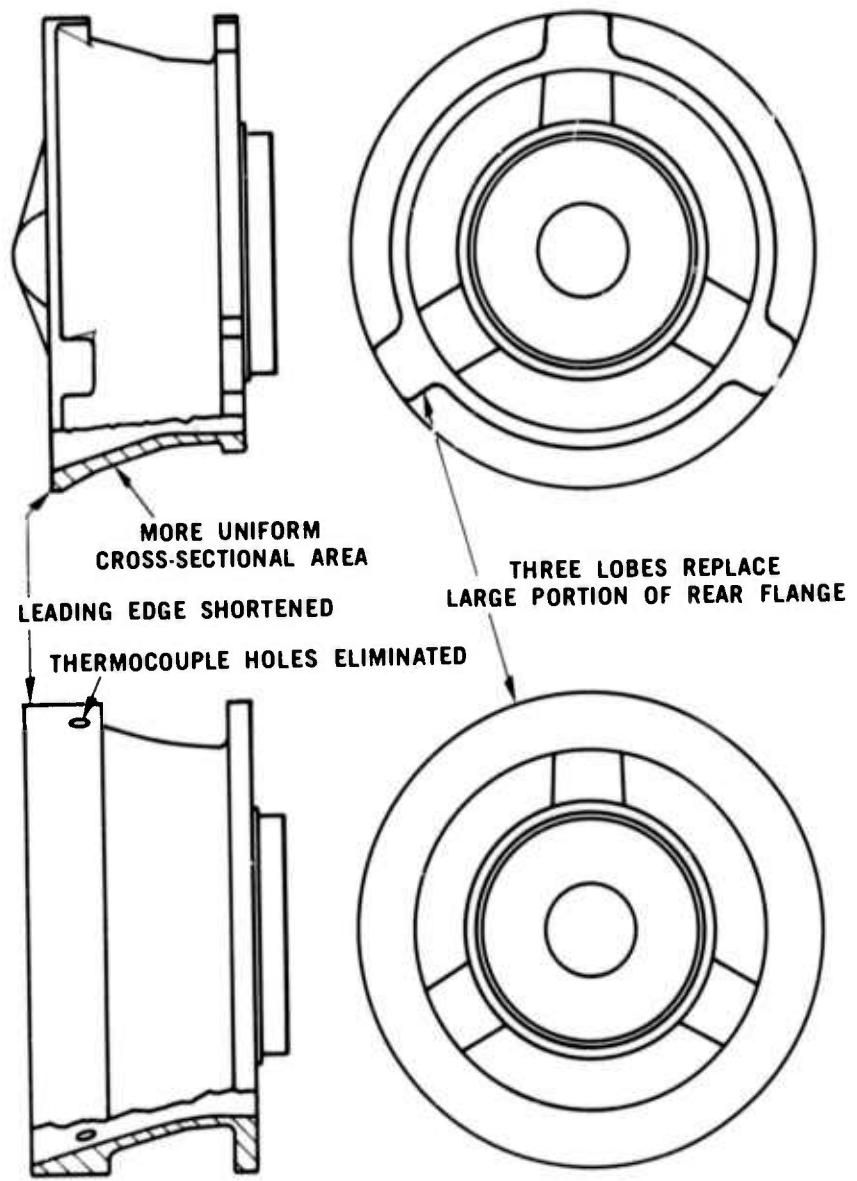


Figure 3.62 Comparison of Modified and Design B Nose Cones

## 4.0 PROGRESS ON THE STATIONARY TURBINE PROJECT

### 4.1 STATOR VANE DEVELOPMENT

#### Summary

The three piece design, for the use of ceramic materials in stationary gas turbines as stator vanes, is discussed with respect to the first static rig test. Eight of twenty silicon nitride stator vane assemblies were selected for inclusion in the initial test configuration which represents a one-eighth segment of the full turbine stator row. A static rig test at 2200°F has been planned to evaluate total system performance at one third to seventy-five percent simulation, depending upon the compressor ratio employed. Testing is scheduled for July, 1973, in a new test facility which is described.

Contact stress analyses at the airfoil-end cap, the major end cap-insulator and the interlocking minor end cap-insulator interfaces were completed. A maximum tensile stress of 5180 psi is expected at the airfoil end cap interface during shutdown from 2500°F. Stress at the major end cap insulator interface should not exceed 500 psi. Edge loading at the end cap-insulator interlocks could cause a stress maximum of 10,000 psi. The worst conditions are not expected to damage silicon nitride vane assembly components.

A 2 dimensional heat transfer analysis of the first generation silicon nitride end cap indicates that steady state thermal stresses may reach 13,400 psi in the vicinity of the groove. This will be reduced in the second generation stator vane design which is also discussed.

Norton delivered 20 - three piece silicon nitride vane assemblies. The results of inspection which included Xyglo, x-ray radiography, and ultrasonic scanning in addition to dimensional checks is reported. Billets were prepared for the fabrication of silicon carbide vane assemblies.

PRECEDING PAGE BLANK-NOT FILMED

## Introduction

A three piece ceramic stator vane assembly has been proposed for test and demonstration in an advanced stationary gas turbine illustrated schematically in Fig. 4.1. Silicon nitride or silicon carbide stator guide vanes are intended to increase the service temperature from 1955 to 2500° F without cooling the first stage stator row.

The large size of the Westinghouse turbine permits the use of the three piece vane design which is better suited to brittle materials than conventional geometry where the airfoil is integral with the shrouds. This design innovation reduces thermal stress to a minimum by elimination of the transition zone. Each segment presents a relatively uniform cross section and mass to a specific temperature regime. The temperature extremes experienced by either the individual end caps or the airfoils are much smaller than those encountered in an integral vane design. The airfoil segment, for example, will operate at a somewhat higher but more uniform temperature because heat losses are minimized at the interface with the end caps. Radial and longitudinal thermal gradients in the end caps are influenced by gas temperatures at the wall rather than by peak temperatures in mid-stream, except for minimum heat transfer from the airfoil across the contact interface.

The design itself is discussed with respect to the 2200° F static rig test scheduled to begin in July. A second generation stator vane assembly has been proposed with improved aerodynamic characteristics.

Contact stress and heat transfer analyses indicate that silicon nitride and silicon carbide stator vanes should survive in a high temperature turbine environment. Delivery of 20 silicon nitride vane assemblies from Norton and the completion of the static rig test facility make it possible to verify the stress calculations by performance under test conditions.

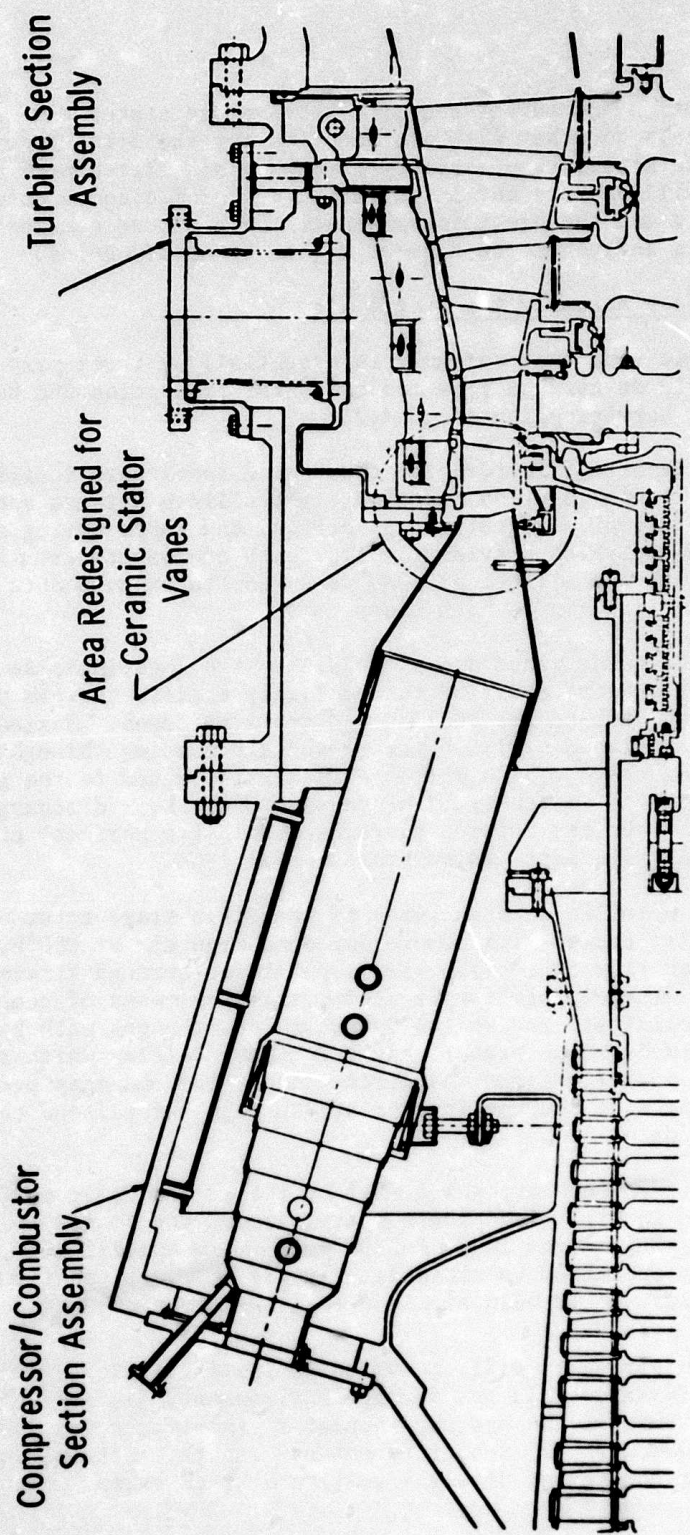


Figure 4.1 – Schematic of 30 Mw Test Turbine Flow Path

#### 4.1.1 DESIGN

##### Introduction

The evolution and advantages of a three piece stator vane design for brittle materials together with its adoption for the first generation silicon nitride stator vane assembly have been considered previously. (1,2,3) This section will discuss the installation of ceramic components in the static test rig and the preliminary aspects of a second generation design which is influenced to a great degree by aerodynamics.

##### Ceramic Vane Test Assembly for Static Rig

The ceramic vane test assembly is essentially a three part structure located directly downstream from the combustor transition and bolted to the static rig barrier plate (Fig. 4.2).

The most important features of the test assembly are identified in Fig. 4.3. The center section contains eight silicon nitride vanes, plus insulators, shoes, pivots, retaining springs, and support ring segments. Metal guide vanes, which provide for flow path continuity from the combustor through the silicon nitride vanes to the exhaust duct, flank the center section on both sides.

These metal guide vanes are of W 251B design (Westinghouse 30 Mw Stationary Gas Turbine) modified to completely enclose the gas path by welding filler plates to the leading and trailing edges. Maximum vane cooling is accomplished by 150°F compressed air passing through cooling holes located on the hot side only. This air is vented to the gas stream through slots in the trailing edges. Compressor discharge air at 650°F washes over the outside surfaces (cool side surface) of the side vane to maintain metal temperatures below 1700°F.

All other metallic substructures of the first stage rotor vane assembly are also cooled with compressor discharge air at 650°F. While restricted flow of cooling air is permitted through strategically located seals, free circulation is accomplished by means of cooling holes. The cooling air is eventually drawn into the gas path by the pressure drop through the stator vane end caps. Baffles which serve to minimize the length (longitudinal direction) of the end caps prevent the direct impingement of the cooling air at the edges of all end caps as it enters the gas path.

The ceramic components, which will be tested initially at 2200°F, are illustrated in Fig. 4.4. These pieces are spring loaded in compression to resist an impinging gas load of 3300 psi. More specifically, this vane design was optimized to minimize critical stresses, particularly at the interfaces, while maintaining a positive position.

Two design variables will be evaluated initially along with the material's performance in a gas turbine environment; (1) the longitudinal radius of curvature at the end cap-insulator interfaces was reduced on one pair of vanes, and (2) two different end cap thicknesses are used within the test compliment of eight silicon nitride vanes.

### Second Generation Ceramic Stator Vane

A second generation design of ceramic stator vane assemblies was developed primarily to correct the aerodynamic inadequacies inherent in the first generation design. The new design (Fig. 4.5) specifies the tapered and twisted airfoil required to create uniform gas flow in a full scale rotating turbine. The airfoil tenon geometry has also been altered to eliminate the trailing edge slot and the unfilled portions of the end cap groove.

In effect, the major airfoil tenon radius has been increased to one-half the appropriate chord width at both ends to provide for the uniform blending of the tenon into the trailing edge. The minor tenon radius is extended beyond the airfoil surface boundary to fit and fill the entire end cap groove. These changes in the airfoil tenon geometry account for a subtle but significant difference in the position of the airfoil loading axis.

Certain mechanical improvements were also instituted as a result of stress analysis and friction measurements. The depth of the groove in the end cap was reduced approximately 12% to decrease the maximum principal stress at the bottom of the groove from 11,700 to 8700 psi. The major radius of curvature at the end cap-insulator interface was reduced by 62.5% to insure positive location at this interface, irrespective of the friction coefficient between silicon nitride or silicon carbide and the insulator material. Both axial and torsional components of the gas load act upon this interface.

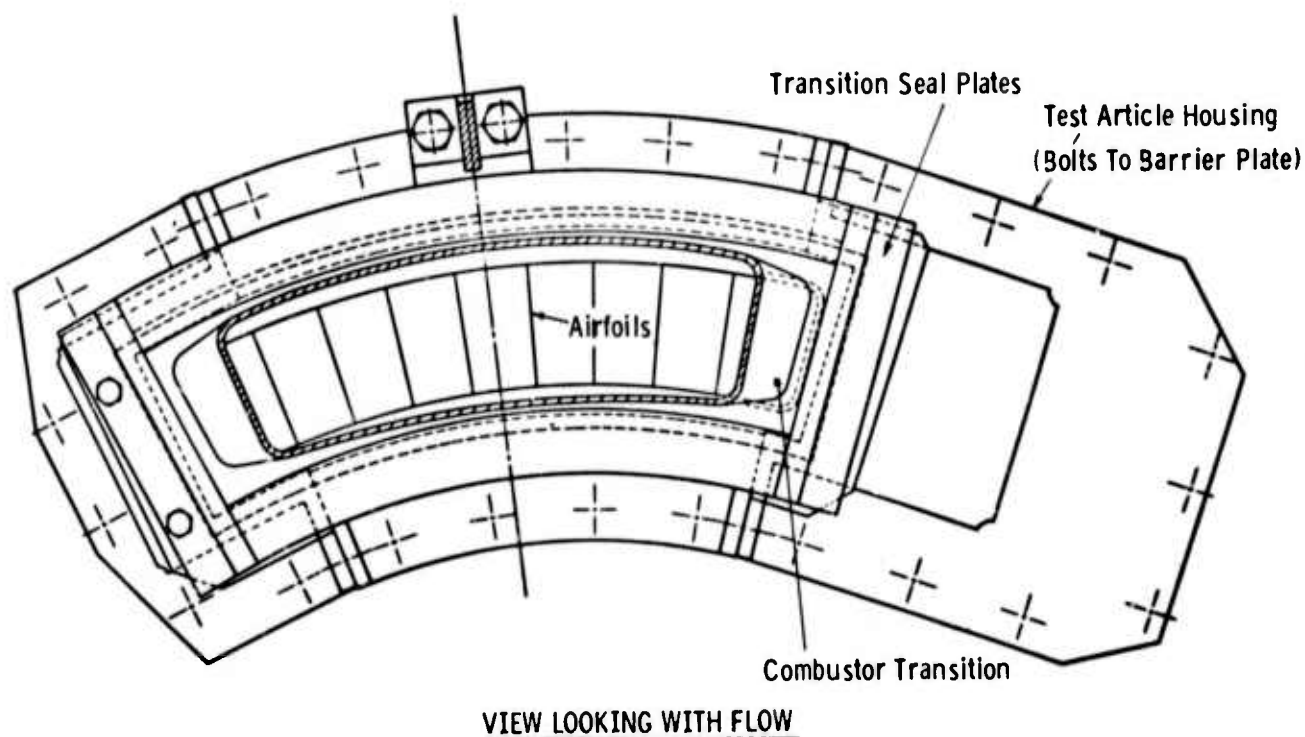


Figure 4.2 -- Static Rig Test Assembly Mounting Arrangement (Circumferential View from Combustor Transition)

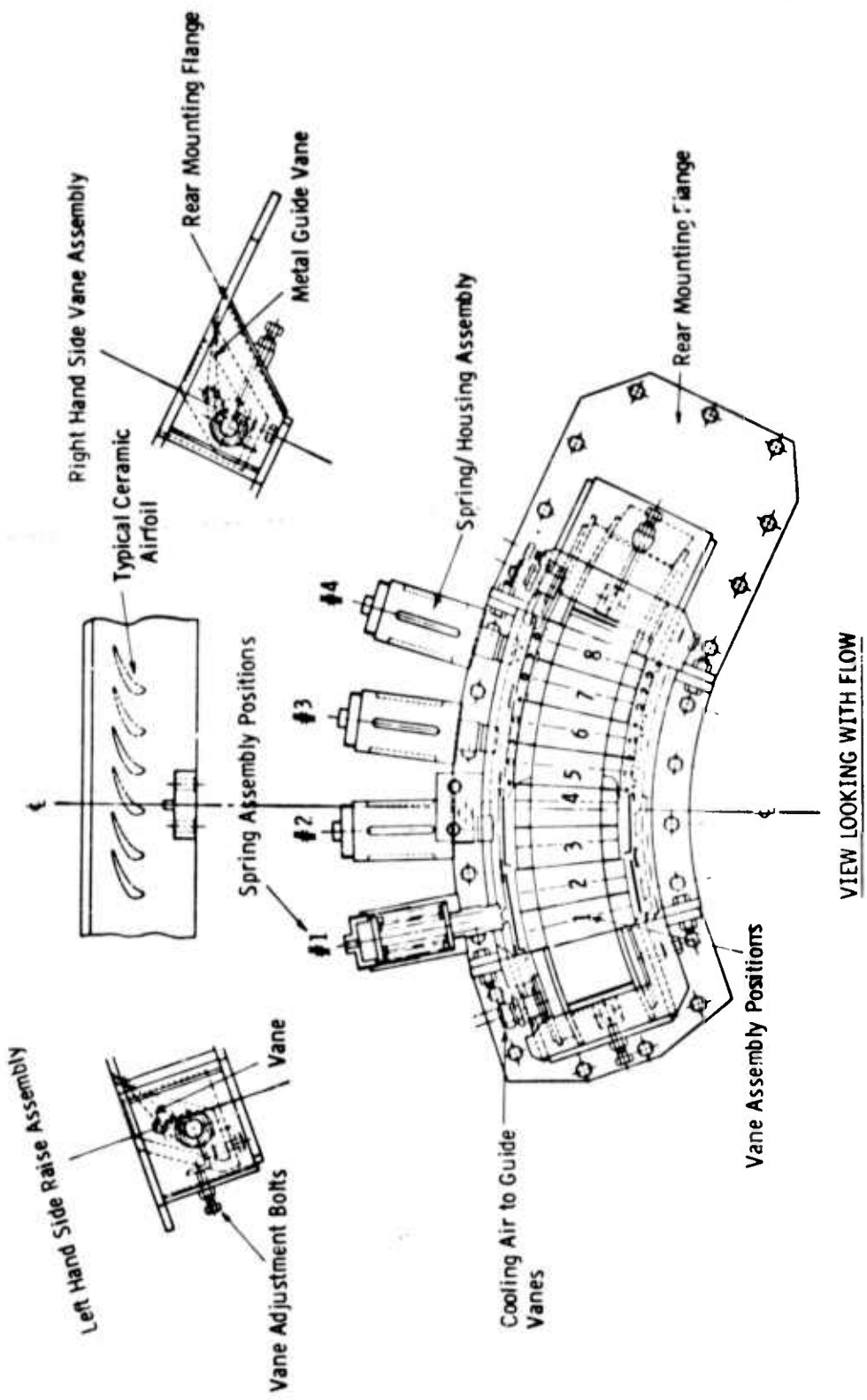


Figure 4.3 -- Circumferential View of Ceramic Vane Static Rig Test Assembly

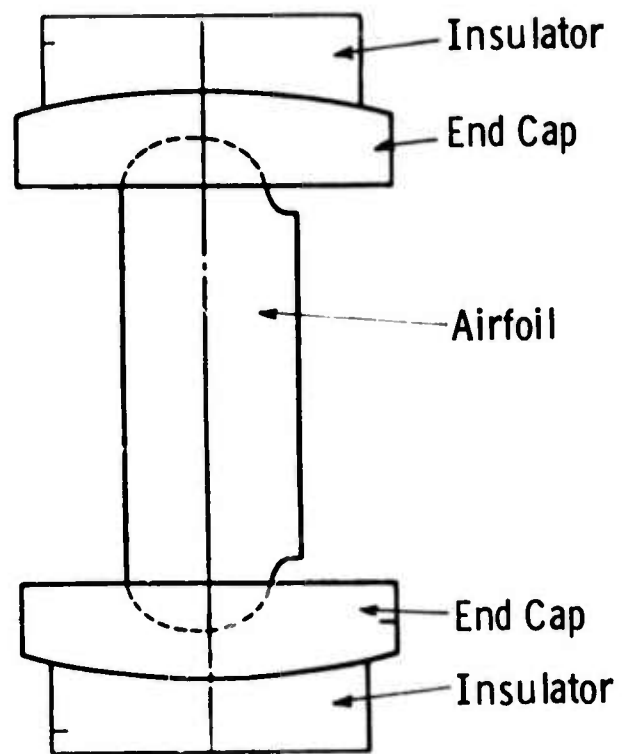


Figure 4.4 -- Ceramic Components of the First Stage Stator Vane Assembly



Figure 4.5 -- Second Generation Vane Assembly

#### 4.1.2 STRESS ANALYSIS

##### Introduction

The influence of boundary conditions on contact stress has been defined for the airfoil-end cap interface, the major end cap-insulator interface, and the minor end cap-insulator interface. A 2-dimensional transient and steady state heat transfer analysis was performed to make an initial determination of the steady state thermal stress distribution within ceramic end caps.

##### Contact Stresses

Considerable effort has been expended in analyzing the stresses at critical interfaces which are inherent in the first generation stator vane assembly design. As reported previously, the vane assembly and support structure (partially illustrated in Fig. 4.4) are subjected to two principal loads acting against each other. The compressive spring load must be great enough to neutralize the three components of the gas load if the airfoils are to remain stable in a high velocity gas stream. Since the stator vane function is to turn the gas stream and since the individual elements of the vane assembly are joined at curved interfaces, the three components of the gas load are defined as:

- (1) The pressure force against the vane acting  $28^{\circ}$  from axial direction.
- (2) The radial compressive force directed ultimately against the spring loaded shoe.
- (3) The twisting moment about the radial axis of the vane.

The stress analysis was performed using 2-dimensional finite element and finite difference computer codes which were expanded to handle specific geometries and conditions.

A sub-routine was developed to describe the interactions at the airfoil tenon-end cap groove interface under conditions of turbine start-up and shutdown. Curved surfaces were employed to reduce the ratio of traction ( $R_T$ ) to normal load ( $R_N$ ) at both the airfoil-end cap and end cap-insulator interfaces. The kinematic nature of the airfoil-end cap interface is restated in Fig. 4.6. Force equilibrium requires that at turbine start-up the contact center of the airfoil and its associated contact surface shift slightly as a function of gas load, geometry and friction. Since friction increases with time at temperature, the shift in airfoil position may not be completely reversible during shutdown when gas loads diminish. Therefore, the radial spring load, thus imposed, is proportional to the retained contact rotation. This spring-derived shutdown traction will increase for lower values of start up coefficient of friction because larger shifts will result. The airfoil will return to its original position if the coefficient of friction returns to its original value.

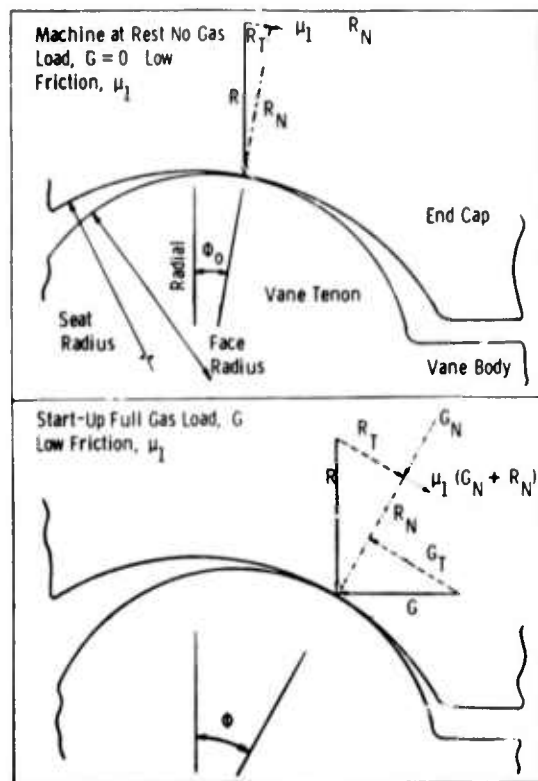


Figure 4.6 -- One-Dimensional Force Equilibrium Diagram for Airfoil End Cap Interface

Another sub-routine was generated to define the elastic contact surface at the end cap groove-airfoil tenon interface. Sufficient radial spring force must be applied to prevent the tenon from moving out of the end cap groove. In fact, any displacement of the contact center that is large enough to reduce the actual contact area, i.e., where the nominal contact surface is moved to extend beyond the pieces in contact or any drastic rearrangement of the pressure surface to compensate for such movement, will result in a much higher stress field or region of contact singularity.<sup>(4)</sup>

#### Stress at Airfoil-End Cap Interfaces

The results of the stress analysis at the airfoil-end cap interface appear in Figs. 4.7-4.9 where the position of the contact area with respect to the airfoil perimeter, and the maximum tensile stresses during start-up and shutdown are discussed. Figure 4.7 indicates that even at very low coefficients of friction, the worst possible shift or rearrangement at the interface will not bring the actual load bearing contact area dangerously close to the edge of the airfoil section for any of the four conditions cited.  $\Delta R$  represents the difference in radii between the airfoil tenon and the end cap groove or the relative fit of the airfoil with respect to the end cap. As seen in Fig. 4.7 the region of safety extends from 0.035 in. If the contact area moves within 0.035 in. of the airfoil edge, edge loading will persist in a so-called region of contact singularity.

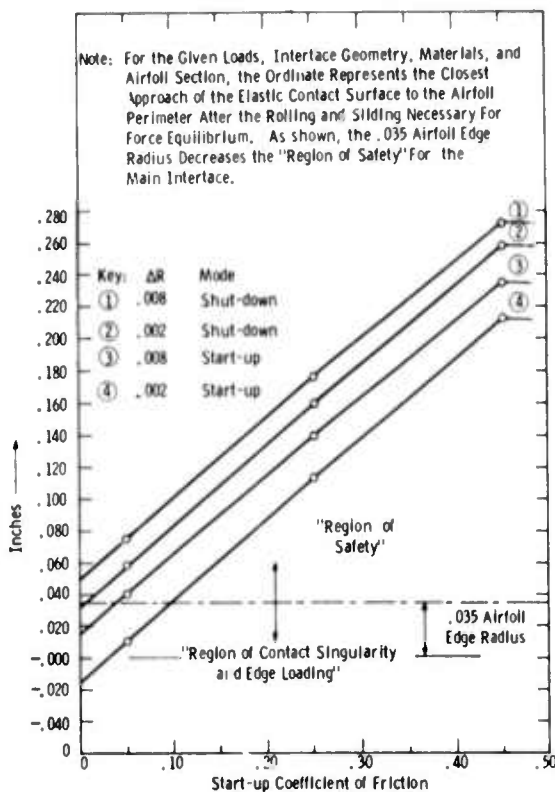


Figure 4.7 -- Vane-End Cap Interface Edge Loading Analysis

Figures 4.8 and 4.9 show the effects of radial difference ( $\Delta R$ ) and the coefficient of friction, independently, on the maximum contact tensile stress developed at the interface for the start-up and shutdown condition, respectively. The stress increases directly with radial difference because the load remains constant while the contact area decreases. For the actual case, where part tolerances establish  $\Delta R = 0.004$  inches and the measured value of friction is  $\mu = 0.25$ , the maximum tensile stresses are 8240 psi for start up and 5180 psi for shut-down.

#### The Major End Cap-Insulator Interface

A combined kinematic and contact stress analyses at the interacting interfaces of four end caps with two insulators has been completed. The major interface in this system (in Fig. 4.4 the contact between the top surface of an outer end cap with the bottom surface of an outer insulator for example) is considered first. The design depends upon friction along a curved surface for positional stability. Since simple contact must be preserved, it is essential to select the minor radius of curvature within the constraints of friction coefficient as related in Fig. 4.10. It is clear that the selection of a 3.0 in. radius makes the design practically independent of frictional effects while the selection of a 10 in. radius requires a coefficient of friction  $> 0.35$  to avoid contact singularity and edge loading. Furthermore, the combined effect of curvature and friction may not be great enough in the case of a large minor radii to prevent movement of the stator vane assembly downstream toward the first stage rotor.

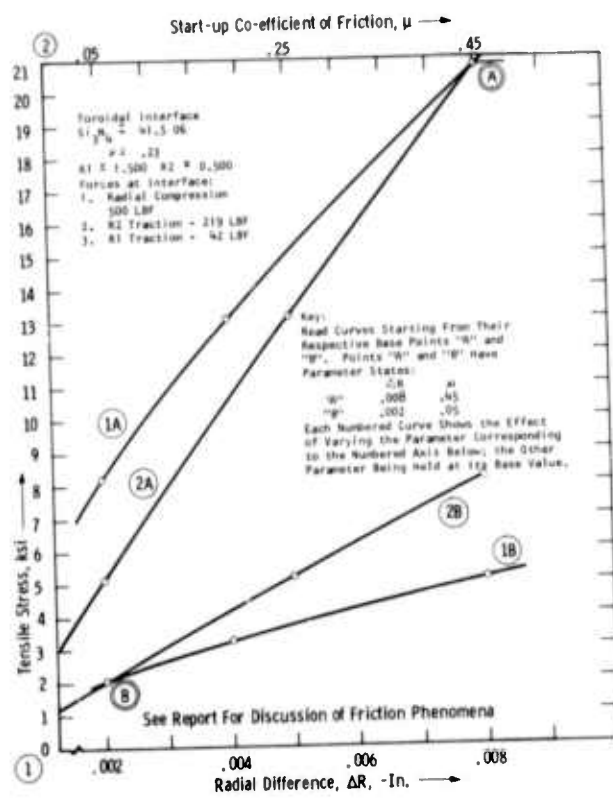


Figure 4.8 -- Start-Up Tensile Contact Stress at Vane-End Cap Interface  
Showing Effects of Parameter Variation

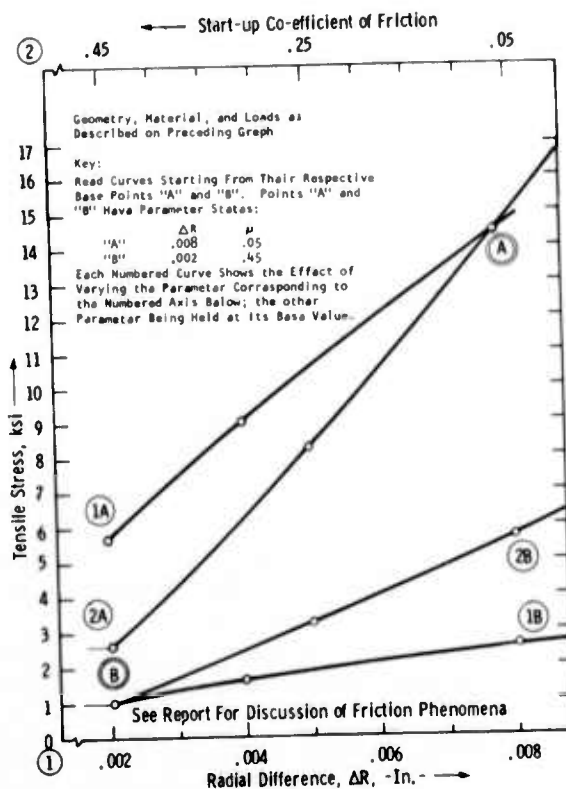


Figure 4.9 -- Shut-Down Tensile Contact Stress at Vane-End Cap Interface  
Showing Effects of Parameter Variation

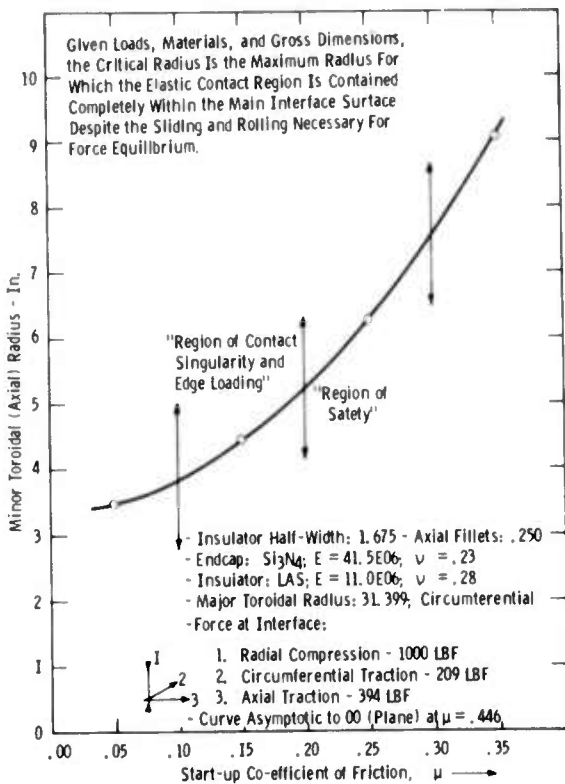


Figure 4.10 -- Critical Axial Radius vs Start-Up Coefficient of Friction at End Cap Insulator Interface

The state of stress at the interface is determined by the minor axial radius ( $R_2$ ), the end cap-insulator radial difference ( $\Delta R$ ), and the coefficients of friction ( $\mu$ ) between the end cap and insulator materials. The effects of these parameters on the maximum contact tensile stress are plotted independently in Figs. 4.11 and 4.12 for turbine start-up and shutdown respectively. Even though the stress varies inversely with the minor axial radius of curvature, stress maxima will only approach 500 psi in the insulator under the least favorable conditions of friction and radial difference ( $\mu = 0.15$  and  $\Delta R = 0.008$  in.). Contact stresses in the end cap are lower still.

The first generation stator vane assembly was initially designed with a large minor radius of curvature at the end cap-insulator interface. When the coefficient of friction between silicon nitride and the insulator material was found to be  $\sim 0.10$  rather than  $> 0.35$ , the radius of curvature was reduced on some pieces of test hardware. Several other modifications have been made on the large radius of curvature end cap-insulator assemblies to be tested.

Analogous to the practice of crowning steel rollers<sup>(4)</sup> (blending large radii to taper the ends), 0.250 in. edge radii have been introduced to alleviate the contact singularities already discussed.

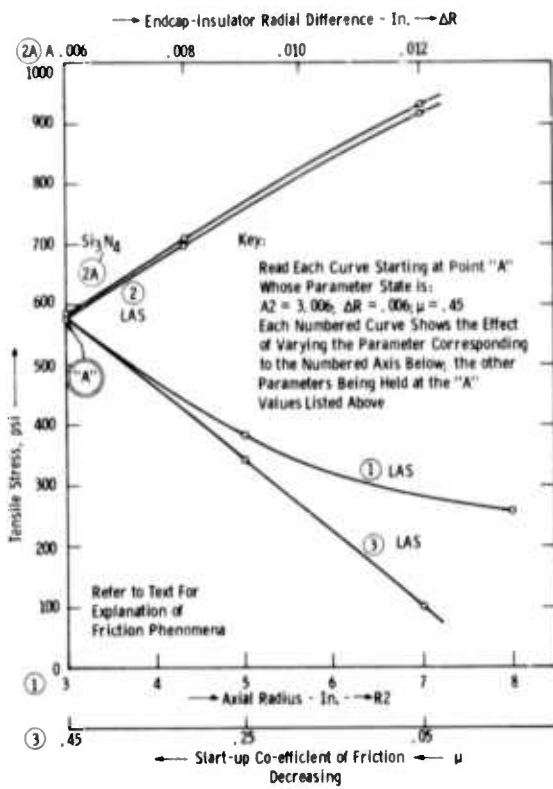


Figure 4.11 -- Start-Up Tensile Contact Stress at End Cap-Insulator Interface Showing Effects of Parameter Variation

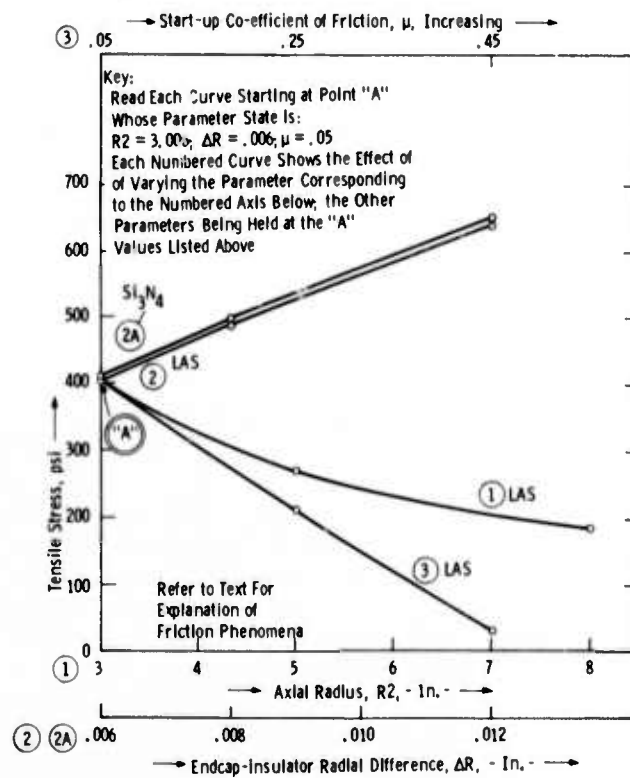


Figure 4.12 -- Shut-Down Tensile Contact Stress at End Cap-Insulator Interface Showing Effects of Parameter Variation

The reduction in the minor axial radius ( $R_2$ ) eliminates the need for an exact analysis of the contact stress field in the vicinity of a second order discontinuity (as at the boundary between the end cap and the insulator edge radius). Several qualitative comments may be made, however. Since the Hertzian pressure on the fillet side (insulator) must be greater than the main radius side (end cap), the stress field from the friction-reacted tractive loads are expected to be skewed considerably.

For the case of simple rolling cylinders, the in-plane normal stress field at the surface due only to traction is symmetric about the line of contact in which a tensile stress exists to the rear and a compressive stress to the front. However, when the pressure field is asymmetric and the traction is applied toward the high pressure side, it is expected that, although the tensile component would rise somewhat, the compressive portion would rise dramatically. The compressive stress at the downstream edge of the 0.250 in. fillets may approximate 30 ksi, in the event of partial edge loading.

The third design change motivated by this analysis is the inclusion of two inch spherical radius ceramic buttons within the downstream lip seals to act as final stops in the event that sliding does occur.

#### Circumferential Edge Loading

This part of the stress analysis deals with the contact stresses generated as the thick end caps slide circumferentially to interlock with the thick insulators. The edge locking interference in this case is 0.200 in. with the circumferential component of the gas load being transmitted across the flat edge. However, an edge radius must be defined in the event of skewed loading.

The load at these interlocks is inversely proportional to the amount of circumferential traction reacted by friction at the major end cap-insulator interface. For the lowest coefficient of friction at this interface,  $\mu = 0.10$ , the normal load at the interlocking interface reaches a maximum. Figure 4.13 illustrates the effect of edge radius on the development of contact tensile stresses under these least favorable conditions where the interlock is so skewed as to cause full edge loading.

#### The Second Generation Interface System

Very little can be said concerning the stress analysis of the second generation stator vane assembly design at this time. The design has been optimized to reflect the results of the first generation vane assembly stress analysis presented above. Preliminary results indicate that contact and thermal stresses may be reduced as much as 50% by reducing the groove depth, filling the groove completely with the airfoil tenon, and reducing the minor radius of curvature at the end cap-insulator interface to 3.0 inches. Edge radii of 0.060 in. have been specified overall to reflect the results appearing in Fig. 4.13. The airfoil tenon geometry may be altered such that the elastic contact surface will remain within the end cap groove even when friction approaches zero.

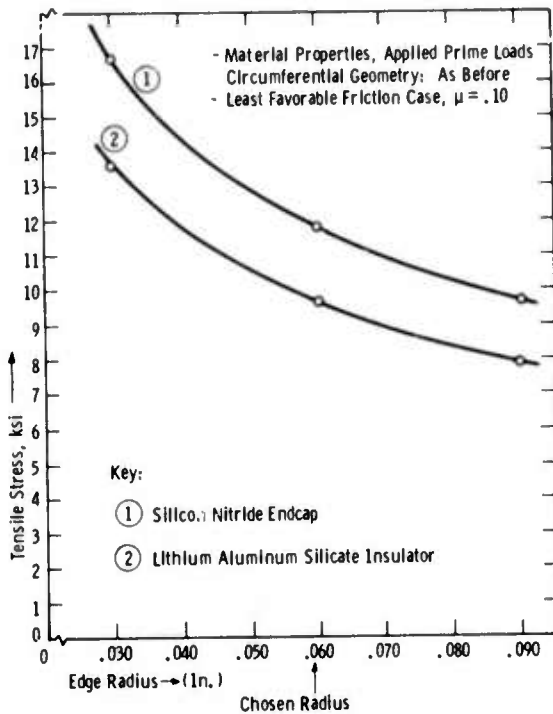


Figure 4.13 -- Circumferential Edge Loading Analysis Hertzian Contact Stresses (Tensile) at Thick-Thin-End Cap-Insulator Interlocks

#### Thermal Stress Calculations

An accurate analysis of heat transfer and the associated stress field within the layered ceramic shroud (end cap, insulator, metal shoe) for both steady state and shutdown transient mode has been completed for the turbine operating at a gas temperature of 2500°F. The shutdown cycle analyzed was much more severe than the one proposed in actual test. Gas temperatures were dropped to compressor discharge levels (650°F) in 2.5 seconds followed by an exponential decay of ambient temperature. The heat transfer coefficients were ramped and decayed similarly. External body temperatures were adjusted for heat capacity and allowed to decay.

For the purposes of the 2-dimensional finite element technique employed, temperature gradients across the interfaces are assumed to be negligible. Convection, conduction, and radiation boundary conditions were applied as required.

Thermal loading for the calculation of steady state and transient thermal stress was obtained from a three-dimensional map of temperature vs time. The map itself was constructed from 2-dimensional thermal contour sections, representing 5 radial slices through the shroud stack from leading to trailing edge. The R-Z plane sections; AA, BB, CC, DD

and EE, shown in Fig. 4.14, model the end cap with a representative groove, the insulator, and the metal shoe. Seventeen heat transfer coefficients, seven gas temperatures, and six external body temperature versus time functions were specified. These functions were derived from theoretical considerations or from appropriately scaled experimental results. The thermal property data, i.e., emissivity, specific heat, and conductivity, were used as functions of temperature for greater accuracy.

Thermal contour maps for a typical end cap under steady state, 5 seconds after shutdown, and 60 seconds after shutdown are shown in Figs. 4.15-4.20. Sections AA and CC are used to illustrate the influence of the groove on the temperature gradient with respect to time. For the steady state condition (Figs. 4.15 and 4.16), the most severe gradients occur downstream of the groove. This is due, in part, to the turbulent decay of film cooling as it flows over the leading edge to wash across the hot face of the end cap. The cooling air flow on the cool surface is also greater at the trailing edge because a significant pressure drop occurs across the stage. The relatively small thermal gradient appearing between the groove and the insulator results from the boundary condition assumption that the rate of heat flow through the shroud is dominated by convection through the end cap rather than conduction across the interface.

Figures 4.17 and 4.18 describe the stack five seconds after quench. Tensile stresses have developed in the lower surfaces as a hot spot emerges in a central location. Thermal relaxation has occurred after 60 seconds (Figs 4.19 and 4.20) as shown by the general cooling and the slow rise of the hot spot to the end cap-insulator interface.

Because the heat transfer program utilized is really two-dimensional axisymmetric operating in the R-Z plane, the five sections yield a five row grid of temperature vs time in the θ-Z plane (normal to the radial axis) at any of the element layers of Fig. 4.14. Unfortunately, this five row grid does not correspond geometrically to the end cap element mesh, (Fig. 4.21), which was chosen to model the groove. Clearly, some rearrangement of temperature values was necessary to make the two finite element programs compatible. To accomplish this task, a two dimensional Lagrangian interpolating routine was required to find the exact value of a function of two variables continuously within the region of interest when the function surface was specified by a rectangular grid and was of an order less than or equal to five. This capability was particularly useful for the establishment of temperature at points on the hot surface of the end cap in the vicinity of the airfoil and groove where a rather abrupt change occurs from the pressure to suction sides.

Final stress calculations have been made from the complete compliment of thermal maps. The results of thermal loading in steady state are plotted as principal isostress lines in the θ-Z plane at the midpoint of the end cap in Fig. 4.22. Since the groove region is predominantly in compression, the superposition of the contact stress field is not expected to present a severe problem. Significant tensile stresses occur in the downstream half of the end cap and in the regions between the edge and the major groove diameter. Fortunately, the overall stress levels due to contact and thermal loads, for steady state, are well below the reported strength of silicon nitride at the operating temperature.

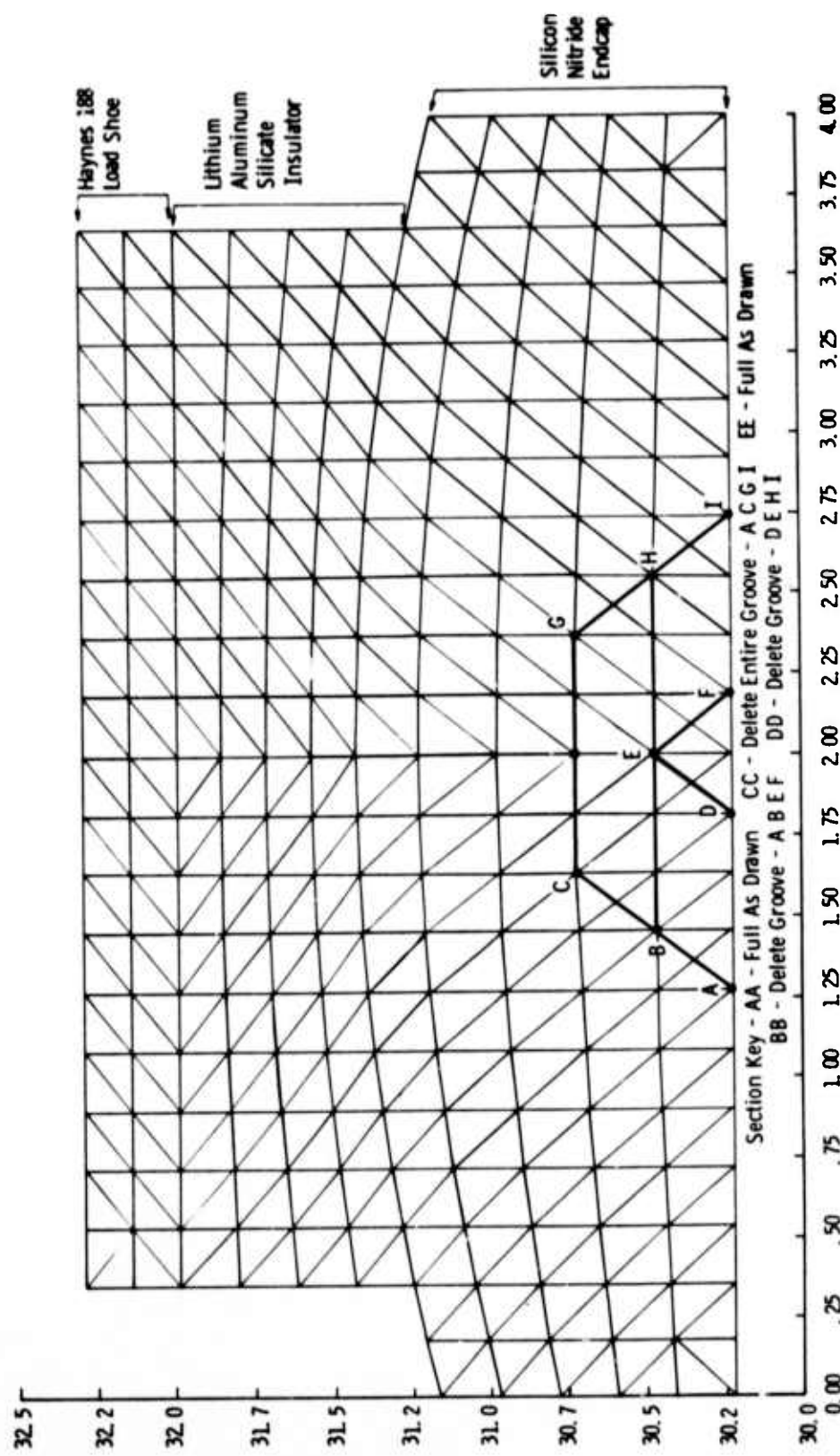
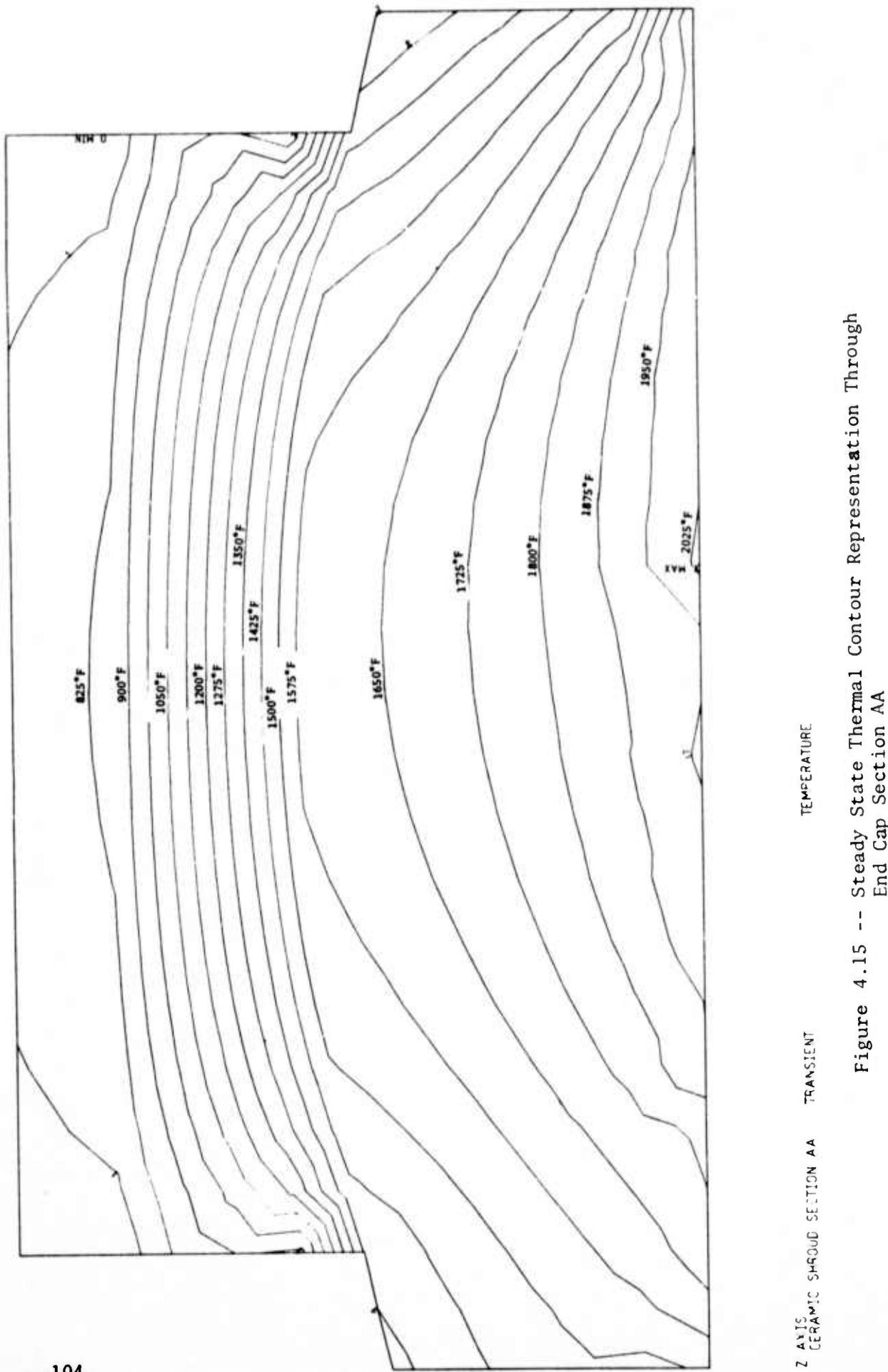


Figure 4.14 -- Two-Dimensional Finite Element Mesh for Heat Transfer in the End Cap Sections AA, BB-CC-DD and EE.



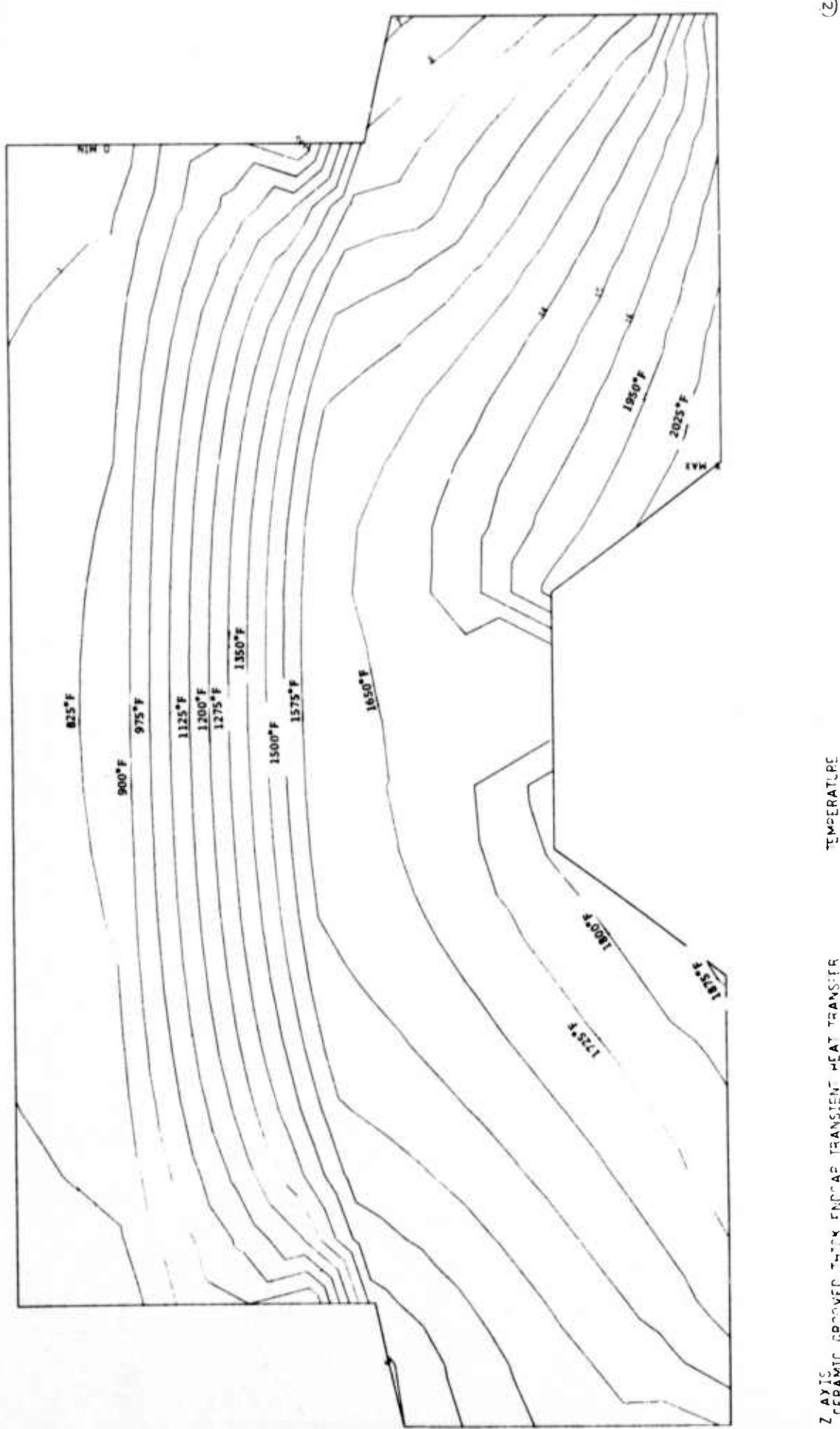


Figure 4.16 -- Steady State Thermal Contour Representation Through  
End Cap Section CC



Figure 4.17 -- Thermal Contour Representation Through End Cap Section AA  
 5 Seconds after Shut-Down

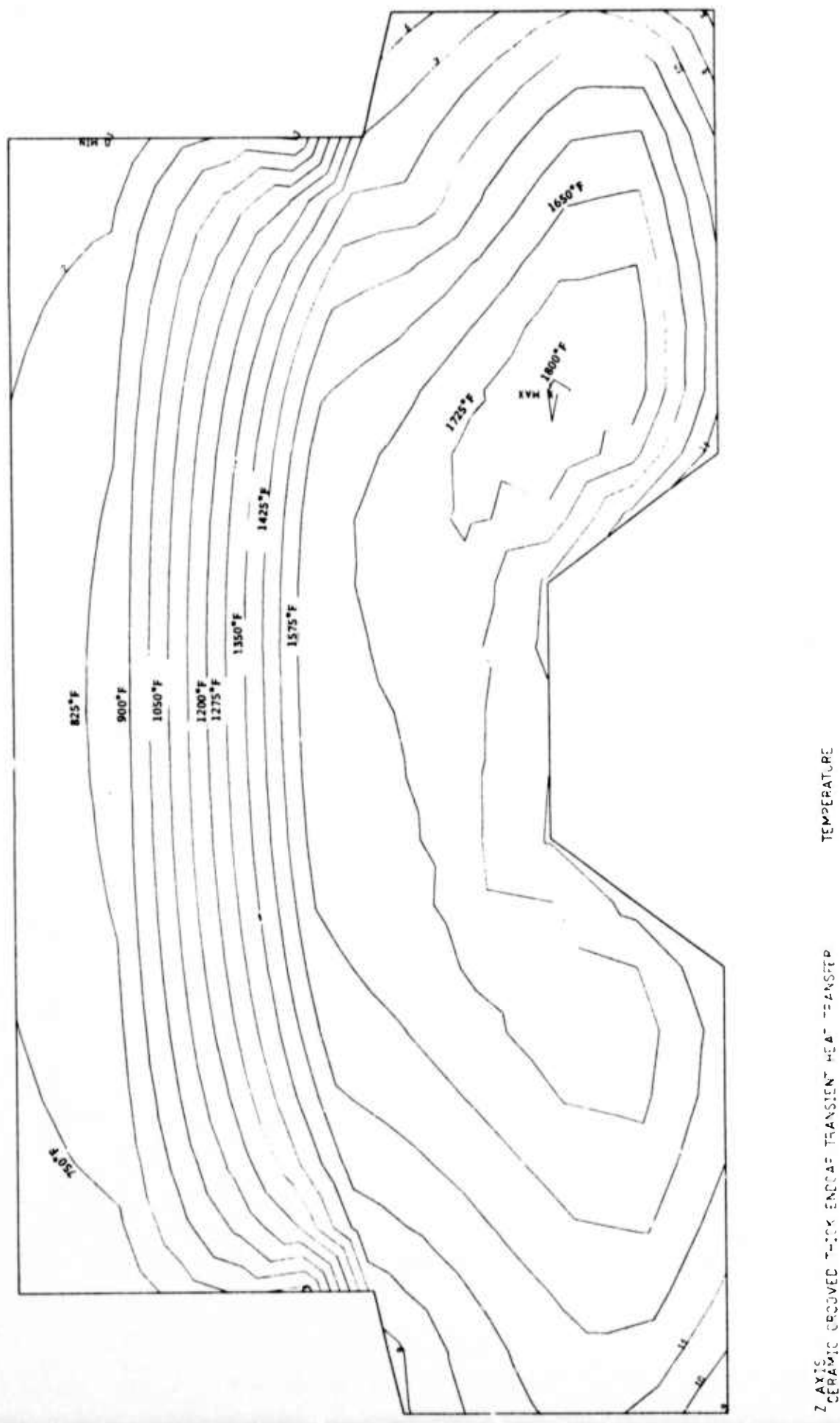


Figure 4.18 -- Thermal Contour Representation Through End Cap Section CC  
5 Seconds after Shut-Down

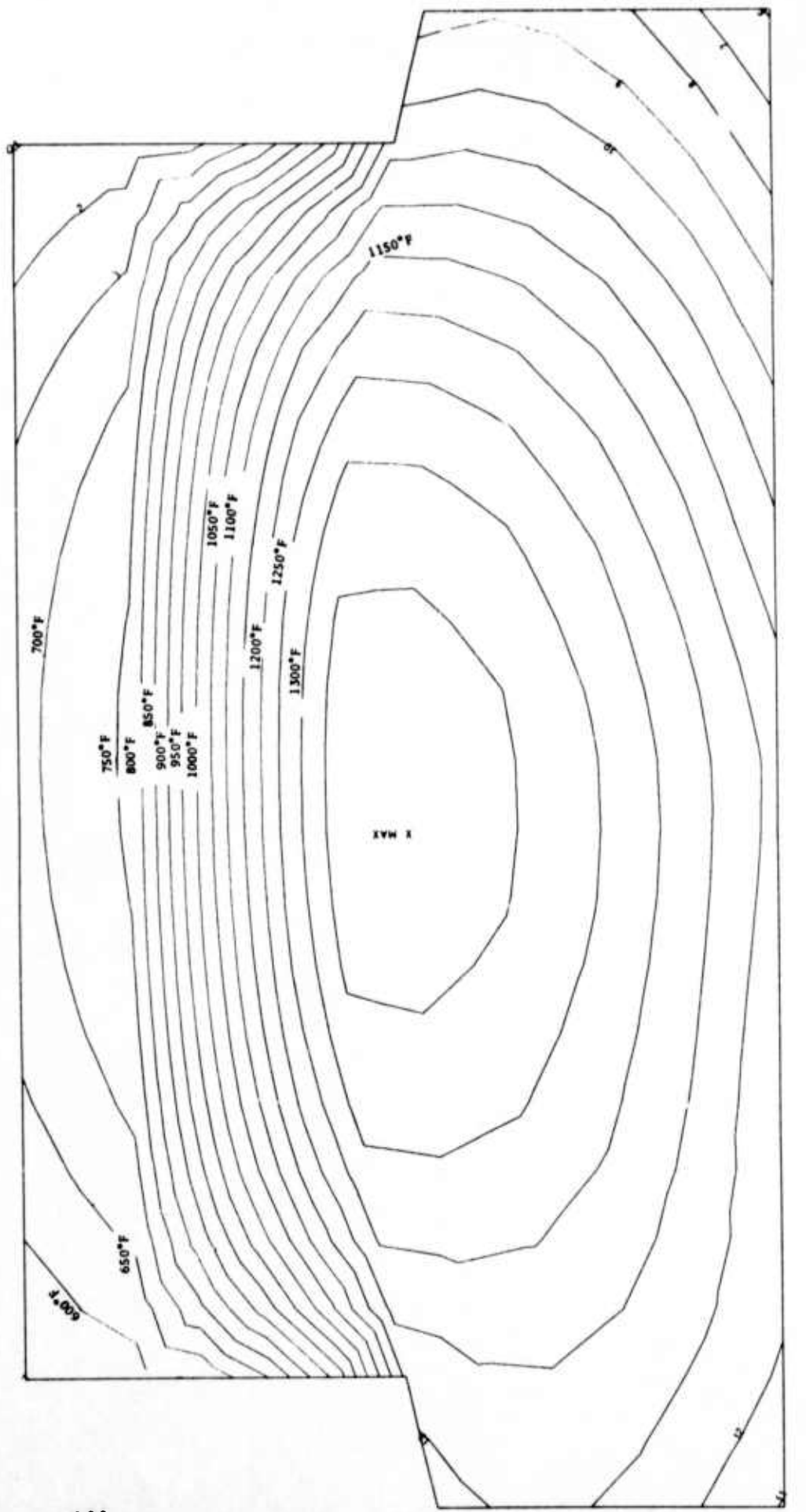


Figure 4.19 -- Thermal Contour Representation Through End Cap Section AA  
6 Seconds after Shut-Down

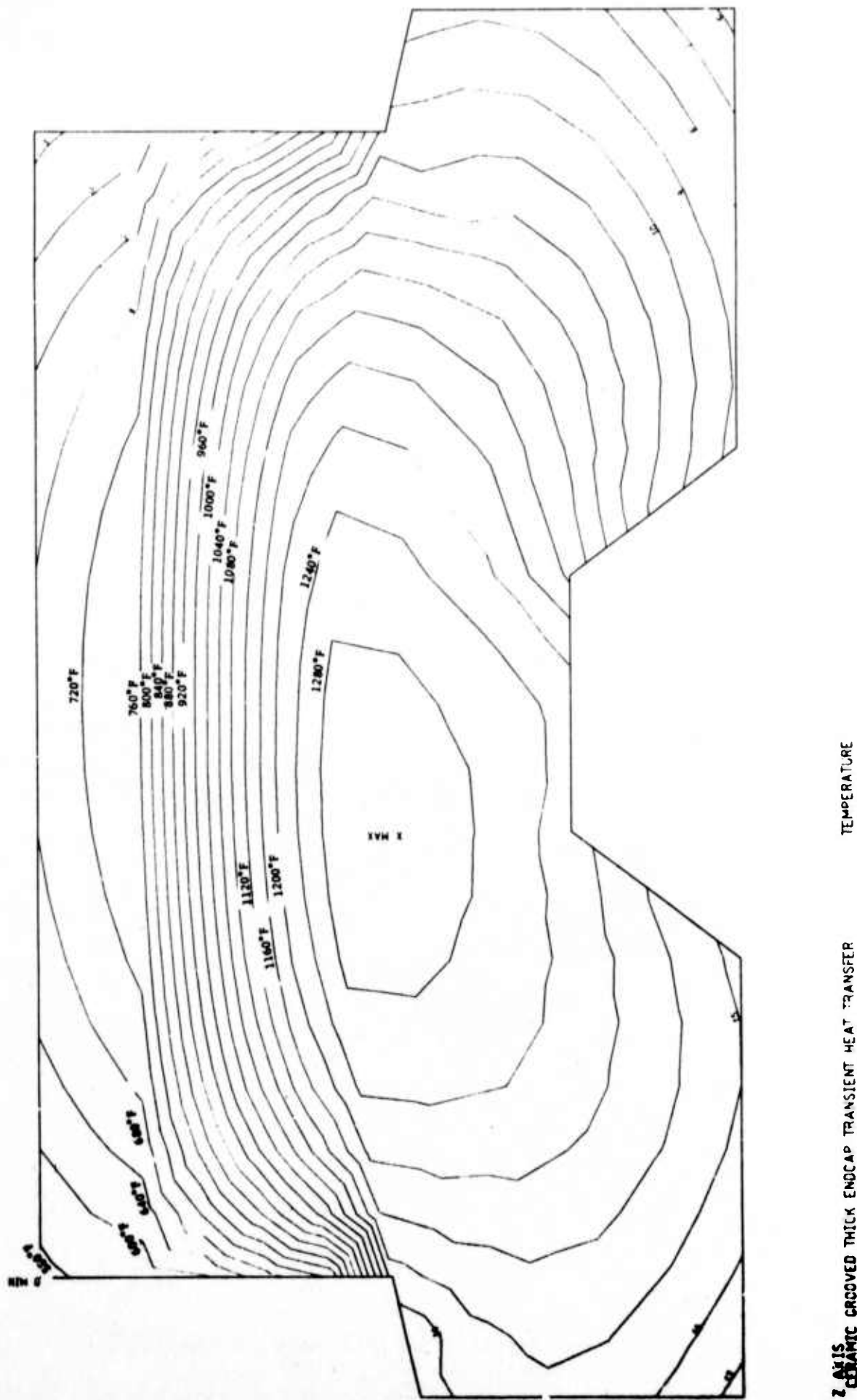


Figure 4.20 -- Thermal Contour Representation Through End Cap Section CC  
 60 Seconds after Shut-Down

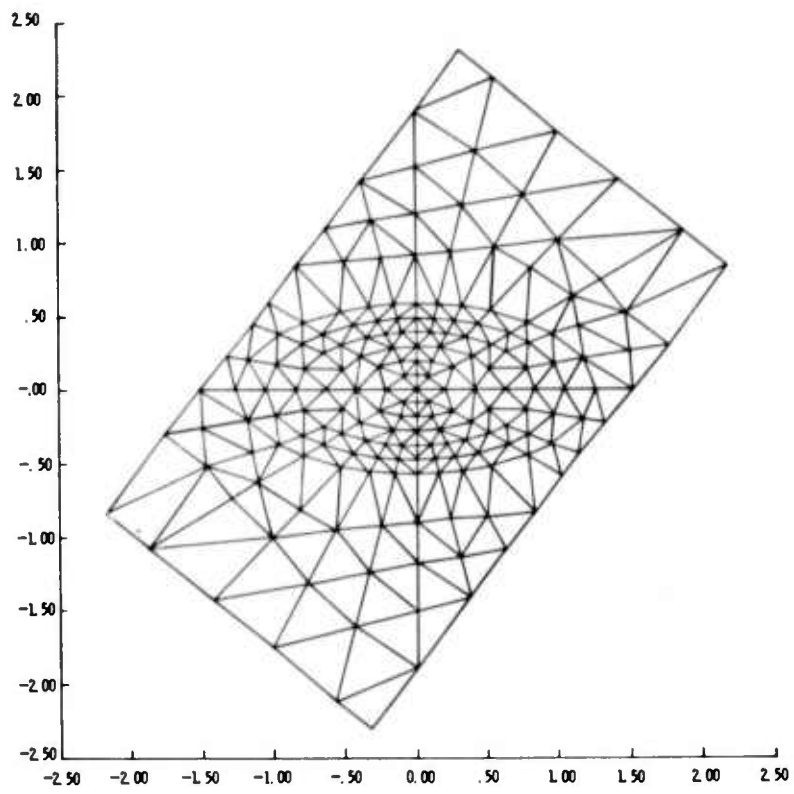


Figure 4.21 -- Two Dimensional Finite Element Mesh for Thermal Stresses in Ceramic End Caps

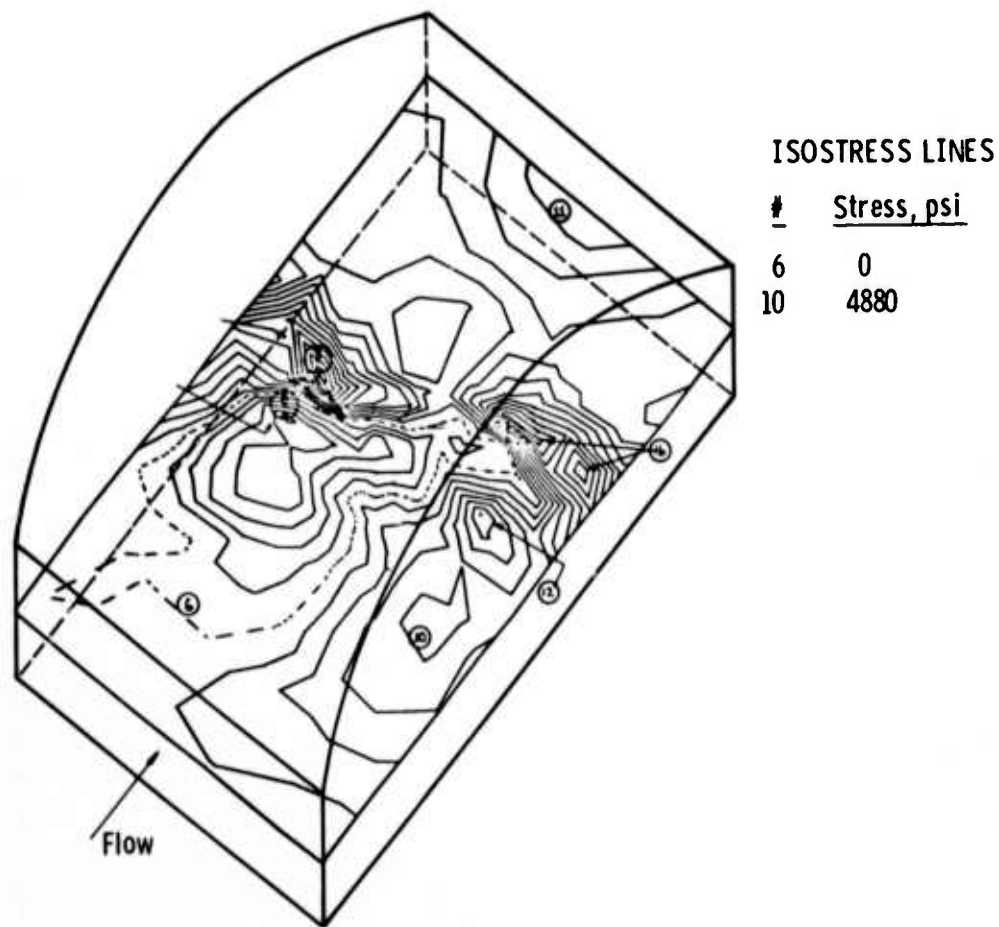


Figure 4.22 -- Thermal Stress Distribution in Ceramic End Caps under Steady State Conditions

The transient analysis of the first generation stator vane will not be completed because the second generation design is expected to be superior in all respects. Recently developed three dimensional finite element techniques will be used to analyze the new design which exhibits different characteristics in contact, groove stress concentration, and heat transfer which cannot be modeled by the plate program. The 3-D finite element code (WISEC) simulates geometry precisely and is equipped to handle non-linear gradients due to abrupt thermal transients.

#### 4.1.3 VANE FABRICATION

##### Introduction

The Norton Company was selected to manufacture ceramic stator vane assemblies of high strength, hot pressed silicon nitride and silicon carbide. They completed their FY 72 sub-contract with the delivery of stator vane assemblies machined from certified HS-130 silicon nitride billets. Additional  $\text{Si}_3\text{N}_4$  and SiC billets have been hot-pressed for the manufacture of vane assemblies for testing at 2500°F.

##### First Generation Silicon Nitride Vane Assemblies

Fifteen airfoil and thirty-seven end caps were received from the Norton Company in April to complete the twenty sets of hardware required for 2200°F tests in the static rig. These components are illustrated in Fig. 4.23 as a cluster of four to demonstrate the concept of alternating thick and thin end caps. All of the end caps and airfoils were subjected to rigorous inspection. Xyglo, x-ray radiography, and ultrasonic scanning was employed to document possible defects and to supplement the extensive inspection record supplied by Norton.

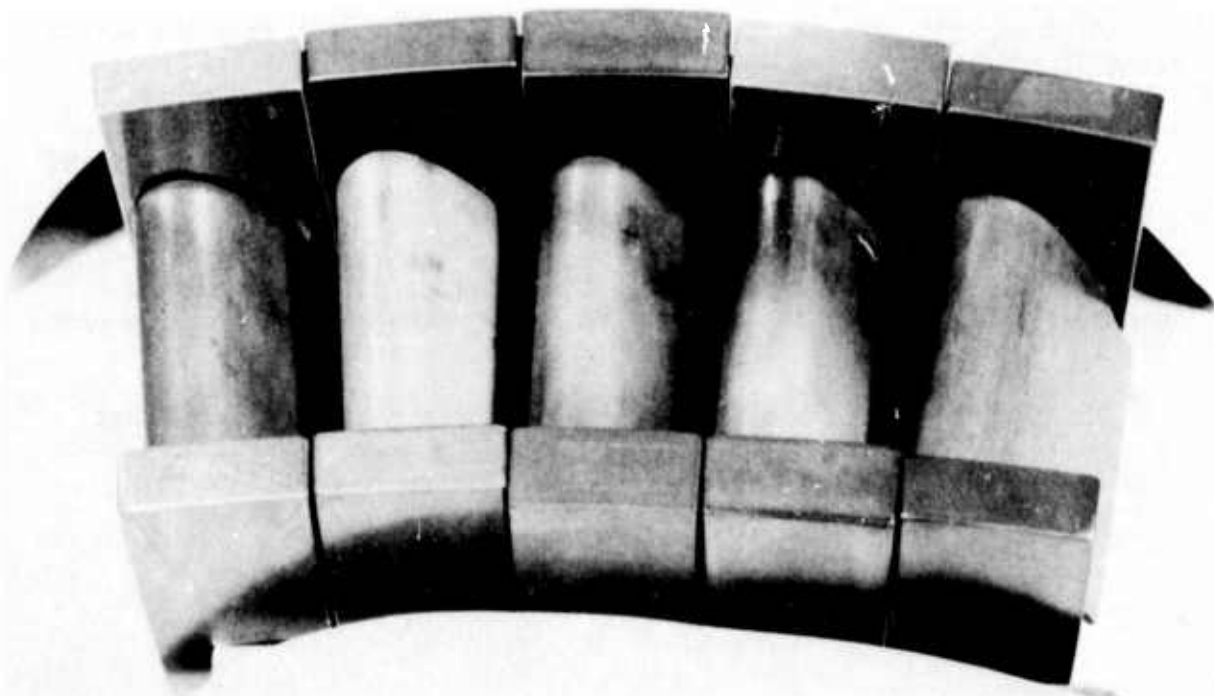


Figure 4.23 -- First Generation Stator Vane Assemblies as Supplied by Norton from HS-130 Silicon Nitride

The Xyglo dye penetrant technique was used primarily to document surface condition. Examination of all surfaces under ultraviolet light revealed a random pattern of extensive scratches. If possible flaws or defects were detected, the component was photographed. Typical results appear in Figs. 4.24 and 4.25. Airfoil 18B (Fig. 4.24) illustrates the surface scratches while airfoil 19B exhibits not only deep scratches but also a rather long crack extending inward from the middle of the trailing edge. Most of the scratches in the end caps were found inside the groove as shown in Fig. 4.25.

X-ray radiographs were prepared from K-type film under normal conditions of 60 KV, 10 amps and a 4-5 minute exposure time. Airfoil 19B was of particular interest because the crack identified by Xyglo was not readily detected by x-ray inspection. Knowledge of its presence, however, led to very close scrutiny and the revelation of a faint image on the film. The use of enhancement methods are currently being studied in order to define the limit of resolution for crack-type flaws. This is important for identification of internal cracks which are inaccessible to dye penetrant techniques.

Other irregularities were observed by radiography which cannot be reproduced from the film for illustration, e.g., numerous high density inclusions. One airfoil that contained a few high density particles about 0.04 in. long was rejected. High density particles less than 0.008 in. were not considered harmful because previous work<sup>(2-3)</sup> has shown that Fe + W concentrations do not cause premature failure.

Due to uneven thickness, it was difficult to conduct a systematic ultrasonic scanning of the airfoils. Procedures are being devised to overcome this problem. Figure 4.26 shows a few examples of defects detected by the A-scan ultrasonic method. The first and last peak displayed on the oscilloscope trace represents the top and bottom surface of the end cap. Any intermediate peak represents reflection from an internal interface or "defect". Experience indicates that the method is only sensitive to low density inclusions and layering. Peak height is no indication of defect size. Six of the end caps displayed these defects, which are suspected to be low density inclusions of poorly densified Si<sub>3</sub>N<sub>4</sub> or BN. However, since none of these inclusions appeared on the surface or at a critical stress point, none of the end caps containing them were rejected.

In all, 3 airfoils and 3 end caps were rejected as a result of non-destructive inspection. Defect maps were constructed to characterize all sixty components of the twenty stator vane assembly sets.

Spot dimensional checks on several of the airfoils revealed that the basic airfoil cross-section was machined to drawing tolerances. However, detailed checking of the end caps and airfoils did reveal numerous deficiencies which could be detrimental.

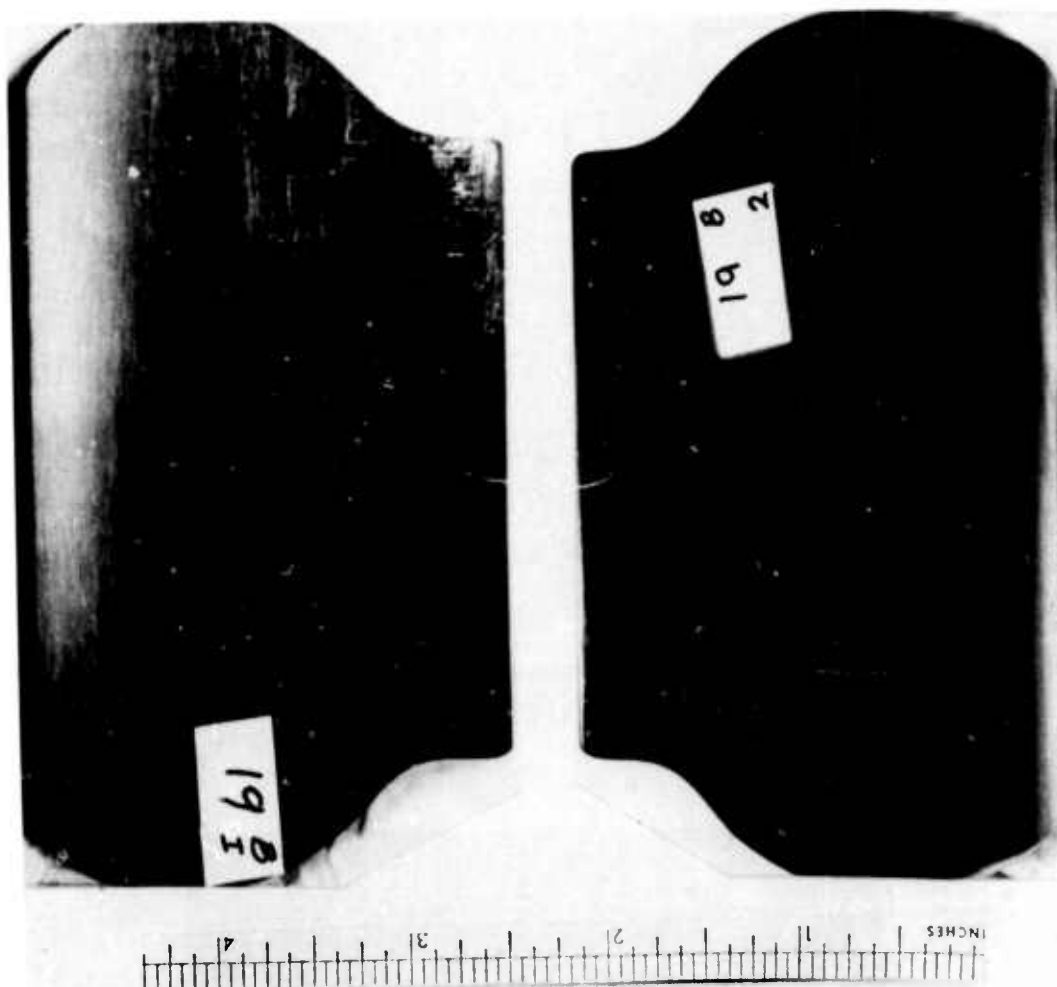


Figure 4.24 -- "Xyglo" Photograph of Two Machined Airfoils - Note: Surface Scratches and Crack on the Trailing Edge of Airfoil #19

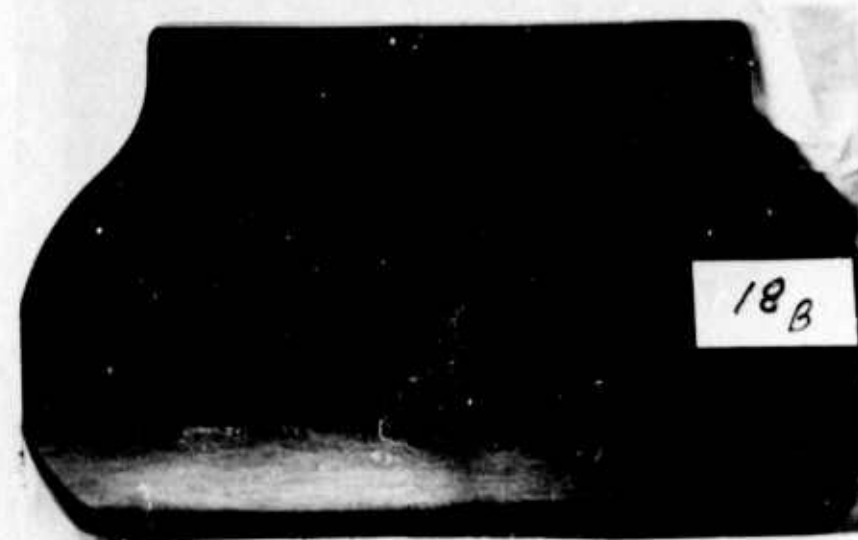




Figure 4.25 -- "Xyglo" Photograph of End Cap Showing Scratches Inside Cavity and Surface Irregularities

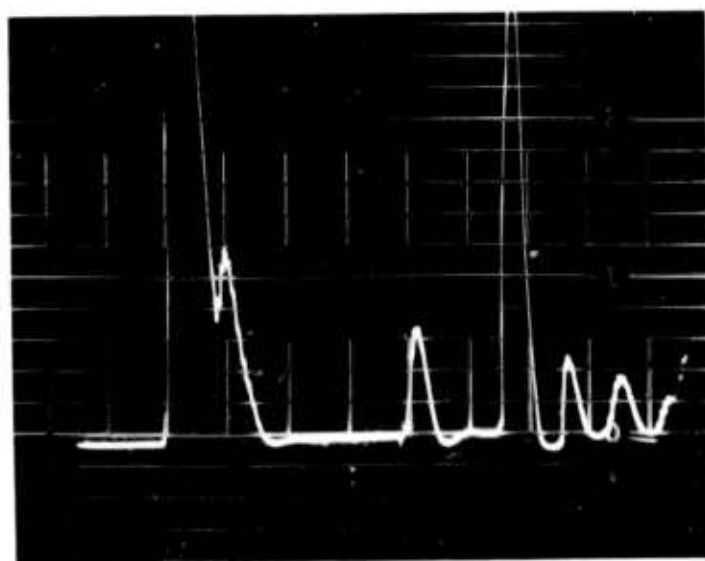


Figure 4.26 -- Ultrasonic Scan of End Cap Indicating Low Density Inclusions (Large Peaks are Reflections from Top and Bottom Surfaces)

The most critical requirement of the airfoil and end cap assembly is proper fit at the toroidal interface. Several of the end caps inspected had both major and minor radii of curvature less than the specified minimum value. All of the airfoils had toroidal surface radii which were greater than the specified maximum value. This condition results in an intolerable edge load stress situation. The depth of the toroidal groove in the inner end cap varied from 0.001 in. too shallow to 0.010 in. too deep. The depth of the toroidal groove

in the outer end caps varied from 0.018 in. to 0.031 in. too deep. This anomaly, together with the fact that the airfoil leading edge relief radius was either too small or non-existent and that the trailing edge relief radius was as much as 0.25 in. too large, would result in further leading and trailing edge loading. In some cases, the airfoil would not seat at all in the bottom of the end cap toroidal cavity. In addition, inspections revealed non-uniform conditions on the toroidal ends of the airfoils.

Several other problem areas were: (1) the edge-contour radii around the periphery of the end cap toroidal grooves and along the end cap boundaries were more like chamfers than radii, and (2) the surface finish in certain critical areas of the airfoil measured as high as 30 rms. For example, in the critical toroidal end cap cavity it was as high as 50 rms. A surface finish no greater than 10 rms overall was specified.

Eight of the best airfoil/end cap pairs were reground at the periphery of the end cap toroidal groove, around the edge of the airfoil tenon ends and at the leading and trailing edge relief radii. This operation was not done to any preselected tolerances. Sufficient material was removed, however, to insure surface area contact at the bottom of the end cap groove as indicated by dye removal. Individual pieces were selected and assembled for the static rig test on a best fit basis.

#### Hot Pressed Silicon Carbide Billets

Norton has hot pressed eighteen Noralide NC-203 silicon carbide billets to be used in the fabrication of first and second generation stator vane assemblies for static rig testing at 2200°F and 2500°F, respectively. Billet certification is summarized in Table 4.1. The flexural strength mean and standard deviations were established on 20-1/8 x 1/8 inch specimens for billets broken in three point loading over a 3/4 inch span at room temperature. These data indicate that all the billets either meet or exceed the minimum requirement that average flexural strength less two standard deviations equal 80,000 psi. Recorded density, in all cases, exceeded the specified value of 3.20 gm/cm<sup>3</sup>.

A portion of these billets are being machined into 7 stator vane assemblies of first generation design. Norton has promised delivery of these items by July 31, 1973 so that they can be included in static rig tests at 2200°F. The remaining billets will be set aside for the machining of 8 stator vane assemblies of second generation design which will be tested in the static rig at 2500°F starting in January, 1974.

TABLE 4.1  
PROPERTIES OF NORTON NORALIDE HC-203 SILICON CARBIDE\*

<u>Billet No..</u>	<u>Size in.</u>	<u>Density gm/cc</u>	<u>Flexural Strength psi</u>	<u>Standard Deviation psi</u>
HX-341-2B	7-3/8 x 3-1/4 x 7/8	3.34	114171	11578
HX-341-3B	7-3/8 x 3-1/4 x 7/8	3.34	111337	9022
HX-341-433836B	11.5 dia. x 1	3.35	126020	8901
HX-341-433842	11.5 dia. x 1	3.35	109495	9207
HX-341-433836A	11.5 dia. x 1	3.35	119002	11754
HX-341-5A	7-3/8 x 3-1/4 x 7/8	3.35	111229	11536
HX-341-5B	7-3/8 x 3-1/4 x 7/8	3.35	105752	7833
HX-341-4B	7-3/8 x 3-1/4 x 7/8	3.35	109543	10310
HX-341-6B	7-3/8 x 3-1/4 x 7/8	3.34	125566	6437
HX-341-3A	7-3/8 x 3-1/4 x 7/8	3.35	109115	9319
HX-341-4A	7-3/8 x 3-1/4 x 7/8	3.37	116021	9314
HX-341-433841A	11-1/2 dia. x 1.35	3.35	109301	10794
HX-341-433841B	11-1/2 dia. x 1.35	3.35	113694	9910
HX-341-021273C	11-1/2 dia. x 1-3/8	3.34	125099	6925
HX-341-012673	11-1/2 dia. x 1-3/8	3.35	120240	5680
HX-341-032073A4	11-1/2 dia. x 1-1/8	3.33	117472	11035
HX-341050873II	9 dia. x 1-3/8	3.36	100421	7927
HX-032073A1	11-1/2 x 1-1/8	3.33	110665	8778

\* Data supplied by Norton to certify silicon carbide billets

Strength values represent the RT average of 20-1/8" x 1/8" x 1" specimens broken in 3 point bending over a 3/4" span at a crosshead speed of 0.02 in/min.

#### 4.1.4 STATIC RIG TESTING

##### Introduction

The start of Static Rig operation is expected in July, 1973. A test specification and plan has been completed and a detailed test schedule has been established for the 2200°F operation.

##### The Static Rig

The static test rig (Fig. 4.27) and the ceramic test assembly (Fig. 4.28) have been installed in the Gas Turbine System Division's Combustion Laboratory. Figure 4.29, which illustrates the mitered section, is included to locate the test assembly and give some indication of size. It may be easier to understand the functional aspects of the rig itself and each of its component parts by comparing the rig photograph (Fig. 4.27) with the schematic flow diagram appearing as Fig. 4.30. The actual flow path components, i.e., the instrumented combustor, the transition piece attached to the ceramic test assembly, and a metal exhaust duct with instrumentation rakes fit inside the five basic components of the refractory lined outer shell structure.

##### Instrumentation and Control

Extensive instrumentation has been provided. Gas passage temperature profiles are measured by fast response thermocouple rake systems located up and downstream of the ceramic stator vanes. All of the metal support hardware is monitored with thermocouples that are strategically located at shoes, air baffles, inner and outer housing rings, side vanes and spring housing.

These thermocouples will be used to evaluate heat transfer analyses, cooling air schemes, and design/analysis characteristics. Specially designed load cells have been installed to monitor the radial load on each pair of vane assemblies during spring installation, load up and during various phases of rig operation.

Unfortunately, attempts to maintain strain gauges on silicon nitride under transient thermal conditions have been unsuccessful. However, a metal airfoil/end cap assembly, instrumented with strain gauges and thermocouples will be substituted for a ceramic assembly in a test run at 1400°F in order to obtain meaningful heat transfer and stress data with which to correlate 2 and 3 dimensional design/analysis techniques.

The control system for the static rig is being modified to provide variable shutdown modes. A valve control device will permit the rig or an operating turbine to be shutdown at a pre-programmed rate in the event of a turbine malfunction. Such a procedure will not only prevent serious damage but also extend component service life, especially in the case of air-cooled metal parts which characteristically suffer thermal fatigue.

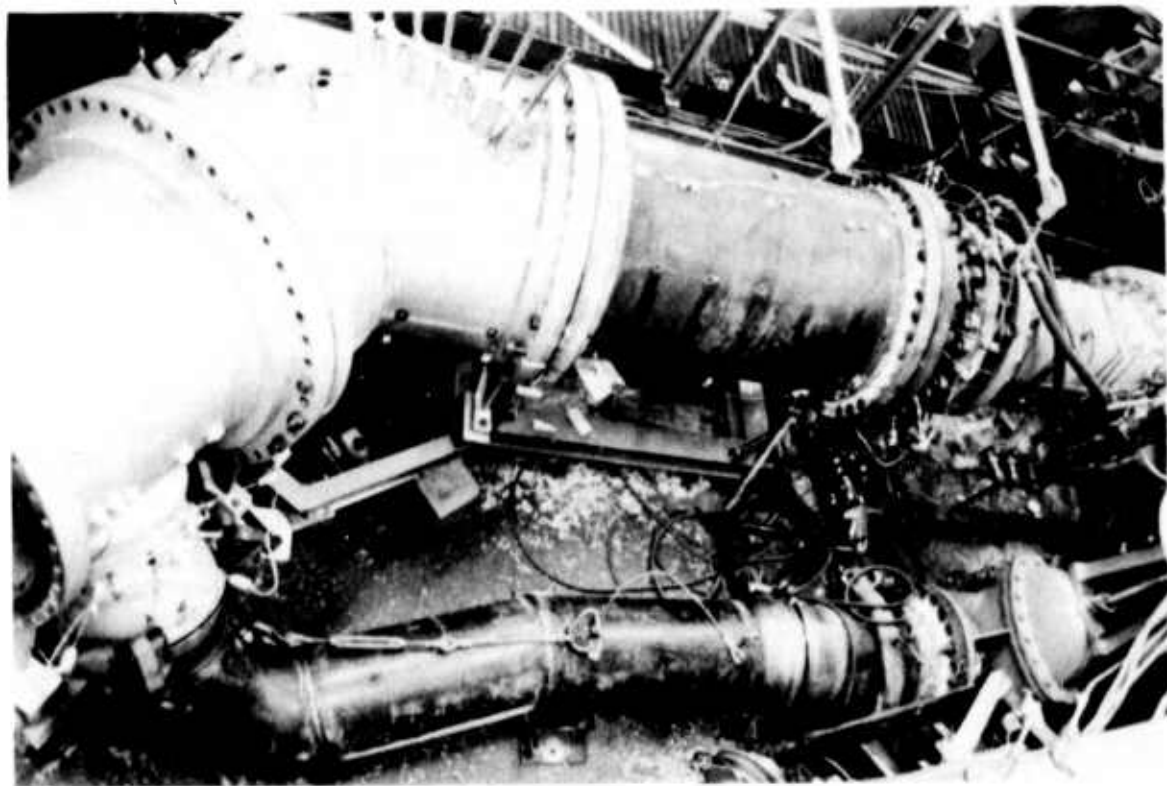


Figure 4.27 -- The Static Rig for Testing Ceramic Stator Vanes at 2200 and 2500°F (Mitered Section is 42 Inches in Diameter)

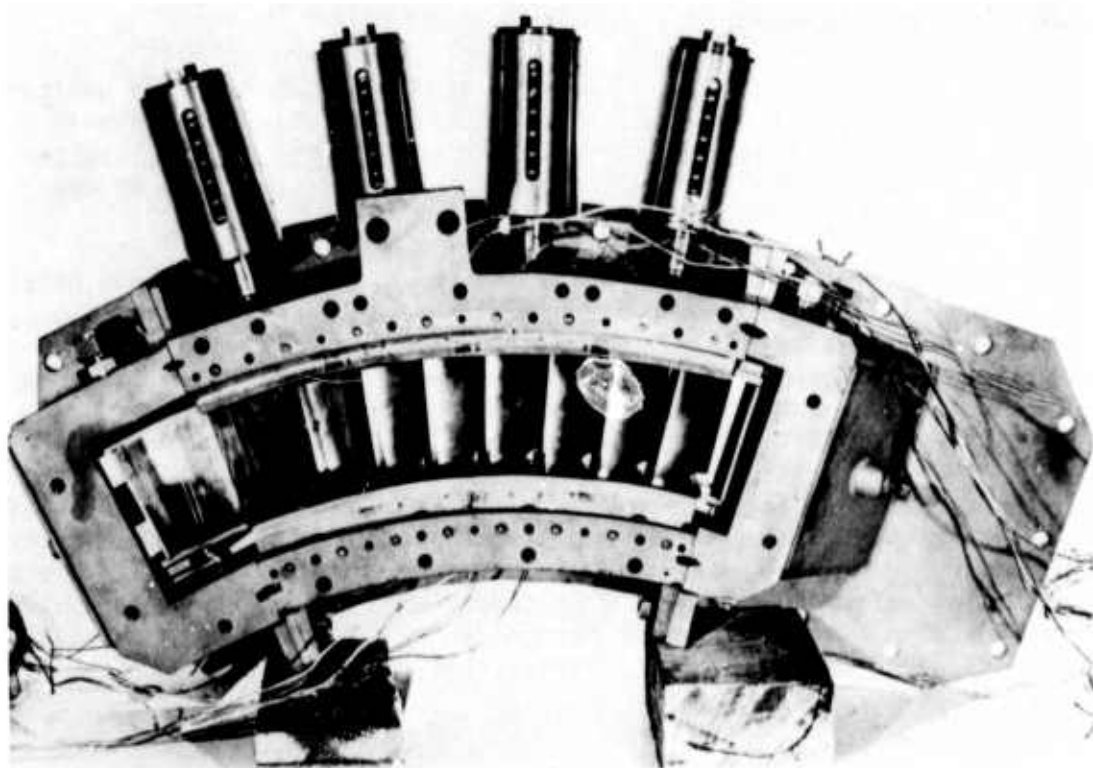


Figure 4.28 -- Silicon Nitride Stator Vanes Assembled with Support Structure for Test at 2200°F

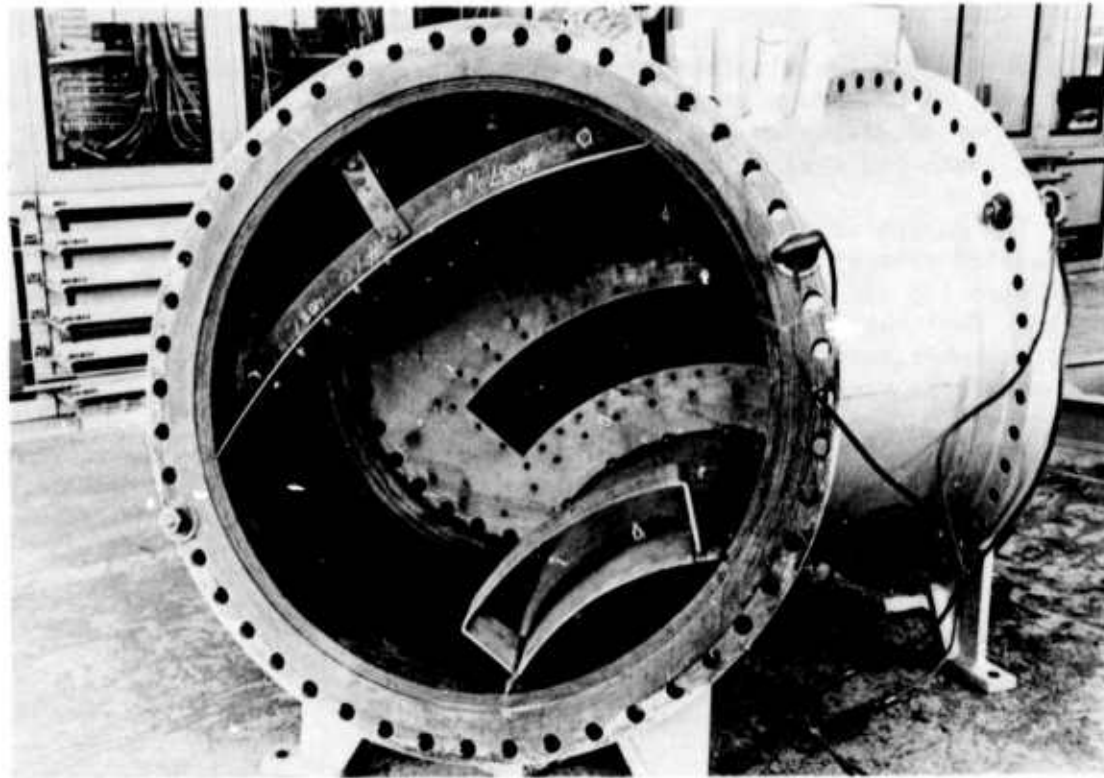


Figure 4.29 -- Mitered Section of Static Rig Showing Barrier Plate for the Installation of the Test Assembly

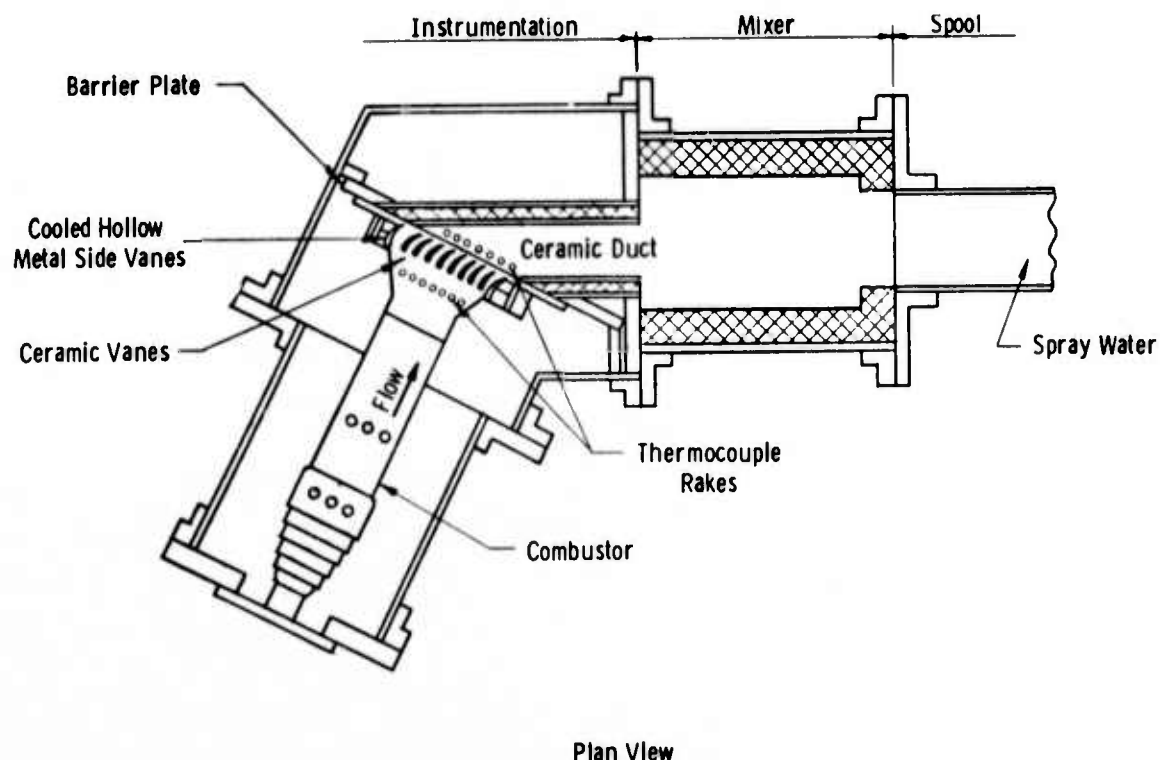


Figure 4.30 -- Static Rig - Schematic Representation

### Problem Areas

Some major installation problems have been encountered with the test rig. A breakdown in the steam turbine drive for the 9:1 compressor in mid-May necessitates the use of a 6:1 backup compressor for initial steady state and cyclic tests at 2200°F.

The design of the test rig for 2500°F required a special nitride-bonded SiC exhaust duct. The procurement time required for this duct precludes its use for the 2200°F test in July. The Haynes 188 hot gas exhaust duct was installed for these first tests. The ceramic duct will be substituted before the start of 2500°F tests of second generation SiC and Si<sub>3</sub>N<sub>4</sub> vanes in January, 1974.

The first experimental set of ceramic (Si<sub>3</sub>N<sub>4</sub>) thermocouple rakes has been fabricated by AME. These rakes will be evaluated at 2200°F in September after completion of the first set of tests. If the Si<sub>3</sub>N<sub>4</sub> performs as expected, the rakes will also be installed for the 2500°F tests.

## 4.2 ROTOR BLADE DEVELOPMENT

### Summary

The Westinghouse Isoparametric Finite Element Stress Analysis Code (WISEC) has been expanded to include a steady state and transient heat transfer capability. This part of the program was verified by comparing problem solutions with the existing results from 2-dimensional finite element and finite difference analyses.

The 3D codes were used to analyze a tentative ceramic rotor blade design subjected to centrifugal loading at 3600 rpm. Stresses as high as 38,000 psi occur in the dovetail root area as a result of contact angle and high friction at the root-disc interface.

#### 4.2.1 THREE DIMENSIONAL FINITE ELEMENT STRESS ANALYSIS

The Westinghouse Isoparametric Element Code (WISEC) for three dimensional elastic stress analysis has been expanded to include the capability for solving problems that involve steady state and transient heat transfer analysis. Besides completing this section of the program, theoretical development on the basic program to include elastic-plastic stress analysis has been completed. Work in progress includes the capability for solving problems that involve anisotropic material properties, and several program improvements such as a mesh generator and a stress plotting capability.

In order to check out the three dimensional finite element program for steady state and transient heat conduction and to compare results with other axisymmetric finite element and finite difference computer programs, several sample problems have been run. One of these problems is illustrated here; namely, an analysis of the flange assembly illustrated in Fig. 4.31. Initially, a steady state condition was established with a fluid flowing through a pipe at 500°F. The outside ambient temperature was 70°F. The fluid temperature then dropped linearly to 400°F over a period of 0.01 hours; after this a final steady state condition was established. The finite element model of a section of the assembly appears in Fig. 4.32. Since the radius of the pipe was large (20") compared with its thickness (1") the curvature of the section was ignored in the finite element model. However, the temperatures on the opposite faces were constrained to have equal values, thus simulating results obtained in an axisymmetric analysis. The agreement between the results of the present analysis with those of the independent finite element and finite difference analysis is excellent. A maximum difference of only one percent was observed. The temperature distribution through the cross-section of the assembly at the end of the temperature drop of the fluid has been superimposed upon the finite element mesh in Fig. 4.32. The problem verifies the steady state and transient heat transfer capability using a three dimensional solid element with convective and conductive heat flow.

Further development of the program will include temperature plotting capabilities. The program has a data transfer capability which allows for the transfer of the appropriate data from the heat conduction to the stress analysis portions of the overall three dimensional finite element program (WISEC).

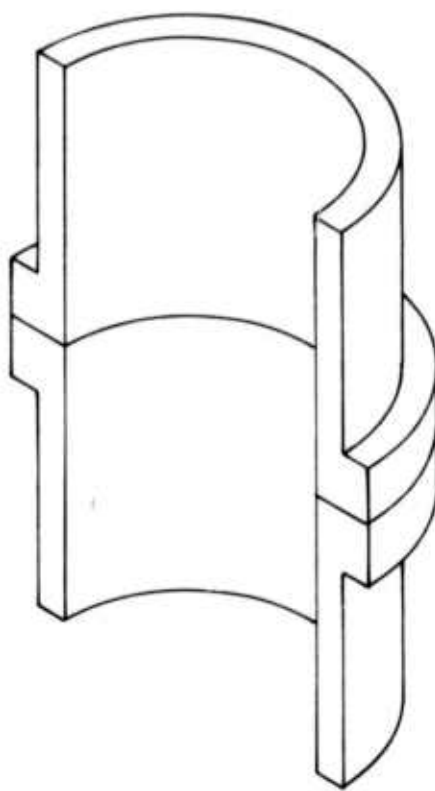


Figure 4.31 -- Flange Assembly Section

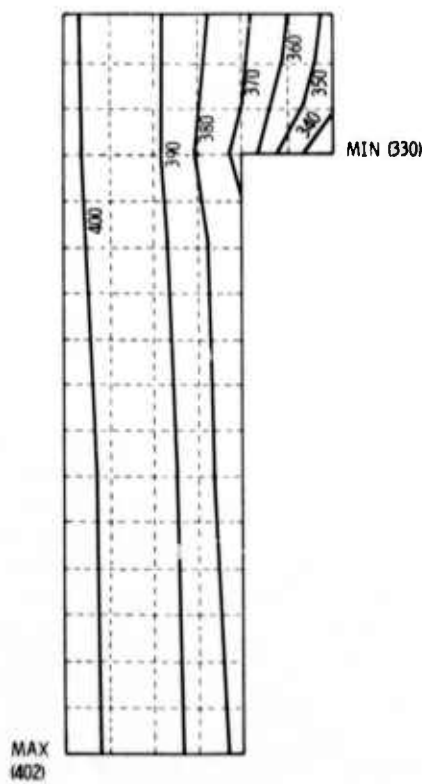


Figure 4.32 -- Finite Element Model of the Flange Assembly with Temperature Distribution at 0.01 Hours Superimposed Upon It

#### 4.2.2 STRESS ANALYSIS OF BLADES

##### Introduction

Activity in the area of preliminary design concepts and stress analysis of ceramic rotor blading has been extended. The previous stress analysis<sup>(1)</sup> was performed assuming that a Si<sub>3</sub>N<sub>4</sub> blade and root were supported by knife edges at the root boundary surface of a dovetail root configuration. The knife edges have been replaced with roller supports to distribute the contact stress in the root area more realistically. Results presented in this section include the effects of area on contact stress as a function of included angle and friction coefficient.

##### Mechanical Stress Development in Rotating Blades

In the present analysis, a shearing force in addition to the normal force is assumed. Both the airfoil and platform geometries are similar to those used currently in heavy duty turbines. The root geometry is based on experience with cermet blading.<sup>(5-9)</sup> The blade and root configuration was loaded analytically by a centrifugal force acting as a result of 3600 rpm rotation. Figure 4.33 illustrates the three dimensional finite element model used.

The results of loading this blade by centrifugal forces are plotted in terms of radial stress contours in vertical cross-sections at the leading edge (Fig. 4.34), at midchord (Fig. 4.35) and at the trailing edge (Fig. 4.36). The location of the roller supports (constraining forces) are identified. A maximum tensile stress of 32,364 psi occurs in the root area near the leading edge of the airfoil.

Several observations can be made from these results. First, the maximum tensile stress occurs between the point of contact and the neck of the root. For this case, the maximum tensile stress in the root is 200% larger than the stress in the root fillet radius. Contrary to previous work,<sup>(5)</sup> this implies there are factors other than notch sensitivity or stress concentrations involved in the optimization of blade roots for brittle materials. The second observation is the chordwise variation of the maximum tensile stress along the root axis. This can be observed from a change in the maximum tensile stress of 32,364 psi near the leading edge to 20,000 psi at midchord and then to 29,000 psi near the trailing edge.

This analysis, which predicts that the maximum tensile stress is in the root, correlates well with the early experimental results.<sup>(6-9)</sup> A survey of cermet turbine blade experience shows that brittle materials were first used as rotor blades in aircraft turbine applications. Root failures predominated when cermets were fabricated from metal blade designs. Various root geometries were evaluated. The dovetail design which minimizes notch sensitivity in brittle materials proved superior to the more conventional fir tree design. While the original state-of-the-art recognized root geometry generally as a critical design parameter, the specific importance of root angle, friction at the dovetail disc interface, and contact area was demonstrated as part of the current work.

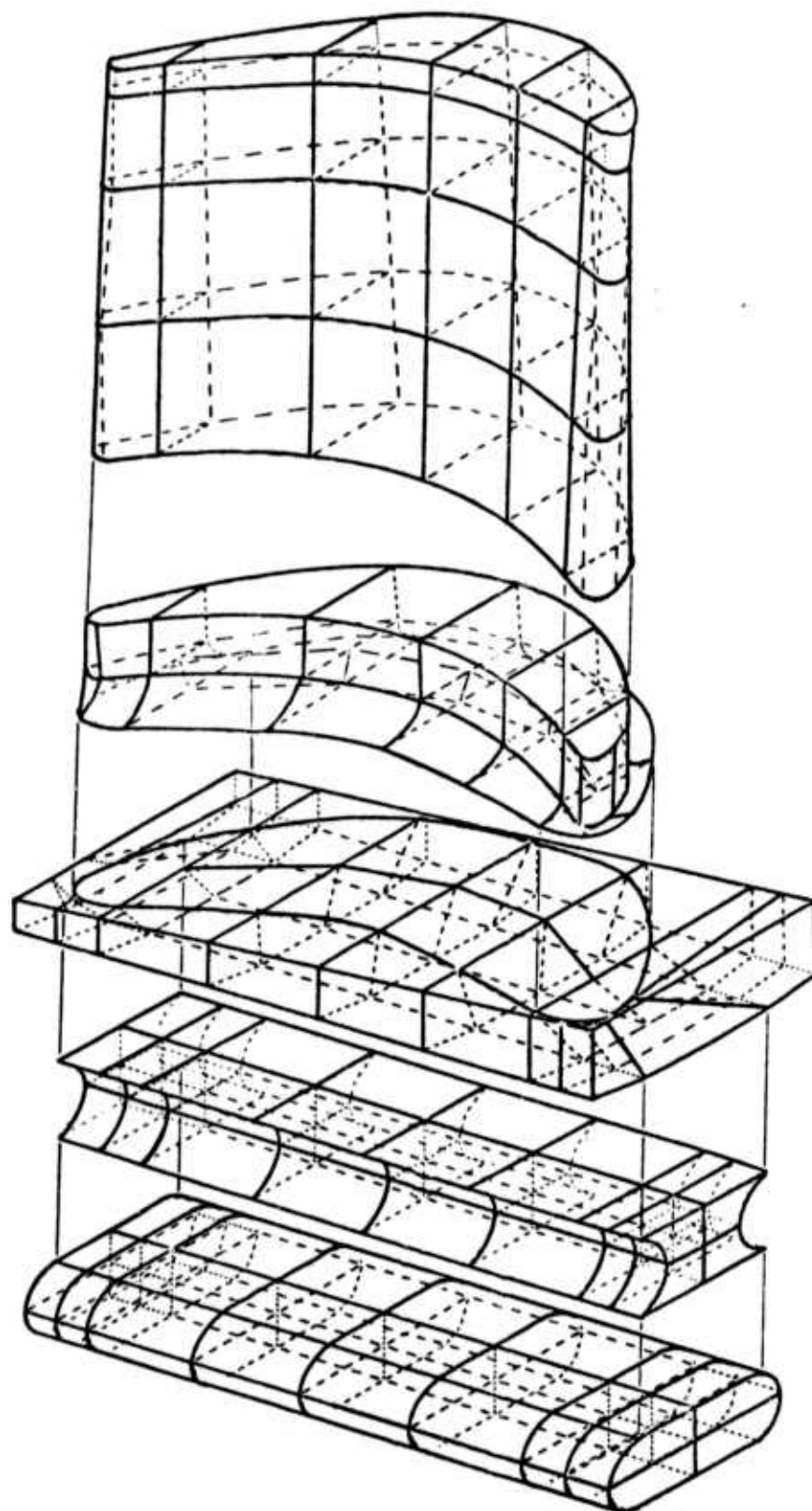
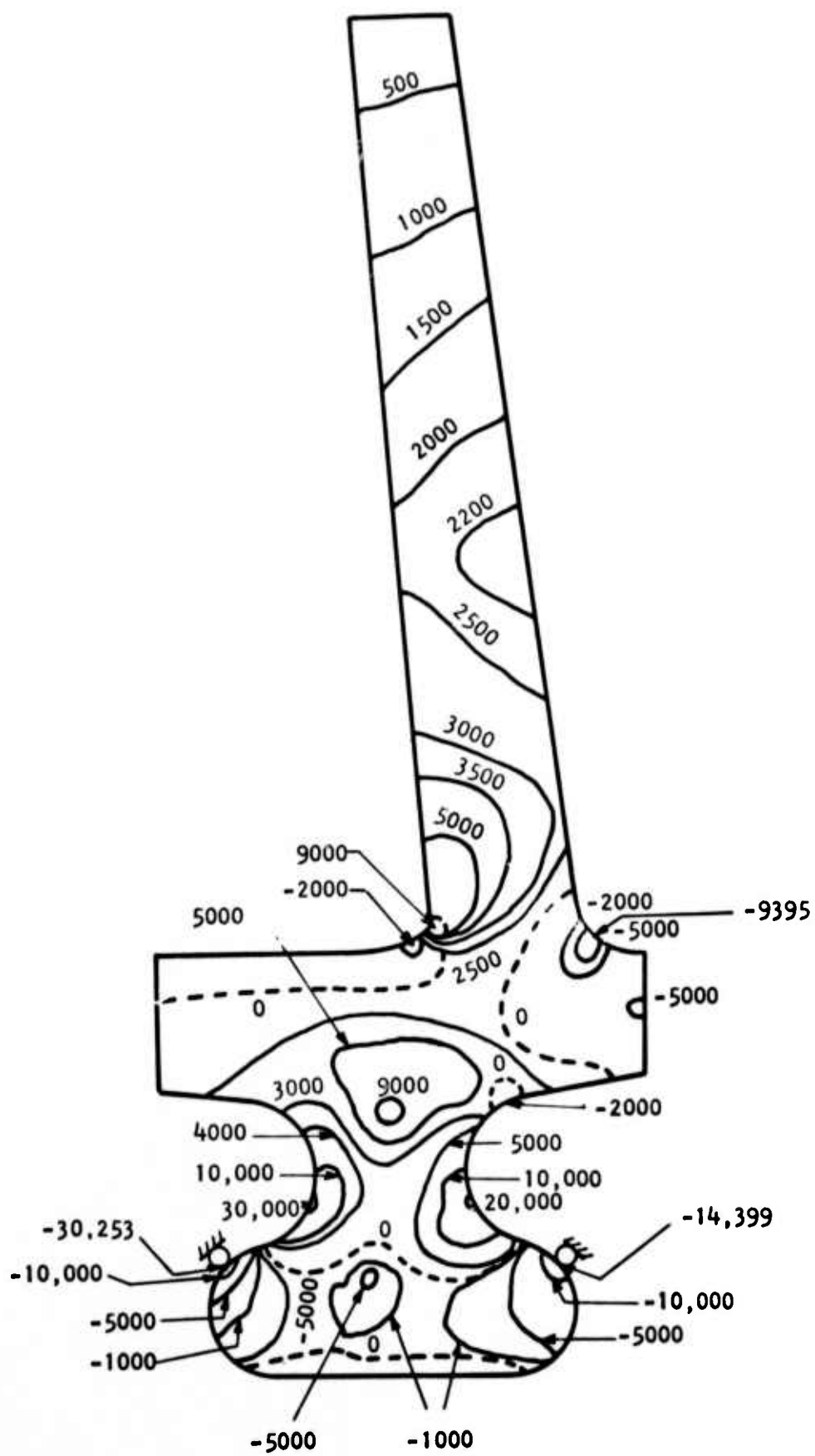


Figure 4.33 -- Exploded View of Three Dimensional Computer Model



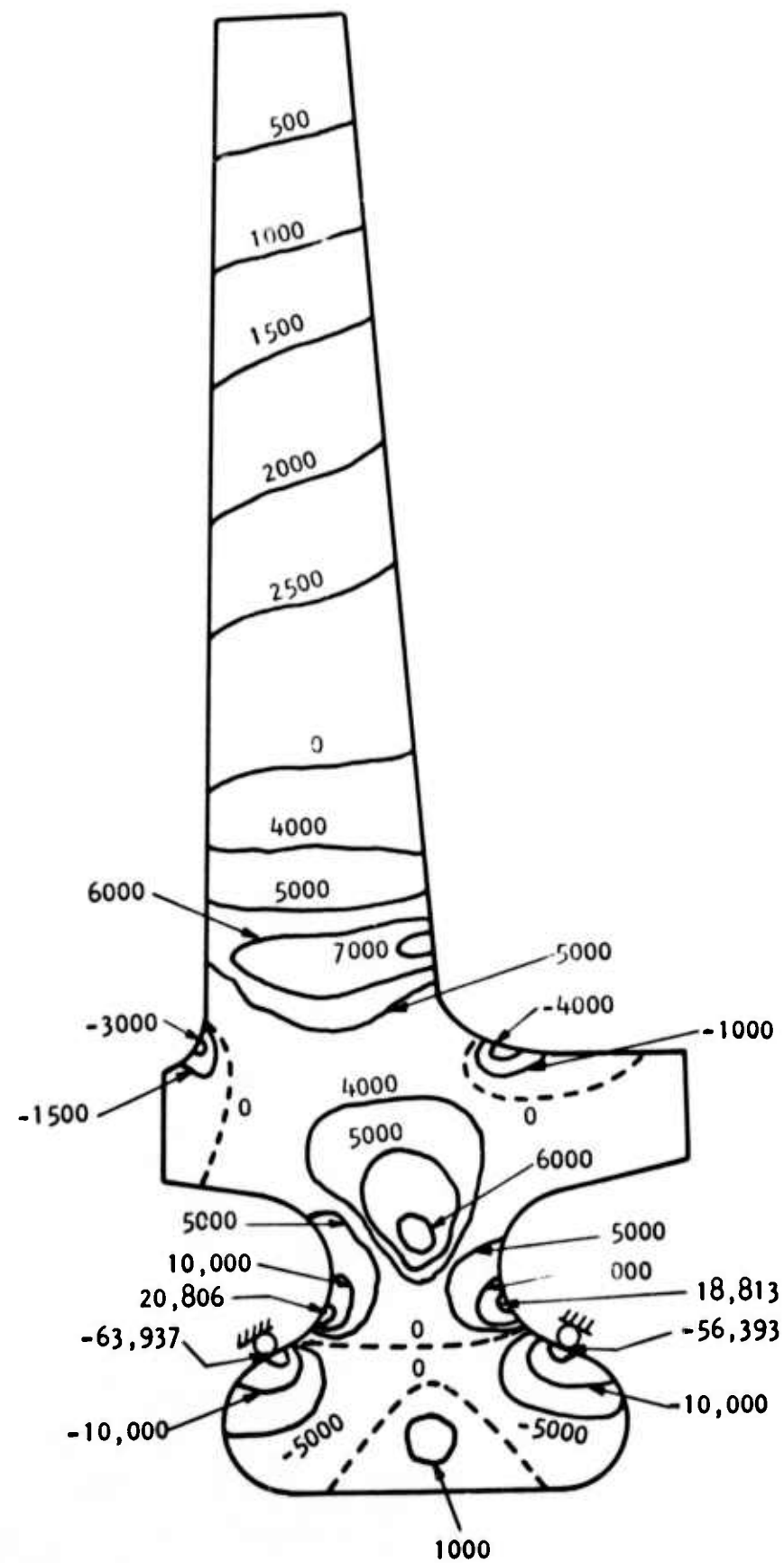


Figure 4.35 -- Radial Stress Contours (psi) on Section 500 of Blade Model

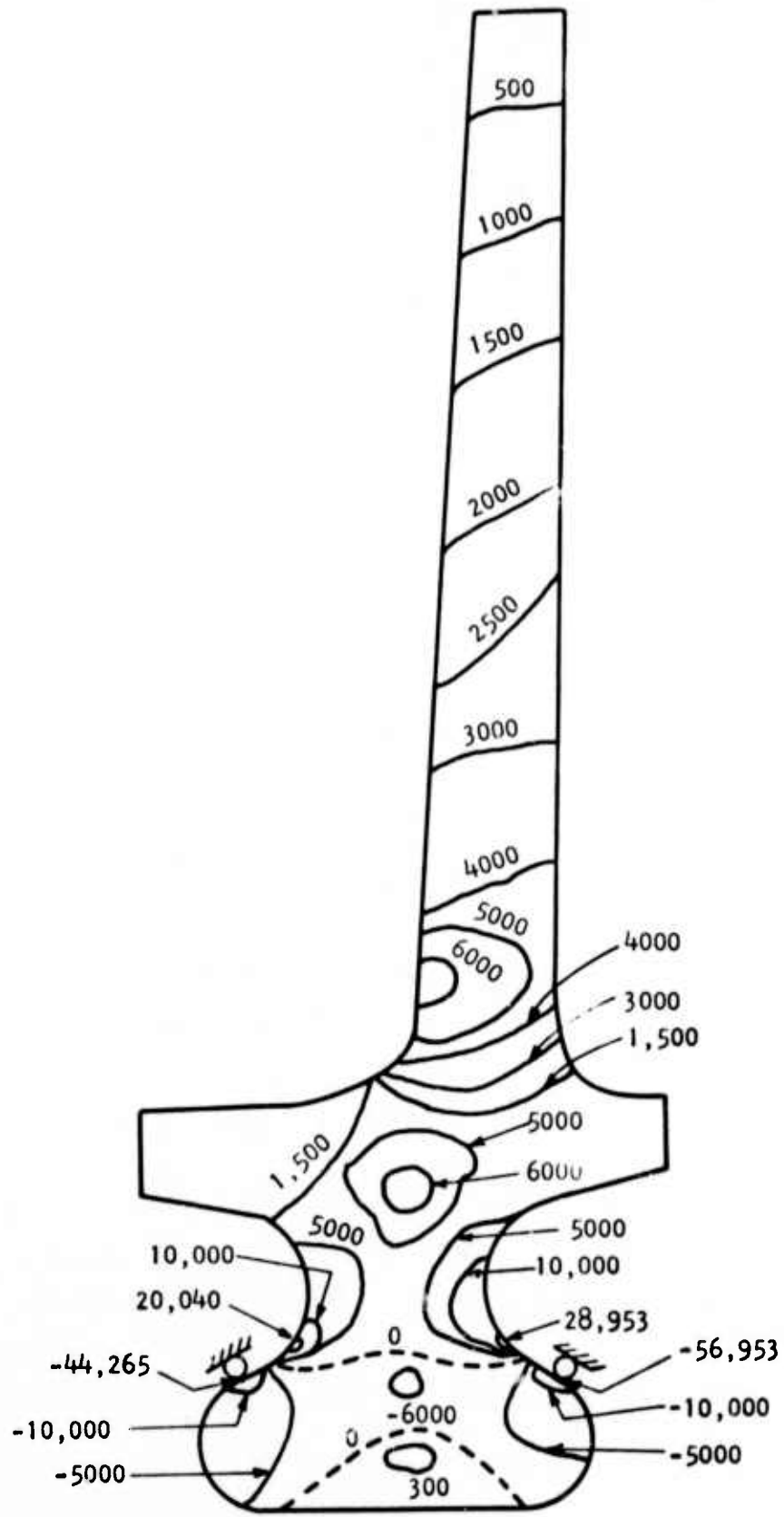


FIG. 4.36 -- Radial Stress Contours (psi) on Section 700 of Blade Model

In order to optimize the root cross-sectional shape, a state of generalized plain strain was assumed to exist in the root. This allowed the two dimensional plain strain model shown in Fig. 4.37 to be used. The centrifugal force,  $F_c$ , as shown in Fig. 4.37, is resisted by normal and shear forces,  $F_n$  and  $F_s$ , whose respective stresses act uniformly over the contact area,  $A_c$ , with conditions of symmetry along the centerline of the root. The disc that holds the root is assumed to be rigid in this model and the shear stress developed is assumed to be the maximum attainable for the given root geometry.

With these assumptions, the effects of several parameters on the stresses induced by  $F_c$  were analyzed; namely, the included angle,  $\alpha$ , the area of contact,  $A_c$ , and the friction coefficient,  $\mu$ . This parametric study was accomplished using finite element models with the objective of minimizing the root stress. For purposes of analysis, the blade roots were subjected analytically to the force  $F_c$  resulting from a rotational speed of 4850 rpm instead of the 3600 rpm specified previously. The higher speed was chosen because it is representative of the actual turbine in which a ceramic blade is being considered. The consequence of this higher speed is higher stress in the root. Specifically, the new stresses will be proportional to the square of the speed ratio times the stresses developed at a speed of 3600 rpm.

Turning to the parameters studied to reduce the root stress, Fig. 4.38 is representative of the finite element models used to examine the effect of the included angle,  $\alpha$ , when it is made equal to 30°, 45° and 60°. The finite element mesh for these models consisted of constant strain triangles. The results of the first parametric study in which the friction coefficient,  $\mu = 0$ , and area of contact,  $A_c = 0.675$  sq. in. based on a root length of 4.1 in., are shown in Fig. 4.39. As may be seen, a maximum stress of 24,000 psi occurs in the fillet radius of the root. This result was expected based on stress concentration and notch sensitivity data reported in the literature. (5-10)

When the study was extended by introducing a shear stress on the contact area,  $A_c$ , a marked effect on the root stress was obtained. This shear stress, as calculated from Coulomb's Law ( $F_s \geq \mu F_n$ ), was distributed uniformly over the contact area. Furthermore,  $F_s$  was assumed equal to  $\mu F_n$  where  $\mu$  is taken as the angle of static friction,  $\mu = \tan(90-\alpha)$ . Where  $\alpha = 30^\circ$ , the friction coefficient,  $\mu = 1.73$ , gives the maximum obtainable shear stress that can develop on the contact area of the root. The result of this particular analysis is shown in Fig. 4.40. As may be seen, the effect of friction on the contact area is to increase the maximum tensile stress and shift it from the fillet radius to a point slightly above the contact area. This phenomenon was not predicted by pull tests<sup>(5)</sup> or stress concentration studies.<sup>(10)</sup> For the root geometry described above, the maximum stress increases from 24 to 38 ksi as the coefficient of friction increases from 0 to 1.73. Thus, friction has a pronounced effect not only on the magnitude but also on the distribution of maximum stress in the root. The average stress across the neck of the root, which offsets the centrifugal force on the blade, is 11 ksi for both cases of  $\mu = 0$  and 1.73.

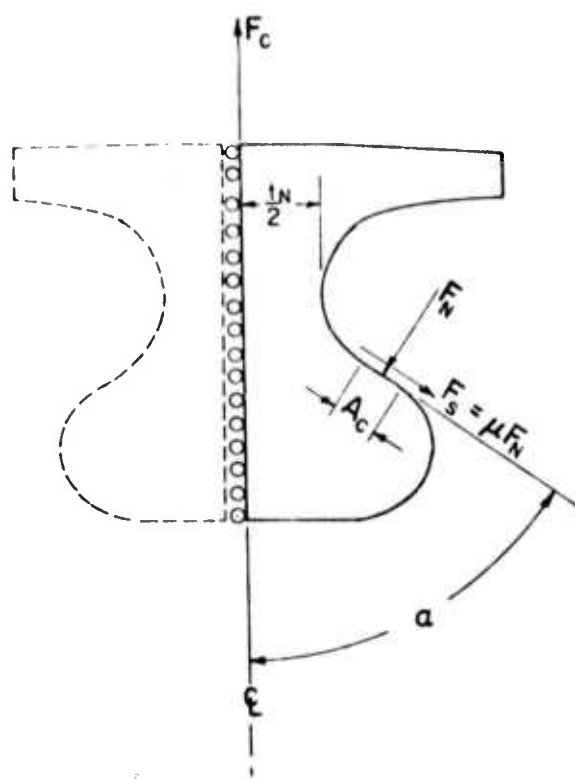


Figure 4.37 -- Two-Dimensional Blade Root Model

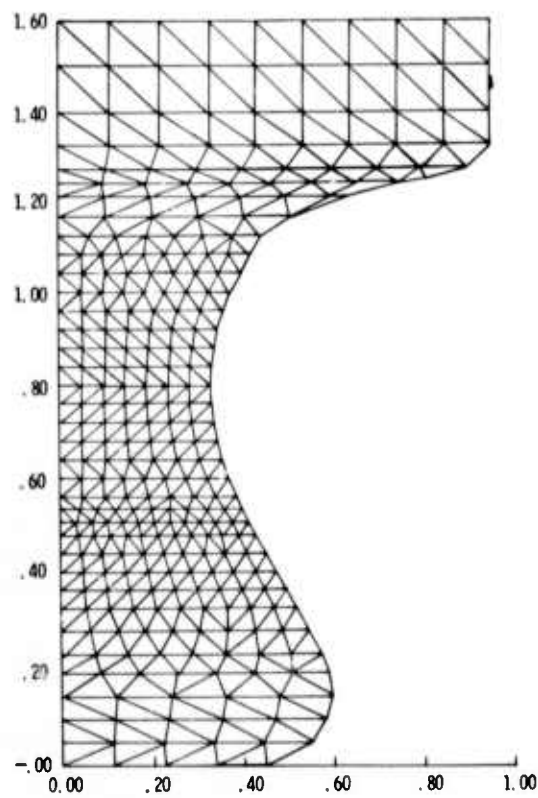


Figure 4.38 -- Two-Dimensional Computer Model for a  $30^\circ$  Blade Root

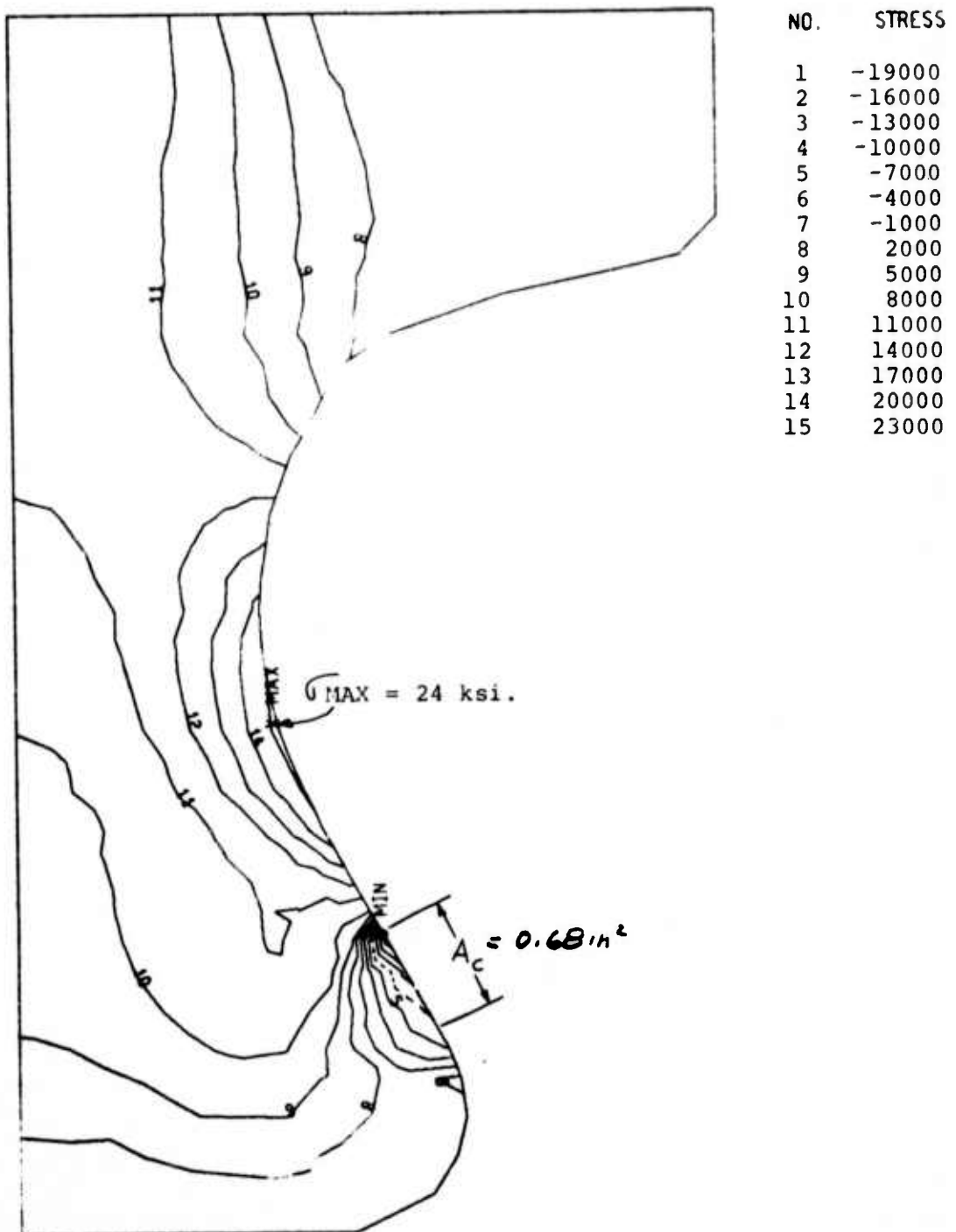


Figure 4.39 -- Maximum Principal Stress Contours in a 30° Blade Root  
(No Shear,  $\mu = 0$ )

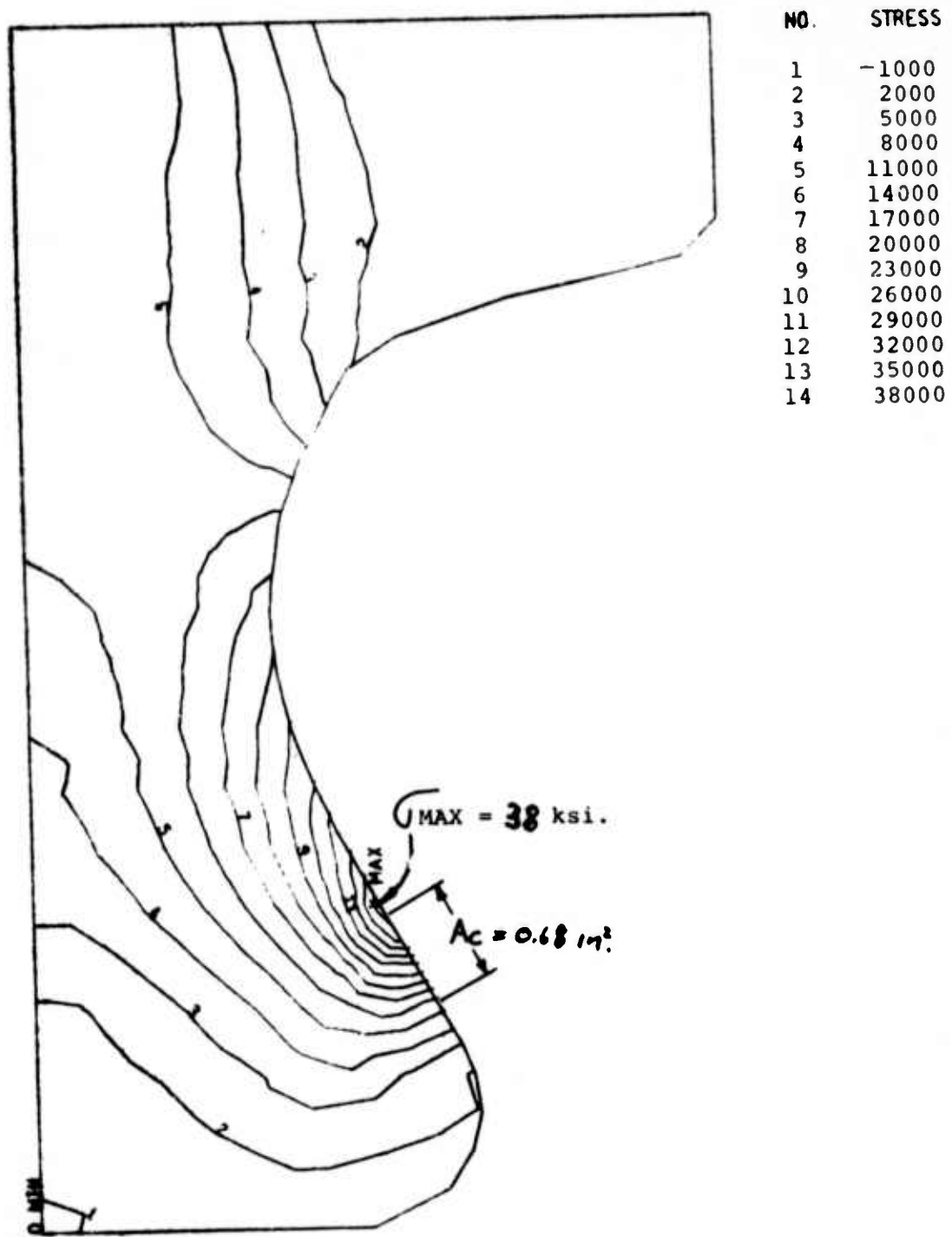


Figure 4.40 -- Maximum Principal Stress Contours in a  $30^\circ$  Blade Root  
(With Shear,  $\mu = 1.73$ )

The foregoing analysis was repeated on a  $30^\circ$ ,  $45^\circ$  and  $60^\circ$  root for a contact area of 1.35 sq. inches based on the root length of 4.1 inches. The results are plotted in terms of the maximum tensile stress as a function of angle,  $\alpha$ , for the case with and without friction in Fig. 4.41. The values of  $\mu$  for the root angles of  $45^\circ$  and  $60^\circ$ , were 1.0 and 0.58, respectively. Friction causes higher stresses in the root as observed from Fig. 4.41. The maximum tensile stress occurs slightly above the contact area for the roots if there is friction, but it shifts back to the fillet radius of the root when friction is eliminated. Increasing the angle  $\alpha$ , when friction is present, has little effect on the maximum tensile stress in the root (Fig. 4.40). This is due to the fact that as  $\alpha$  increases the angle of static friction,  $\tan(90^\circ - \alpha)$ , decreases, hence  $\mu$  is reduced. A reduction in  $\mu$  has the effect of keeping the maximum tensile stress fairly constant as  $\alpha$  varies from  $30^\circ$  to  $60^\circ$ . Elimination of friction results in lower maximum stresses in the root for the cases studied. The largest reduction in stress occurs for a root angle of  $30^\circ$ . For this case, eliminating friction results in a 45% drop in stress. Furthermore, the maximum tensile stress follows the value of the theoretical stress concentration of the root when friction is not present. The concentration factor for the  $60^\circ$  root is slightly smaller than the factor for the  $45^\circ$  root; 1.25 compared to 1.27. This accounts for a slightly higher stress in the  $45^\circ$  root for the frictionless case.

To better understand the role of friction in brittle root designs, the coefficient of friction on a  $30^\circ$  root with a contact area of 1.35 sq. inches was varied from 0 to 1.73. The maximum root stress associated with this range of friction coefficients is shown in Fig. 4.42. The stress varies non-linearly with  $\mu$ . A higher rate of increase in stress occurs at lower values of  $\mu$ ,  $0 \leq \mu \leq 1.0$ . Since the stress increases from 23.4 ksi to 33.8 ksi as  $\mu$  varies from 0 to 1.73, for example, there is an obvious benefit from reducing the coefficient of friction between a ceramic and metal interface. One possibility would be to employ a low friction material between this interface.

The last parameter studied was the effect of contact area on the root. A contact area of 1.35 sq. inches was used to study the effect of friction and root angle on the maximum tensile stress. In general, the contact area can vary from the design area to a line load in the limiting case. The effect of contact area on the maximum tensile root stress, for a range of  $0.25 \leq A_c \leq 1.35 \text{ in.}^2$ , is given in Fig. 4.43. These are the results for a  $30^\circ$  root, with  $\mu = 1.73$ . Decreasing the contact area increases the maximum tensile stress in the root. For example, lowering the contact area from 1.35 sq. inches to 0.25 sq. inches raises the maximum tensile stress from 33.8 ksi to 40.6 ksi, i.e., an increase of 20%.

The maximum stress in a rotating blade can be reduced by 30% if hollow geometry is used. This concept is illustrated in Fig. 4.44. The use of a hollow airfoil has the effect of reducing the mass of the blade and, therefore, the centrifugal force acting on the root.

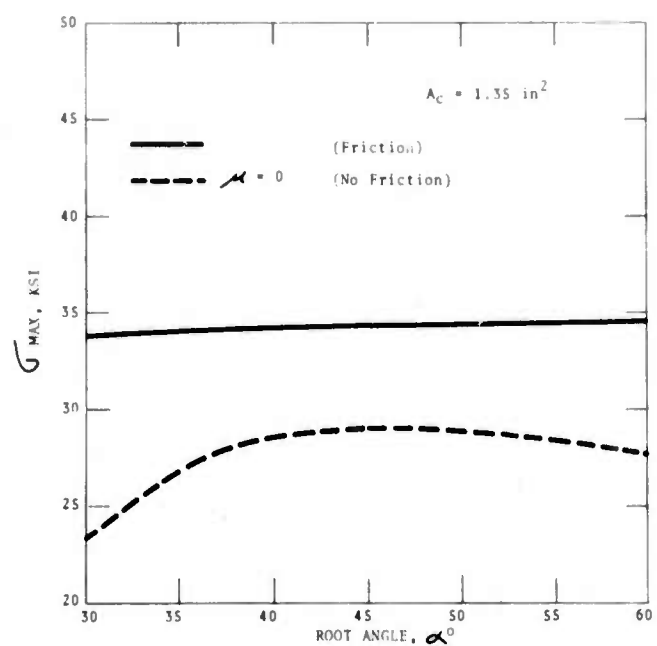


Figure 4.41 -- Effect of Root Angle and Maximum Stress in a Blade Root

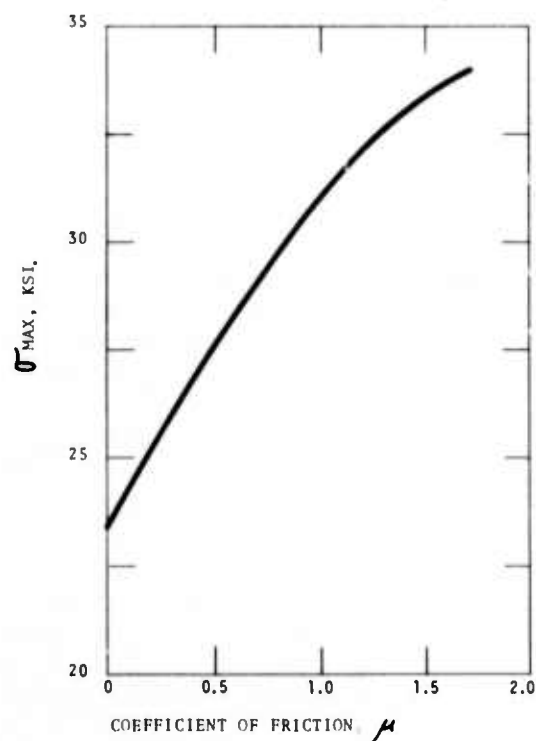


Figure 4.42 -- Effect of Friction Coefficient on Maximum Stress in a Blade Root

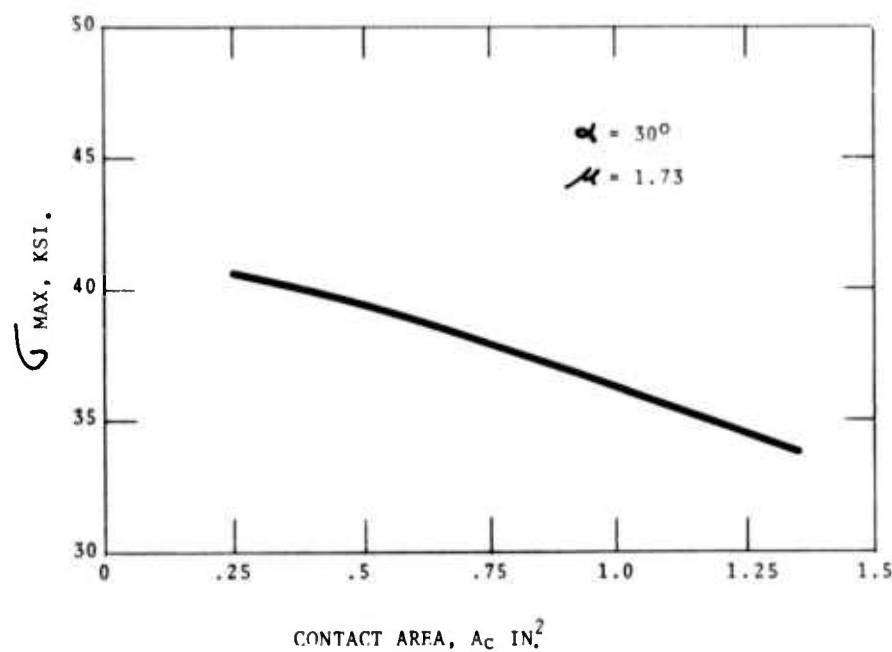


Figure 4.43 -- Effect of Contact Area on Maximum Stress in a Blade Root

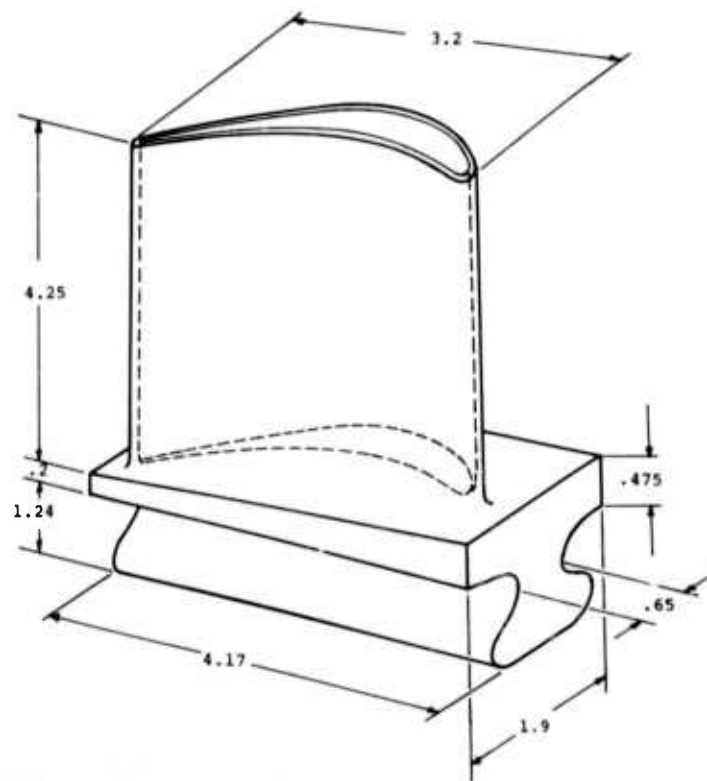


Figure 4.44 -- Hollow Ceramic Rotor Blade

The stresses in SiC blades are essentially the same as those developed in  $\text{Si}_3\text{N}_4$  blades. The effect of a change in Poisson's ratio from 0.23 ( $\text{Si}_3\text{N}_4$ ) to 0.17 (SiC) is a 0.5% reduction in maximum tensile<sup>(11)</sup> stress. Both materials have similar densities, and the difference between the elastic constants of the two materials has little effect on the root stresses caused by centrifugal force loads.

The effects of critical design parameters on the development of maximum tensile stresses in ceramic rotor blades is summarized in Table 4.2.

TABLE 4.2  
EFFECT OF CRITICAL DESIGN PARAMETERS ON  
MAXIMUM TENSILE STRESS

Case	Root Angle	Airfoil Geometry	Coefficient of Friction $\mu$	Contact Area $A_c$ , in. <sup>2</sup>	Maximum Stress, ksi @ Rotational Speed	
					3600 rpm	4850 rpm
1	30°	Hollow	0	1.35	9.1	16.6
2	30°	Hollow	1.73	1.35	13.3	23.6
3	30°	Solid	0	1.35	12.9	23.4
4	30°	Solid	1.73	1.35	18.6	33.8
5	30°	Solid	1.00	1.35	17.0	31.0
6	30°	Solid	0.50	1.35	14.9	27.0
7	30°	Solid	1.73	1.00	20.0	36.2
8	30°	Solid	0	0.7	13.2	24.0
9	30°	Solid	1.73	0.7	20.9	38.0
10	30°	Solid	1.73	0.25	22.4	40.6
11	45°	Solid	0	1.35	15.9	38.9
12	45°	Solid	1.00	1.35	18.8	34.2
13	60°	Solid	0	1.2	15.3	37.7
14	60°	Solid	0.25	1.2	16.2	29.4
15	60°	Solid	0.58	1.2	19.0	34.5

## 5. PROGRESS ON MATERIALS TECHNOLOGY - VEHICULAR AND STATIONARY TURBINE PROJECTS

### 5.1 MATERIALS ENGINEERING DATA

#### SUMMARY

Design technology is highly dependent upon physical properties of the materials being used. This section deals with work performed during the reporting period on the acquisition of physical property information. Many of the materials being investigated are in the development stage and improvements in properties are anticipated; this will require that some, if not all, of the physical properties must from time to time be re-determined. Therefore, property characterization of the ceramic materials for turbine engine use is a task which will continue throughout the life span of the contract.

The program to determine mechanical properties of candidate ceramic materials is continuing. Progress has been made in the use of Weibull statistics to calculate tensile strength of hot-pressed silicon nitride based upon flexural strength measurements, and some correlation was obtained. Tensile strength and elastic modulus measurements were made using a gas-bearing load train which is in agreement with previous determinations. The tensile strength and elastic modulus of Norton hot-pressed silicon carbide vs temperature were also measured. Additional determinations of flexural strength of both these materials and Refel silicon carbide is reported.

Creep testing of Norton HS-130 hot-pressed silicon nitride has established that creep rate and creep strain are significantly higher in air than values previously reported in a helium atmosphere. (1) Preliminary creep testing results for Norton hot-pressed silicon carbide, measured in a helium atmosphere, indicated no significant creep. The evaluation of creep of Ford reaction-sintered silicon nitride has shown that calcium is a major cause of high creep, similar to observations made on hot-pressed material.

Thermal conductivity, thermal diffusivity, specific heat, and thermal expansion measurements were performed on Norton hot-pressed silicon carbide. The thermal conductivity of this material is considerably greater than that of hot-pressed silicon nitride, as expected. Thermal conductivity and specific heat were also determined for Ford reaction-sintered silicon nitride.

Additional corrosion-erosion tests carried out on hot-pressed silicon nitride and silicon carbide, using barium-free diesel fuel, showed that both of these materials have excellent resistance to this environment.

### 5.1.1 PHYSICAL PROPERTIES OF HOT PRESSED MATERIALS

#### Introduction

The comprehensive program to evaluate the mechanical and thermal properties of many varieties of silicon nitride, silicon carbide, and lithium aluminum silicate in gas turbine applications is continuing. These data not only contribute valuable fundamental information about the materials but also are considered essential to an optimum design with brittle materials in order to provide the maximum safety factor. All of the candidate materials have been improved significantly. Since the potential for greater improvement exists, the Material Engineering task is expected to continue for the full term of the turbine project.

Recent data tend to confirm the properties of Norton HS-130 silicon nitride as previously reported. Creep strains, however, are much higher in air than in helium. The strength of reaction sintered material as expected continues to be lower than that displayed by hot pressed silicon nitride. Reliable engineering estimates of both mechanical and thermal properties of Norton hot pressed silicon carbide have been provided for stator vane design and stress analysis. Weibull theory has been used to establish a flexural to tensile strength relationship for hot pressed silicon nitride.

Refel reaction sintered silicon carbide is compared to the Norton hot pressed material on a flexural strength basis.

#### Statistical Aspects of Mechanical Responses

The Weibull analysis and predictions of tensile strength based upon 3 point flexural loading of silicon nitride samples at room temperature and 4 point flexural loading at 2300°F were presented in the previous progress report.(1) Data available at that time indicated that the area integral

$$\int \left( \frac{\sigma - \sigma_u}{\sigma_o} \right)^m dA$$

predicted tensile strength more precisely at room temperature while the volume integral

$$\int \left( \frac{\sigma - \sigma_u}{\sigma_o} \right)^m dV$$

appeared to be more appropriate at 2300°F. (In these expressions,  $m$  = Weibull modulus,  $\sigma_u$  = value of stress below which no failures are expected and  $\sigma_o$  = normalizing stress.) The analysis has been extended to reflect flexural and tensile results at 1800°F using three parameter Weibull in addition to the two parameter representation.

Briefly stated, the observed strength of brittle material is determined by the distribution of critical flaws within a body. Size sensitivity with respect to strength is related to the probability of encountering critical flaws which are randomly distributed. Strength, therefore, should vary inversely with size on either a volume or area

basis. This flaw concept is applied in the Weibull expression for the probability of failure

$$P = 1 - e^{- \int \left( \frac{\sigma - \sigma_0}{\sigma_0} \right)^m dS}$$

where S denotes size in terms of volume (V) or area (A) integrals.

When the failure probability is plotted with respect to strength, the Weibull modulus may be determined from the slope of the straight line portion of the curve. This modulus represents the standard deviation of values about the mean which reflects a degree of randomness with respect to the distribution of critical flaws at the surface or within the volume under stress.

Room temperature data for hot pressed silicon nitride based on 30-4pt. bend test results are plotted as a function of stressed area or volume for specified test modes in Fig. 5.1. The critical Weibull parameters  $m$  and  $\sigma_0$  are 5.0 and 50,738 psi for the area integral and 5.0 and 40,034 psi for the volume integral, respectively.

Two and three parameter Weibull results for both the area and volume integrals are compared with measured tensile values at 1800 and 2300°F in Table 5.1. The data fit the two parameter representations better than the three parameter at both temperatures. Thus, only the two parameter results appear graphically in Figs. 5.2 and 5.3 where strength is plotted against the volume and area under stress, respectively. The correlation at 1800°F is poor. At 2300°F, both the area and volume based predictions of strength fit the experimental data well.

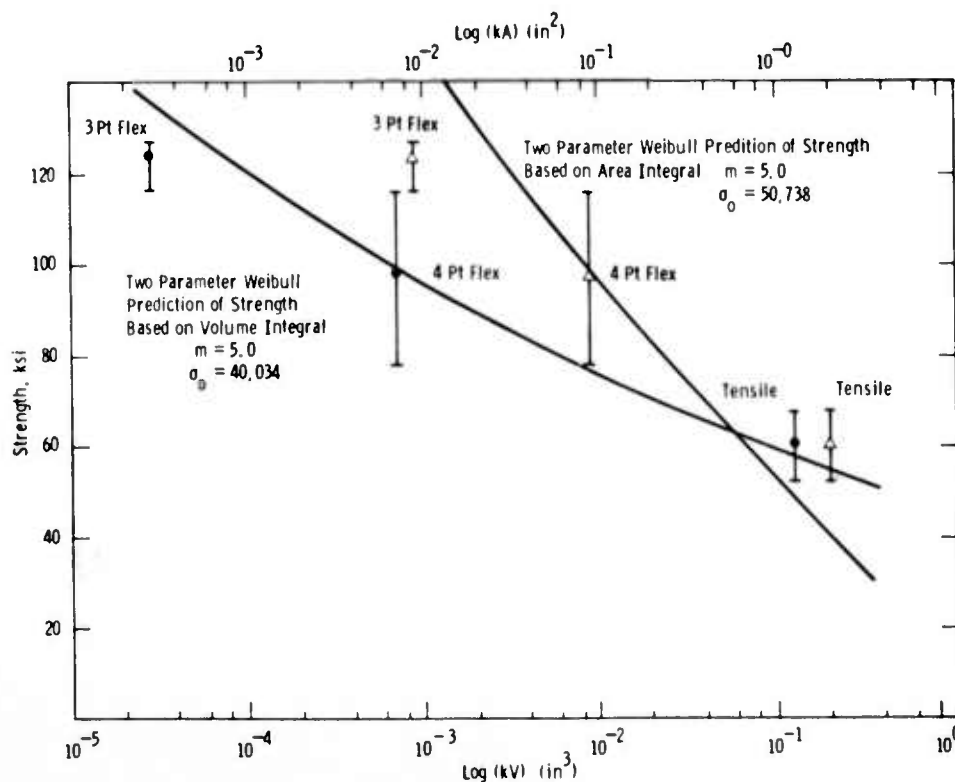


Figure 5.1 -- Room Temperature Strength of Hot Pressed  $\text{Si}_3\text{N}_4$  (HS-130) as a Function of Test Mode (Weibull Analysis Based on Area and Volume)

TABLE 5.1  
COMPARISON OF 2 AND 3 PARAMETER WEIBULL RESULTS

Weibull Basis	<u>m</u>	1800°F			2300°F				
		$\sigma_0$ (psi)	$\sigma_u$ (psi)	Predicted Strength(psi)	<u>m</u>	$\sigma_0$ (psi)	$\sigma_u$ (psi)	Predicted Strength (psi)	
Area	2 parameter	7.2	58,810	0	58,176	7.1	38,900	0	35,700
	3 parameter	4.5	28,100	41,580	69,374	2.8	9,583	33,100	41,200
Volume	2 parameter	7.2	50,950	0	80,303	7.1	26,400	0	35,800
	3 parameter	4.5	22,350	41,580	87,290	2.8	4,541	33,100	43,200
Mean measured stress									
4 pt. flex (psi)		105,100			54,600				
Tensile (psi)		42,500			32,400				

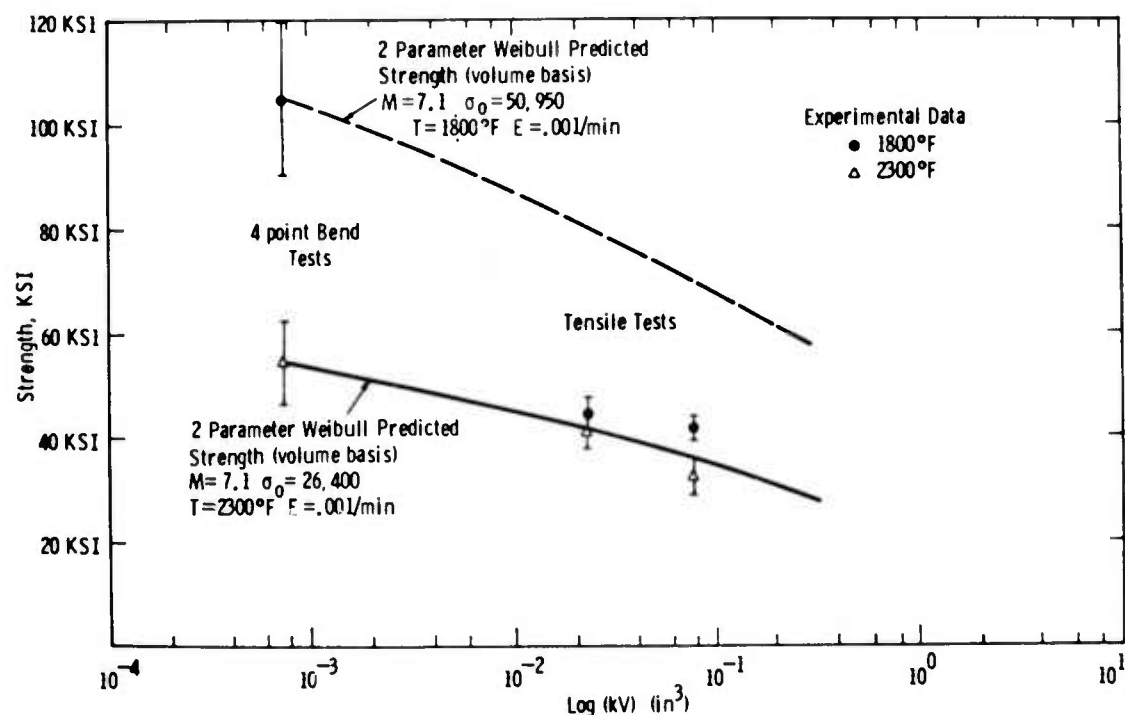


Figure 5.2 -- Two Parameter Weibull Volume Prediction of Failure Stress in  $\text{Si}_3\text{N}_4$  for Flexural and Tensile Test Modes

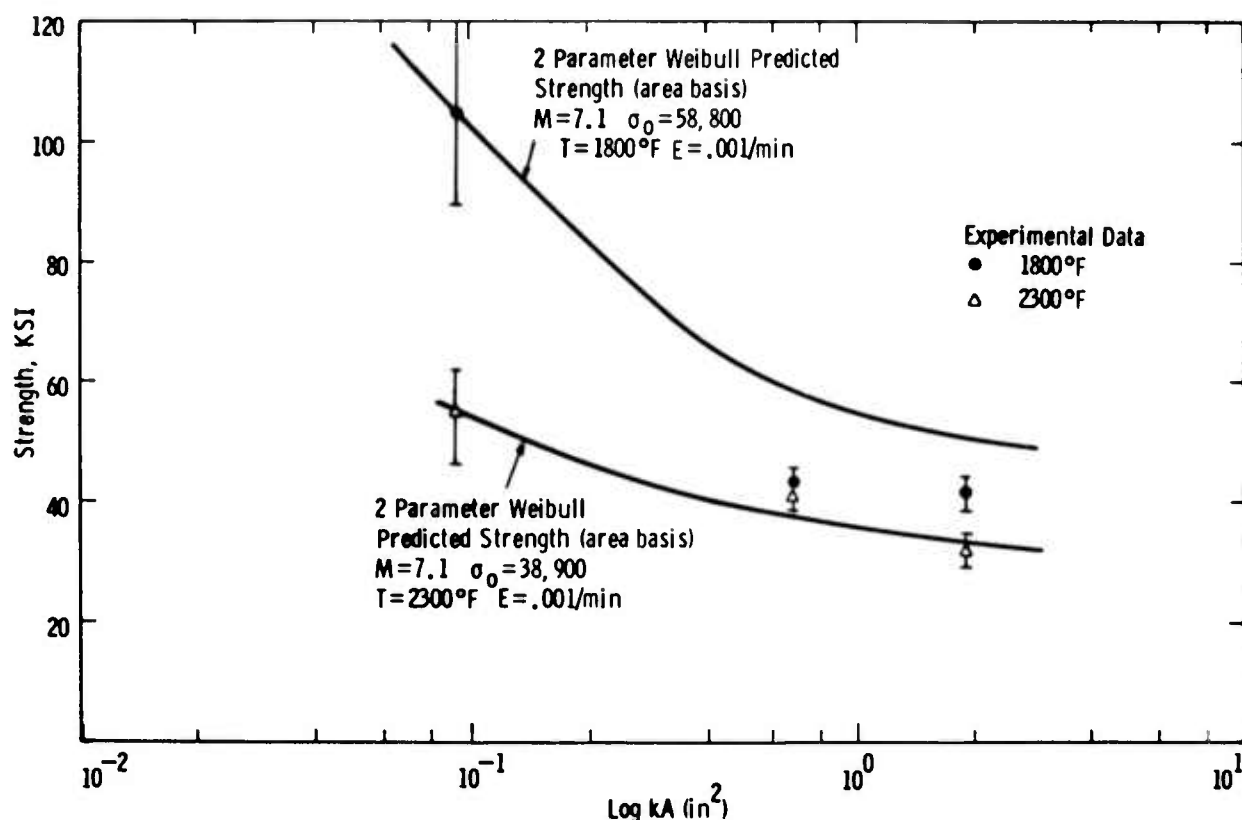


Figure 5.3 -- Two Parameter Weibull Area Prediction of Failure Stress in  $\text{Si}_3\text{N}_4$  at Elevated Temperature for Flexural and Tensile Test Modes

If the experimental values of strength for given volumes or areas under stress are known, it is possible to fit a curve to the data points by the reiterative adjustment of  $m$ . This was done in Fig. 5.4 to establish the relationship of flexural to tensile strength based on area at 1800°F. A final curve fitting Weibull modulus of 5.3 was used for this plot. There is danger in the use of this technique, however, because adjustment of the Weibull modulus, in effect, imposes an artificial standard deviation upon the statistical population. In the case cited, the standard deviation implied by  $m = 5.3$  is much higher than that established by the actual data.

Before the Weibull approach is accepted as a valid representation of tensile strength based on measured flexural strength measurements of silicon carbide or silicon nitride, it will be necessary to verify the analytical results with experimental data for specimens of specific size within the range  $10^0 - 10^{-4}$  KV or  $10^0 - 10^{-5}$  KA using both the tensile and flexural modes of testing. These tests are in progress.

#### Tensile Strength

The initial set of tensile tests to characterize Norton HS-130 hot pressed silicon nitride is complete. Ultimate strength was determined as a function of temperature with respect to atmosphere and strain rate for specimens of three different sizes (Fig. 5.5).<sup>(1,2)</sup> The strength vs

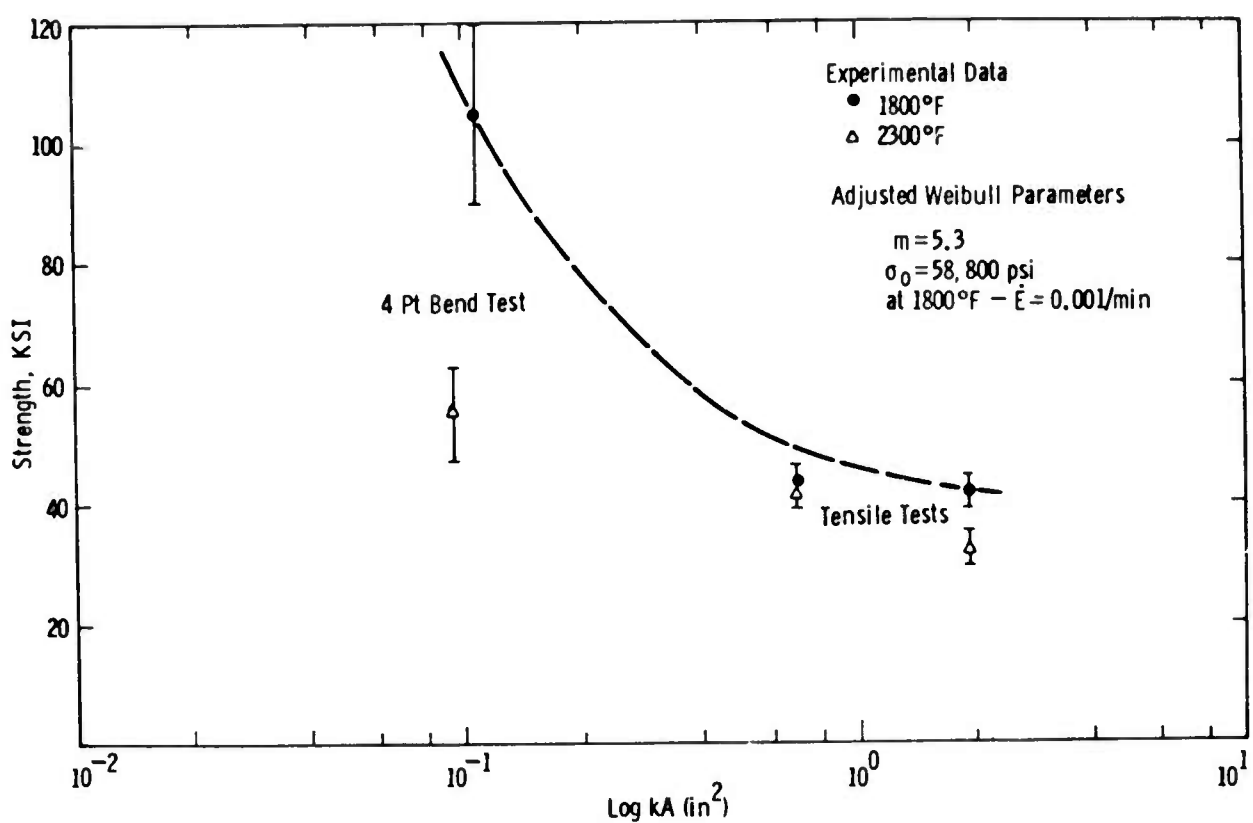


Figure 5.4 -- The Relationship Between Flexural Stress with Tensile Stress as Adjusted by 2-Parameter Weibull Statistics Based on Area

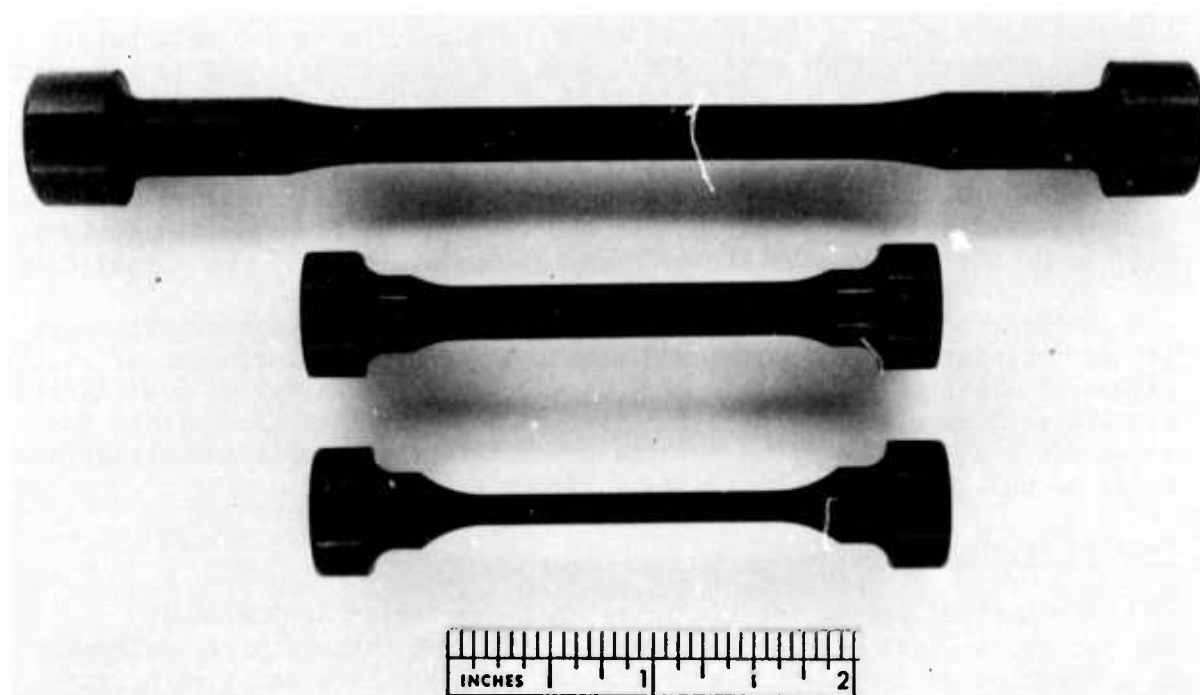


Figure 5.5 -- Tensile Test Specimens

temperature data presented in Fig. 5.6 and Table 5.2 fail to indicate any size effect or strain rate sensitivity. Furthermore, there is an apparent difference in either test technique or an effect of atmosphere as shown by comparing the Astronuclear Laboratory results with those obtained by Westinghouse R&D. It may be noted that specimens typically failed within the gauge length. However, in the Astronuclear tests failure was observed near the fillet radius on small diameter specimens as indicated in Fig. 5.7.

Southern Research Institute (SRI) reported the tensile properties of Norton HS-130 silicon nitride at room temperature and 2350°F for Ford. Specimens (Fig. 5.8) were cut from two 5 in. dia. x 1-5/8 in. thick billets according to the specified sectioning plan shown in Fig. 5.9. The test procedure employed gas bearings in the load train which eliminate unknown uniaxial loads. Strain was monitored optically at 2350°F.

The SRI procedure for specimen alignment was to use a precision ground alignment bar at loading conditions of 100 and 1400 lbs. The results of the alignment check appear in Fig. 5.10. A maximum bending stress of 875 psi was calculated and the difference in strain on opposite sides of the specimen did not exceed 40 microinches/in. Strain gauges located 180° apart were also used to verify alignment up to 20,000 psi within 4%.

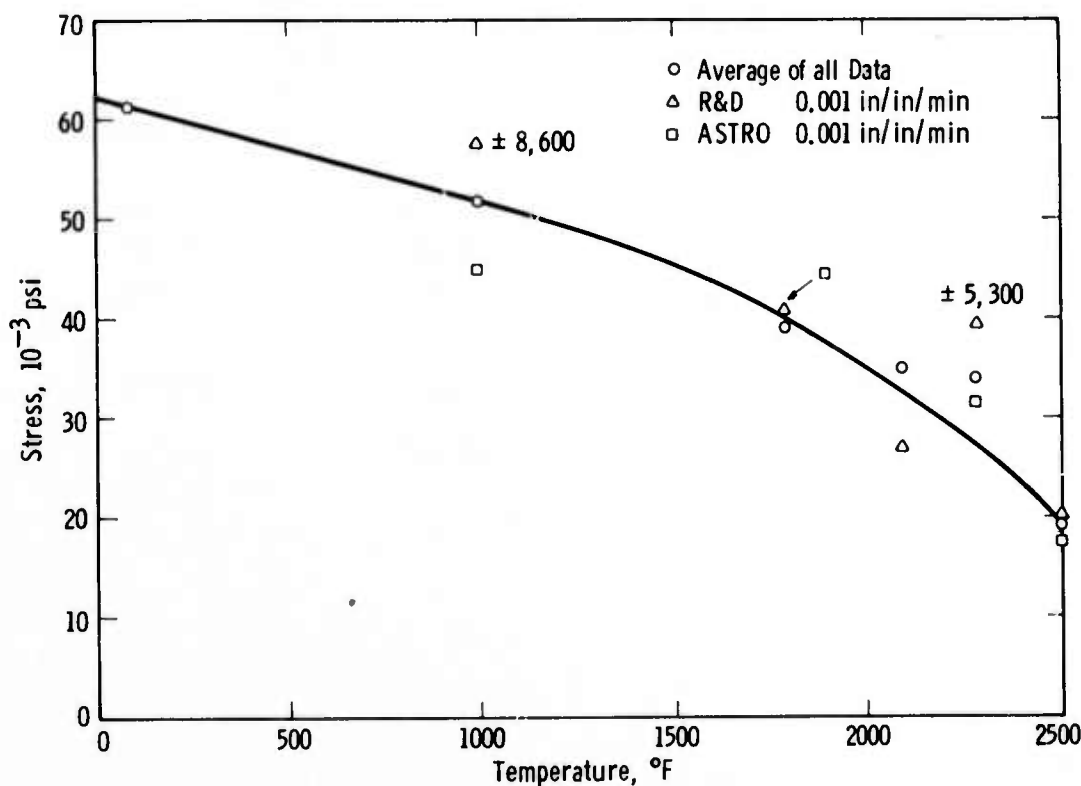


Figure 5.6 -- Tensile Strength of Norton HS-130 Silicon Nitride

TABLE 5.2  
TENSILE PROPERTIES OF NORTON HS-130 SILICON NITRIDE

Source	Strain Rate in/in/min	RT	Tensile Strength, psi				
			1000°F	1800°F	2100°F	2300°F	2500°F
R&D	0.001	59,650	72,050	36,550	31,450	36,250	13,450
		54,650	56,100	48,000	32,750	42,100	20,200
		69,800	64,300	42,250		45,400	20,000
			60,000	40,800		46,400	20,100
			36,850	36,850		30,250	25,250
						38,200	
		61,367	57,860	40,890	32,100	39,767	19,800
Astro	0.001		41,500	49,200	35,800	31,400	16,200
			42,600	48,800		33,400	17,400
			52,400	30,900		26,200	19,800
			43,200				
			44,925	42,967	35,800	30,333	17,800
R&D	0.0001		29,800	39,100		22,950	
			42,600	24,950			
				41,800			
				37,350			
				37,800			
			36,200	36,200		22,950	
Astro			41,000			25,500	
			48,600			26,600	
			44,800			27,550	
R&D	0.01		42,550			46,650	
Astro			49,000			35,700	
						42,900	
						39,300	

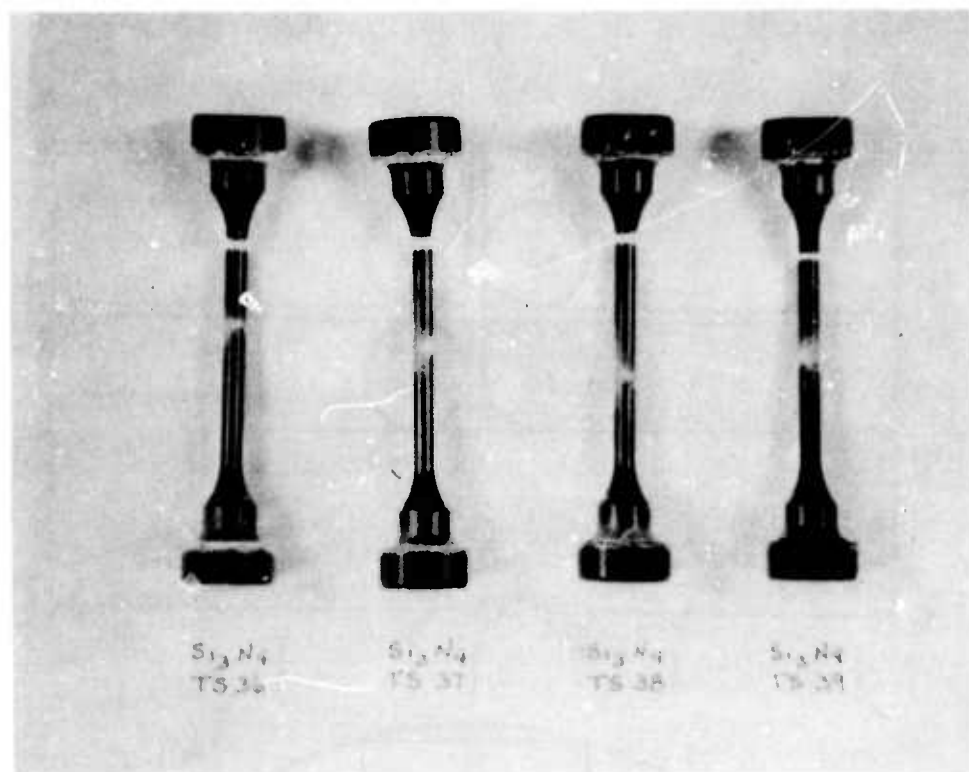
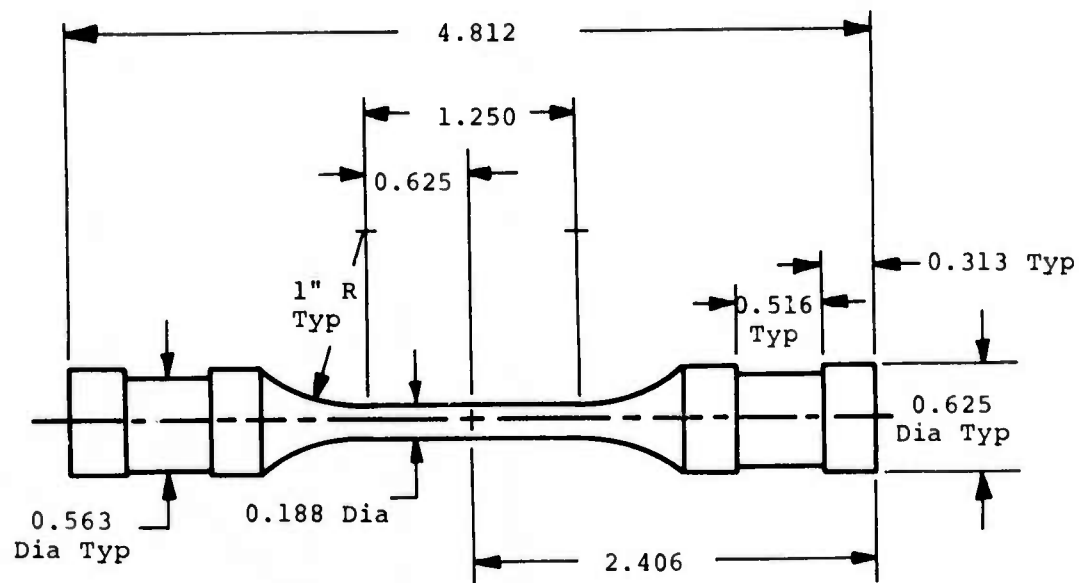


Figure 5.7 -- Failed Silicon Nitride Tensile Specimens



Notes:

1. All Diameters True and Concentric to 0.0005"
2. Both Ends Flat and Perpendicular to 0.0005"
3. Tolerance Unless Otherwise Noted:  
All Lengths  $\pm$  0.005  
All Diameters  $\pm$  0.001

Figure 5.8      Tensile Specimen Configuration

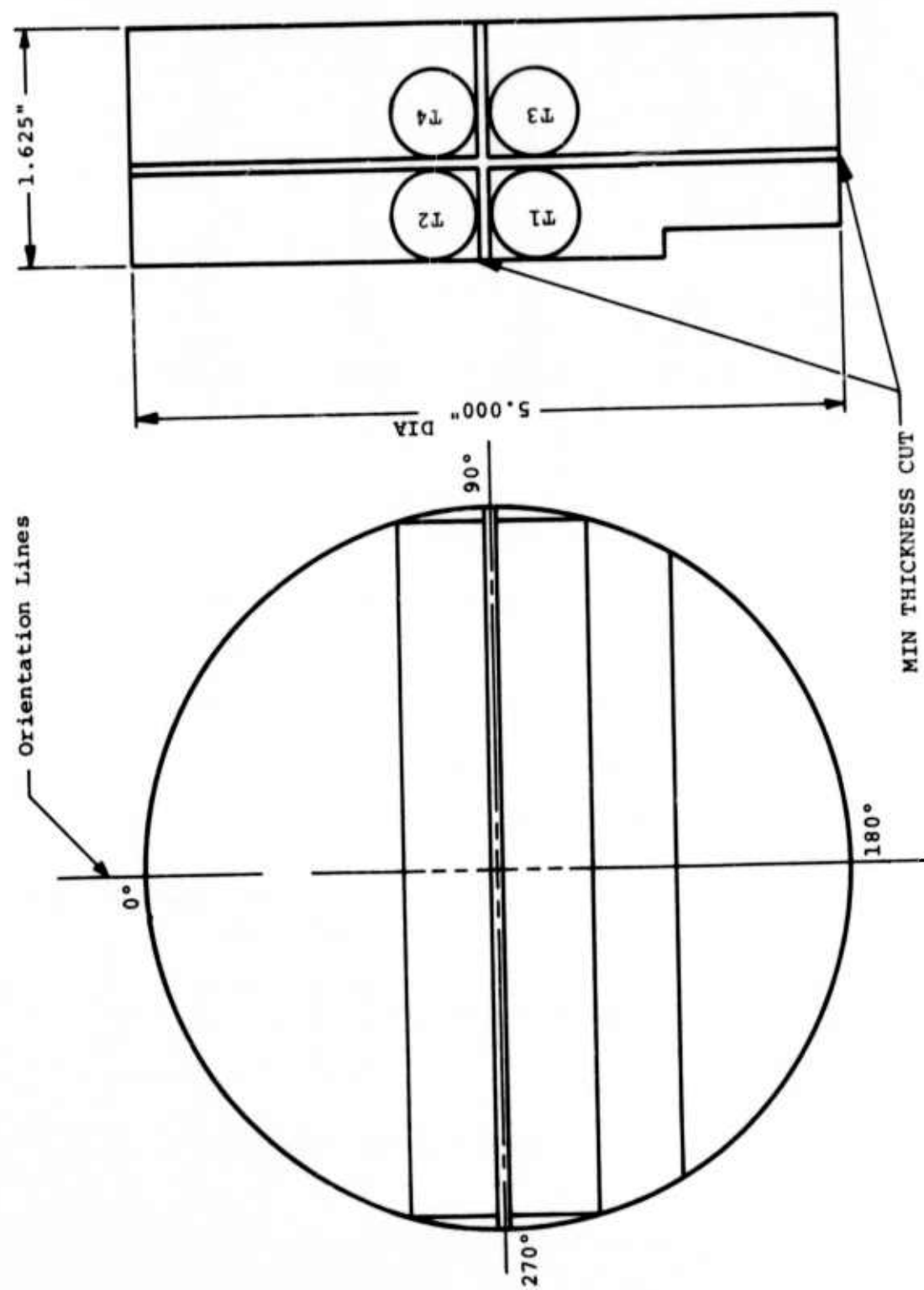


Figure 5.9 Cutting Plan for Hot Pressed  $\text{Si}_3\text{N}_4$  Billets

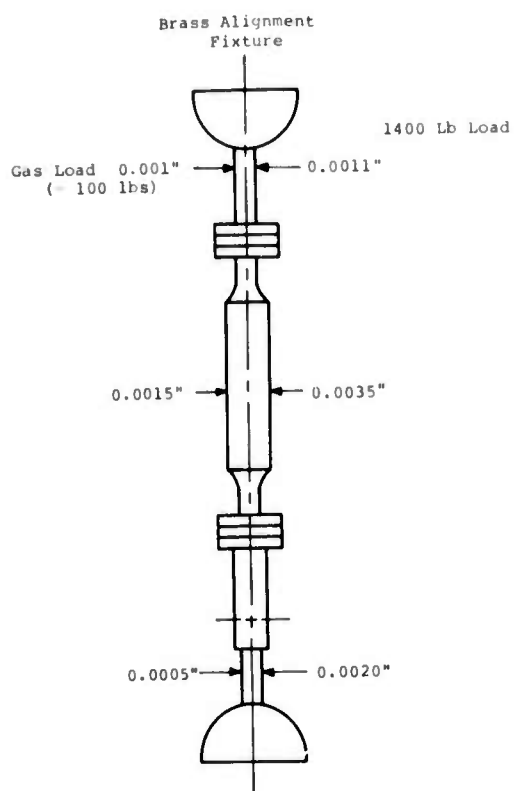


Figure 5.10 Results of the Load Train Alignment Check (TIR)

Stress-strain curves for the actual tensile tests appear in Fig. 5.11. The ultimate strength is plotted in Fig. 5.12. These data agree generally with the Westinghouse data (Fig. 5.6). The elastic modulus at room temperature and 2350°F, as shown in Fig. 5.13, is in excellent agreement with Westinghouse measurements at a strain rate of 0.001 in/in/min (Fig. 5.14) over a similar range of temperatures.

The tensile strength of Norton hot pressed silicon carbide at various temperatures is described in Fig. 5.15 and Table 5.3. These data were obtained from 2 different size specimens (the 1/4 in. dia. x 1-1/2 gauge length, and 1/4 in. dia. x 2-1/2 gauge length) at various strain rates between 0.1 and 0.001 in/in/min. No size effect or strain rate sensitivity can be detected. A single test point was determined in helium at 2300°F and found to be consistent with the results obtained in an air atmosphere. The specimens, for the most part, failed within the gauge length as shown in Fig. 5.16.

The modulus of elasticity of hot pressed SiC was also determined between room temperature and 2500°F at a strain rate of 0.001 in/in/min in air. These data are reported in Fig. 5.17. Although the elastic modulus of silicon carbide tends to drop at elevated temperature, the effect is less severe than that observed for silicon nitride.

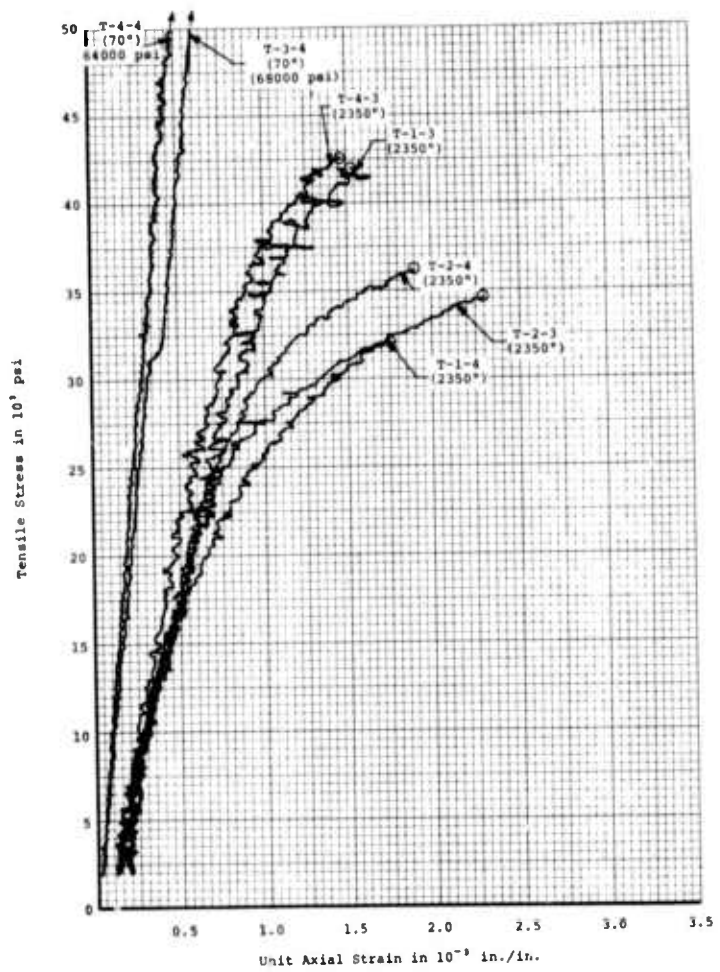
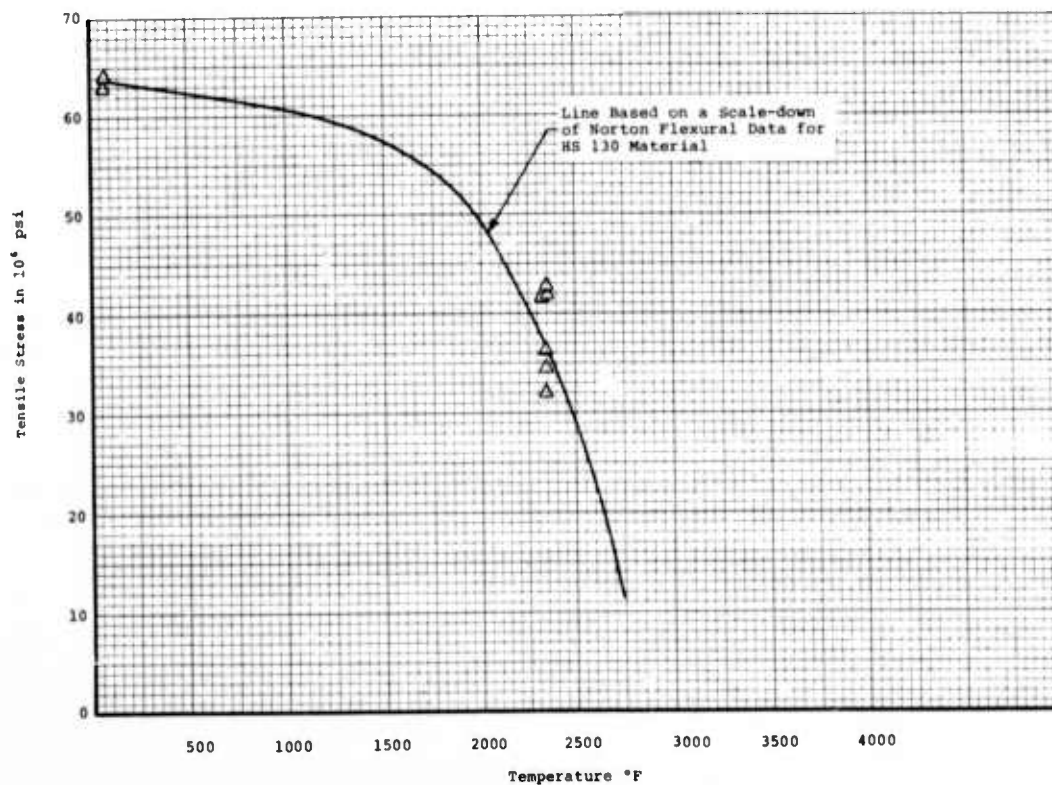


Figure 5.11 Tensile Stress versus Axial Strain for Axial Tensile Specimens of Norton HS 130 Silicon Nitride



148 Figure 5.12 Tensile Stress versus Temperature for Axial Tensile Specimens of Norton HS 130 Silicon Nitride

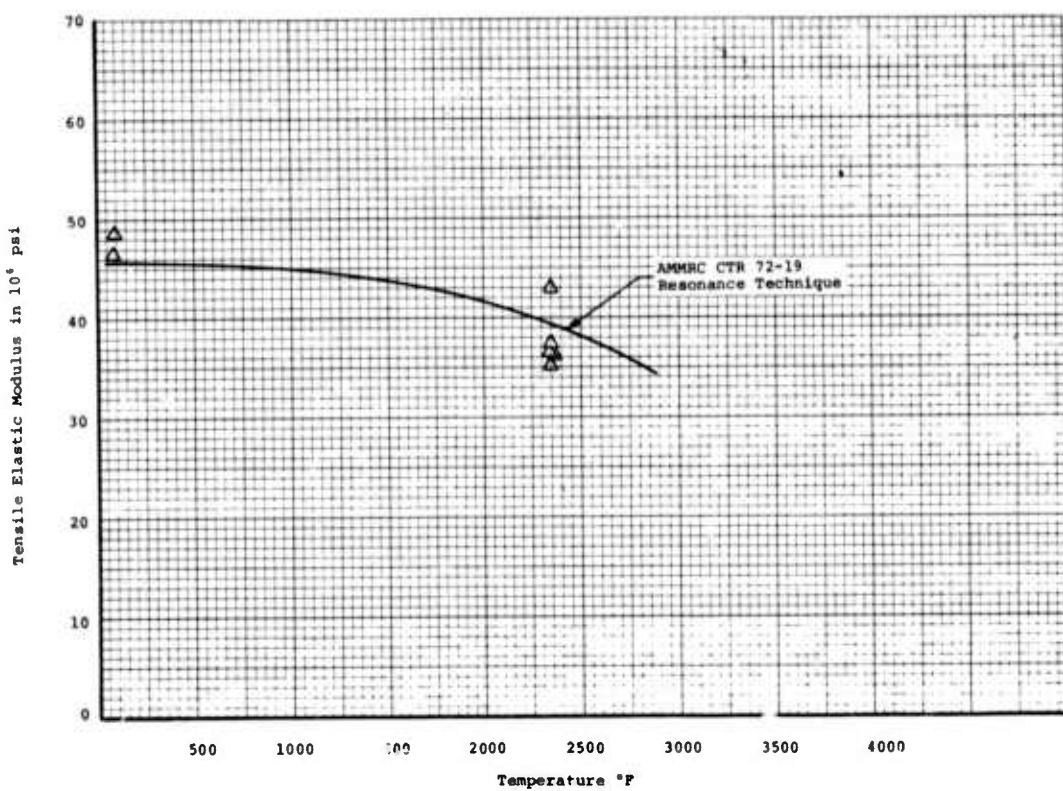


Figure 5.13 Tensile Elastic Modulus versus Temperature for Axial Tensile Specimens of Norton HS 130 Silicon Nitride

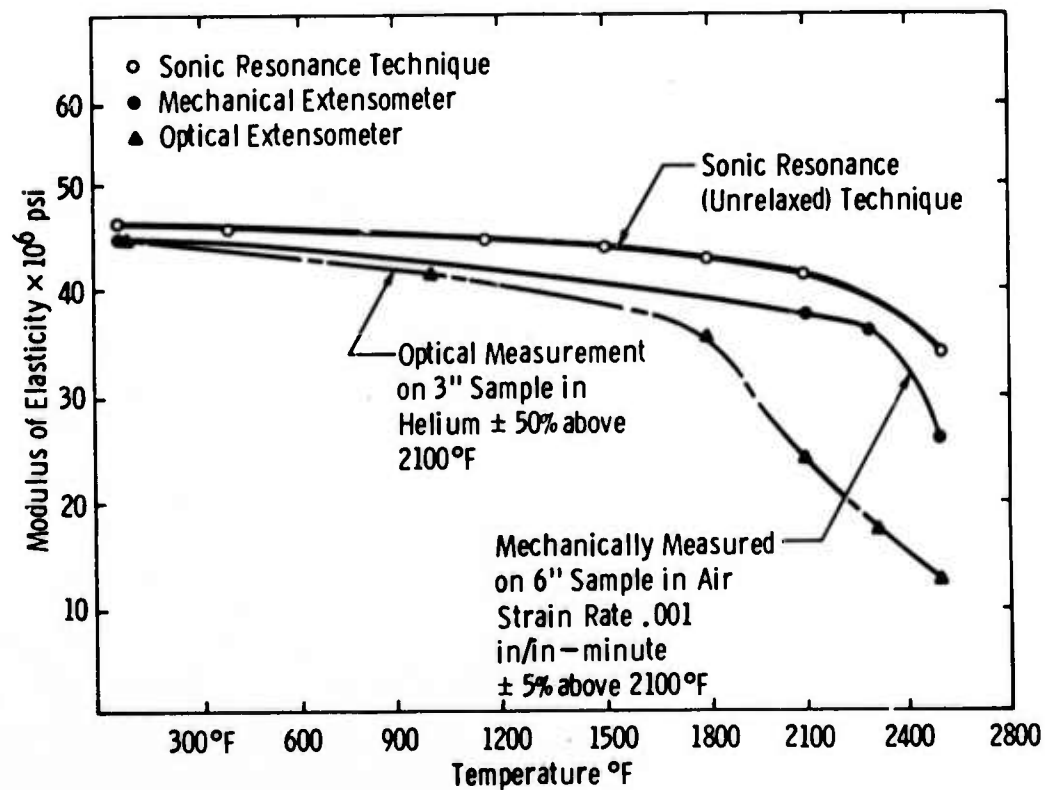


Figure 5.14 -- Effect of Temperature on the Elastic Modulus of Norton HS-130 Silicon Nitride

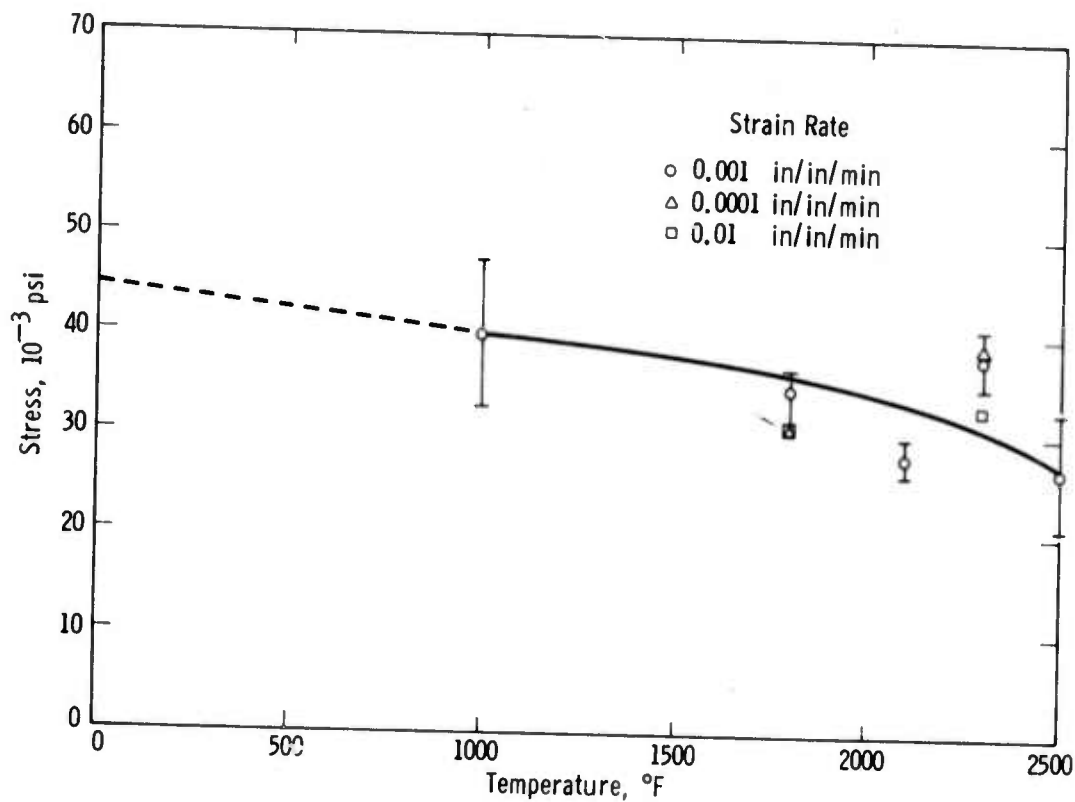


Figure 5.15 -- The Tensile Strength of Norton Hot Pressed Silicon Carbide

TABLE 5.3  
TENSILE PROPERTIES OF NORTON HOT PRESSED SILICON CARBIDE

Strain Rate in/in/min	Tensile Strength, psi				
	1000°F	1800°F	2100°F	2300°F	2500°F
.001	47,100	35,950	25,450	35,150	28,950
	43,000	31,750	30,400	52,700	33,150
	30,100	36,400	28,950	37,800	18,900
	$40,070 \pm 7,400$	$34,700 \pm 2,100$	$28,267 \pm 2,100$	$38,550 \pm 3,100$	$27,000 \pm 6,000$
0.0001				39,150	
		29,400		41,300	
		31,250		36,600	
			$30,325 \pm 1,000$	$39,017 \pm 1,900$	
0.01		30,900		30,100	
				32,650	
				38,300	
				$33,683 \pm 3,500$	

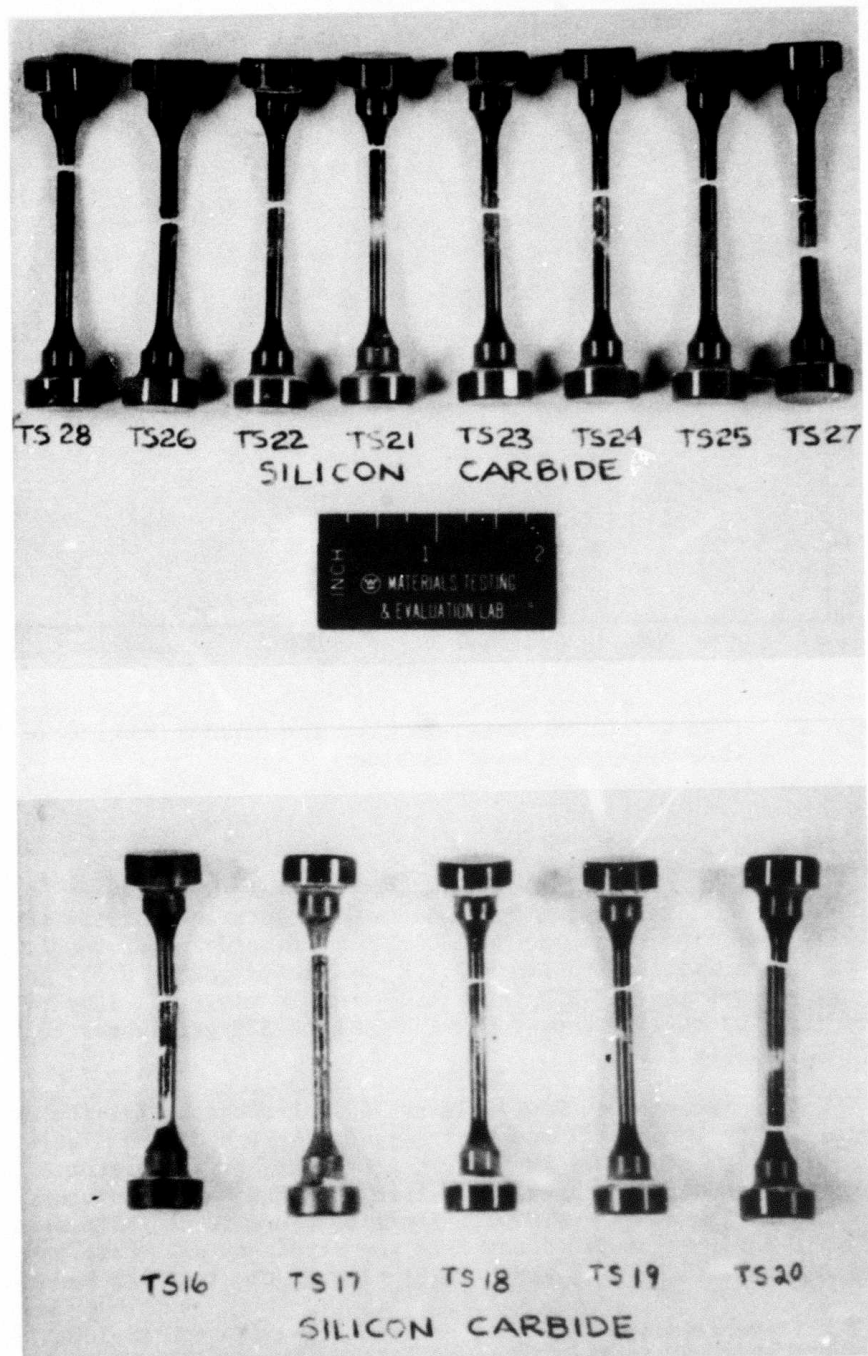


Figure 5.16 -- Failed Silicon Carbide Tensile Specimens

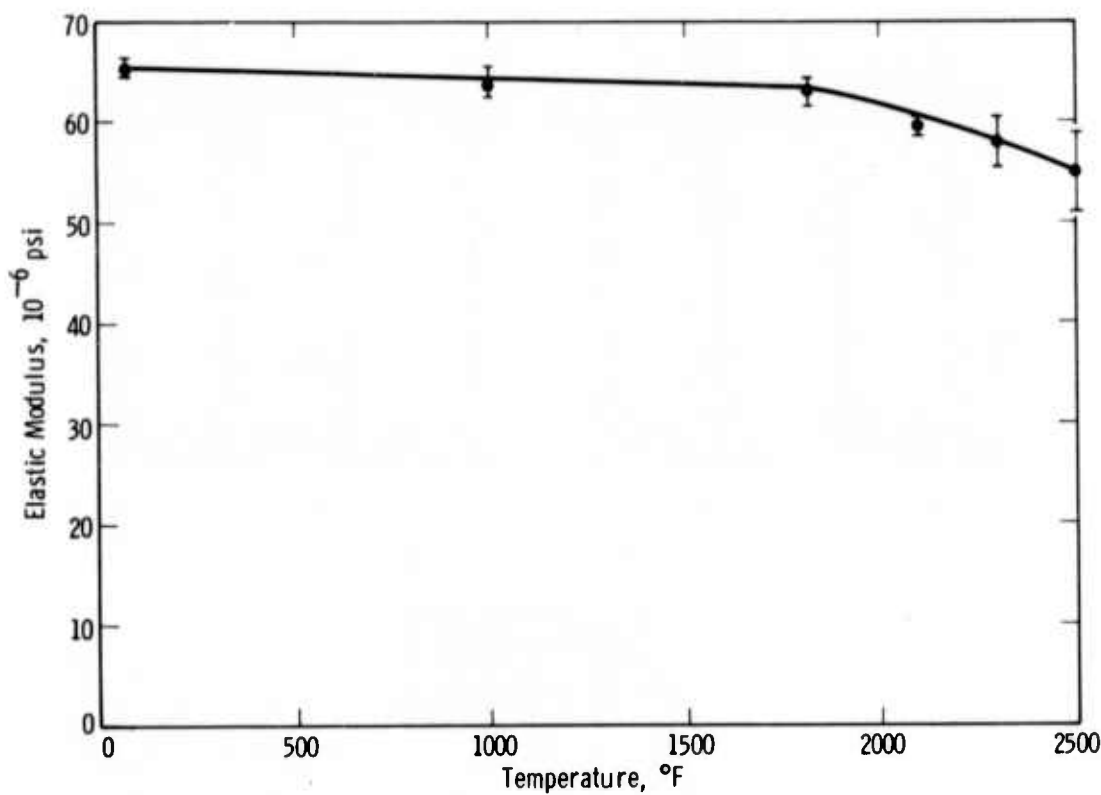


Figure 5.17 -- The Effect of Temperature on the Elastic Modulus of Norton Hot Pressed Silicon Carbide

#### Flexural Strength

Westinghouse is continuing to accumulate data to describe the flexural properties of Norton HS-130 silicon nitride under conditions of 4-point loading (outer span = 0.875 in., inner span = 0.375 in., using a specimen 0.125 in. x 0.250 in. x 1.25 in.) in air. All samples were ground parallel to length on four sides with a 320 grit wheel to insure a uniform surface finish.

The data reported in Fig. 5.18 and 5.19 are characteristic of the material in the strong (↓) and weak (||) directions, respectively. Strain rate sensitivity continues to persist at the higher temperatures although this effect tends to be somewhat obscure at certain temperatures. At the slower strain rates < 0.0001 in/in/min, there is definite evidence of plastic deformation as observed in the stress-strain curve and by actual deformation without crack initiation in the specimen before failure.

The flexural strength of hot pressed  $\text{Si}_3\text{N}_4$  (Norton HS-130) is compared with Ford reaction-sintered silicon nitride in Fig. 5.20. Reaction-sintered silicon nitride is much weaker than the hot pressed material at this stage of development. However, its strength, 17,500 psi, is retained to a temperature of 2550°F.

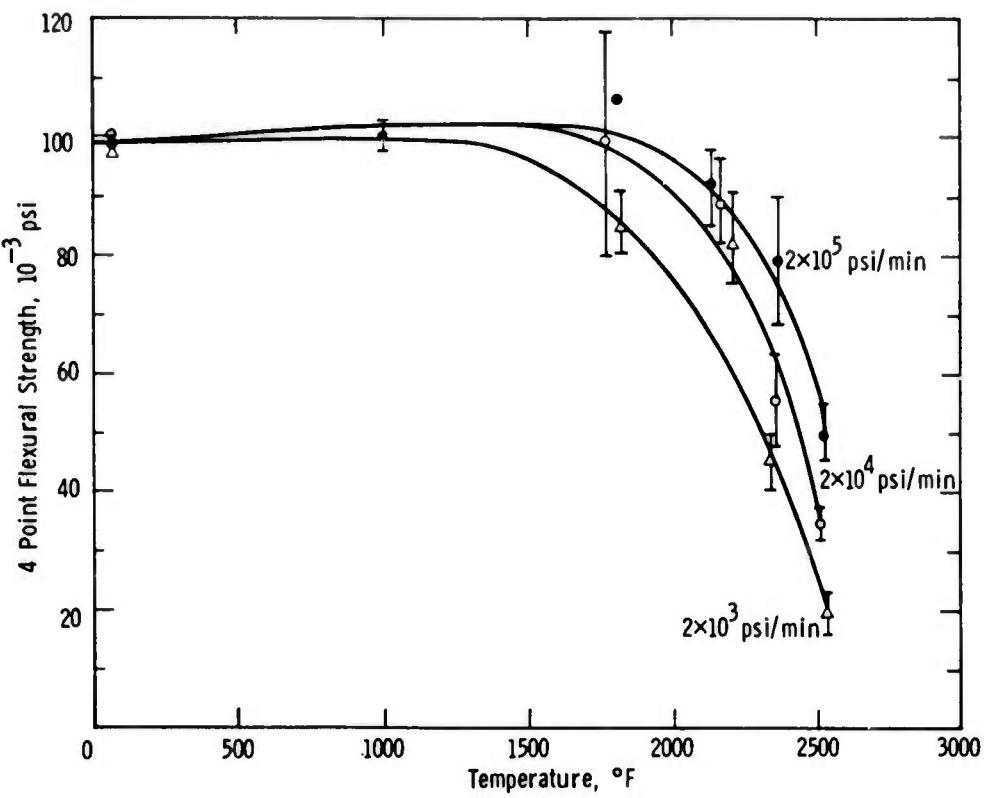


Figure 5.18 -- The Effect of Temperature and Strain Rate on the Flexural Strength of Norton HS-130 Silicon Nitride (Strong, Perpendicular to Hot Press, Direction)

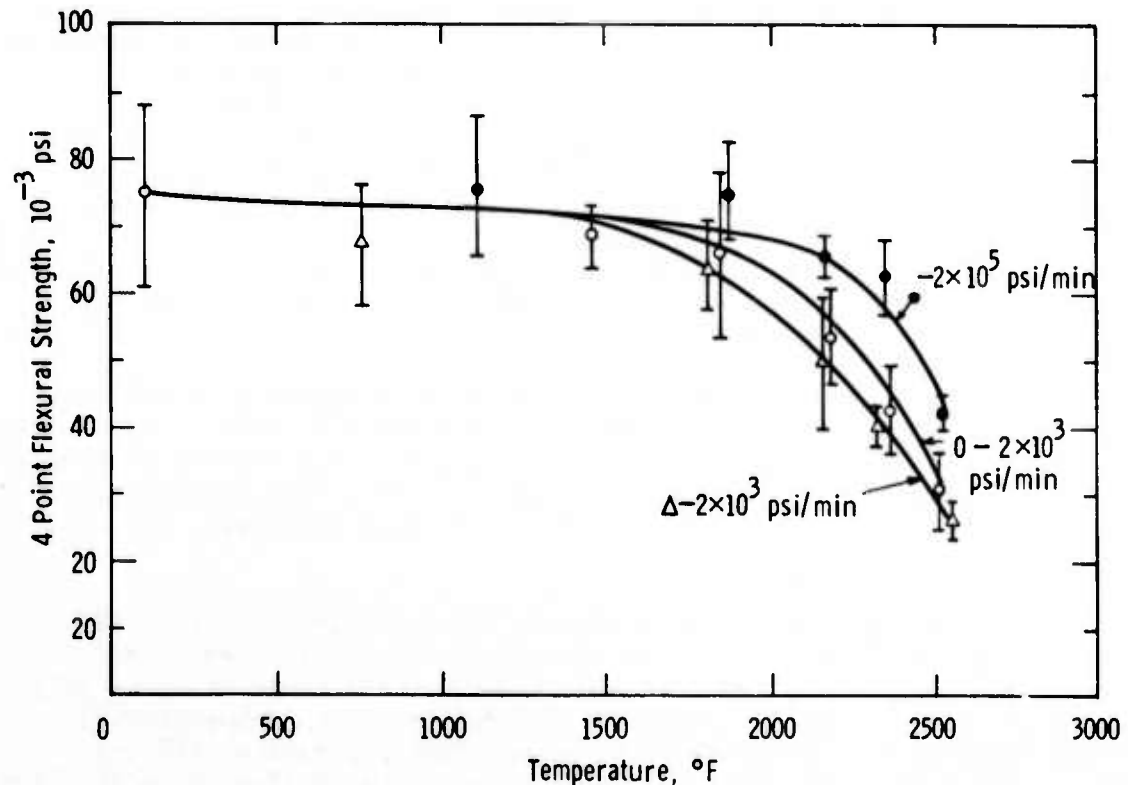


Figure 5.19 -- The Effect of Temperature and Strain Rate on the Flexural Strength of Norton HS-130 Silicon Nitride (Weak, Normal to Hot Pressing, Direction)

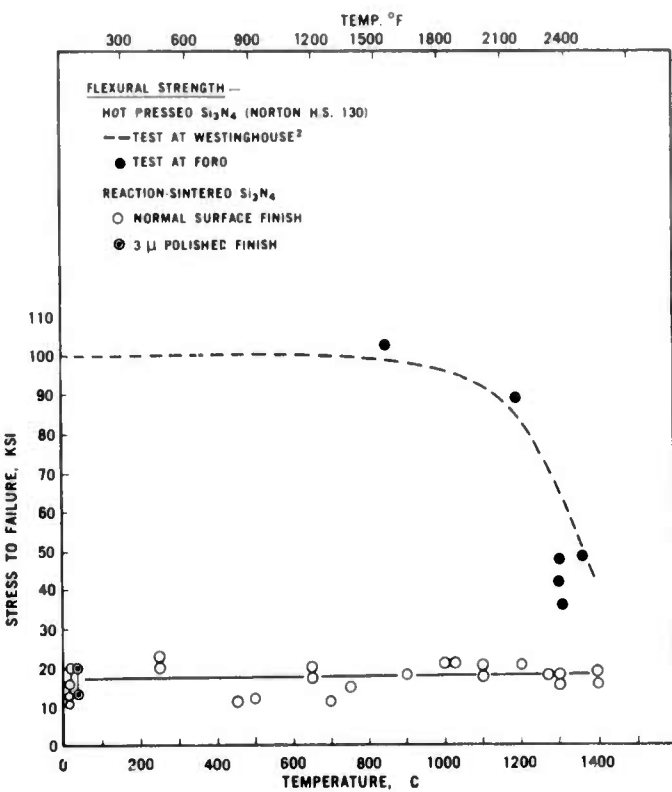


Figure 5.20 Flexural Strength versus Temperature of Hot-Pressed and Reaction-Sintered Silicon Nitrides

Edge effects appear to influence flexural strength of Norton hot-pressed silicon carbide in that approximately 90% of the fracture origins were observed on the edge of the specimen. The edges characteristically contained chips and large cracks apparently created during the machining operation. In order to establish the proper specimen preparation procedure, three different sets of specimens were prepared. Table 5.4 illustrates that the highest strengths and lowest standard deviations result when the edges of the specimens are beveled to minimize edge cracks. Because of this effect, the flexural strength of SiC was re-examined as a function of temperature. These current data are reported in Fig. 5.21. These results represent specimens that were cut both parallel and perpendicular to the hot-pressed direction. No significant effect of pressing direction was observed.

There is a trend toward strain rate sensitivity in silicon carbide as shown in Fig. 5.22. The slopes at 2290°F, 2370°F, 2550°F are 0.0454, 0.0566 and 0.0430, respectively. This indicates that silicon carbide is much less susceptible to sub-critical crack growth than silicon nitride, i.e., under stress both materials exhibit delayed fracture. However, silicon nitride will fail first.

Ford conducted additional flexural tests on Norton silicon carbide to compare the results with Refel reaction sintered silicon carbide. Four point bending was employed over a temperature range of RT to 2550°F using specimens 0.125 in. x 0.250 in. x 0.8 in. This comparison is illustrated in Fig. 5.23 where the dashed line represents previous Westinghouse data.<sup>(1)</sup> As may also be seen in Fig. 5.23, surface finish apparently affects the strength of Refel reaction sintered silicon carbide. The strength values of specimens with ground surfaces agree closely with the strength of the hot pressed material. The Refel, in an as-received condition, is significantly weaker.

TABLE 5.4  
EFFECT OF SURFACE PREPARATION ON FLEXURAL STRENGTH  
OF HOT-PRESSED SiC

<u>Specimen Preparation</u>	<u>Strength (psi)</u>	<u>Average Strength (psi)</u>
Diamond cut, 3 surfaces finished with 220 grit diamond wheel	75,100 71,800 95,600 50,500 71,900	73,000 ± 22%
As above, plus refinished with 320 grit diamond wheel	85,500 99,100 109,000 92,100 71,500	91,400 ± 15%
As above, plus two edges beveled	98,200 97,700 96,100 107,300 83,500	96,600 ± 9%

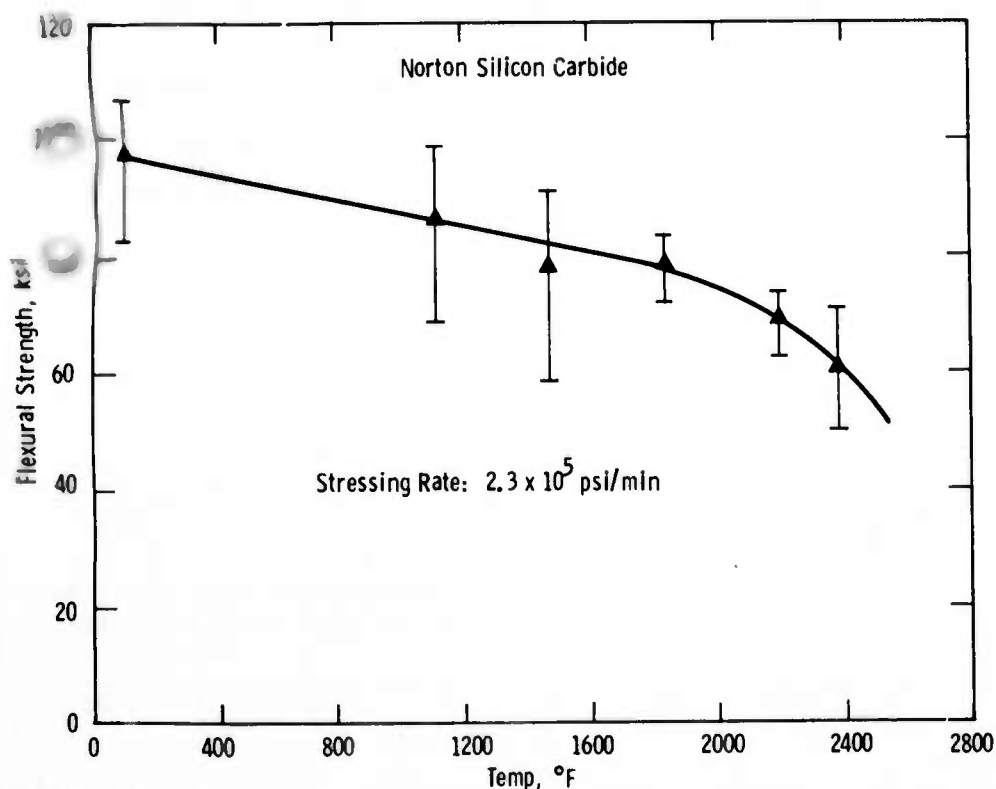


Figure 5.21 -- The Effect of Temperature on the Flexural Strength of Norton Hot Pressed Silicon Carbide

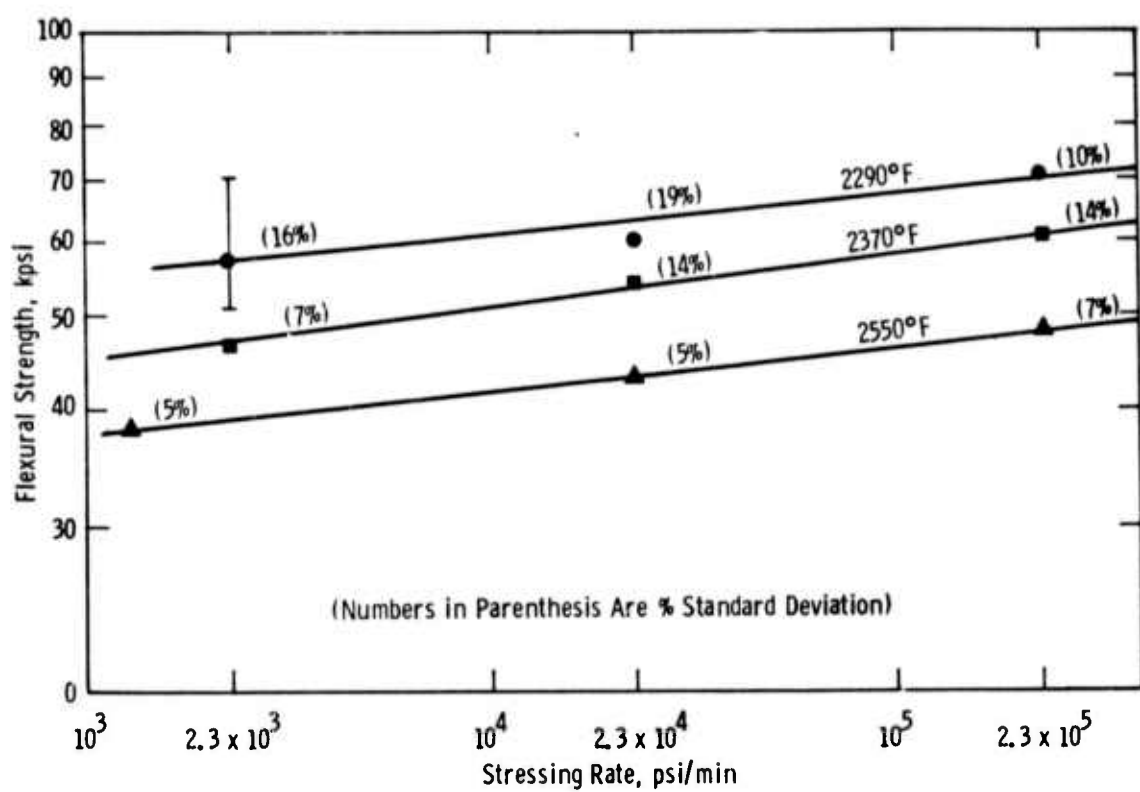


Figure 5.22 -- The Effect of Stress Rate on the Flexural Strength of Norton Hot Pressed Silicon Carbide

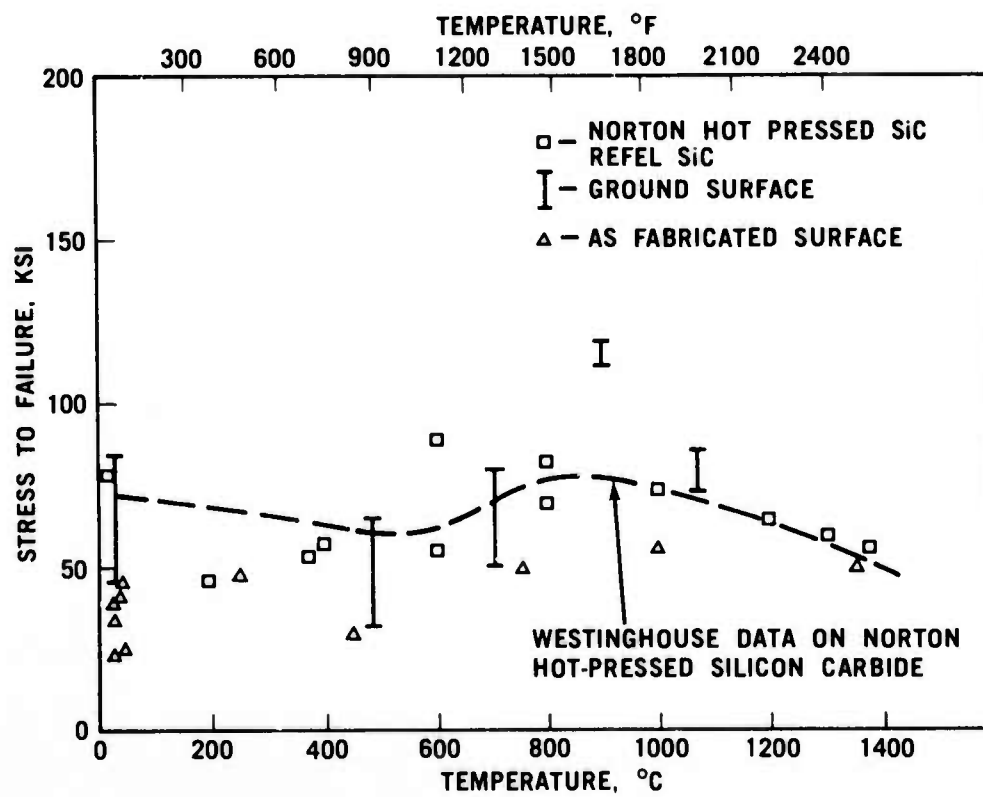


Figure 5.23 Flexural Strength versus Temperature of Hot-Pressed and Refil Silicon Carbides

### Compressive Strength

Preliminary compression data for Norton hot pressed silicon carbide and Norton HS-130 silicon nitride, as measured by Ford, appear in Fig. 5.24. The room temperature values for silicon nitride are significantly lower than the 450,000 psi stress reported by Westinghouse on a specimen that did not fail.<sup>(1)</sup> There is no reference with which to compare the silicon carbide results at this time.

The compressive strength of reaction sintered  $\text{Si}_3\text{N}_4$  drops from 95,000 psi to 57,000 psi with temperatures from RT to 2550°F. These data also appear in Fig. 5.24.

### Thermal Property Testing

The thermal properties of Norton hot pressed silicon carbide, i.e., conductivity, diffusivity expansion and specific heat, were measured by the Battelle Memorial Institute. Although the test methods were identical to those previously reported for silicon nitrides,<sup>(2)</sup> a brief description of these methods are provided for convenience.

Thermal expansion is measured directly by tracking the relative displacement of fiducial marks on the silicon nitride specimens with telemicroscopes fitted with filar eye pieces. The apparatus is illustrated schematically in Fig. 5.25. Suitably marked specimens are supported within a tube furnace which is enclosed in an insulated vacuum/atmosphere chamber. Dilation on heating or cooling is tracked manually with the microscopes. Specimen temperature is measured by either a thermocouple or an optical pyrometer. Dilations of the order of  $7 \times 10^{-6}$  inches can be measured on specimens nominally 2-3/4 inches in length.

Thermal conductivity is measured by a flash thermal diffusivity method. The diffusivity is determined by the transient behavior of a specimen subjected to a short-time thermal pulse on one of its sides. The apparatus appears in Fig. 5.26. A thin disc-shaped specimen is placed in the isothermal zone of a furnace and irradiated on the front face by a short-duration laser pulse. As the heat pulse travels through the specimen, its back-face temperature rise is recorded as a function of time. The temperature-time history can be related directly to the thermal diffusivity of the specimen according to the equation

$$d = \frac{0.139L^2}{t_{1/2}}$$

where  $d$  = thermal diffusivity

$L$  = specimen thickness

$t_{1/2}$  = time required for back face temperature to reach 1/2 its maximum temperature rise.

Thermal conductivity is derived as the product of thermal diffusivity, density, and specific heat.

Specific heat values were determined from enthalpy data obtained in a Bunsen ice calorimeter. The apparatus is shown in Fig. 5.27.

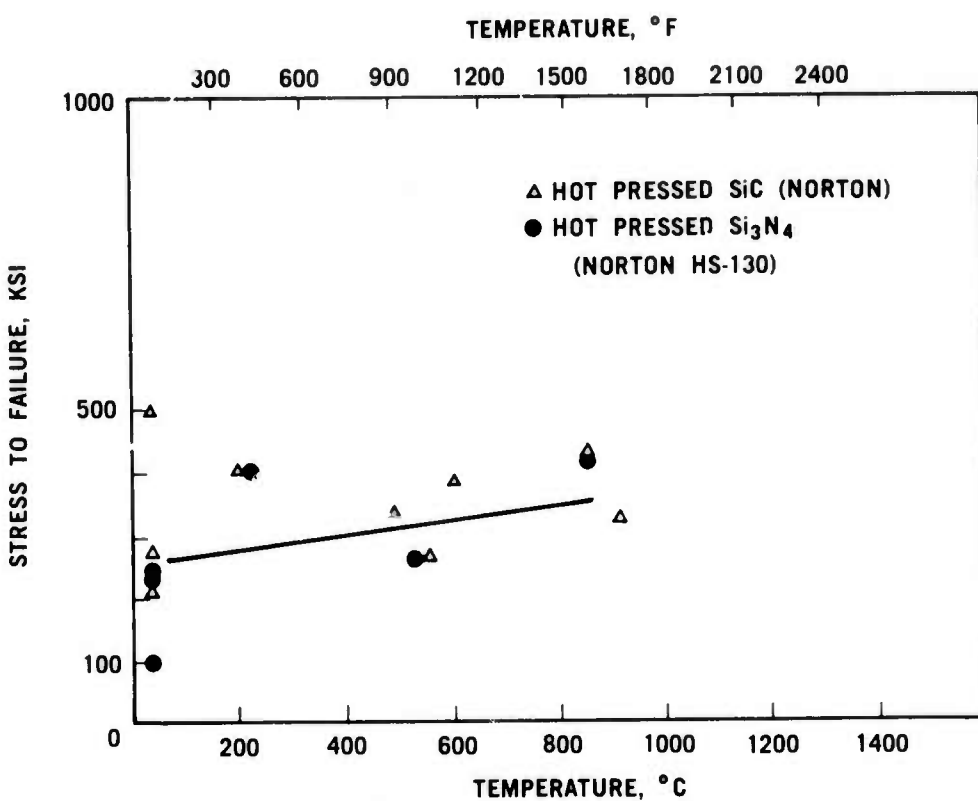


Figure 5.24 Compressive Strength versus Temperature of Hot-Pressed Silicon Carbide and Silicon Nitride

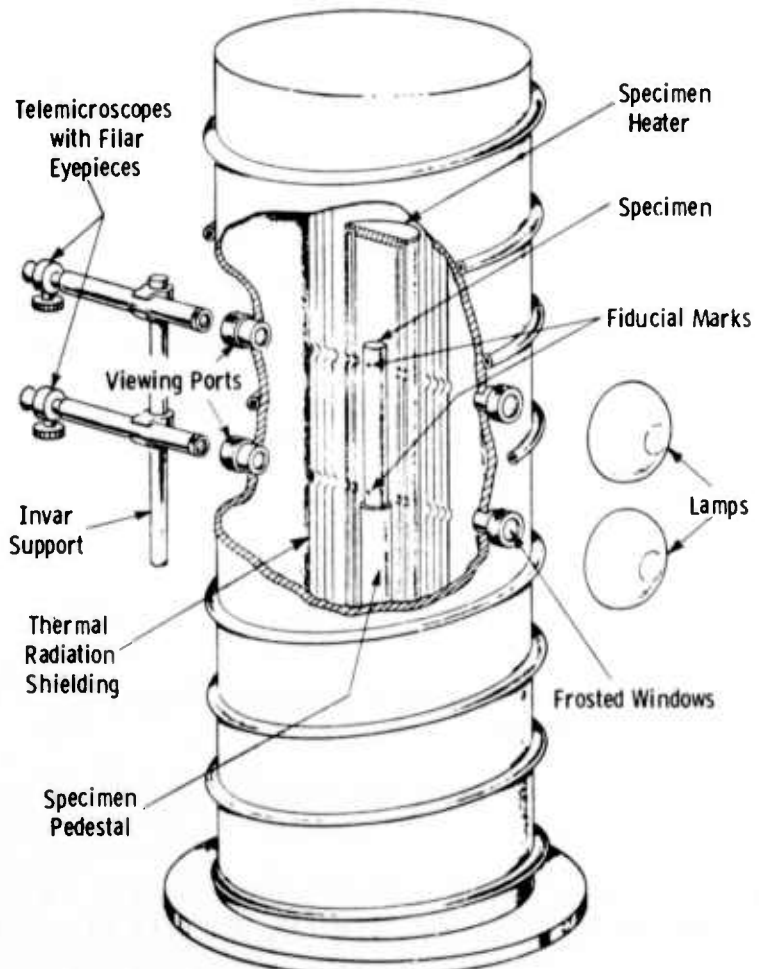


Figure 5.25 -- Battelle High Temperature Dilatometer for Direct View Expansion Measurements

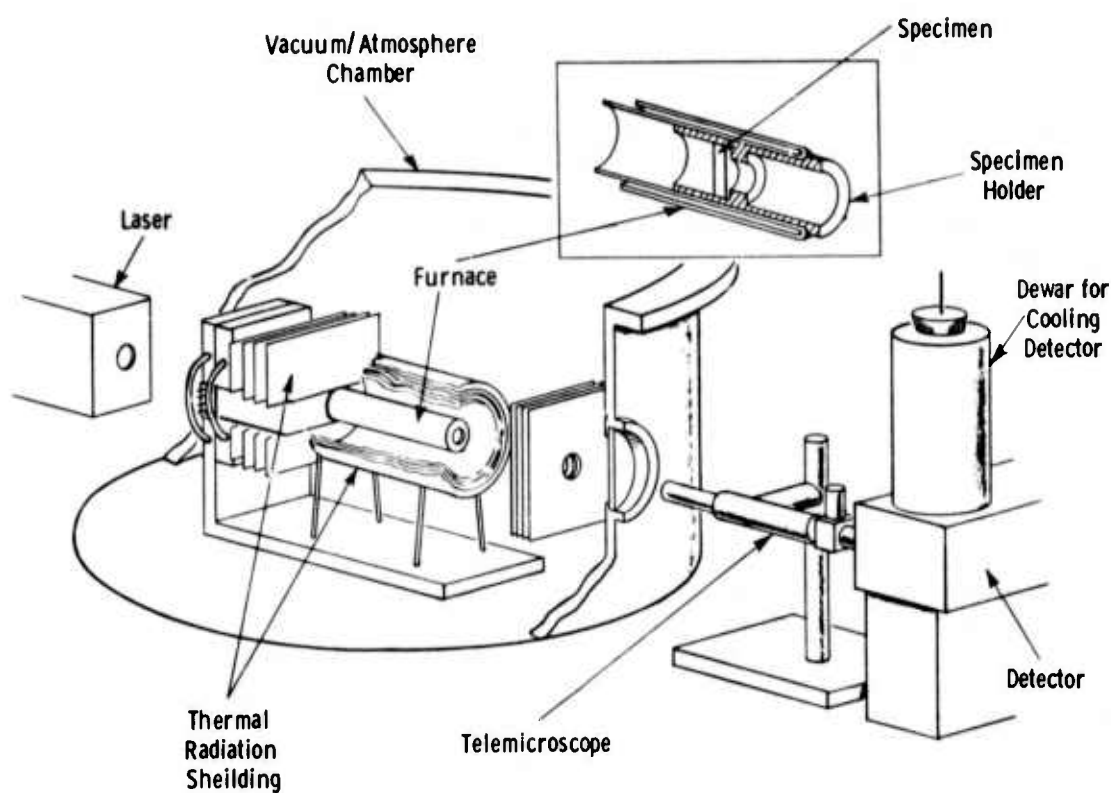


Figure 5.26 -- Battelle Thermal Diffusivity Apparatus

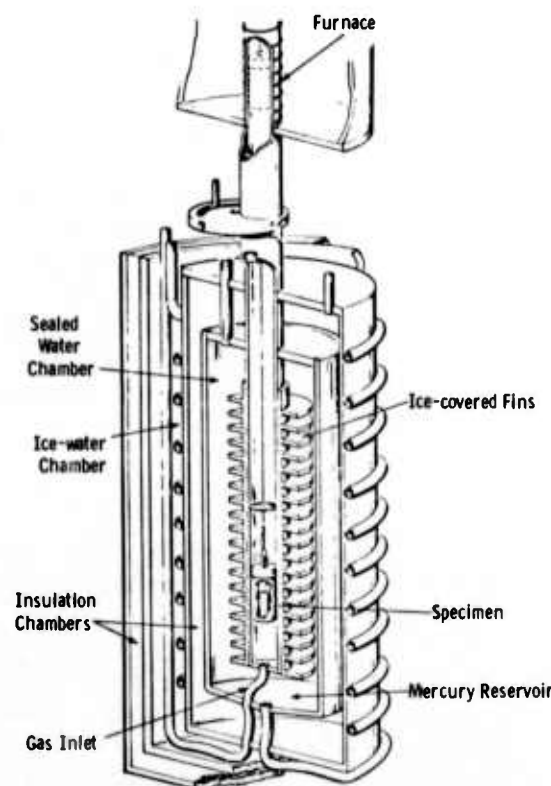


Figure 5.27 -- Battelle Ice Calorimeter

In the Bunsen ice calorimeter, heat given up by the specimen melts ice which is in equilibrium with outgassed distilled water in the closed calorimeter well. Mercury enters the systems from an external weight accounting source to make up the change in volume. The weight of the mercury making up the volume change is directly proportional to specimen enthalpy or heat liberated by the specimen when cooling from an elevated temperature to the ice point. Specific heat is then calculated by the relation

$$C_p = \frac{dH}{dT}$$

where  $C_p$  = specific heat at elevated temperature  
 $H$  = enthalpy  
 $T$  = temperature

The silicon carbide sample was encapsulated in tantalum and heated in a furnace above the calorimeter well. The sample was dropped into the well and allowed to cool. Separate drops of an empty capsule of the same material and surface emittance conditions as the specimen capsule determined the contribution of heat of the specimen by difference. The process was repeated through the temperature range of interest to establish an enthalpy versus temperature curve which was used in conjunction with the specific heat equation to obtain the specific heat.

Specific heat values for hot pressed silicon carbide are given in Fig. 5.28 and Table 5.5 for a nominal uncertainty of  $\pm 2\%$ .

Thermal expansion was measured parallel and perpendicular to the hot press direction on 16 specimens (Table 5.6). The results are plotted in Fig. 5.29 for the parallel and normal directions. Comparison of these indicates that the material is essentially isotropic with respect to thermal expansion within a possible experimental error of  $\pm 2\%$ .

The thermal diffusivity data from room temperature to 2600°F appear in Fig. 5.30 and Table 5.7, again, for the two directions of hot pressed silicon carbide. These results were used to calculate thermal conductivity over the same temperature range. The typical thermal conductivity data is shown in Fig. 5.31 and Table 5.8. A scatter of  $\pm 5\%$  in the diffusivity data is reflected in the  $\pm 7\%$  scatter observed in the thermal conductivity calculations. The isotropic nature of the material was confirmed by these experiments.

#### Creep Testing of Si<sub>3</sub>N<sub>4</sub>

Nine creep tests have been conducted in air. Two significant variations from previously established creep data were prominent: (a) creep rates in air are higher than in helium for a given condition of stress and temperature and (b) total creep strain in air is also higher than in helium. The total effect on stress rupture time cannot fully be established due to insufficient data. It seems, however, from the preliminary results that at 2300°F (1260°C) stress rupture time of over 1000 hrs, but less than 2000 hrs, can be obtained at stresses of 5000 psi. At 2100°F (1150°C) stress rupture time of over 5000 hrs has been estimated for tests at a stress of 15,000 psi.

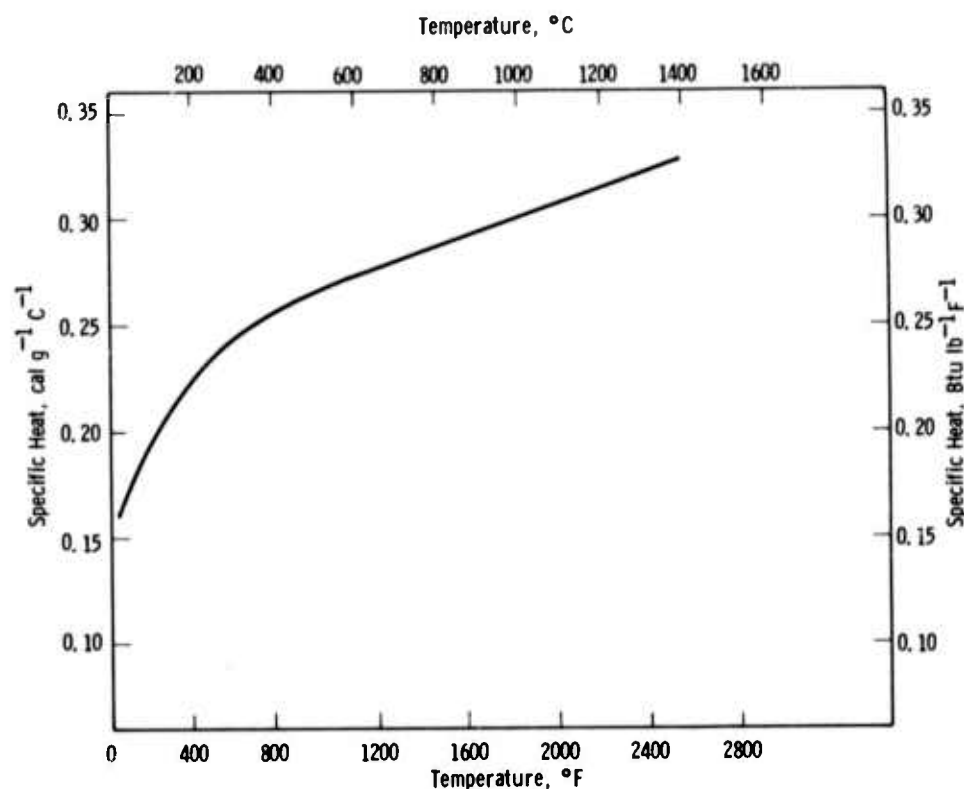


Figure 5.28 -- Specific Heat of Norton Hot Pressed Silicon Carbide

TABLE 5.5  
SPECIFIC HEAT OF HOT PRESSED SILICON CARBIDE

Temperature,		Specific Heat	
$^{\circ}\text{F}$	$^{\circ}\text{C}$	$\text{Cal g}^{-1} \text{C}^{-1}$	$\text{Btu lb}^{-1} \text{F}^{-1}$
77	25	0.162	0.162
212	100	0.195	0.195
392	200	0.224	0.224
572	300	0.243	0.243
752	400	0.256	0.256
932	500	0.265	0.265
1112	600	0.273	0.273
1292	700	0.280	0.280
1472	800	0.287	0.287
1652	900	0.294	0.294
1832	1000	0.301	0.301
2012	1100	0.308	0.308
2192	1200	0.315	0.315
2372	1300	0.322	0.322
2552	1400	0.328	0.328

Table 5.6  
THERMAL EXPANSION OF SILICON CARBIDE

<u>Temperature</u>		Parallel to Hot Pressing Expansion, Percent	
<u>C</u>	<u>F</u>	<u>Sample No. 3</u>	<u>Sample No. 4</u>
25	77	0.000	0.000
319	606	0.069	0.071
647	1197	0.217	0.219
965	1769	0.391	0.391
1091	1996	0.461	0.463
1193	2179	0.530	0.533
1303	2377	0.579	0.590
1370	2498	0.613	0.624
1249	2280	0.547	0.556
1155	2111	0.495	0.500
1049	1920	0.428	0.433
832	1530	0.303	0.309
501	934	0.150	0.152
122	252	0.001	0.004

<u>Temperature</u>		Perpendicular to Hot Pressing Expansion, Percent	
<u>C</u>	<u>F</u>	<u>Sample No. 1</u>	<u>Sample No. 2</u>
25	77	0.000	0.000
300	572	0.075	0.069
644	1191	0.226	0.215
979	1794	0.426	0.434
1095	2003	0.487	0.503
1203	2197	0.567	0.575
1311	2392	0.632	0.645
1375	2507	0.667	0.680
1247	2277	0.588	0.602
1153	2107	0.523	0.534
1043	1909	0.463	0.466
828	1522	0.306	0.311
497	927	0.152	0.169
145	293	0.020	0.033

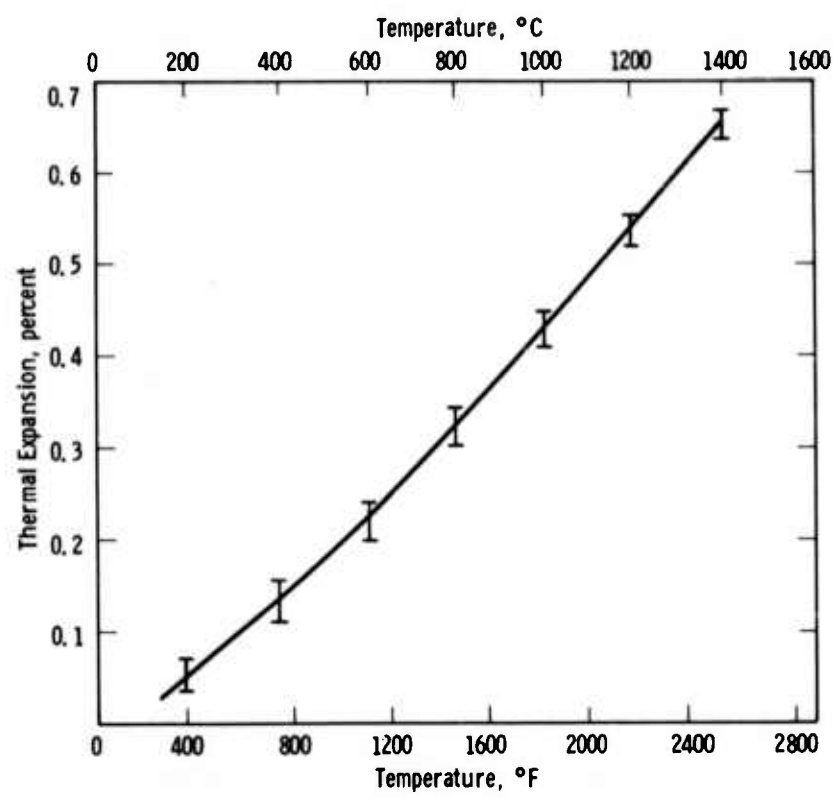


Figure 5.29 -- Thermal Expansion of Norton Hot Pressed Silicon Carbide

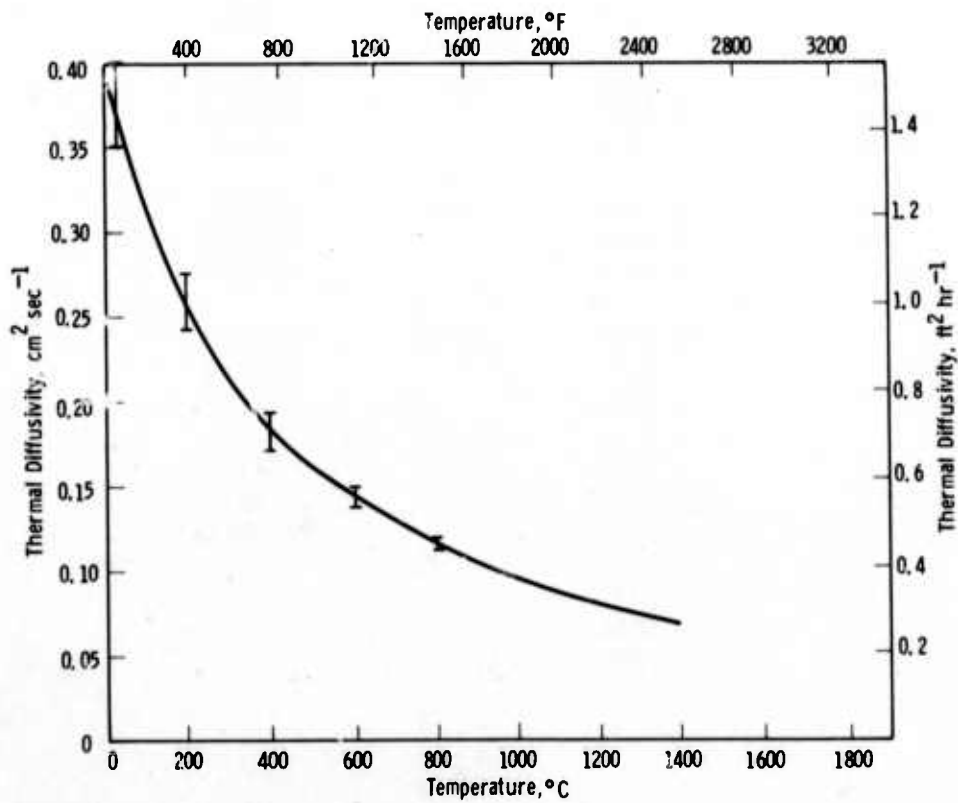


Figure 5.30 -- Thermal Diffusivity of Norton Hot Pressed Silicon Carbide

Table 5.7  
THERMAL DIFFUSIVITY OF NORTON SiC

Temp. °F	Parallel to Hot Pressing Thermal Diffusivity		Temp. °F	Perpendicular to Hot Pressing Thermal Diffusivity	
	cm <sup>2</sup> sec <sup>-1</sup>	ft <sup>2</sup> hr <sup>-1</sup>		cm <sup>2</sup> sec <sup>-1</sup>	ft <sup>2</sup> hr <sup>-1</sup>
73	0.4043	1.5667	77	0.4162	0.6128
	0.4121	1.5069		0.4267	1.6535
	0.4157	1.6108		0.4317	1.6728
329	0.3004	1.1641	298	0.2800	1.0850
	0.2974	1.1524		0.2772	1.0742
	0.2974	1.1524		0.2835	1.0986
597	0.2186	0.8471	565	0.2044	0.7921
	0.2154	0.8347		0.2088	0.8091
	0.2231	0.8645		0.2059	0.7979
931	0.1430	0.5541	1186	0.1354	0.5247
	0.1431	0.5545		0.1359	0.5266
	0.1415	0.5483		0.1360	0.5270
1818	0.0991	0.3840	1791	0.0940	0.3643
	0.1002	0.3883		0.0967	0.3747
	0.1000	0.3875		0.0952	0.3689
1998	0.0882	0.3418	2026	0.0848	0.3286
	0.0868	0.3364		0.0843	0.3267
	0.0872	0.3379		0.0847	0.3282
2174	0.0797	0.3088	2194	0.0776	0.3007
	0.0802	0.3108		0.0789	0.3057
	0.0801	0.3104		0.0779	0.3019
2367	0.0743	0.2879	2363	0.0736	0.2852
	0.0743	0.2879		0.0718	0.2782
	0.0753	0.2918		0.0727	0.2817
2498	0.0697	0.2709	2494	0.0693	0.2685
	0.0697	0.2709		0.0694	0.2689
	0.0701	0.2717		0.0693	0.2685
2275	0.0784	0.3038			
	0.0782	0.3030			
	0.0772	0.2992			

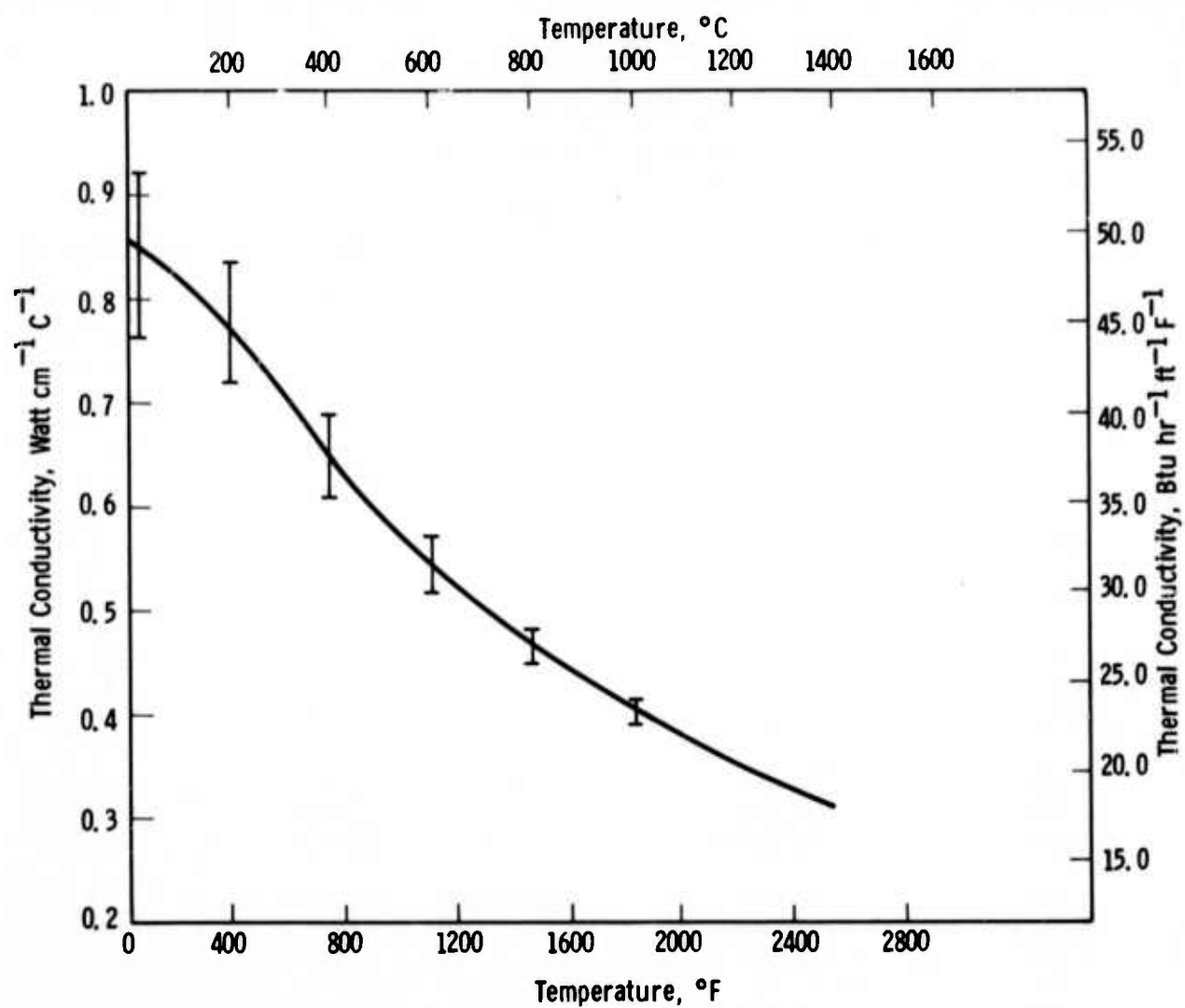


Figure 5.31 -- Thermal Conductivity of Norton Hot Pressed Silicon Carbide

Table 5.8  
THERMAL CONDUCTIVITY OF NORTON SiC

Temp. °F	Watt cm <sup>-1</sup> C <sup>-1</sup>	BTU hr <sup>-1</sup> ft <sup>-1</sup> F <sup>-1</sup>	Temp. °F	Watt cm <sup>-1</sup> C <sup>-1</sup>	BTU hr <sup>-1</sup> ft <sup>-1</sup> F <sup>-1</sup>
77	0.918	53.041	73	0.895	51.712
	0.941	54.370		0.913	52.752
	0.952	55.006		0.921	53.214
298	0.807	46.628	329	0.894	51.654
	0.799	46.165		0.885	51.134
	0.817	47.205		0.885	51.134
565	0.674	38.943	597	0.741	42.814
	0.689	39.810		0.731	42.236
	0.679	39.232		0.757	43.739
1186	0.510	29.467	931	0.549	31.721
	0.511	29.525		0.550	31.778
	0.512	29.583		0.544	31.432
91	0.385	22.245	1818	0.413	23.863
	0.396	22.880		0.418	24.152
	0.390	22.534		0.417	24.094
2026	0.358	20.685	1998	0.375	21.667
	0.356	20.569		0.370	21.378
	0.358	20.685		0.371	21.436
2194	0.334	19.298	2174	0.346	19.992
	0.340	19.645		0.349	20.165
	0.335	19.356		0.348	20.107
2363	0.323	18.663	2367	0.331	19.125
	0.315	18.200		0.331	19.125
	0.319	18.431		0.335	19.356
2494	0.309	17.854	2498	0.315	18.200
	0.309	17.854		0.315	18.200
	0.309	17.854		0.316	18.258
			2275	0.345	19.934
				0.344	19.876
				0.340	19.645

The effect of an air environment on the general shape of the creep curve is shown in Fig. 5.32. Both the primary and secondary stages are affected by air. There is a small reduction in activation energy for creep in air, as compared to the He atmosphere (Fig. 5.33). Nevertheless,  $\Delta H$  remains high, and falls within the range of the activation energy for viscous shear of silicate glass.<sup>(3)</sup>

The effect of an air environment on creep parameters is illustrated in Table 5.9 which compares test in air to tests at various stresses, and temperatures for two grades of  $\text{Si}_3\text{N}_4$ .

One compressive creep test was performed in air. The data are reported in Fig. 5.34.

#### Creep Testing of SiC

Preliminary tensile creep data for Norton hot pressed silicon carbide were recorded in He using refractory metal grips in a Brew Furnace. No significant creep was observed at 2300°F or 2500°F after 1000 hrs at a static stress of 10,000 psi. A specimen failed after 6 hrs at 2500°F under a static stress of 20,000 psi. In all cases, the creep strain did not exceed 0.5%.

A test in air at 2300°F, 15,000 psi stress is currently in progress. The temperature and stress represent the highest temperature and stress condition permissible with TD nickel grips and load train parts. If the creep properties in air are similar to those observed in vacuum, it will be necessary to characterize the creep and stress rupture properties of silicon carbide exclusively in an inert atmosphere at temperatures approaching 3000°F. The stress matrix will encompass the 5000 to 15,000 psi range.

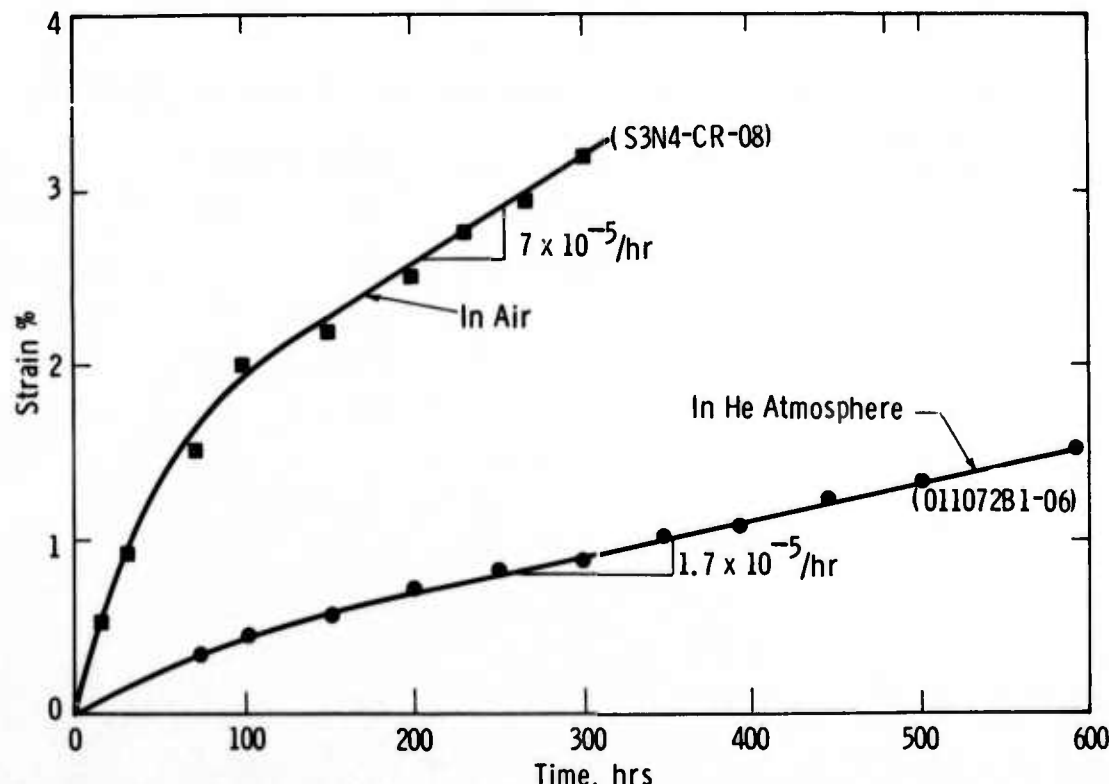


Figure 5.32 -- Creep Properties of Hot Pressed  $\text{Si}_3\text{N}_4$  at 10,000 psi, 2300°F

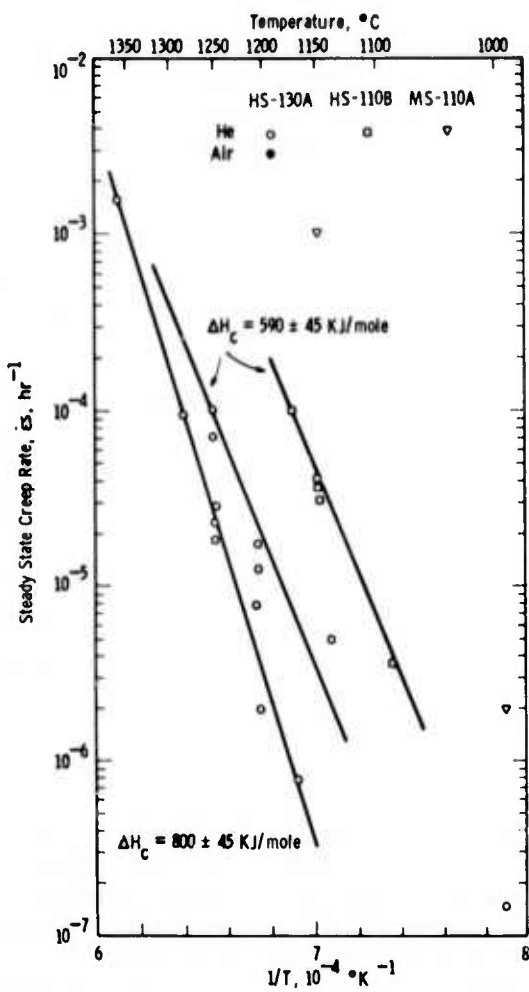


Figure 5.33 -- Effect of Temperature on the Creep Properties of Norton HS-130 Silicon Nitride in Air

Table 5.9

EFFECT OF ATMOSPHERE ON CREEP PARAMETERS, HOT PRESSED HS-130  $\text{Si}_3\text{N}_4$

Test Temperature °F	Applied Load 1000 psi	$\epsilon_s \text{ hr}^{-1}$		Total Elong. %		Comments
		He	Air	He	Air	
1800	10		$1.5 \times 10^{-7}$			Term. 2000 hr
2050	10	$2 \times 10^{-5}$		0.5		HS-110, 0.2% Ca
2100	10	$2 \times 10^{-6}$		0.3		
2150	12			0.2		HS-110, 0.2% Ca
2200	10		$1.6 \times 10^{-5}$		1.7	
2200	12					
2300	8		$6 \times 10^{-5}$		3.1	
2300	10	$2 \times 10^{-5}$	$1 \times 10^{-4}$	0.6	3.3	
2300	12	$3 \times 10^{-5}$		0.5	2.9	
2300	14	$4 \times 10^{-5}$		0.5		
2400	10				2.8	
2500	10	$2 \times 10^{-3}$		0.6		

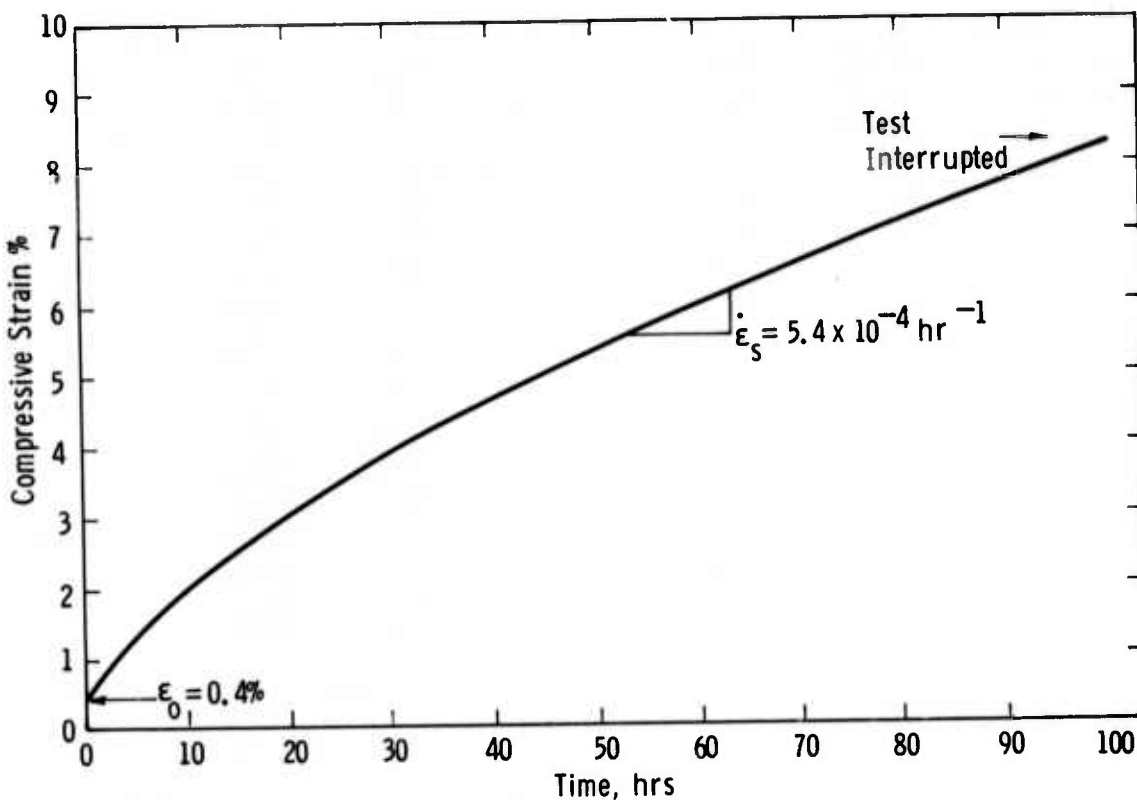


Figure 5.34 -- Compressive Creep of Norton Hot Pressed Silicon Nitride in Air at  $1 \times 10^5$  psi, 2500°F

#### Corrosion-Erosion Testing

The corrosion-erosion experiments conducted previously in pressurized turbine test passage<sup>(1,2,3)</sup> were carried out in Gulf No. GT-2 diesel fuel, containing the 4 ppm barium. The barium was added by the manufacturer to inhibit smoke formation and to prevent the formation of gum during oil storage. Results indicate that this barium addition played a major role in the corrosion-erosion behavior of both hot pressed  $\text{Si}_3\text{N}_4$  and SiC by the formation of semi-viscous barium silicate on the specimen surface. Recent tests were performed with barium-free, diesel fuel manufactured by Exxon to the following specification:

sulfur	0.35 wt % (max)
ash	0.01 wt % (max)
water and sediment	nil
carbon residue	0.2 wt % (max)

The details of the turbine passage and the experimental procedure were given in an earlier report.<sup>(3)</sup> However, its operation may be summarized as follows: Air compressed to 45 psi and preheated to about 600°F is fed into a 6" diameter combustor located in a thick-walled stainless steel cylindrical tube. Diesel oil is injected into the combustor through a pressurized fuel nozzle and burned with the compressed air. Combustion gases and secondary cooling air impinge on an array of nine 2" x 1/4" x 1/4" test specimens contained in a silicon nitride holder. Pressure is maintained in the passage by a water-cooled barrier plate acting as a variable pressure valve. The exhaust gases are vented to the atmosphere through an extensive muffler system. The degree of corrosion-erosion attack on test specimens was determined by changes in the weight of the specimens and by surface examinations.

Figure 5.35 shows the front and back surfaces of hot pressed silicon nitride and silicon carbide specimens which have been exposed for 250 hours at 3 atm pressure to combustor gases at 500 ft/sec velocity obtained using barium-free Exxon diesel oil. The surfaces of both silicon nitride and silicon carbide specimens remained smooth and free of any surface deposits even after 250 hours of exposure. X-ray diffraction analysis of these specimen surfaces confirmed the absence of any oxide or other external deposits on the surfaces. This is in sharp contrast to the massive surface deposits (containing barium silicate with Fe, Mg, Ni, Cr, etc.) which were formed when barium-containing Gulf diesel oil was used as fuel.<sup>(1)</sup>

The average weight change for hot pressed silicon nitride as a function of corrosion time at 2000°F appears in Fig. 5.36. All specimens lost weight with time almost linearly and this weight loss can be expressed in terms of average surface recession by the following expression:

$$R(Si_3N_4) = 1.29 \times 10^{-2} - 5.26 \times 10^{-4} t$$

where R is the average surface recession in mils and t is the corrosion time at 2000°F in hours.

Figure 5.37 is a similar curve for hot pressed silicon carbide. The specimens again lost weight with time but the magnitude of weight loss for SiC was slightly lower than that for silicon nitride. The average surface recession for silicon carbide can be expressed by the following expression:

$$R(SiC) = 8.67 \times 10^{-4} - 3.87 \times 10^{-4} t$$

where again, R is the average surface recession in mils and t is the corrosion time at 2000°F in hours.

In the highly oxidizing atmospheres of the test passage, both  $Si_3N_4$  and SiC form a thin layer of silica on the surface. However, the impingement of high velocity combustor gases cause this oxide layer to erode away as it is formed. The specimen surfaces remain clean. This simultaneous corrosion-erosion phenomenon results in a loss in the weight of the specimens. However, the magnitude of this corrosion-erosion attack at 2000°F is extremely small; for example, the average surface recession after 250 hours of exposure at 2000°F is only about 0.0001 mil for silicon carbide and about 0.00011 mil for silicon nitride.

After surface examination and weight change measurements, flexural strengths of the corroded  $Si_3N_4$  and SiC specimens were measured to determine the effect, if any, of the turbine environment on strength. The flexural strength was measured under conditions of 4-point loading (outer span 1.5", inner span 0.5") at 2000°F using a cross-head strain rate of 0.001 in/in/min. The specimen size as mentioned previously was 2" x 1/4" x 1/4". Flexural strength data for  $Si_3N_4$  and SiC (at 2000°F) is plotted as a function of corrosion time in Fig. 5.38.

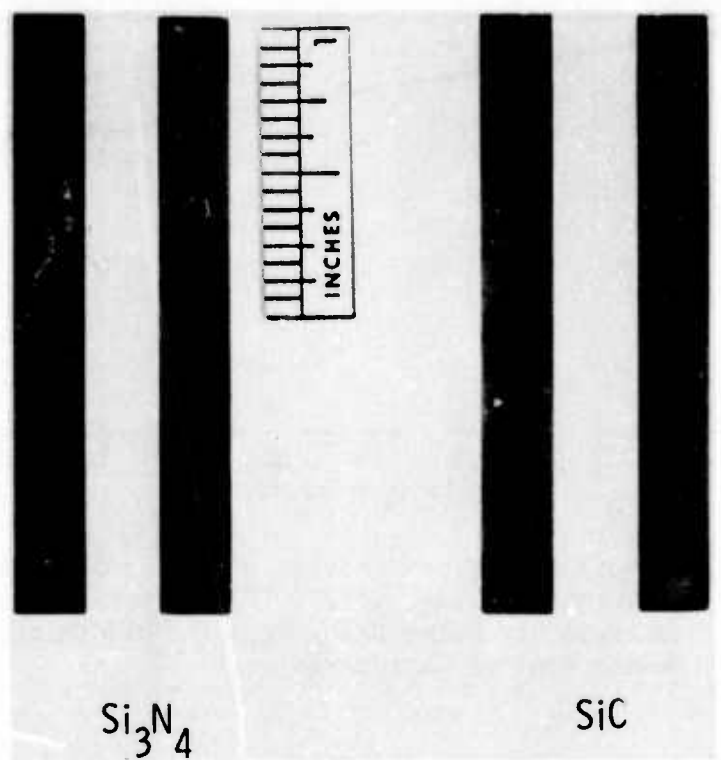


Figure 5.35 -- Surface Appearance of  $\text{Si}_3\text{N}_4$  and  $\text{SiC}$  after 250 hours at 2000°F (Turbine Passage Test at 3 atm Using Exxon #2 Diesel Oil)

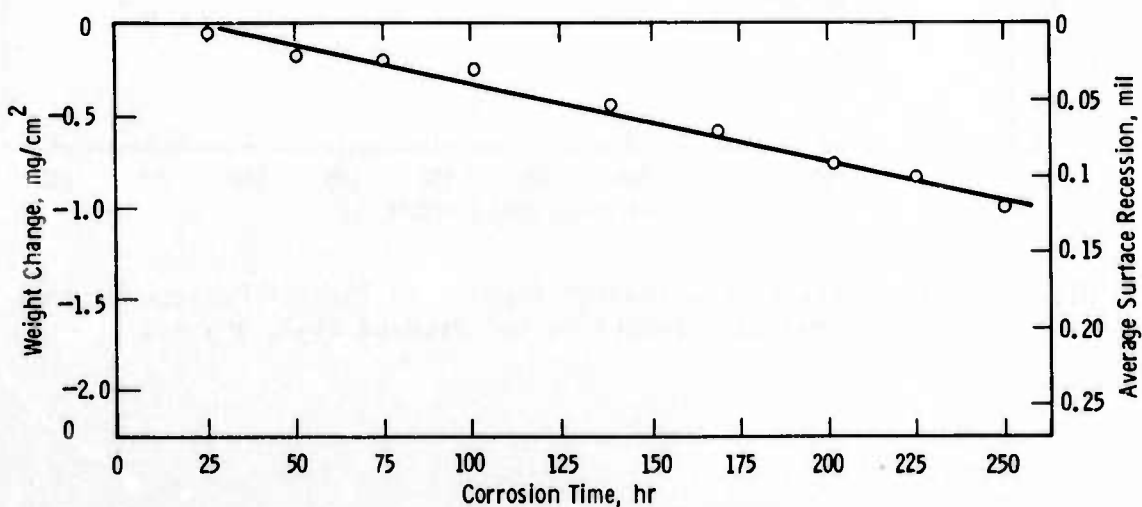


Figure 5.36 -- Corrosion-Erosion Behavior of Hot Pressed Silicon Nitride in Turbine Passage at 2000°F, 3 atm and 500 ft/sec Gas Velocity Using Exxon GT-2 Oil (Microscopic Measurement of Surface Recession)

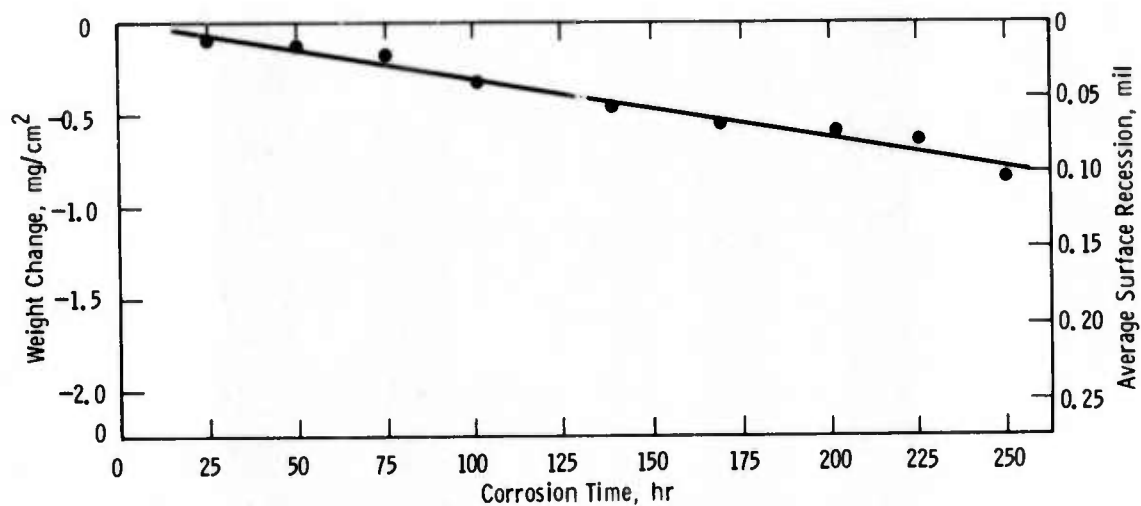


Figure 5.37 -- Corrosion-Erosion Behavior of Hot Pressed Silicon Carbide in Turbine Passage at 2000°F, 3 atm Pressure and 500 ft/sec Gas Velocity Using Exxon No. GT-2 Oil (Microscopic Measurement of Surface Recessions)

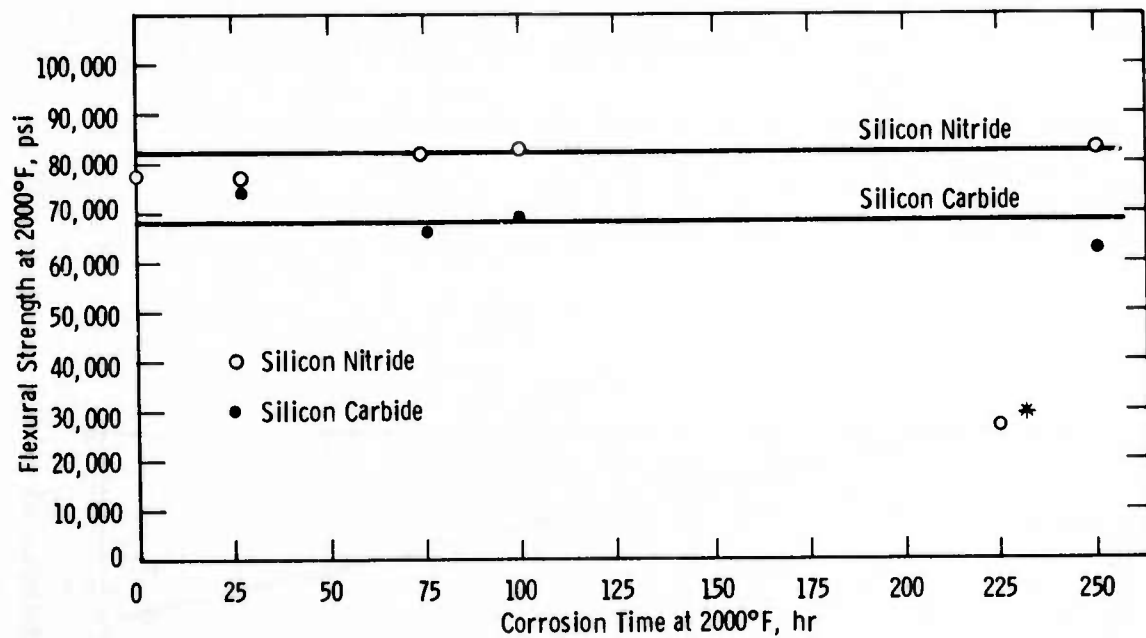


Figure 5.38 -- Effect of Corrosion-Erosion in Turbine Passage on the Flexural Strength of Hot Pressed Si<sub>3</sub>N<sub>4</sub> and SiC

The flexural strength of uncorroded  $\text{Si}_3\text{N}_4$  and SiC measured under the same testing conditions are included in the figure. The flexural strength remained almost constant for specimens exposed to combustor gases for different periods of time up to 250 hours. There was no degradation in strength of the corroded specimens as compared to uncorroded specimens. One silicon nitride specimen exposed for 225 hours failed at 26,800 psi. However, the scanning electron microscope examination of the fracture surface of this specimen revealed the presence of a large non-densified  $\text{Si}_3\text{N}_4$  inclusion which apparently caused the lower flexural strength.

#### Corrosion-Erosion Testing at 2500°F

The turbine test passage was rebuilt to extend corrosion-erosion testing from 2000 to 2500°F. A schematic of the modified turbine passage is shown in Fig. 5.39. The modification was accomplished as follows. The stainless steel liner in the passage housing was replaced by 1" thick alumina lining which was formed in situ by pouring castable alumina cement over a removable core. The alumina lining was formed to accept a Hastelloy-X combustor at one end and blend into a 2" x 4" rectangular transition zone at the other end. The test section is a 310 stainless steel flange, Fig. 5.40, machined to hold four pieces of 1" thick hot pressed  $\text{Si}_3\text{N}_4$  blocks. These  $\text{Si}_3\text{N}_4$  blocks form a 2" x 4" rectangular opening which holds the 1/4" x 1/4" x 2" test specimens immediately downstream of the transition zone. The exhaust duct was also lined with the castable alumina as far back as the water-cooled pressure valve plate. The temperature sensing system and controller were converted from chromel-alumel to Pt/Pt-10% Rh thermocouples.

The rebuilt test passage has been used to determine the corrosion-erosion behavior of hot pressed  $\text{Si}_3\text{N}_4$  and SiC at 2500°F and 3 atm pressure with combustor gases obtained by burning Exxon No. GT-2 diesel oil. Exposures up to 25 hours indicate that the surfaces of both  $\text{Si}_3\text{N}_4$  and SiC were oxidized minimally and no mechanical damage (bending, breaking, etc.) was observed. These tests at 2500°F will continue for a total exposure time of 250 hours.

**2" x 4" Rectangular Opening  
Formed by Four Si<sub>3</sub>N<sub>4</sub> Inserts  
in the Steel Flange**

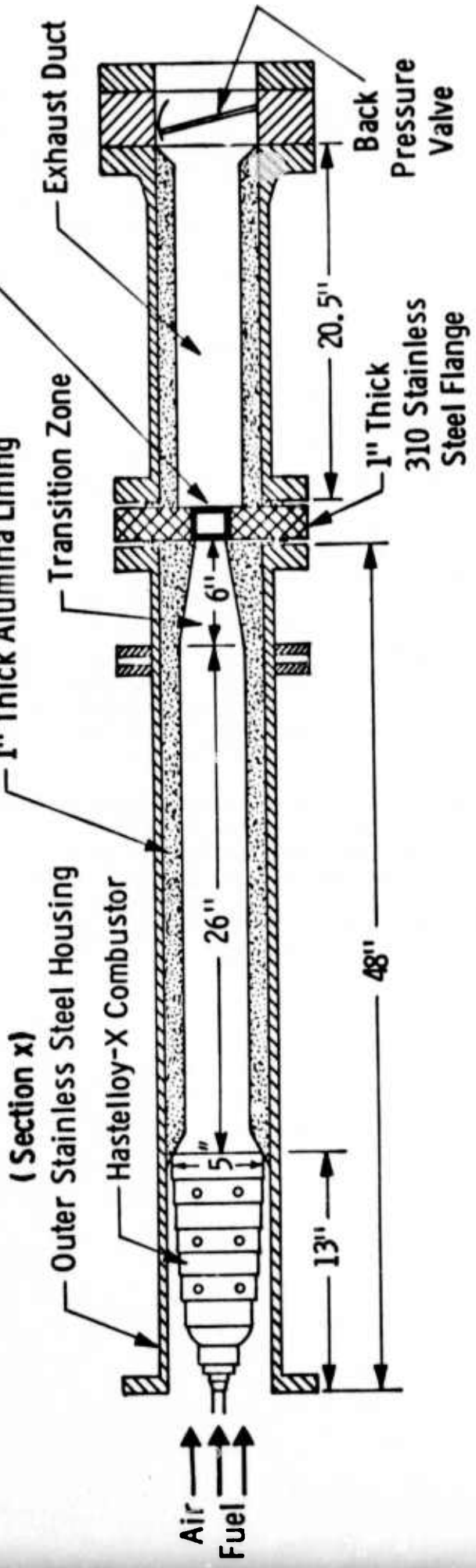


Figure 5.39 -- Gas Turbine Passage as Modified for 2500°F Testing

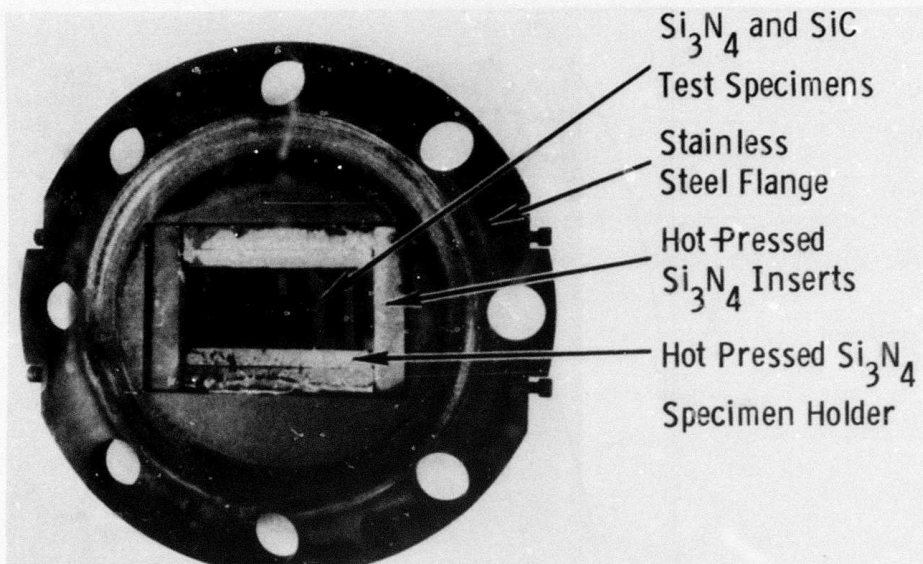


Figure 5.40 -- Stainless Steel Flange and Test Section for 2500°F Turbine Passage

#### Low Cycle Fatigue

Low cycle fatigue tests, in the flexural mode were carried out at 1800°F (982°C) and 2300°F (1260°C) in an attempt to model the effect of thermal fatigue.<sup>(1)</sup> The samples were 0.125 x 0.25 x 1.25 inches long finished parallel to the long dimension with a 220 grit diamond wheel. Four point loading was employed using inner and outer span distances of 0.375 inch and 0.875 inches, respectively. Silicon carbide dowel pins were used for bearing surfaces on the silicon nitride test fixture. Load was applied without reversal to avoid alignment problems.

The cyclic load conditions and test results are presented in Fig. 5.41. These data indicate that plastic strain is cumulative since there does not seem to be any difference between interrupted and non-interrupted tests. It follows that the low cycle fatigue strength as measured under the specific conditions of the test, is strain controlled. Specimen 2 exhibited an accumulated plastic strain of ~ 2%, without failure after 2000 cycles. In normal flexural tests in air, where the specimen is loaded to failure within one hour, the maximum plastic strain at failure is of the order of 0.5%. However, significant strength degradation was observed when specimens 2 and 6 were stressed to failure in a flexural test at room temperature. Flexural strengths of 58,600 and 67,800 psi were recorded for specimens 2 and 6, respectively, compared to an average value of 85,000 psi for  $\text{Si}_3\text{N}_4$  (in the weak direction) of the material. The deterioration probably can be attributed to damage accumulation resulting from fatigue.

If mechanical cycling at constant temperature can be used as an accurate indicator, thermal cycling is expected to influence vane life. Since specimens fatigued to 800 cycles (3 and 5) had room temperature strengths of 78,000 and 87,500, respectively, the threshold of fatigue damage should occur at some point beyond 800 cycles.

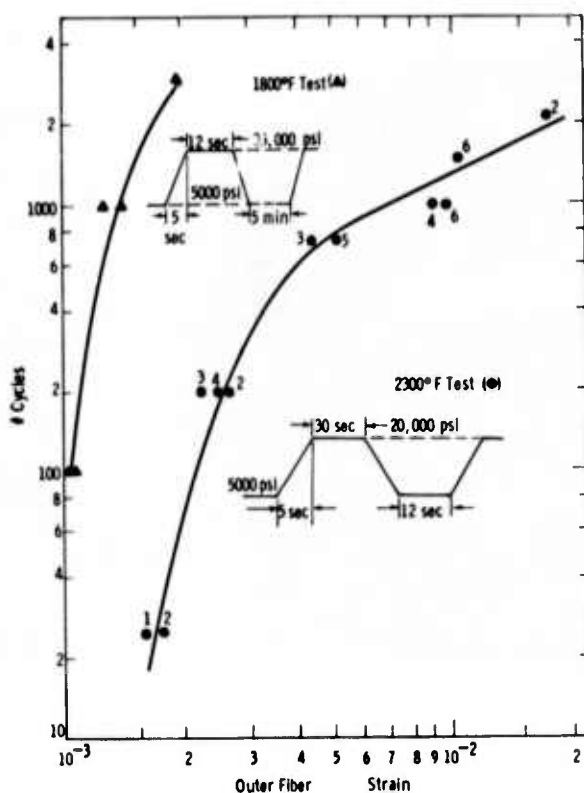


Figure 5.41 -- Low Cycle Fatigue - 4 Pt. Bend Test, in Air for Norton HS-130 Si<sub>3</sub>N<sub>4</sub>

Low cycle fatigue testing will continue in an effort to model the long range effects of thermal cycling. While the flexural mode of testing will be retained, the tests will be strain controlled and fully reversible. A double saddle, 4-point loading fixture has been designed to meet the requirement.

#### Shear Modulus

Ultrasonic pulse-echo measurements at 10 MHz, on Norton HS-130 silicon nitride have been extended to temperatures above 1832°F. The shear modulus was obtained by methods similar to those previously described.(1) Ultrasonic attenuation, which is a measure of the sound absorption in the sample, was obtained by a standard sample-and-hold technique.(2,3) (The relation between ultrasonic attenuation  $\alpha$ , logarithmic decrement  $\sigma$  and sound wavelength  $\lambda$  is  $\sigma = \alpha\lambda$ .) It was found that the attenuation increases quite rapidly above 1832°F, as shown in Fig. 5.42. At about 2282°F, the sound absorption is so strong that further data at higher temperatures could not be obtained.

It is not known whether this high temperature sound absorption is caused by a simple melting of hot pressing additives at grain boundaries or whether it represents a genuine inelastic or creep related phenomenon. In the former case, the attenuation should continue to rise indefinitely, while, in the latter, it should go through a maximum. Experiments at lower frequencies are planned to clarify this point.

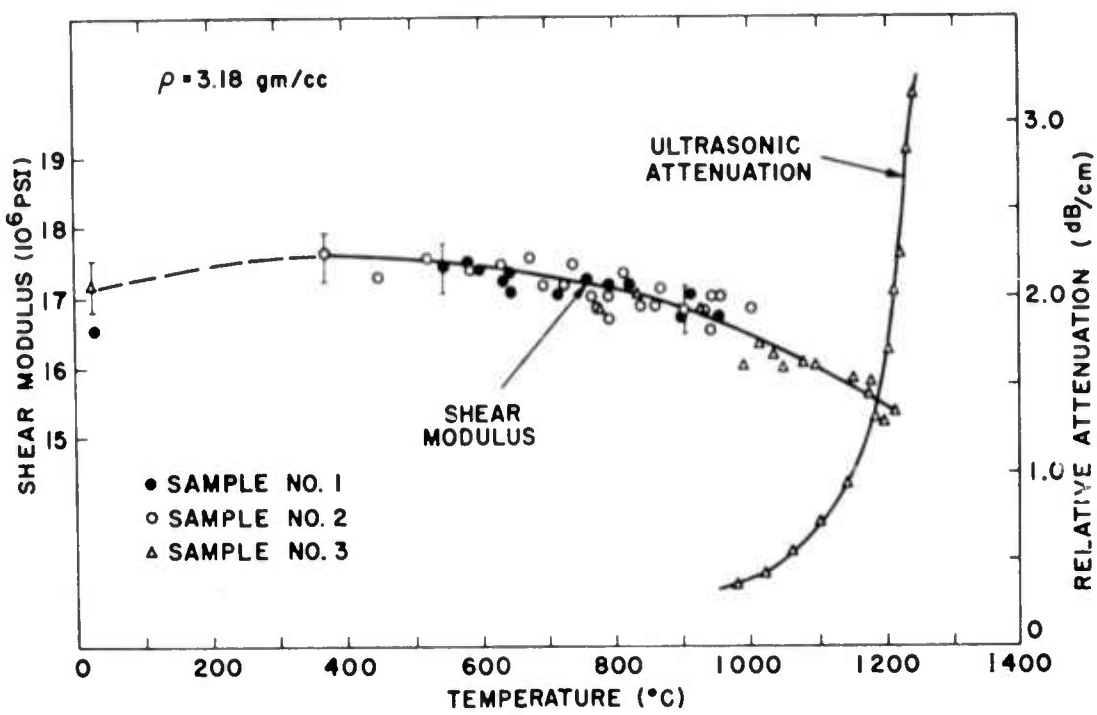


Figure 5.42 Shear Modulus versus Temperature for Norton HS-130 Hot-Pressed Silicon Nitride

### 5.1.2 PHYSICAL PROPERTIES OF REACTION SINTERED SILICON NITRIDE

#### Introduction

The program to characterize both injection molded and slip cast reaction sintered silicon nitride has been expanded to include the measurement of mechanical and thermal properties at elevated temperatures. Creep measurements were made on injection molded silicon nitride. These data are considered essential to the design of turbine components using brittle materials.

Thermal conductivity and high temperature flexual strength measurements of slip cast silicon nitride indicate the potential value of this high density form of reaction sintered silicon nitride for turbine components.

#### Creep Studies of Injection Molded Si<sub>3</sub>N<sub>4</sub>

The Ford duo-density turbine rotor employs molded reaction-sintered Si<sub>3</sub>N<sub>4</sub> for the blades and rim. Because the blades and rim are subjected to stresses at high temperatures, it is important to understand the creep behavior of injection molded silicon nitride. Improvements in creep resistance would also be extremely beneficial in solving some of the fabrication problems encountered to date in this rotor development program (refer to Section 3.1.2 of this report).

Creep tests were performed in ambient air in an electrically heated furnace using a four point bending fixture (Figure 5.43). Weights acting through a lever system were employed to apply the load, which was transmitted to the sample using a hot pressed SiC loading anvil with 1/8 in. diameter sapphire knife edges. Platinum foil was used to minimize the reaction between the knife edges and the sample. The outer fiber stress was calculated from the standard equation for four point bending of an elastic beam. Strain (E) was obtained from the deflection ( $\delta$ ) within the region of pure bending. Deflection was measured using three LVDT's coupled directly to sapphire rods which contacted the tension side of the specimen. This positioning of the sapphire rods eliminated the effect of the knife edges on true displacement at high temperature, and the influence of thermal expansion of contact rods and support column. A multi-channel potentiometric recorder monitored the deflection from each transformer continuously. The outer fiber strain was calculated using the equation

$$\epsilon = \frac{4h\delta}{b^2 + 4\delta^2}$$

where h is the specimen thickness and b is the distance between the inner load points on the compression side of the creep sample.

Two grades of Si<sub>3</sub>N<sub>4</sub> material were chosen for initial evaluation, with the difference between the two being impurity content (Table 5.10). The major differences in the two materials is the amount of calcium impurity. Silicon Type A had CaF<sub>2</sub> added as a nitriding aid, while silicon Type B had only a small level of calcium present as an impurity in the raw material. These materials were nitrided in slightly different nitriding cycles, (Table 5.11) however, their room temperature strengths are approximately equal.

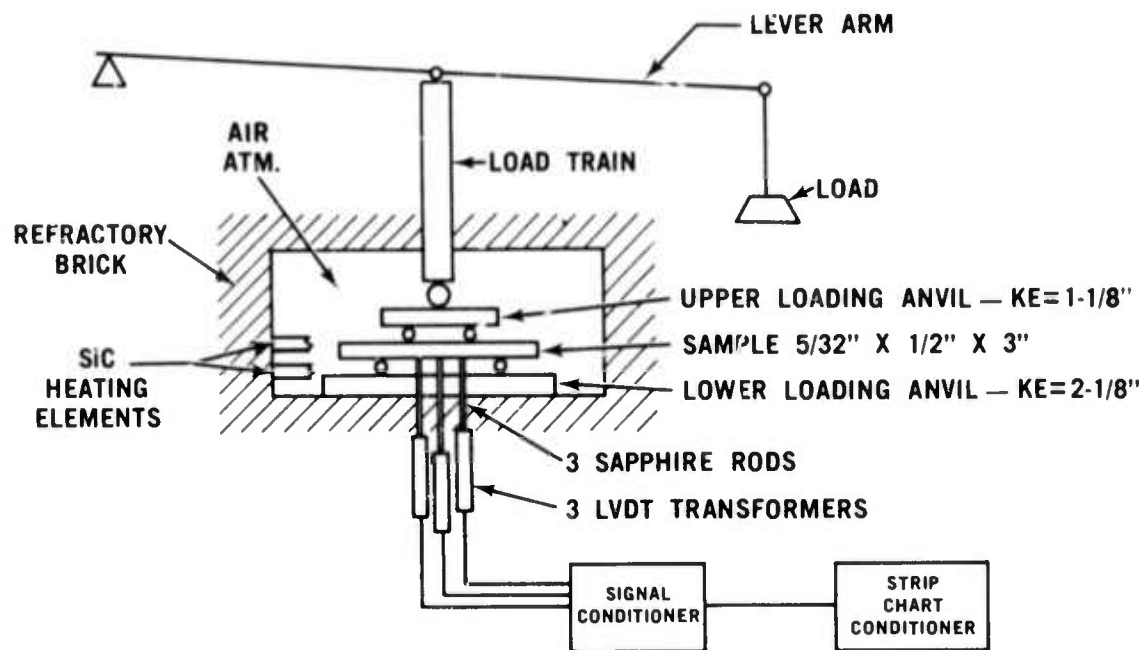


Figure 5.43 Creep Test Rig

Table 5.10 IMPURITY ANALYSIS OF SILICON METAL

<u>Impurity Element</u>	<u>Silicon Type A (wt. %)</u>	<u>Silicon Type B (wt. %)</u>
Fe	0.50-0.70	0.66-0.76
Al	0.35-0.48	0.38-0.60
Ca	0.40	0.02-0.08
Mg	0.03	0.02
Ni	0.02	0.02
W	<0.01	<0.01
Co	<0.01	<0.01
V	0.01	0.01

Table 5.11 TEST SAMPLE HISTORY

Silicon Type	Nitriding Cycle	Nitriding Atmosphere	Nominal RT Bonding Strength
Material A A	24 hours @ 2300°F 24 hours @ 2660°F	N <sub>2</sub>	19,000 psi
Material B B	36 hours @ 2300°F 24 hours @ 2660°F	N <sub>2</sub>	19,000 psi

A summary of the creep tests are given in Table 5.12. Tests 8A and 8B were preliminary checks on the injection molded  $\text{Si}_3\text{N}_4$ , and due to the short duration of the tests, the actual steady state creep rate could possibly be lower than reported. The other experiments were conducted for sufficient times to insure the material was in the steady state creep region. With the exception of runs 14 and 15, all tests were terminated before rupture occurred.

Figure 5.44 is a typical plot of total strain (elastic + plastic) as a function of time at temperature. This curve shows the large differences observed between Material A and Material B. Material A (high calcium) was tested at  $2000^{\circ}\text{F}$  and 5000 psi stress, and exhibited 1.8% strain after 100 hours. Material B (low calcium) was also tested at 5000 psi for 100 hours, but at a higher temperature of  $2300^{\circ}\text{F}$ . Despite the higher temperature, the low calcium material exhibited only 0.9% strain. These results show that by reducing the amount of Ca impurity, the creep resistance of  $\text{Si}_3\text{N}_4$  can be drastically improved over  $\text{Si}_3\text{N}_4$  with high calcium impurity.

Figure 5.45 is a plot of steady state strain rate as a function of stress for the two materials tested. Again, the difference in creep behavior is noted. For example, Material A tested at  $2210^{\circ}\text{F}$  and 1000 psi had a creep rate of  $1 \times 10^{-4}$  in/in/hr. while a Type B sample tested at the same temperature but at 5000 psi had a creep rate of  $2 \times 10^{-6}$  in/in/hr., a considerable improvement. Due to the limited number of data points, very little is apparent relative to the slopes of these lines in relation to the possible mechanisms of creep.

In summary, by reducing the calcium impurity content, marked improvements have been made in the creep resistance of injection molded  $\text{Si}_3\text{N}_4$ . The initial material with the high calcium level was found to be completely unacceptable for use in a turbine rotor, while the improved material has the potential of meeting requirements. However, work must still be done to further improve the creep characteristics of the injection molded material, and also to define the stress-rupture properties of reaction-sintered  $\text{Si}_3\text{N}_4$ .

#### Specific Heat of Reaction-Sintered Silicon Nitride

Specific heat of reaction-sintered silicon nitride was measured at the Battelle Memorial Institute using a Bunsen ice calorimeter. The apparatus and test procedure is discussed in detail in Section 5.1.1 of this report.

The silicon nitride used in this test was an injection molded material having a nitrided density of 2.23 gms/cm<sup>3</sup>. No attempt was made to measure the specific heat on higher density slip cast silicon nitride as the assumption was made that the data obtained could be used for either type silicon nitride. This assumption is justified by the fact that specific heat is a function of specimen composition and mass, and is independent of porosity, density or small compositional variation.

The results of specific heat measurements are shown in Figure 5.46. These data indicate a specific heat of 0.148 cal/gm/ $^{\circ}\text{C}$  at  $0^{\circ}\text{C}$ , rising to 0.300 cal/gm/ $^{\circ}\text{C}$  at  $1400^{\circ}\text{C}$ .

Table 5.12 Creep Test Results

Test No.	Sample History	Test Temp. (°F)	Stress psi	Duration of Test (hrs)	$\dot{\epsilon}_s^\circ$ (in/in/hr)	Total Strain At End Of Test (in/in)
8A	Mat'1 A	2210	2500	15	$6 \times 10^{-4}$	.015
8B	Mat'1 A	2210	5000	13	$7.5 \times 10^{-4}$	.015
12	Mat'1 A	2210	1000	113	$1.2 \times 10^{-4}$	.022
13	Mat'1 A	2000	5000	110	$4.3 \times 10^{-5}$	.019
14	Mat'1 A	2000	7500	.67	-	Ruptured
15	Mat'1 A	2000	7500	1.8	-	Ruptured
16	Mat'1 A	2000	2500	150	$2.4 \times 10^{-5}$	.018
18	Mat'1 B	2210	5000	96	$3 \times 10^{-6}$	.0068
19	Mat'1 B	2210	10,000	71	$7.2 \times 10^{-5}$	.02
21	Mat'1 B	2300	5000	120	$3 \times 10^{-5}$	.010
22	Mat'1 B	2300	7500	115	$5.3 \times 10^{-5}$	.015

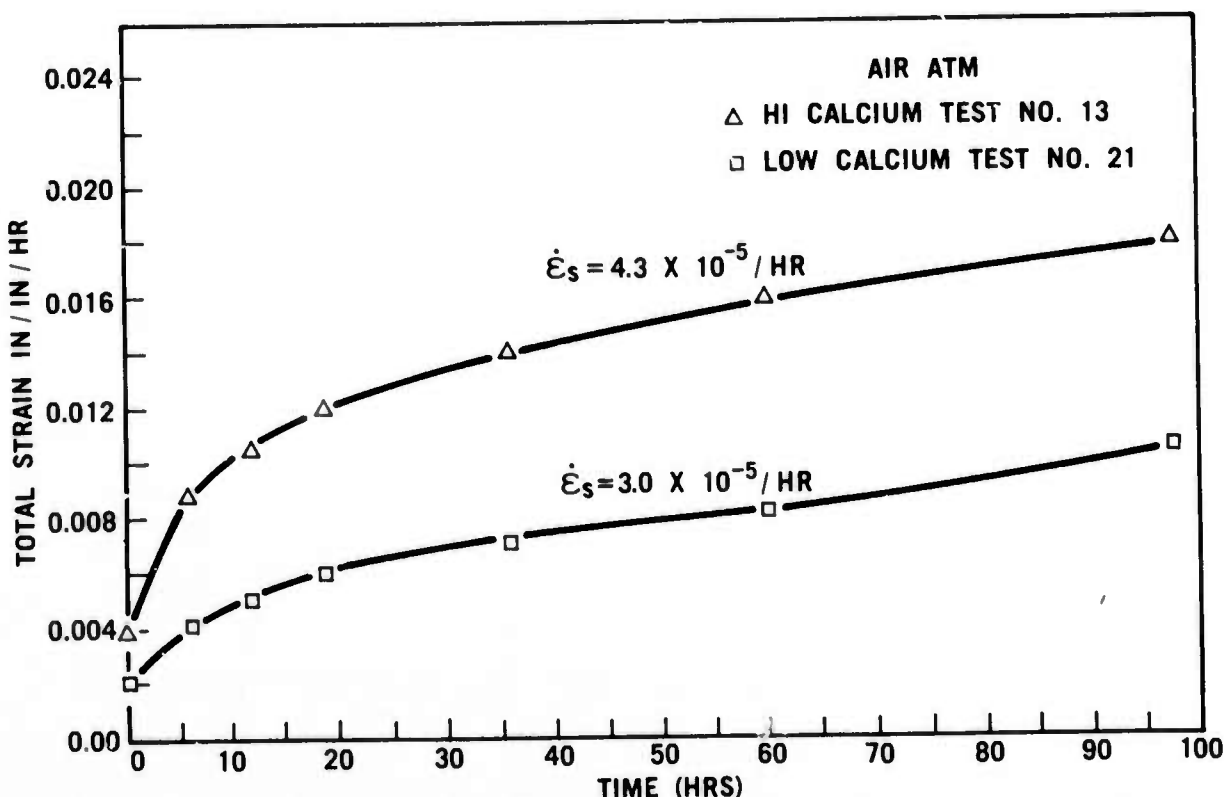


Figure 5.44 Total Strain Versus Time for Two Types of Reaction-Sintered Silicon Nitride

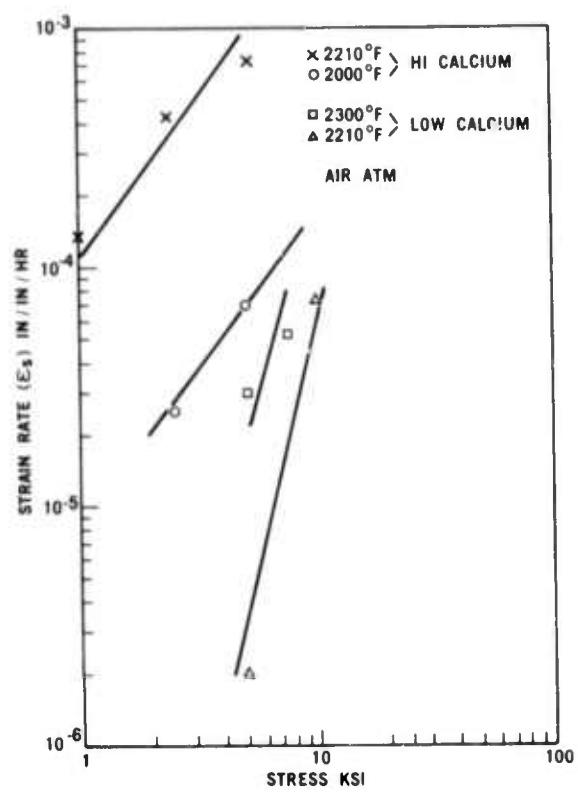


Figure 5.45 Steady State Strain Rate Versus Stress for Two Types of Reaction Sintered Silicon Nitride

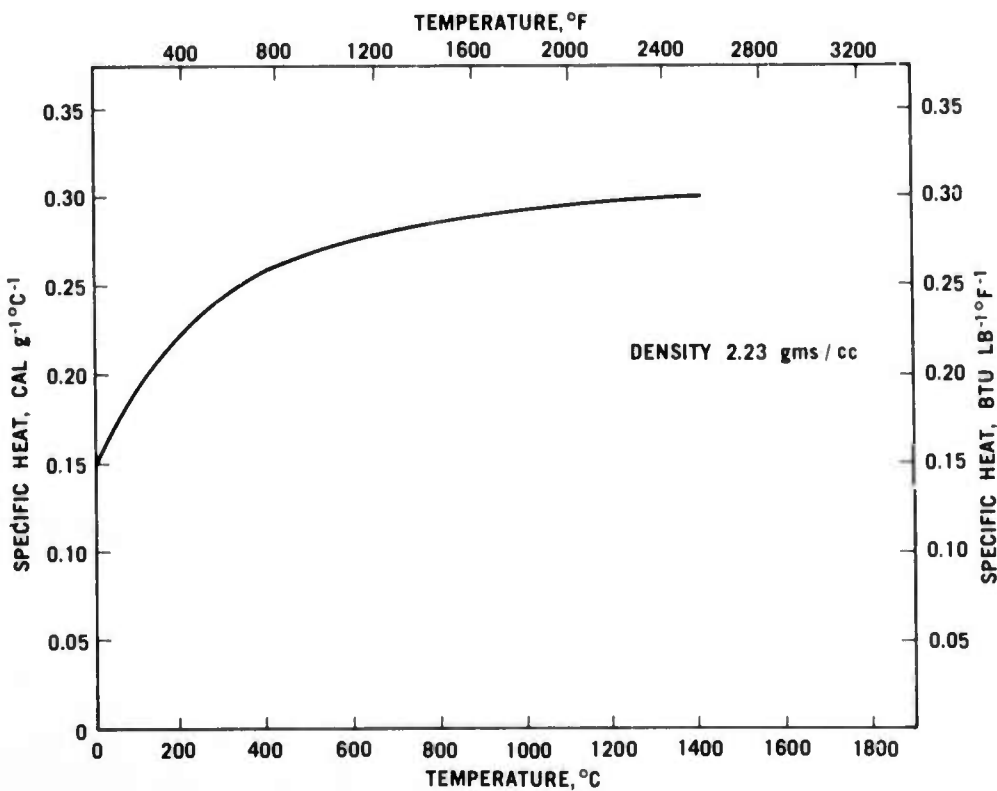


Figure 5.46 Specific Heat of Injection Molded Reaction-Sintered Silicon Nitride

### Thermal Conductivity of Injection-Molded and Slip-Cast Silicon Nitride

The thermal conductivity of both injection molded and slip-cast silicon nitride was measured by Battelle Memorial Institute using the flash diffusivity method. This technique is described in detail in Reference 2 and in Section 5.1.1 of this report.

Two types of reaction-sintered silicon nitride are produced by Ford, injection molded and slip-cast. The density of the molded version was measured to be 2.23 gms/cm<sup>3</sup>, and the slip cast measured to be 2.68 gms/cm<sup>3</sup>.

Figure 5.47 presents the thermal conductivities for the two silicon nitrides. The thermal diffusivity data used in the calculation of thermal conductivity are shown in Figure 5.48. It is apparent from these curves that the thermal conductivity is approximately 50% higher for slip cast Si<sub>3</sub>N<sub>4</sub>. This difference holds true throughout the temperature range of measurement. Both types of materials are similar in composition and nitriding history. One can thus assume the thermal conductivity difference to be reflected by their differences in density or porosity.

### Hot Strength of Slip Cast Silicon Nitride

Slip-cast reaction-sintered Si<sub>3</sub>N<sub>4</sub> has recently come into use on the vehicular turbine project for stator and rotor shrouds. Work has therefore been initiated to characterize this material.

The hot strength of slip-cast reaction-sintered silicon nitride was measured utilizing a three point bend test fixture. The test system consisted of a resistance heated furnace with hydraulically loaded refractory test fixtures. A silicon carbide hearth with carbide knife edges on 3 in. centers was used. The loading ram was silicon carbide which applied an incremental load through a hand operated hydraulic system. Crosshead speed was approximately 0.1 in/min. The load was measured directly from a dial indicator which is actuated by a mechanical deflection load cell. Air cooling was used to protect the bearing and hydraulic systems. Temperature capability of the furnace was 2600°F.

Test specimens 1/4" x 1/4" x 4" were cut from slip cast pre-sintered bar stock (1" x 1" 12"). The 1/4 in. bars were sintered utilizing a three stage firing cycle; 2000°F for 18 hours, 2300°F for 24 hours, and 2660°F for 18 hours. The furnace environment consisted of nitrogen gas flowing at the rate of 20 C.F.H.

After sintering, the 1/4 in. test specimens were diamond ground to 0.230 in. square bars 4 in. long. These samples had a final average density of 2.6 gms/cc. Eight bars were tested at various temperatures. Bars were individually introduced into the furnace after the furnace had reached the desired temperature; after a 15 to 20 minute soak the bar was fractured and the failure load recorded.

The flexural strength at each temperature level is shown in Figure 5.49. As can be seen the room temperature strength was 41,500 psi, dropping to a low of 36,300 psi at 2500°F. For comparison purposes, the room temperature flexural strength is also shown in Figure 5.49 for both 3 point and 4 point testing.

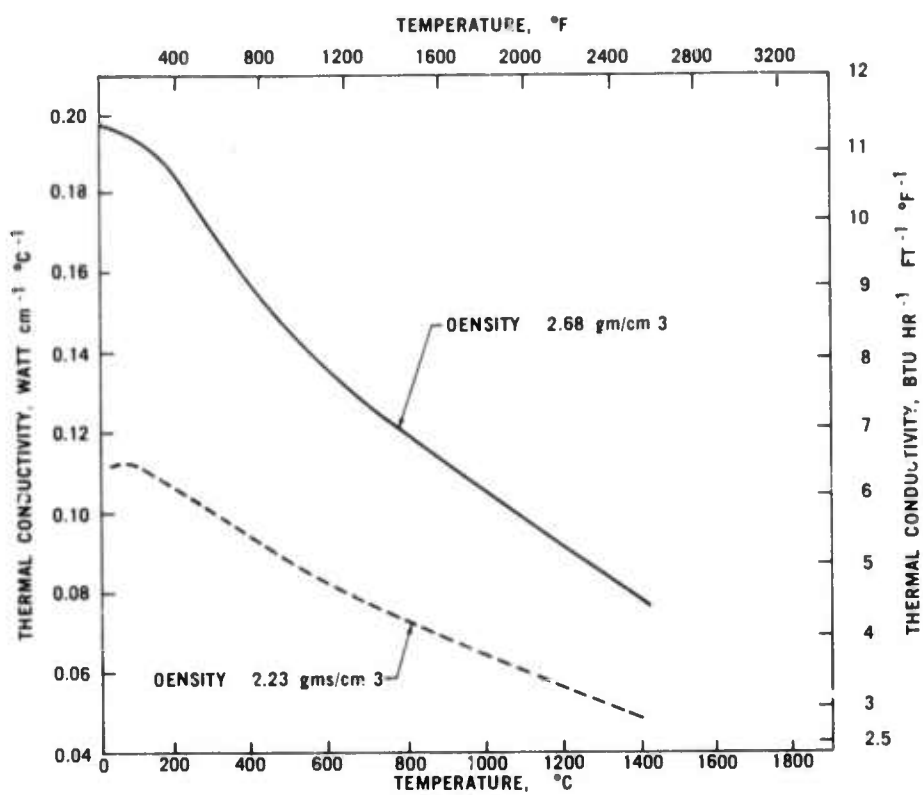


Figure 5.47 Thermal Conductivity of Injection-Molded and Slip-Cast Silicon Nitride

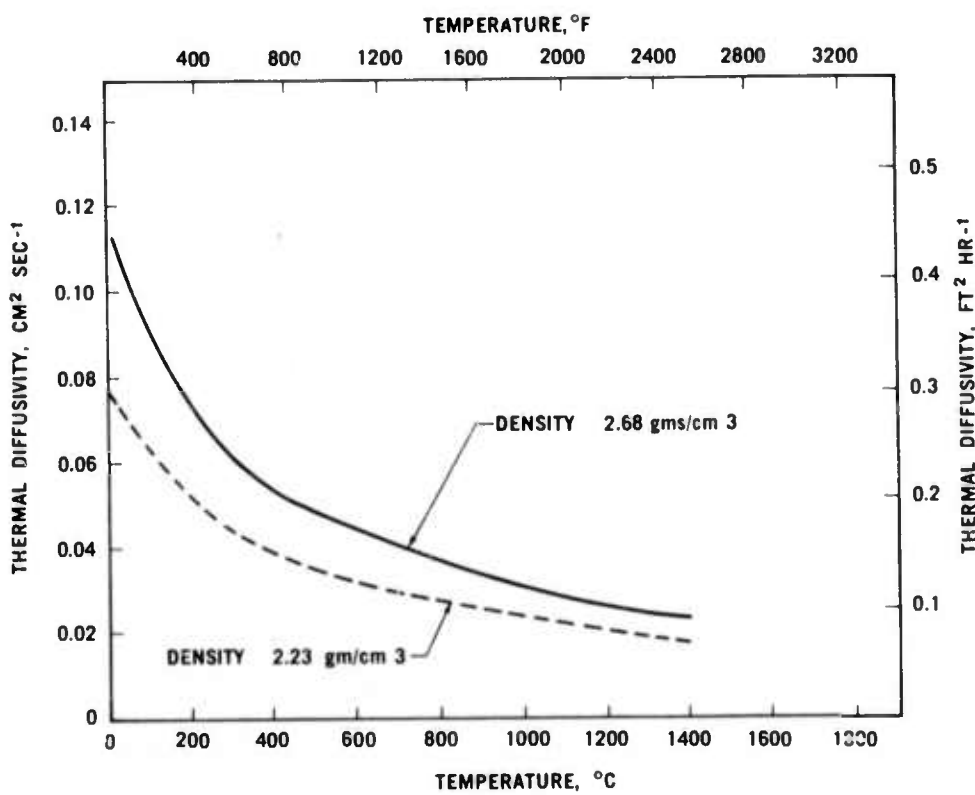


Figure 5.48 Thermal Diffusivity of Injection-Molded and Slip-Cast Silicon Nitride

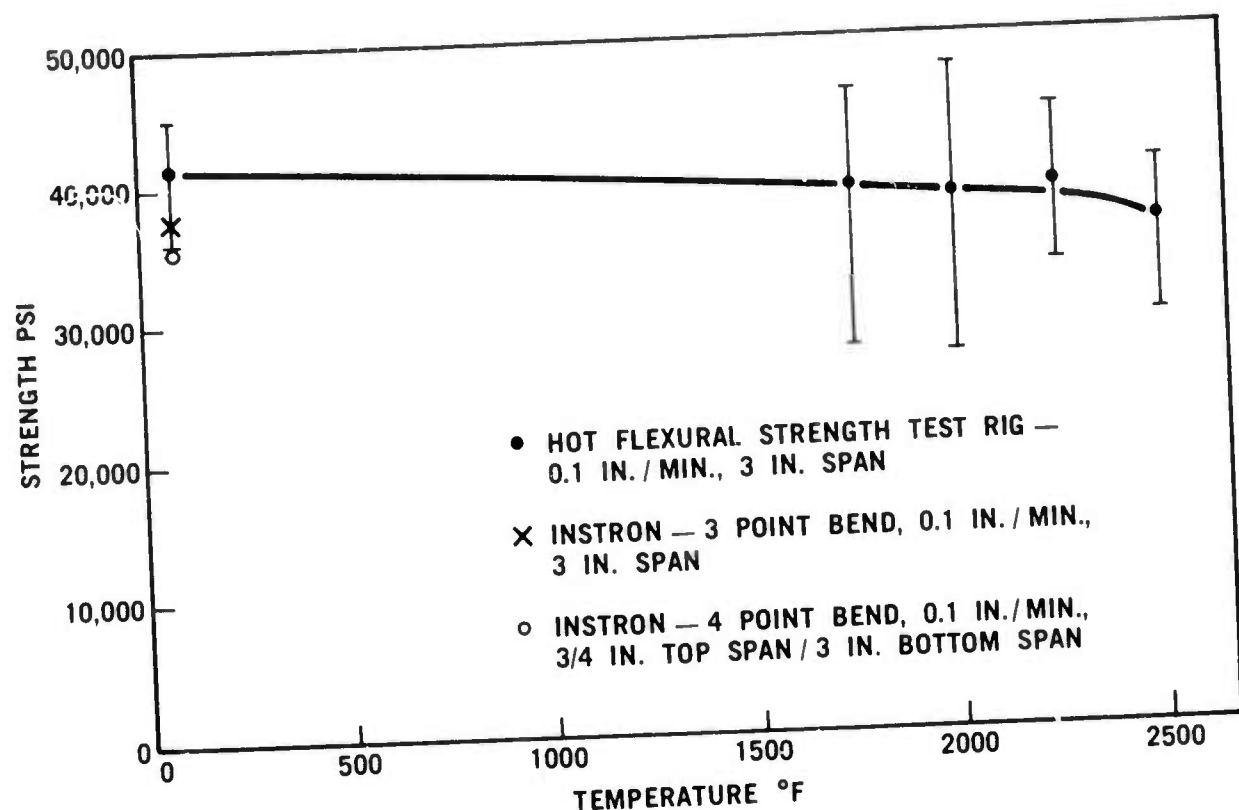


Figure 5.49 Strength Versus Temperature for Slip Cast Silicon Nitride

## 5.2 MATERIAL SCIENCES

### SUMMARY

The purpose of detailed investigations into material sciences is to develop an understanding of material behavior which will lead to improved material through better control of composition, processing, and fabrication. This is of particular importance since the ceramic materials being utilized in the turbine engines are relatively new and appear capable of considerable improvement. Various phases of the material sciences investigation will be continued throughout the life of the program.

Studies of the microstructure of Norton hot-pressed silicon carbide were carried out. The major impurities, iron and aluminum, were found to be evenly distributed, and to exist mainly in the form of discrete particles in the grain boundaries.

An investigation was made of the effects of oxygen and nitrogen partial pressures on oxidation of hot-pressed silicon nitride and silicon carbide. It was concluded that the oxidation of silicon nitride is independent of both oxygen and nitrogen partial pressures. The oxidation rate of both hot-pressed silicon nitride and silicon carbide in wet oxygen is somewhat higher than in dry oxygen. Studies of the oxide layer formed on silicon carbide have shown that all the impurities except tungsten diffuse outward during the oxidation process.

Additional work on fabrication parameters of reaction-sintered silicon nitride showed that density could be improved by altering particle size distribution of the silicon metal powder raw material, but no corresponding improvement in strength was noted. The strength of reaction sintered silicon nitride was significantly improved when a small amount (1-2%) of hydrogen was added to the normal nitrogen atmosphere.

PRECEDING PAGE BLANK-NOT FILMED

### 5.2.1 MICROSTRUCTURAL CHARACTERISTICS OF HOT PRESSED SILICON CARBIDE

#### Introduction

The microstructural characterization of hot pressed silicon nitride has been reported.<sup>(1-3)</sup> This section describes the microstructure of Norton hot pressed silicon carbide.

#### Hot Pressed Silicon Carbide

As indicated in the previous report,<sup>(1)</sup> Norton hot pressed silicon carbide contains a few percent Al, mostly in the form of  $\text{Al}_2\text{O}_3$  and a few percent W, mostly in the form of WC.

The qualitative distribution of the major impurity elements in SiC are shown in Fig. 5.50. These are images of five elements obtained on a Secondary-Ion-Mass-Spectrometer. The relative intensities do not relate to concentration. The micrographs show a relatively uniform distribution of all elements with Al indicated in the highest concentration based on particle density.

On a finer scale, the impurities are found to be concentrated mostly in the form of discrete particles as seen by the SEM micrographs in Fig. 5.51. The bright particles indicate areas of higher mass, as compared to the base material. Dispersive energy analysis shows that the particles are either rich in Al or in W. Based on the x-ray diffraction and probe analyses<sup>(1)</sup> it is possible to conclude that these particles are structurally similar to  $\text{Al}_2\text{O}_3$  or WC although the exact composition of the particles is not yet known.

Exposure to high temperatures for a long time in inert atmospheres, apparently causes a loss of  $\text{Al}_2\text{O}_3$ . This is shown in the SEM micrograph, Fig. 5.52. The surface examined was from a creep specimen, held for over 1000 hrs. at 2500°F. Al was not present in any of the many bright particles appearing in Fig. 5.52. Examination of the creep specimen in the microprobe will determine whether  $\text{Al}_2\text{O}_3$  was lost by evaporation or diffusion into the SiC matrix.

High magnification transmission micrographs are shown in Figs. 5.53 and 5.54. When compared to Figs. 5.51 and 5.52 there are indications of a high distribution of foreign particles ranging in size from a few microns in diameter to about 1000 Å. The dark field micrograph, Fig. 5.53 clearly indicates the particles at grain boundaries. However, the diffraction pattern was not clear enough for positive identification.

Figure 5.54 shows a few particles within the grain (A). The occurrence of a high density of stacking faults and dislocations is most revealing. A more detailed analysis of the faults will be performed in the future. However, it is possible that these faults constitute very active sites for nucleation of failure. The cleavage and generally low strength of SiC at low temperatures may be related to this inherently faulty structure.

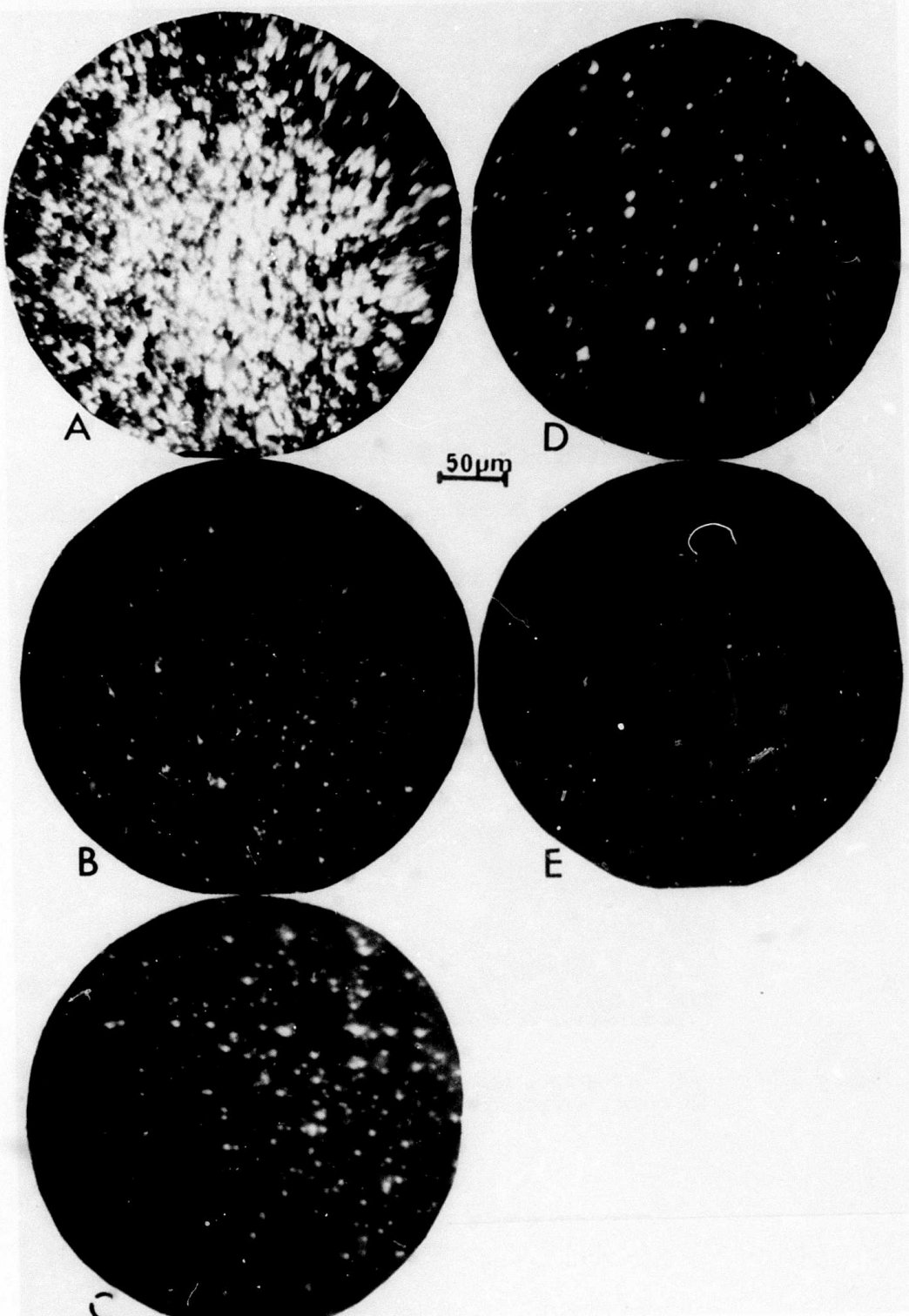


Figure 5.50 -- Secondary-Ion-Mass Spectrometer Micrographs of Major Impurities in SiC - A-Al, B-W, C-Ti, D-B and E-Fe

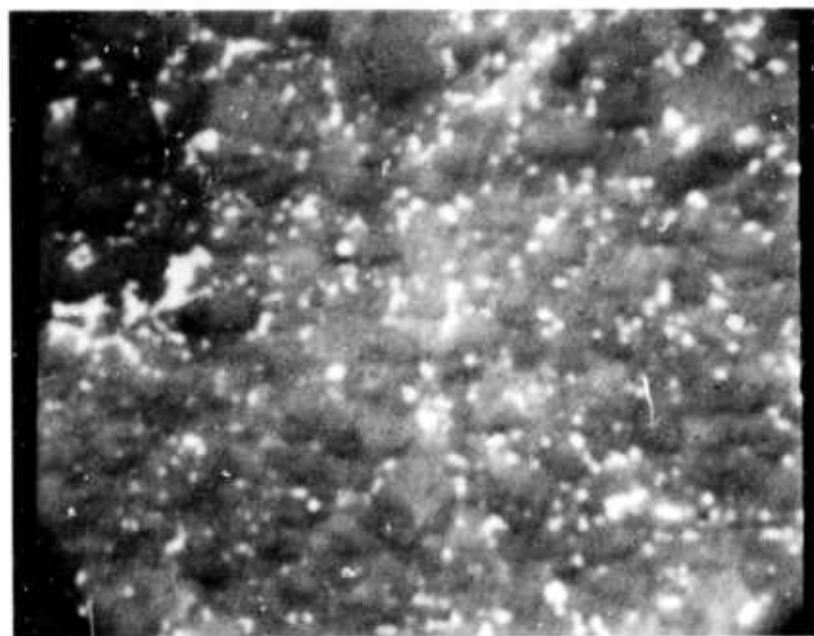


Figure 5.51 -- SLM Micrograph of Polished SiC Showing Impurities (2000 X)

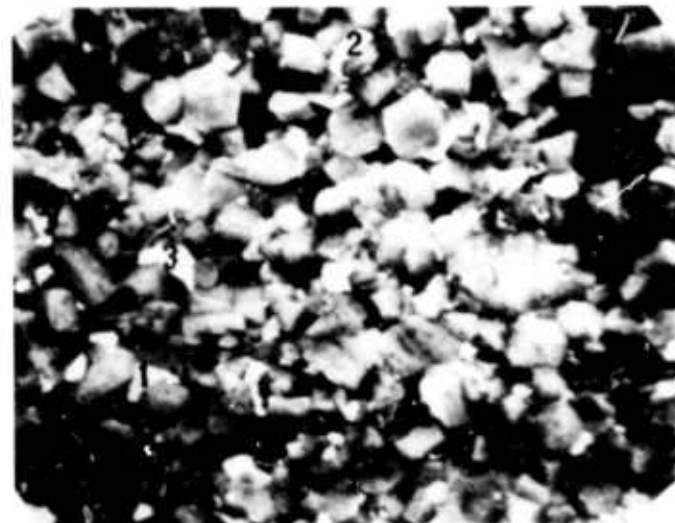


Figure 5.52 -- SEM Micrograph, Thermally Etched, Hot Pressed SiC Creep Specimen, (Particles Show Si, W and Traces of Ti and Fe - No Al)

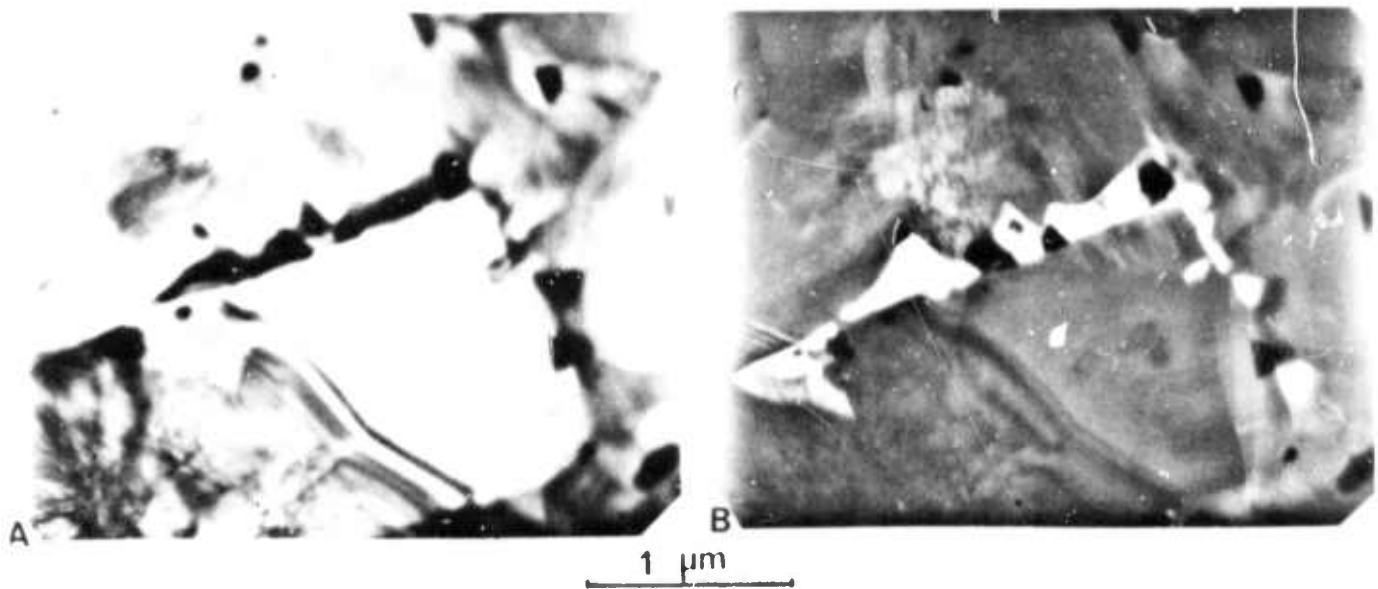


Figure 5.53 -- Transmission Electron Micrographs Showing Inclusions in Grain Boundaries of Hot Pressed SiC  
A - Bright Field; B - Dark Field (1000 KV)

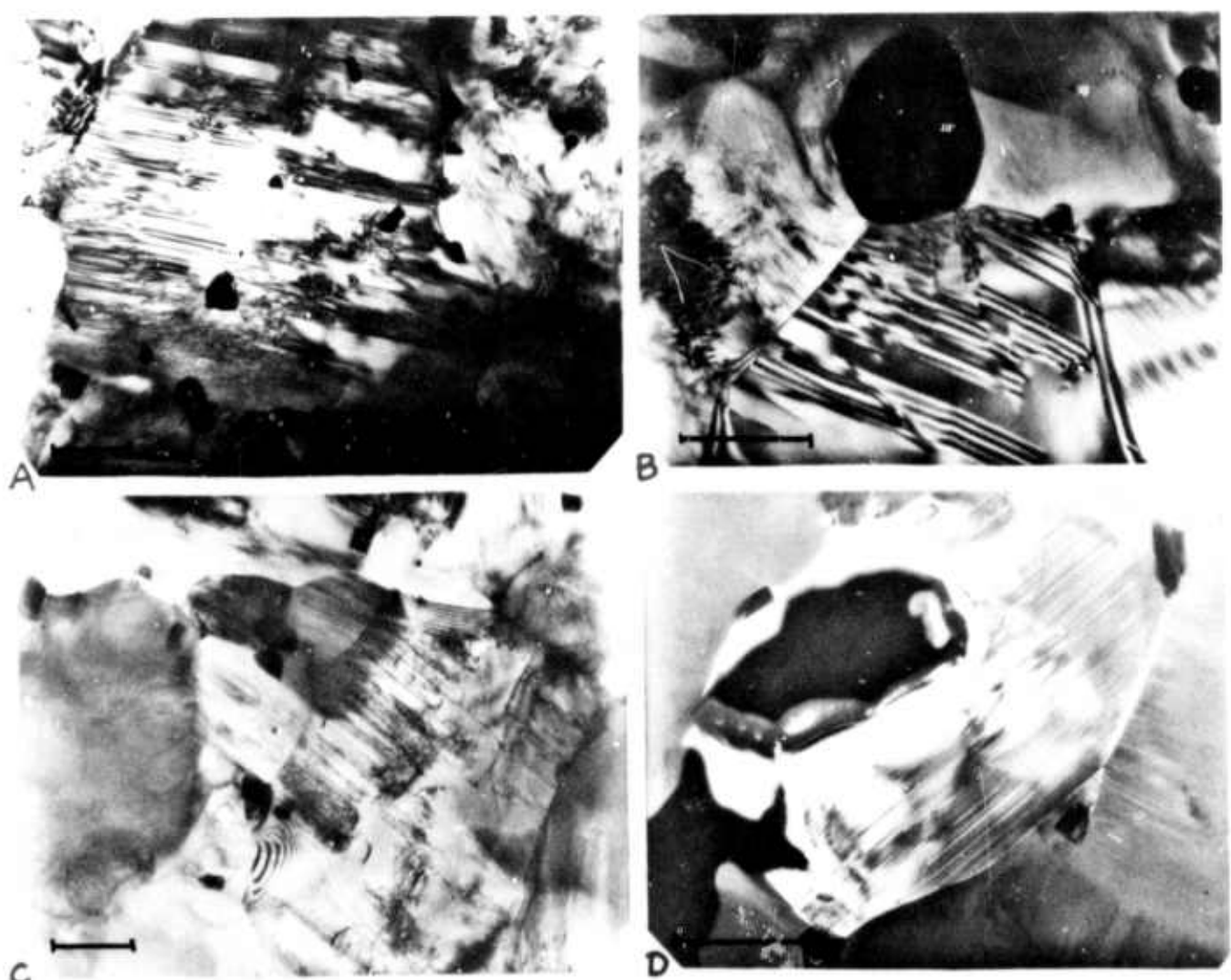


Figure 5.54 -- Typical Microstructural Details in Hot Pressed SiC  
(1 μm Scale Bar)

### 5.2.2 GAS-SOLID REACTIONS

#### Introduction

An investigation of the kinetic processes involved in the static oxidation and sulfidation of silicon nitride and silicon carbide is continuing. Work during this report period was directed toward (1) the effect of oxygen and nitrogen partial pressures on oxidation kinetics of hot pressed  $\text{Si}_3\text{N}_4$  and (2) the oxidation of hot pressed  $\text{Si}_3\text{N}_4$  and  $\text{SiC}$  in wet oxygen.

#### Effect of Oxygen and Nitrogen Partial Pressures on Oxidation Kinetics of Hot Pressed $\text{Si}_3\text{N}_4$

The preliminary experiments to study the effect of oxygen partial pressure on oxidation kinetics of  $\text{Si}_3\text{N}_4$  were reported in the second report.<sup>(2)</sup> However, these experiments were carried out on specimens from several different  $\text{Si}_3\text{N}_4$  billets. It is well known now that compositional variations from billet to billet can result in greatly different oxidation rates. Therefore, effect of oxygen and nitrogen partial pressures on oxidation kinetics of  $\text{Si}_3\text{N}_4$  was studied using specimens cut from the same billet. The billet used for these experiments was designated Norton WC 050972A.

The oxidation experiments were conducted, using the Cahn automatic electrobalance, described earlier,<sup>(3)</sup> at 2500°F in  $\text{O}_2$  and Ar gas mixtures with oxygen partial pressures in the range 0.01 to 1 atm at a total pressure of 1 atm. Following gas mixtures were used:

- (a) 1%  $\text{O}_2$  + 99% Ar
- (b) 5%  $\text{O}_2$  + 95% Ar
- (c) 10%  $\text{O}_2$  + 90% Ar
- (d) 30%  $\text{O}_2$  + 70% Ar
- (e) 50%  $\text{O}_2$  + 50% Ar
- (f) 70%  $\text{O}_2$  + 30% Ar
- (g) 90%  $\text{O}_2$  + 10% Ar
- (h) Pure  $\text{O}_2$

Both oxygen and argon gases were dried by passing them through anhydrous calcium silicate. Mixing was accomplished using glass capillary flowmeters.

The weight gain vs time curves for all these gas mixtures were identical within the range of experimental uncertainties ( $\pm 0.025 \text{ mg/cm}^2$ ), and approximated a parabola. Figure 5.55 shows a typical parabolic plot for the oxidation of  $\text{Si}_3\text{N}_4$  at 2500°F in these gas mixtures, which gives a parabolic rate constant of  $6.2 \times 10^{-12} \text{ gm}^2 \text{ cm}^{-4} \text{ sec}^{-1}$ . This value

PRECEDING PAGE BLANK-NOT FILMED

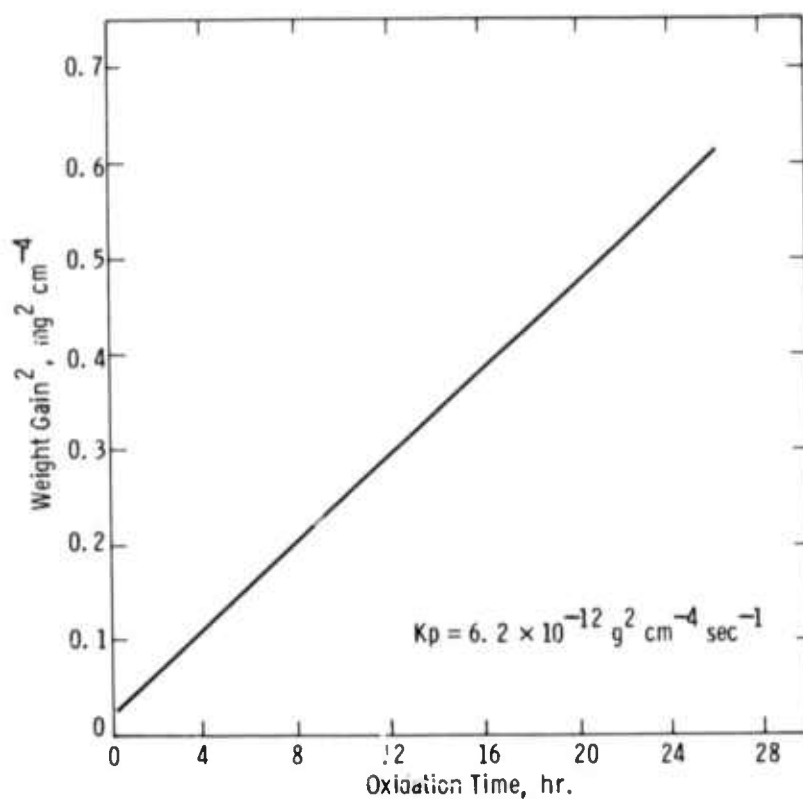


Figure 5.55 -- Typical Parabolic Oxidation of Hot Pressed Silicon Nitride in  $O_2 + N_2$ ,  $O_2 + Ar$ , and  $O_2 + Ar + N_2$  Gas Mixtures at  $2500^{\circ}F$  1 atm Total Pressure

for billet #050972A agrees very well with that of  $5.00 \times 10^{-12} \text{ gm}^2 \text{ cm}^{-4} \text{ sec}^{-1}$  obtained earlier for  $Si_3N_4$  billet #309902-1. Figure 5.56 shows the parabolic rate constants ( $k_p$ ) as a function of oxygen partial pressure. It is clear that the oxidation rate is independent of oxygen partial pressure in the range of 0.01 to 1 atm.

Similarly, in order to study the effect of nitrogen partial pressure on the oxidation kinetics of  $Si_3N_4$ , experiments were conducted at a fixed oxygen partial pressure (0.2 atm) and a fixed total pressure (1 atm) by varying the nitrogen partial pressure. The following gas mixtures were used for this series of experiments:

- (i) 10%  $N_2$  + 20%  $O_2$  + 70% Ar
- (ii) 20%  $N_2$  + 20%  $O_2$  + 60% Ar
- (iii) 30%  $N_2$  + 20%  $O_2$  + 50% Ar
- (iv) 40%  $N_2$  + 20%  $O_2$  + 40% Ar
- (v) 50%  $N_2$  + 20%  $O_2$  + 30% Ar
- (vi) 60%  $N_2$  + 20%  $O_2$  + 20% Ar
- (vii) 70%  $N_2$  + 20%  $O_2$  + 10% Ar

The weight gain vs time curves in all these gas mixtures were identical to those obtained in various  $O_2 + Ar$  gas mixtures and can be represented by the parabolic plot in Fig. 5.55 within the range of experimental error. The parabolic rate constants,  $k_p$ , at different nitrogen partial pressures are plotted in Fig. 5.57, which indicates that the oxidation rate is also independent of ambient nitrogen partial pressure.

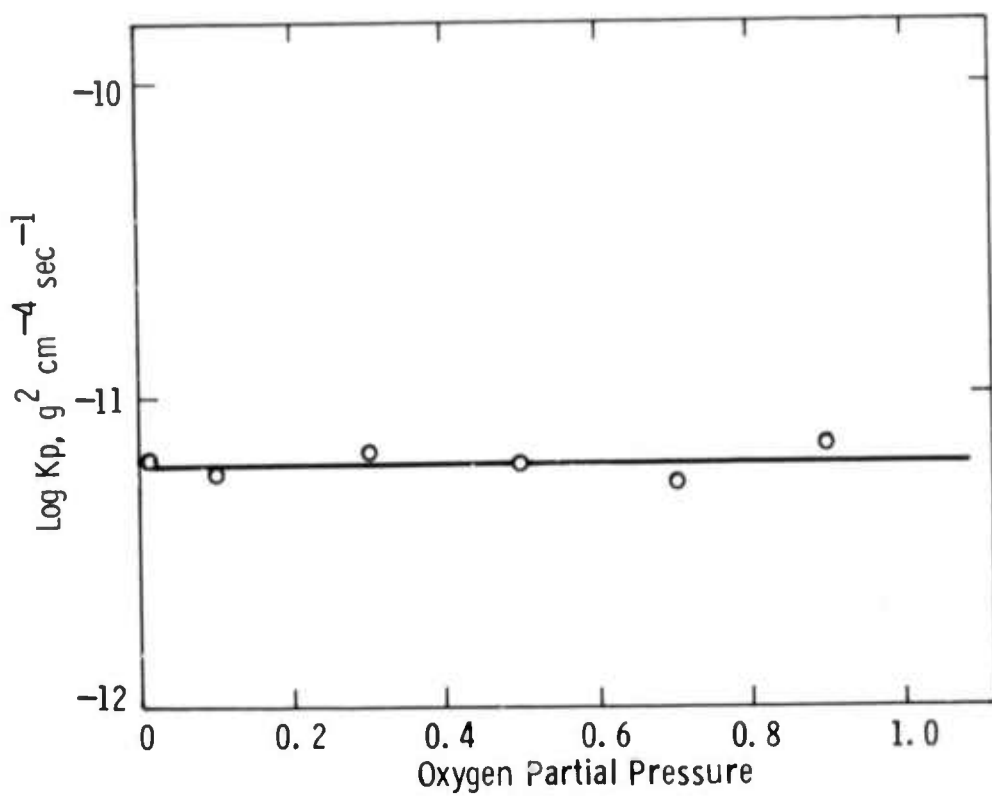


Figure 5.56 -- The Oxidation of Hot Pressed  $\text{Si}_3\text{N}_4$  in  $\text{O}_2 + \text{Ar}$  Gas Mixture  
at  $2500^\circ\text{F}$ , 1 atm Total Pressure

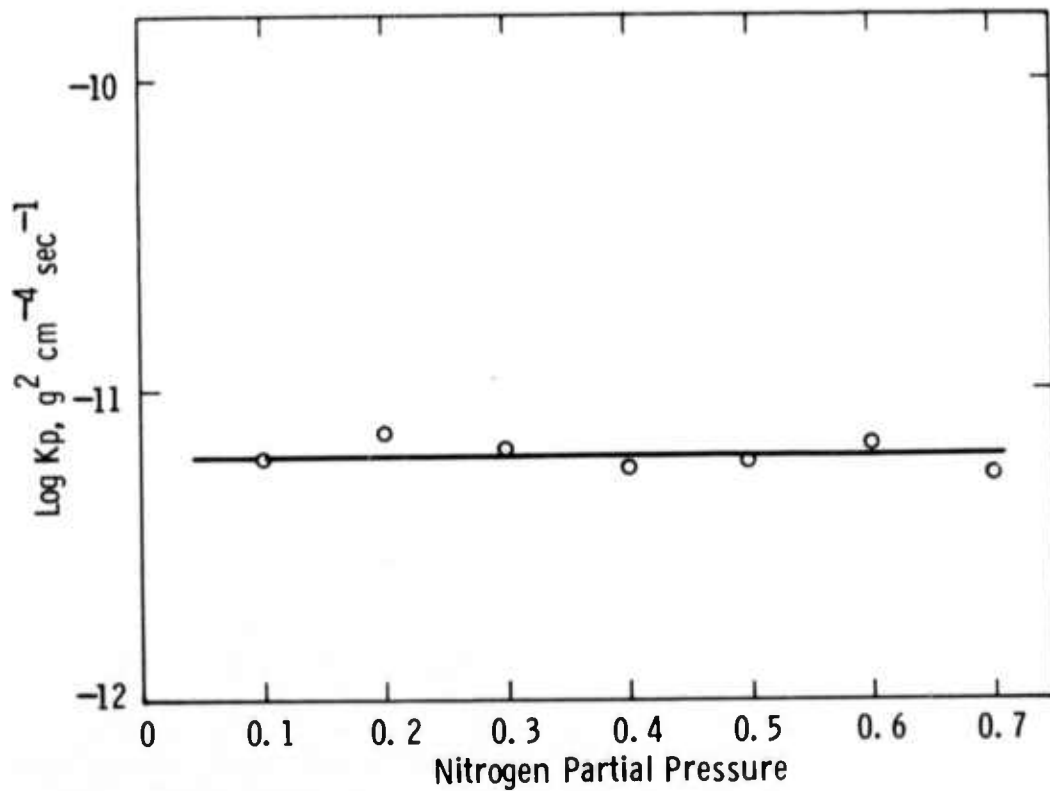


Figure 5.57 -- The Oxidation of Hot Pressed  $\text{Si}_3\text{N}_4$  in  $\text{O}_2 + \text{Ar} + \text{N}_2$  Gas  
Mixture at  $2500^\circ\text{F}$  ( $P_{\text{O}_2} = 0.2$  atm,  $P_{\text{total}} = 1$  atm)

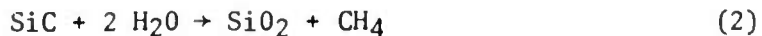
A series of oxidation experiments were conducted in  $O_2 + N_2$  gas mixtures by varying the  $O_2$  content from 10% to 90% while keeping the total pressure at 1 atm. Again, the weight gain vs time curves in all these gas mixtures were identical to the one shown in Fig. 5.55, conclusively proving that the oxidation rate of  $Si_3N_4$  (passive oxidation) is independent of ambient oxygen and nitrogen partial pressures.

#### Oxidation of Hot Pressed $Si_3N_4$ and SiC in Wet Oxygen

The previously reported oxidation experiments on  $Si_3N_4$  and SiC in dry oxygen were extended to wet oxygen. The oxygen gas was bubbled through water at room temperature ( $P_{H_2O} = 3.3 \times 10^{-2}$  atm) and then passed over the sample suspended from the Cahn electrobalance by a sapphire fiber. The specimens were in the form of approximately 0.5" x 0.5" x 0.070" thick square plates which were cut from billet #309902-1 ( $Si_3N_4$ ) and billet #NSC 472-1 (SiC). The changes in the weight of the specimens were continuously recorded as a function of time on a strip chart recorder.

The weight gain vs time curves in the temperature range 2200 to 2500°F were parabolic and similar to those obtained in dry oxygen. The oxidation products formed on  $Si_3N_4$  and SiC in wet oxygen were identical to those obtained in dry oxygen as reported earlier.<sup>(1)</sup> However, the magnitude of oxidation was slightly higher in wet oxygen for both  $Si_3N_4$  and SiC. The parabolic rate constants for oxidation of  $Si_3N_4$  and SiC in wet and dry oxygen as a function of temperature are shown in Figs. 5.58 and 5.59, respectively. The activation energy for oxidation of  $Si_3N_4$  in wet oxygen is calculated to be 116.7 kcal/mole compared to 89.5 kcal/mole in dry oxygen. Similarly, the activation energy for oxidation of SiC in wet oxygen is about 126 kcal/mole compared to 115 kcal/mole in dry oxygen. These higher activation energies for oxidation in wet oxygen may result from the diffusion of  $OH^-$  ion through the surface oxide layer.

The gases exiting from the system after passing over the hot  $Si_3N_4$  or SiC samples were analyzed by mass spectrometer to determine the extent of reaction with water vapor. The possible reactions include:



No  $NH_3$  or  $CH_4$  was detected in the exiting gases showing that these reactions did not occur as a result of oxidation by wet oxygen.

#### Characterization of Oxide Layer Formed on SiC

As reported previously,<sup>(1)</sup> the oxide layer on SiC consisted mostly of aluminum silicate ( $3 Al_2O_3 \cdot 2 SiO_2$ ) and cristobalite ( $SiO_2$ ). The oxide layer on SiC was further analyzed by a Cameca ion probe mass spectrometer. A SiC specimen oxidized at 2500°F for 24 hr. in pure dry oxygen was bombarded with an oxygen primary beam and the identity of the secondary ions arising from the surface of the oxide layer was determined by mass spectrometric analysis. Figure 5.60 shows the ion images for Si, O, Al, W, Na, and K in the oxide layer on the SiC specimens, clearly indicating that the various impurity elements in SiC diffuse outwards during oxidation and concentrate in the oxide layer. The concentration profiles for W, Al, and oxygen shown as a function of depth in the oxide layer in Fig. 5.61 also confirm that aluminum is present in the oxide layer in much greater quantity than in the SiC itself. The concentration of W in the oxide layer is roughly equal to that in the SiC substrate.

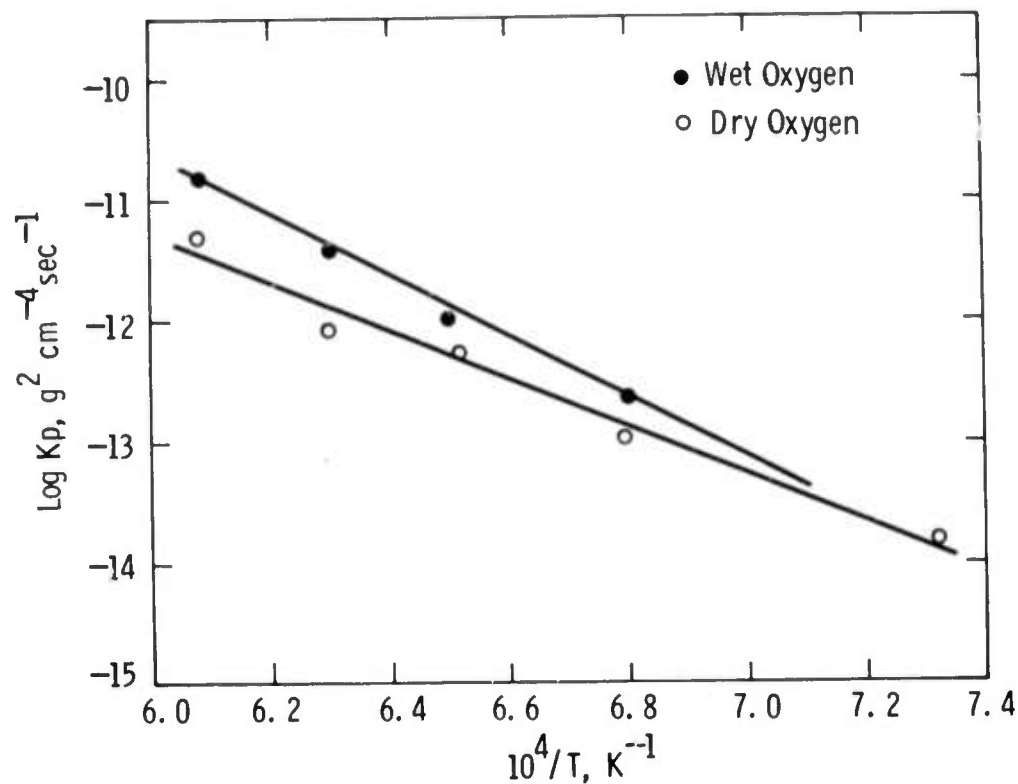


Figure 5.58 -- The Parabolic Rate Constants for the Oxidation of Hot Pressed  $\text{Si}_3\text{N}_4$  in Dry and Wet Oxygen as a Function of Temperature

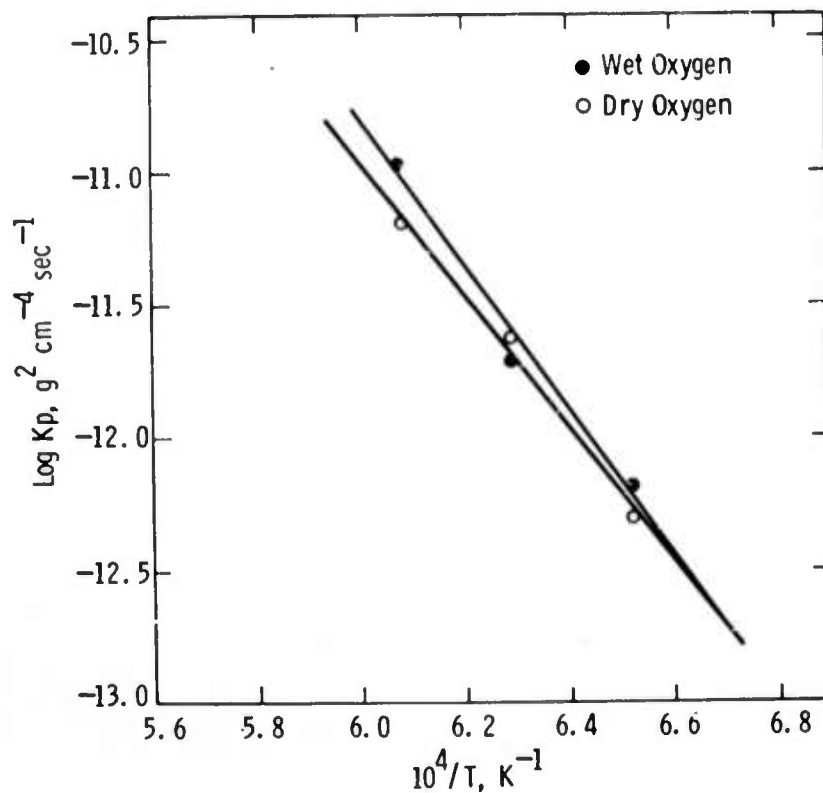
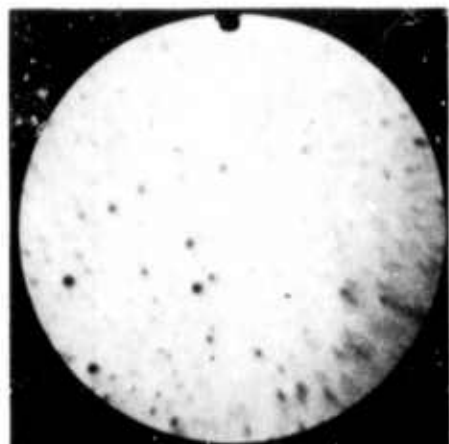
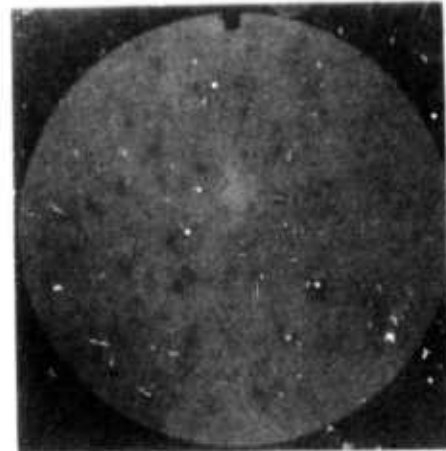


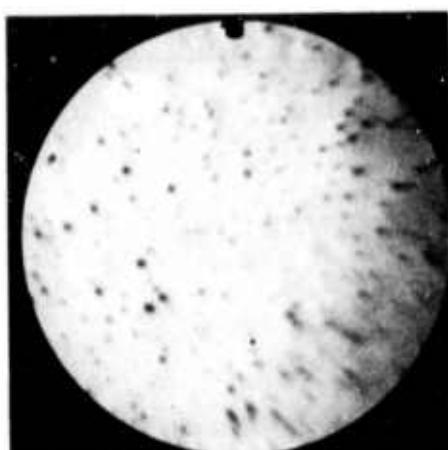
Figure 5.59 -- The Parabolic Rate Constants for the Oxidation of Hot Pressed  $\text{SiC}$  in Dry and Wet Oxygen as a Function of Temperature



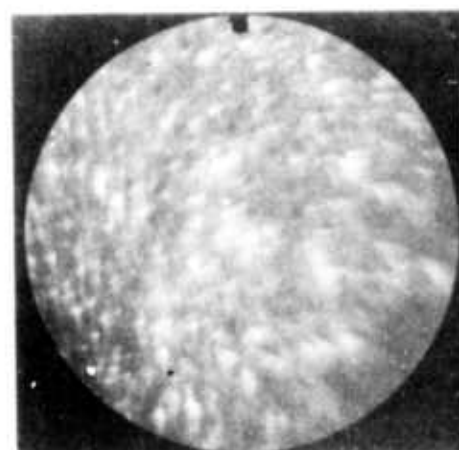
Si



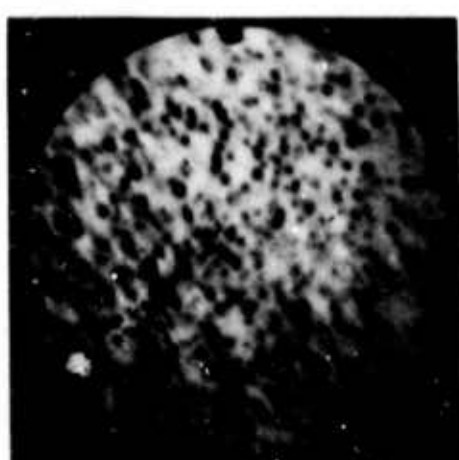
O



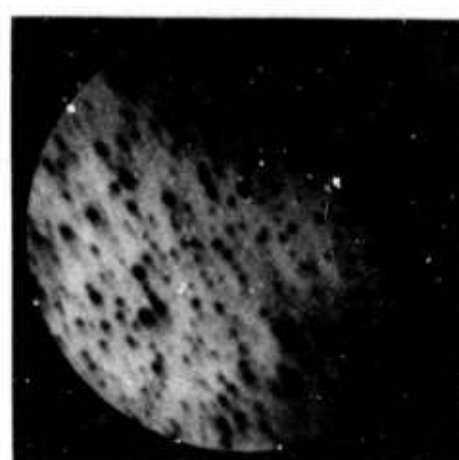
Al



W



Na



K

200  $\mu$ m

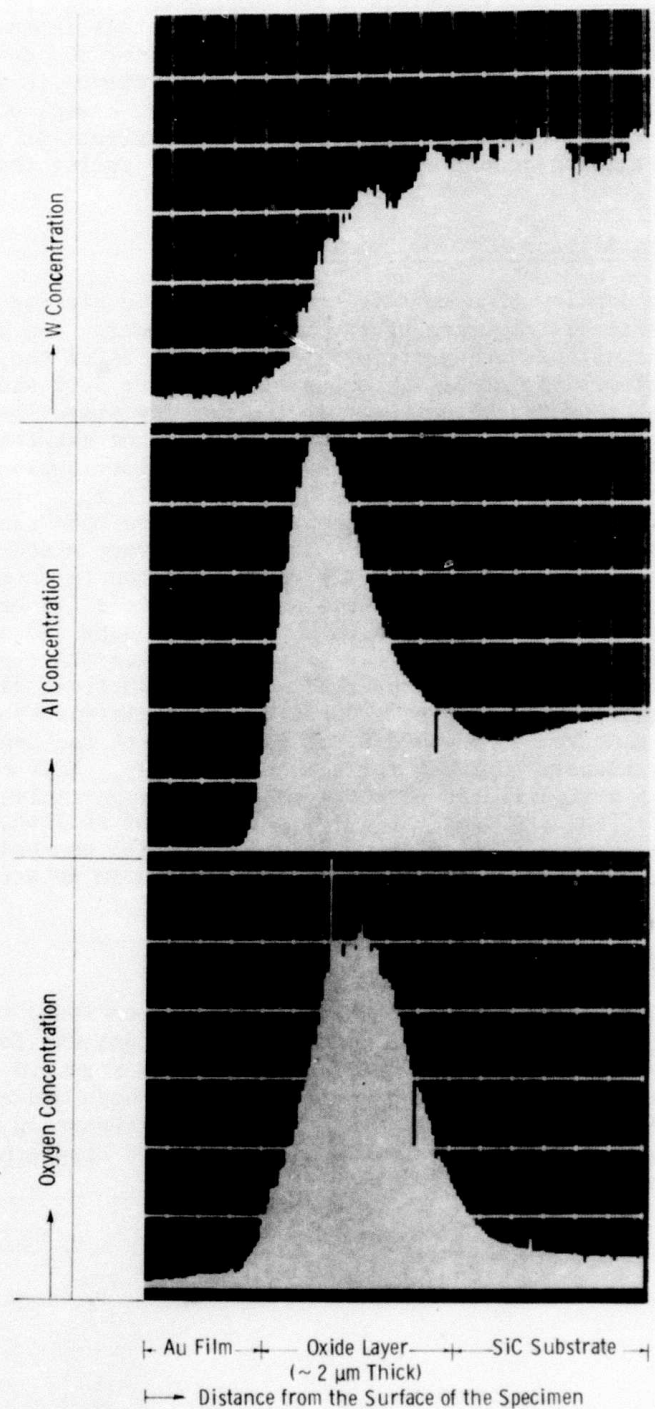


Figure 5.61 -- Oxygen, Aluminum, and Tungsten Profiles Across the Oxide Layer on a Hot Pressed SiC Specimen Oxidized for 24 hours at 2500°F in Pure, Dry Oxygen

### 5.2.3 DEVELOPMENT OF INJECTION MOLDED Si<sub>3</sub>N<sub>4</sub>

#### Introduction

The standard grade of injection-molded Si<sub>3</sub>N<sub>4</sub> has been characterized with regard to both room temperature and high temperature properties.<sup>(1,2)</sup> On the basis of strength values, it was concluded that improvements were needed in order to satisfy the stress requirements of the duo-density turbine rotor. This section will be concerned with improvements in room temperature properties only. (The high temperature properties, creep, etc., have been discussed in Section 5.1.2 of this report.) The effects of variations in density and nitriding conditions were investigated during this reporting period.

#### Improvements in Silicon Nitride Density

The green density of a ceramic component can be altered by changing the particle size distribution of the starting powders. An investigation was made of the effects of particle size distribution of the silicon metal powder used for molding of Si<sub>3</sub>N<sub>4</sub> components. Figure 5.62 shows the particle size distribution of two materials selected for investigation. Both materials came from the same basic lot of silicon metal, so the chemistry of the powders remained constant. The size ratios of these two distributions satisfies the requirements of the Particle Packing Theory; that is  $r_{\text{fine}} = 0.414 r_{\text{coarse}}$ . The effects of various mixtures of these two powders upon sintered density and bending strength were evaluated. The powders were mixed in a V-blender for 1/2 hour to insure homogeneous distribution, then injection molded into test bars and nitrided using a typical nitriding cycle (24 hours at 2300° F and 24 hours at 2660° F). Figure 5.63 shows the density and strength of the test samples as a function of different particle size fractions. This shows that the density can be increased by altering the particle distribution, with the maximum density occurring at a 50/50 particle distribution. It should also be noted that the strength did not increase with the density, but remained approximately constant for all compositions. This could be due to the presence of a significant percentage (5-10%) of particles over 44 $\mu$ . Evans<sup>(12)</sup> and Messier<sup>(13)</sup> indicate that the large particles of silicon, when nitrided, are responsible for critical flaws. Future work will concentrate on altering the maximum particle size of the silicon metal used in an attempt to verify these findings.

#### Nitriding Studies

The strength of reaction-sintered Si<sub>3</sub>N<sub>4</sub> has been found to depend heavily on the nitriding cycle. The room temperature strength was found to increase by 20% by varying the nitriding cycle. The maximum strength attained was 20,500 psi. This was accomplished using a nitrogen atmosphere and cycle of 36 hours at 2300° F followed by 4 hours at 2660° F. During this reporting period, the effect of nitriding atmosphere was evaluated in relation to strength.

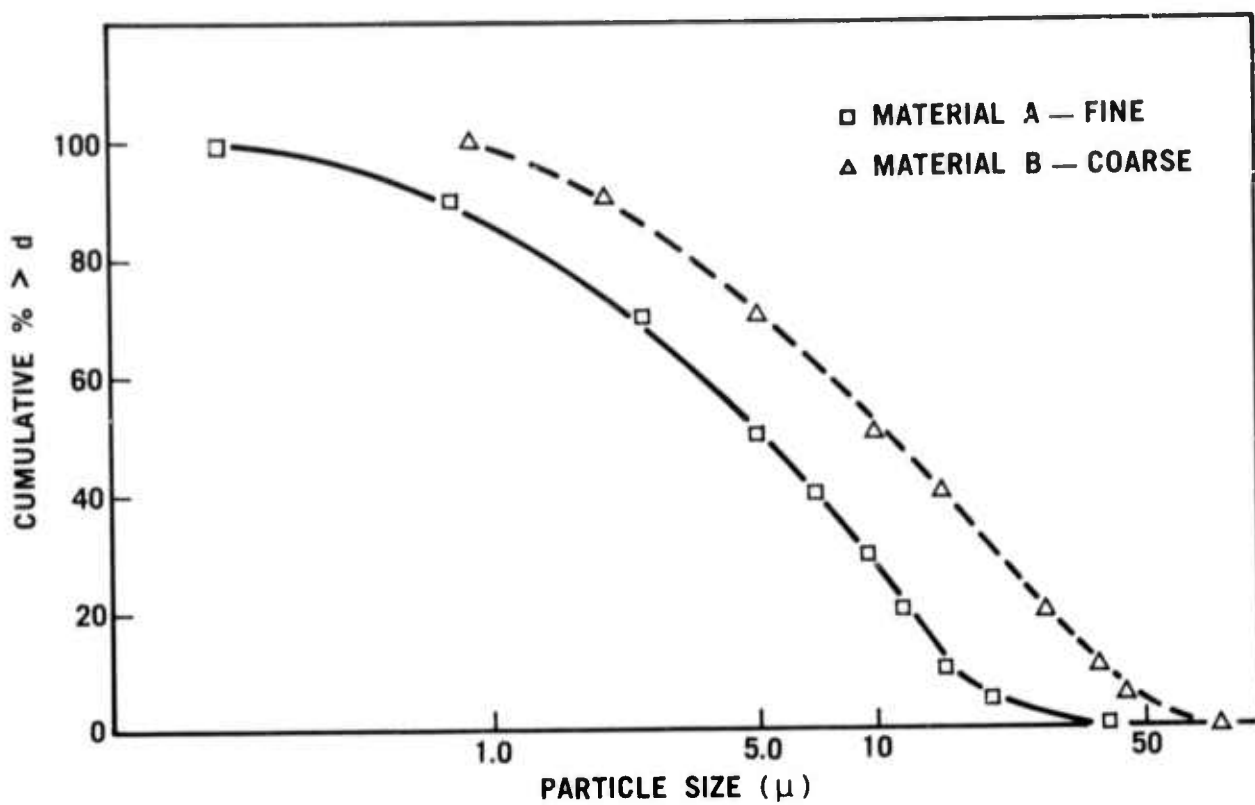


Figure 5.62 Particle Size Distribution of Silicon Metal Powder

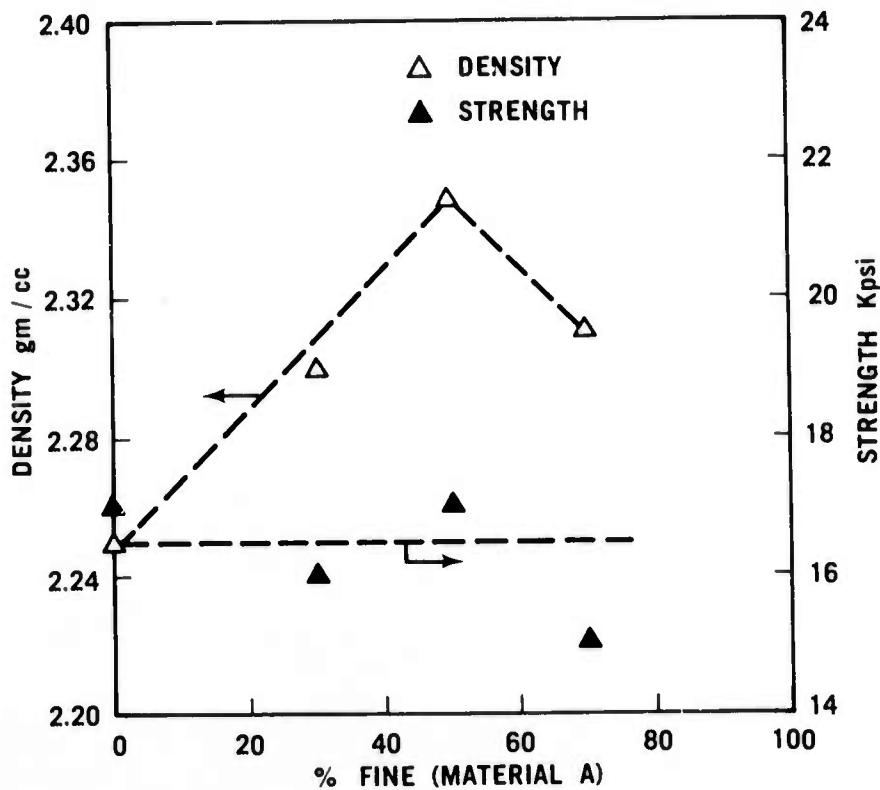


Figure 5.63 Density and Strength of Injection-Molded Silicon Nitride as a Function of Particle Size Variation of Silicon Metal Powder

The most significant results were obtained when small amounts of hydrogen were added to the nitrogen. The strength results for  $\text{Si}_3\text{N}_4$  test samples made from two different types of silicon powder are given in Table 5.13. The Type A silicon has a high level of calcium impurity, while the Type B is low in calcium. Complete analysis of these powders is shown in Table 5.10 of Section 5.1.2 of this report. For a 36/24 time-temperature cycle, the strength of the high calcium material reaches a maximum of 27,000 psi using a 1%  $\text{H}_2$  + 99%  $\text{N}_2$  mixture. This is a 40% improvement with respect to the standard 36/24 cycle and a 60% improvement over the standard grade of material using a 24/24 nitriding cycle.

The low calcium  $\text{Si}_3\text{N}_4$  appears less sensitive to the amount of hydrogen present. All strength results are in the 22,000 to 25,000 psi range, with the maximum of 24,780 psi occurring at the 1% hydrogen level. This is a 35% improvement in strength over the baseline 36/24 nitriding cycle.

A limited number of other time-temperature cycles were studied, with the 36/24 cycle being chosen as the optimum cycle.

Table 5.13 also shows that the density of the low calcium material also seems to increase as a function of the percent hydrogen addition. The mechanism involved with this density increase is not understood, and will be the subject of further investigation.

Table 5.13 Nitriding Results

Cycle *	Atmosphere	Silicon Type A		Silicon Type B	
		Strength (psi)	Density (gm/cm <sup>3</sup> )	Strength <sup>o</sup> (psi)	Density (gm/cm <sup>3</sup> )
36/24	$\text{N}_2$	19,100 ± 2200	2.25	18,150 ± 1770	2.31
36/24	$\text{N}_2 + 1.0\% \text{ H}_2$	27,100 ± 2900	2.32	24,780 ± 1560	2.38
36/24	$\text{N}_2 + 1.8\% \text{ H}_2$	22,800 ± 2700	2.27	22,100 ± 1300	2.31
36/24	$\text{N}_2 + 4\% \text{ H}_2$	18,650 ± 1625	-	23,850 ± 2275	2.46
36/24	$\text{NH}_3$	19,225 ± 950	2.25	23,350 ± 4100	2.45

\* 36/24 Cycle is defined as 36 hrs. at 2300° F and 24 hrs. at 2600° F

\* 4-Point Bending, 1/4" dia x 4" sample, 1" x 3" Fixture dimensions, 0.10 in/min cross-head speed

o 4-Point Bending, 1/8" x 1/8" x 1-1/2" sample, 3/8" x 3/4" Fixture dimensions, 0.10 in/min cross-head speed

### 5.3 NON-DESTRUCTIVE EVALUATION OF MATERIALS

#### SUMMARY

Activity during this reporting period was concentrated on the use of NDE procedures on hot-pressed silicon nitride. This effort included ultrasonic defect detection, surface crack detection by acoustic emission techniques, and an evaluation of x-ray xeroradiography. Much of this work consisted of an exploration of new systems and techniques aimed at expanding the capabilities for non-destructive evaluation of turbine ceramic materials.

Studies were conducted using a computer-aided ultrasonic system to measure discontinuities in hot-pressed silicon nitride. The results of this work indicated that a system with a frequency capability of greater than 5 MHz is needed to characterize the discontinuities in hot-pressed  $\text{Si}_3\text{N}_4$ . The computer-aided system was shown to possess greater sensitivity for flaw detection than the water-immersion system.

Acoustic emission (AE) equipment was employed to measure the response of surface flaws in hot-pressed silicon nitride. The flaws were preferentially induced in hot-pressed  $\text{Si}_3\text{N}_4$  by thermal shocking with a  $\text{CO}_2$  laser. Varying degrees of AE response were noted relative to the power density of the laser. A relationship was established between the AE detected during laser thermal shocking and a reduction in flexural strength of the  $\text{Si}_3\text{N}_4$ . The laser was then used at reduced energy levels to extend the previously induced cracks. Relationships between the propagation of these cracks and AE response were determined. These results indicate the usefulness of AE as a means of detecting unknown surface flaws.

A comparison was made between conventional x-ray radiography and xeroradiography, a process developed by the Xerox Corporation, using a hot-pressed  $\text{Si}_3\text{N}_4$  step block standard. The results of this work showed that the xeroradiography process permits a wider range of material thickness to be imaged without a subsequent loss in radiographic quality.

### 5.3.1      ULTRASONIC NDE

#### Introduction

Previous investigations (1,2,3) have shown that ultrasonic pulse-echo techniques may be applied to ceramic systems with an inherently high level of discontinuities which will provide information about the quality of the material. While the techniques developed thus far have detected many material discontinuities, situations were noted where the discontinuity was too small to be detected using conventional equipment. This is especially evident in theoretically dense ceramics where fabrication processes minimize gross defects and the resulting high sonic velocities necessitate evaluation at increasingly higher frequencies. The ultrasonic evaluation system could therefore be improved by increasing its sensitivity.

Continuing efforts to utilize all available means to non-destructively evaluate ceramics resulted in funding the University of Michigan to investigate applying a previously developed ultrasonic pulse-echo technique (14) to ceramic rotor materials. This consisted of a new computer-assisted system capable of increased flaw resolution and sensitivity using conventional ultrasonic instrumentation, which yields basically the same results as the use of higher frequencies. Both in-house hot-pressed and Norton HS-130 hot-pressed silicon nitride were submitted for evaluation. The data obtained have verified the fundamental concepts of this new approach, but equipment problems were encountered which limited the utilization of this technique.

#### Ultrasonic Evaluation of Hot-Pressed Silicon Nitride

Two engineering goals were established at the beginning of this program; (1) the existing computer-aided technique would be modified so that it would interface easily with the Ford ultrasonic test equipment, and (2) this system would be used to demonstrate increased ultrasonic sensitivity for the evaluation of hot-pressed  $\text{Si}_3\text{N}_4$ . The only piece of equipment in the modified computer-aided ultrasonic system not available at the beginning of the project was a device that would generate precise delays, under the control of a computer, for signal averaging purposes. This necessitated construction of a less versatile substitute which would function in an identical manner to the commercial equipment but only up to 5 MHz. While operation of the substitute device at higher frequencies was known to be unpredictable, this approach did allow evaluation of the constructed system up to the 5 MHz limit.

While the equipment necessary to implement the computer-aided ultrasonic system was being assembled, some hot-pressed  $\text{Si}_3\text{N}_4$  test samples were inspected with the conventional water immersion ultrasonic system. It was found that the computer-aided ultrasonic testing equipment was significantly more sensitive than the equipment used for previous experiments. Using this increased sensitivity, the following observations were made:

1. Echo amplitudes from targets in hot-pressed  $\text{Si}_3\text{N}_4$  were of the same order of magnitude as the amplitude of ultrasonic scattering from the microstructure of the test pieces.

2. The echo amplitude from the microstructure varied considerably when measured in test samples representing different lots of material.

Figure 5.64 shows the microstructure scattering from four different  $\text{Si}_3\text{N}_4$  ceramic samples. These sections contain no apparent discontinuities, and the echoes were recorded under identical experimental conditions.

Once the necessary equipment had been assembled and tested for accuracy and stability, a series of experiments was undertaken to investigate the operating characteristics of the system using a 2.25 MHz ultrasonic transducer. These experiments demonstrated that the computer-aided ultrasonic system was capable of the following improvements as compared with a conventional system:

1. Processed data have 20 dB more sensitivity than unprocessed data when the primary noise source is electrical noise.
2. Processed data have 6 dB more sensitivity than unprocessed data when the primary noise source is microstructure scattering.

Unfortunately, several factors prevented the above experiments from being performed on ceramic test samples. The sensitivity of the immersion test system is limited by electrical noise while the sensitivity of the computer-aided ultrasonic test system is limited by microstructure scattering. Thus, it was necessary to simulate the electrical noise experienced by Ford, and this was done with a plastic test sample loaded with micron-sized metallic particles. Also, as the amplitude of the microstructure scattering is a strong function of frequency, it was impossible to duplicate the actual test conditions performed at 15 MHz with the computer-aided system operating at 2.25 MHz.

Figure 5.65 demonstrates the sensitivity enhancement capability of the computer-aided ultrasonic system. The target is a flat-bottom hole in a plastic test sample leaded with micron-size metallic particles. In Figure 5.65A, only one digital sample was taken per waveform position. Thus, this figure represents what would be displayed on the CRT of a conventional ultrasonic system. In Figure 5.65, the statistical average of ten digital samples per waveform position is plotted. The improvement in sensitivity is due to the fact that the statistical average of the electrical noise tends toward zero as the number of samples increases while the statistical average of the target signal is constant. Figure 5.65 shows this effect to a greater extent since the statistical average of 100 samples per waveform position is plotted and results in an overall sensitivity gain of 20 dB.

It was found that reducing the microstructure scattering noise is more difficult than reducing the electrical noise. Since the microstructure noise is related to the target echo through the fixed geometry of the scattering centers, target, and transducer, this noise can only be reduced by moving the transducer. Transducer movement will cause both the target signal and the scattering noise to change, but because the target signal changes are predictable and the scattering noise is random, data processing techniques can be used to decrease the effect of the noise.

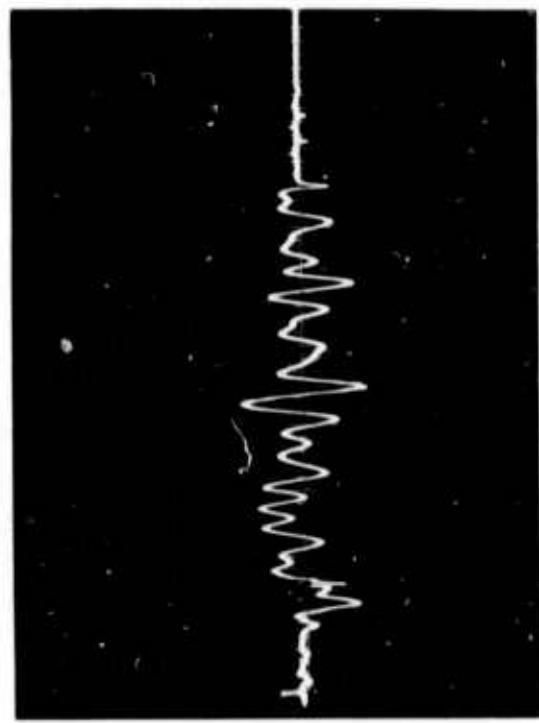
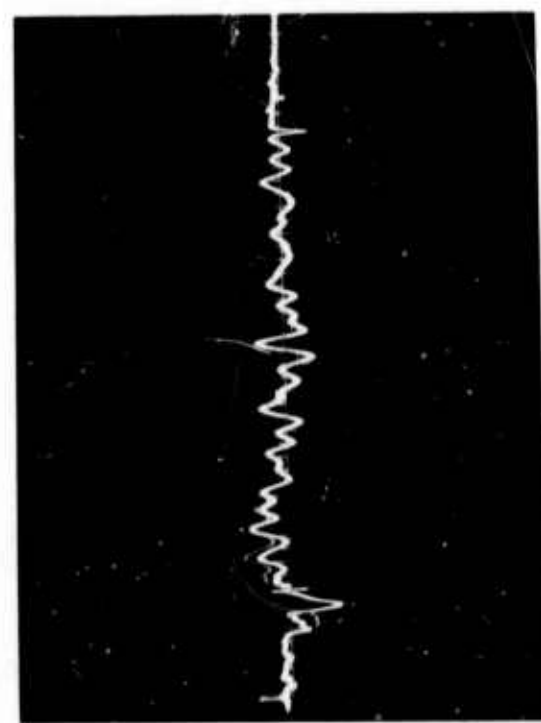
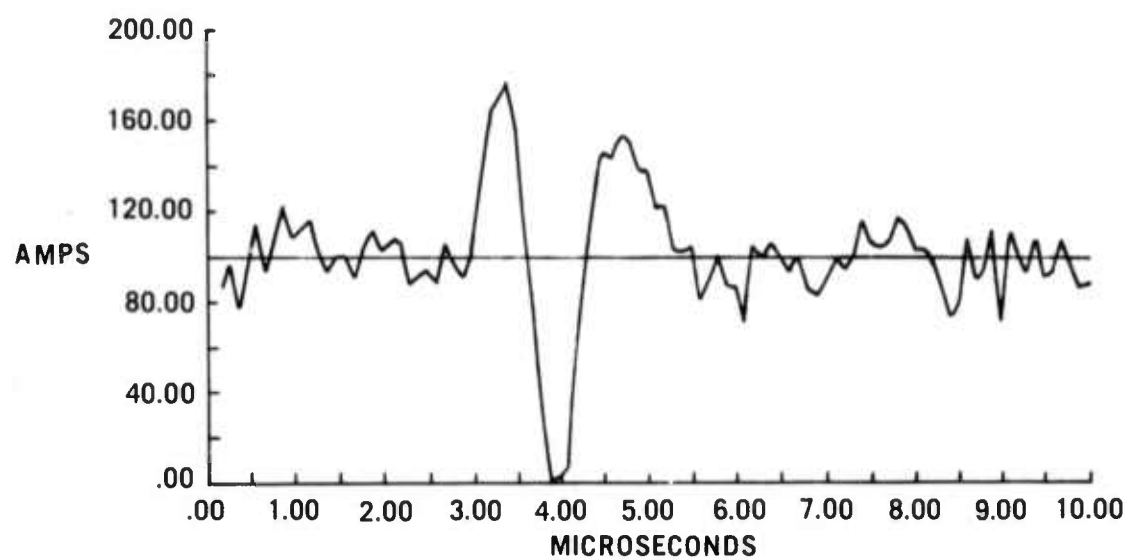
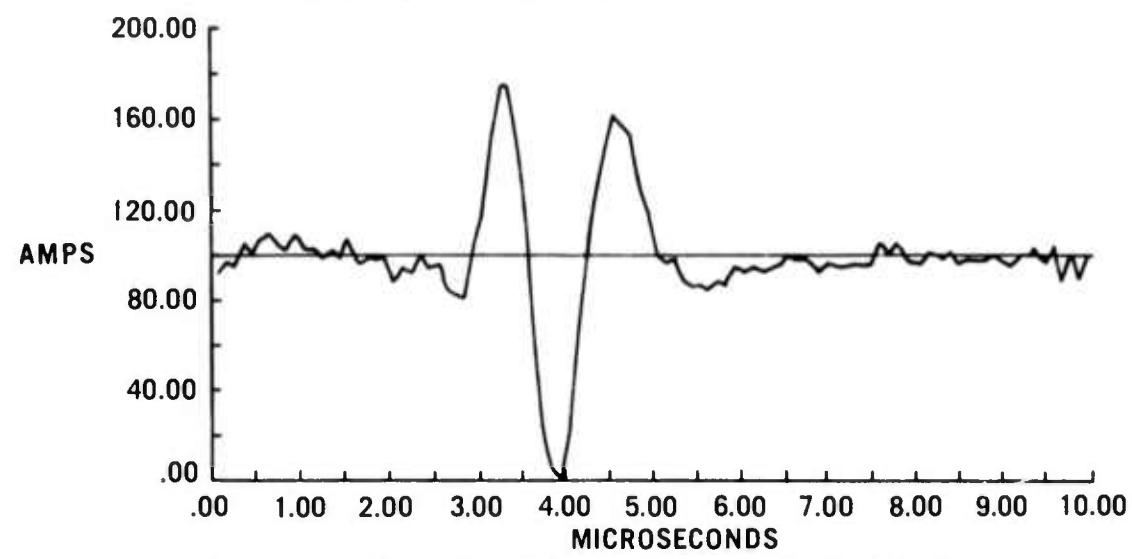


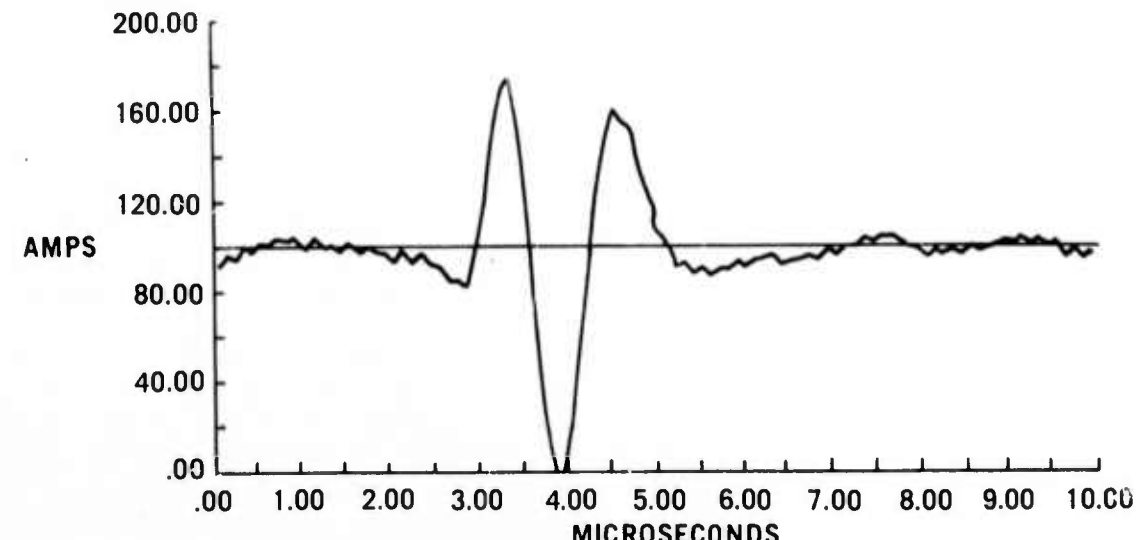
Figure 5.64 Microstructure Scattering of Ultrasonic Echoes in Hot-Pressed Silicon Nitride, A,B,C-Ford Material, D-Norton HS-130 Material



A) One Digital Sample per Waveform Position



B) Ten Digital Samples per Waveform Position



C) One Hundred Digital Samples per Waveform Position

Figure 5.65 Digital Recordings of Electrical Noise and Ultrasonic Echoes From Flat-Bottomed Hole in Plastic Specimen.

### 5.3.2 ACOUSTIC EMISSION

#### Introduction

A program was initiated to evaluate the surface of dense silicon nitride using acoustic emission (AE) to monitor the response of applied thermal stresses. The goals were to develop the important testing parameters on flexural test specimens and to establish the feasibility of evaluating an unknown surface such as a hot-pressed  $\text{Si}_3\text{N}_4$  rotor disk. The use of a  $\text{CO}_2$  gas laser to preferentially damage the  $\text{Si}_3\text{N}_4$  surfaces, and then to thermally stress the near surface for flaw detection by AE techniques, was investigated. The results indicate the potential usefulness of such a non-destructive evaluation procedure in terms of detecting surface flaws and their effects upon structural integrity. The acoustic emission response of hot pressed silicon nitride and silicon carbide to mechanical stress by four point bend tests was investigated in an attempt to develop a proof test monitoring capability. The detection of Hertzian cone crack initiation in  $\text{Si}_3\text{N}_4$  was also investigated.

#### Thermal Stress Monitoring

The program of thermal stress monitoring consisted of: (1) obtaining test specimens of dense silicon nitride, (2) inducing small surface cracks in these specimens with a focused  $\text{CO}_2$  laser, (3) subjecting these damaged specimens to four-point bending to determine the effect of the induced cracks on strength, and (4) thermally exciting the induced flaws using the  $\text{CO}_2$  laser at low power density levels to allow detection by AE instrumentation while insignificantly affecting structural integrity. Although these specific objectives initially appear discrete, the use of AE monitoring while inducing surface cracks actually serves as an indicator of the extent of damage and links them together. This AE data is then correlated to the reduction in flexural strength so that damage levels could be repeated for the thermal excitation/detection portion of the test program. The overall program plan is shown in Figure 5.66. The test specimens were fabricated in-house by sectioning plates of Ford hot-pressed silicon nitride. Densities of  $3.19 \text{ gm/cm}^3$  were attained and machining by diamond grinding produced surface finishes of 7-16 microinches. The specimen dimensions were 0.100 in. x 0.31 in. x 3.0 in. Some testing was also conducted on commercially obtained hot-pressed silicon nitride (Norton HS-130 and HS-110). Care was taken to remove residual contamination on the surfaces prior to laser thermal shocking. Ultrasonic absorption during laser scanning for surface flaws. Variations or randomness in the laser shocking sequence could be tolerated since a wide range in damage levels could be obtained. This was sufficient to determine the effects of various crack levels since a correlation between the AE detected during shocking and a reduction in flexural strength was achieved. It was then possible to repeat these damage levels, as indicated by the AE detected during shocking, on test specimens to be used only for flaw detection by laser scanning.

Varying magnitudes of surface damage were achieved by 10 millisecond pulses with a 400 watt focused  $\text{CO}_2$  laser. The spot size was 0.020 in. in diameter and surface cracks were usually confined to this region. Several levels of crack severity as well as varying crack orientation were obtained. The AE detected also varied with the observed surface crack branching and therefore served as an indicator of the extent of surface damage.

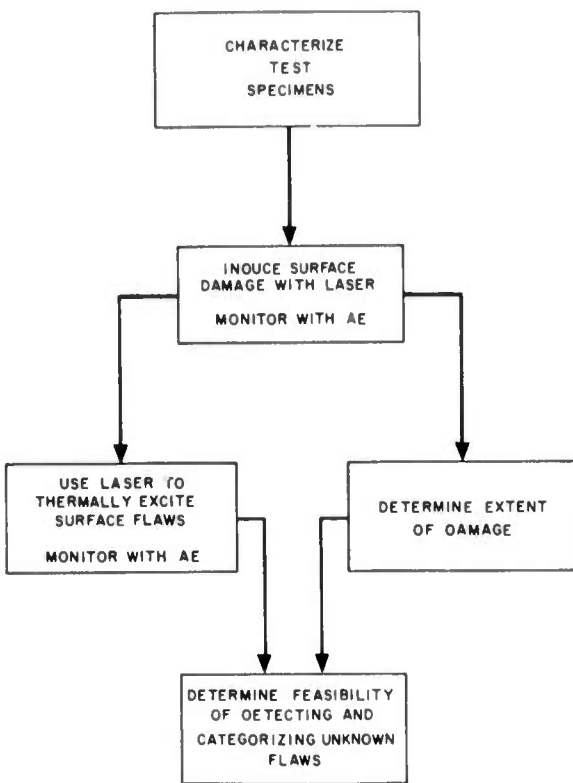


Figure 5.66 Program Plan For Thermal Stress Monitoring

Monitoring the thermal shocking, flexural testing, and laser scanning processes was accomplished with Dunegan 3000 series equipment. An amplifier bandwidth of 100 - 300 KHz was used with a piezoelectric transducer having a nominal resonance of 140 KHz in all tests to detect the occurrence of AE events.

The optics of the laser system produced a converging-diverging beam. Positioning the test specimens at various levels in the converging portion resulted in controlling, to some degree, the extent of surface damage achieved. Thermal excitation of previously induced cracks was accomplished by utilizing the diverging portion of the beam to approach the required stress levels necessary to slightly propagate the surface cracks. The crack extension resulted in a release in stored strain energy which was then detected by AE instrumentation.

An Instron testing machine was used to determine the effects of flaws on four-point flexural strength. The bending fixture had 0.25 in. diameter knife edges, an upper span of 0.75 in. and a lower span of 2.0 in. Guide pins served to position the test specimen perpendicular to the knife edges and to locate the upper half of the fixture over the lower half. Teflon sleeve bushings and teflon tape on the knife edges were used to minimize noise generated at moving surfaces. A constant crosshead rate of 0.02 in/min. was used during loading.

Laser scanning to detect the various known levels of surface damage was achieved with the CO<sub>2</sub> laser thermally stressing the near surface of the material. Combinations of laser power density and scanning speeds were obtained by proper positioning of the test specimen and a programmable table.

For the majority of tests conducted, successful detection of surface flaws was accomplished using a constant scanning rate of 0.20 in/sec. and incrementally increasing the available thermal energy until slight crack extension was displayed with no other observable damage to the surface of the material. However, other combinations of scanning rate and defocus distance also proved capable of activating surface cracks and allowed for detection by the AE monitoring instrumentation.

#### Effects of Flaws

The process of inducing surface cracks in dense silicon nitride vividly indicates the notch sensitivity of high elastic modulus material. As the laser power density increased, a rapid increase in detected AE was also noted. Figure 5.67 reveals the damage threshold of the material. As the defocus distance decreased, the focal plane of maximum power in the laser beam was approached, resulting in a sudden increase in detected AE. Confirmation of the extent of damage was established by scanning electron microscopy (SEM) and correlated with the increase in AE. Extensive crack formation would result in an increased release of stored strain energy, therefore yielding high levels of AE.

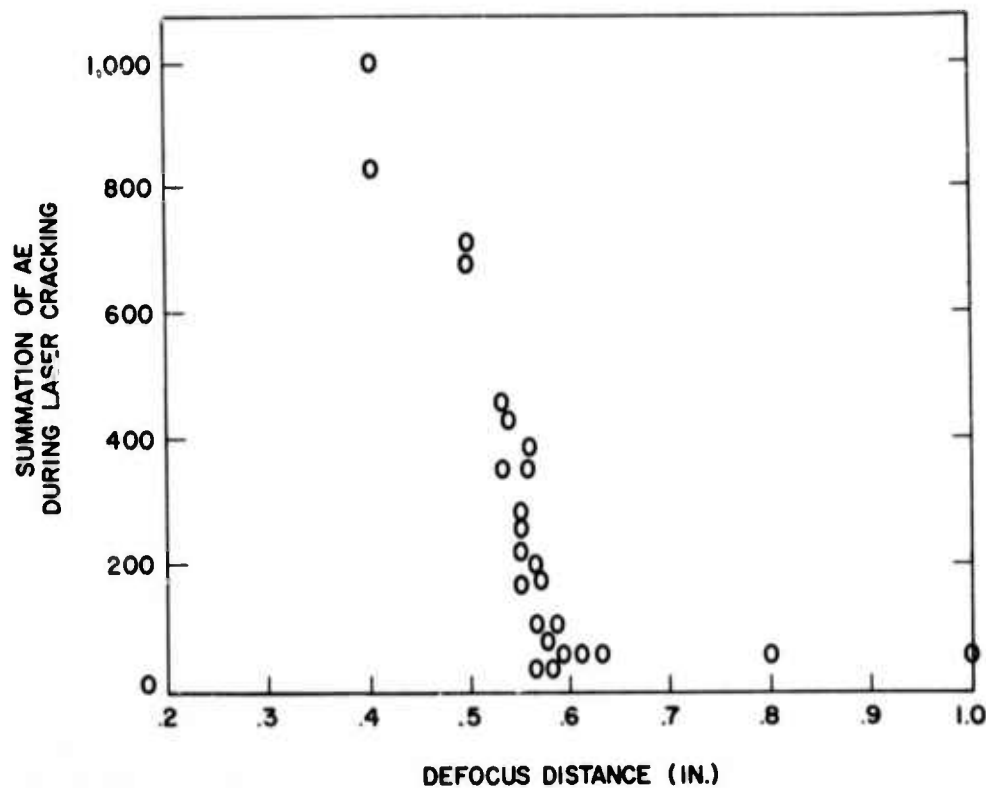


Figure 5.67 Notch Sensitivity of Ford Hot-Pressed Silicon Nitride Shown as a Rapid Increase in AE with Decreasing Defocus Distance (Increasing Power Density).

Several levels of crack severity, as well as a varying crack orientation, are shown in Figure 5.68A and B. A change in crack pattern is indicative of the change in power density of the laser as the defocus distance varies. However, slight increases in power density, at the damage threshold level, resulted in a widely differing AE response. Also, similar results were obtained at a constant power density once the damage threshold was reached. This varying AE response and therefore the extent of damage can be attributed to either the material's response to thermal stress, reflecting a differing notch sensitivity, or to high energy concentrations associated with the short time laser pulses. Some preferential pitting, as shown in Figure 5.69 indicated the presence of the latter condition, but the effects of notches near or at the surface cannot be neglected.

The effects of various flaw damage levels, as indicated by the level of AE detected during laser thermal shocking, are shown in Figure 5.70. A reduction in flexural strength is noted as the AE count increases. While damage levels reducing the strength more than 35% were easily obtained, surface flaws which reduced flexural strength less than this amount were more difficult to produce. This again is related to the notch sensitivity of the materials since a randomness in damage is experienced as the damage threshold is approached. Also noted in Figure 5.70 is the level of AE detected with no apparent reduction in flexural strength. An AE level of about 50 counts may or may not result in a strength reduction of 15%. Since the mass of the test specimens was small, this level of AE may represent that portion of the energy which was transduced to a mechanical compression wave. It was noted that inducing similar damage levels in large specimens, such as a billet of silicon nitride, is extremely difficult. A complete lack of this low level AE response was observed when a billet of Norton HS-130 was subjected to this sequence of inducing surface cracks, even though an instrumentation gain of 99dB was used.

Scanning electron micrographs of fractured surfaces do show an apparent transition from thermally to mechanically created cracks. This must be termed apparent, however since no real change in surface morphology was exhibited within the resolution capabilities of the SEM. Figure 5.71A reveals the apparent heat-affected region and contrasts it with the final fracture surface. Final failure runs through the laser-induced flaw as shown in Figure 5.71B. An undulation is observed corresponding to the crack branches associated with the laser-induced damage.

During flexure testing and monitoring for slow crack growth, slight crack extension was observed. Typical curves are shown in Figure 5.72 where the logarithmic summation of AE is shown to increase prior to final failure. Flexure tests conducted on test specimens that were not laser shocked did not exhibit detectable AE events prior to failure. Ideally, the shocked specimens should be sequentially loaded until extension is observed, as indicated by the magnitude of AE detected, and then inspected for crack extension by SEM. This assumes that crack extension on the surface and in the interior occurs uniformly. Changes in crack density or initial crack length would relate to the level of AE detected, since flexure testing produces the maximum stress at the surface or outermost fiber of the specimen.

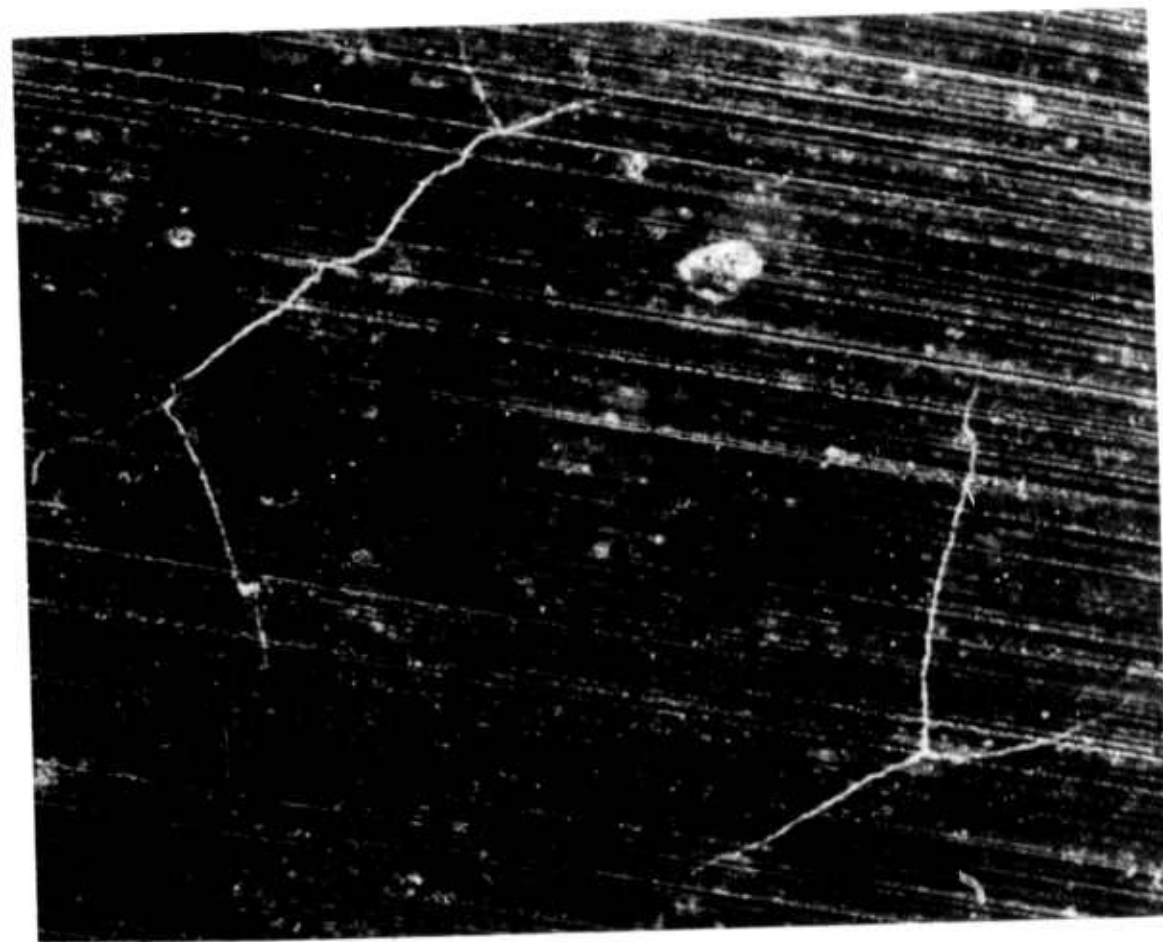
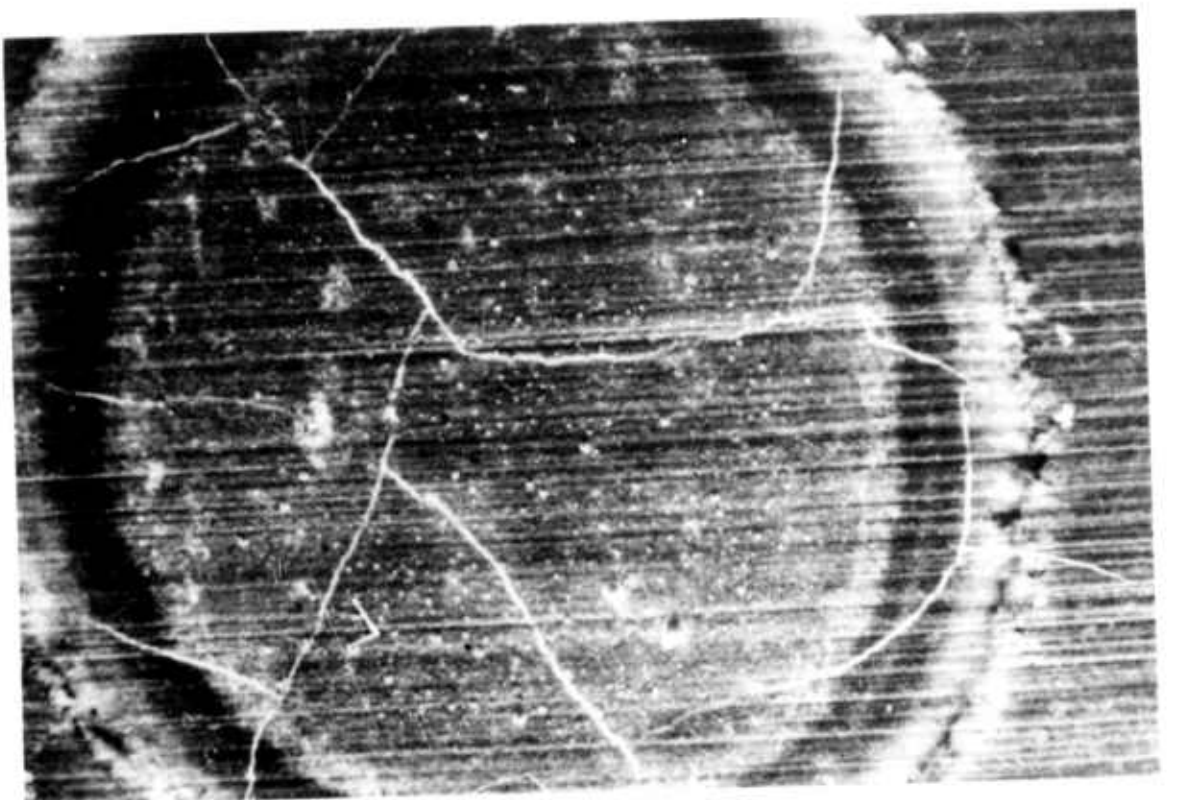


Figure 5.68 Scanning Electron Micrographs of Ford Hot-Pressed Silicon Nitride  
Showing Surface Crack Severity and Orientation. AE Detected  
During Shocking: A) 1255 and B) 219 (80X)



Figure 5.69 Scanning Electron Micrograph of Ford Hot-Pressed Silicon Nitride  
Showing Pitting and Irregular Heat-Affected Area, Indicating Possible  
High Energy Concentrations During Laser Shocking. Total AE Detected  
Was 394. (80X)

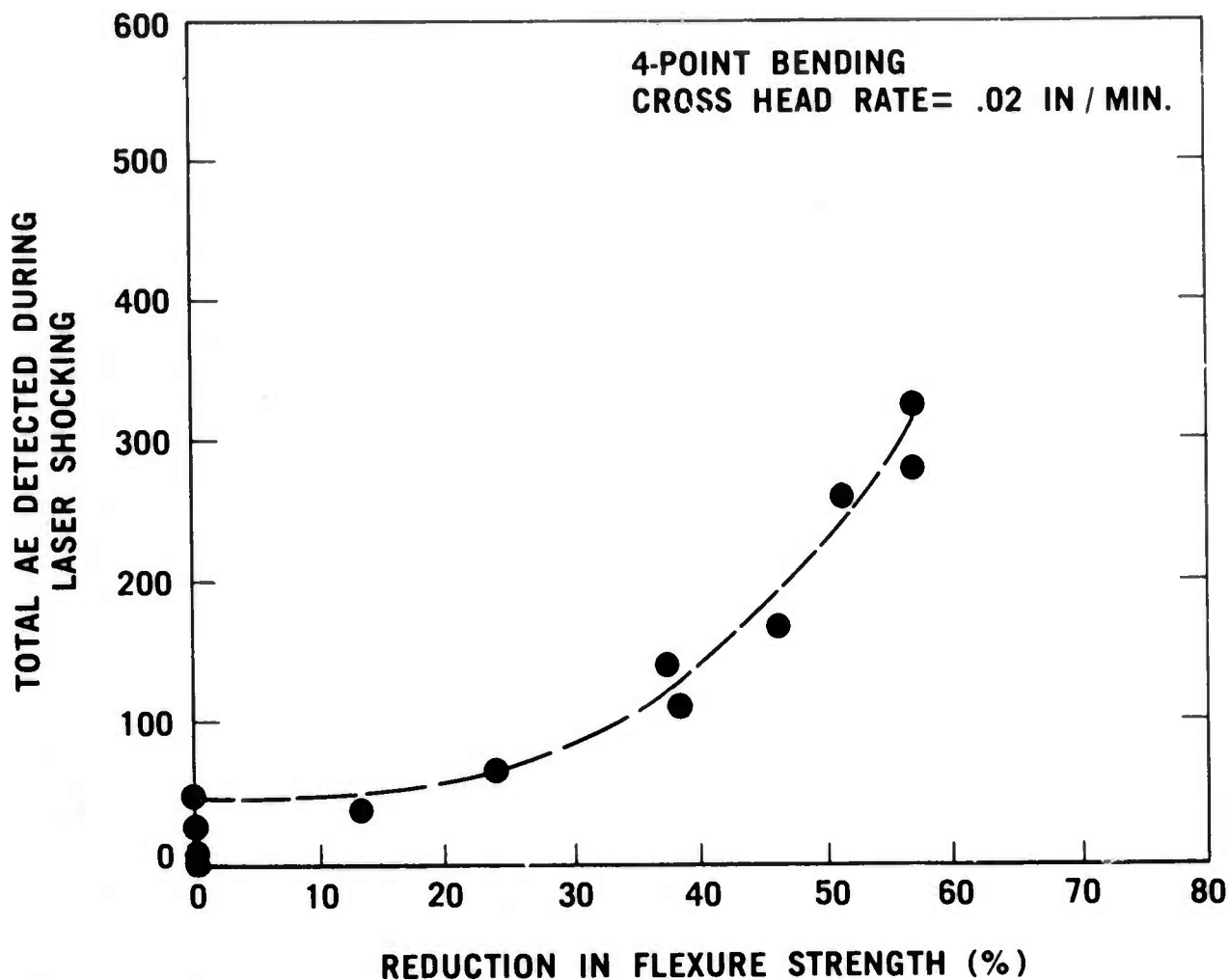


Figure 5.70 Reduction in Flexural Strength vs AE Detected During Laser Shocking the Surface of Ford Dense Silicon Nitride Test Specimens.

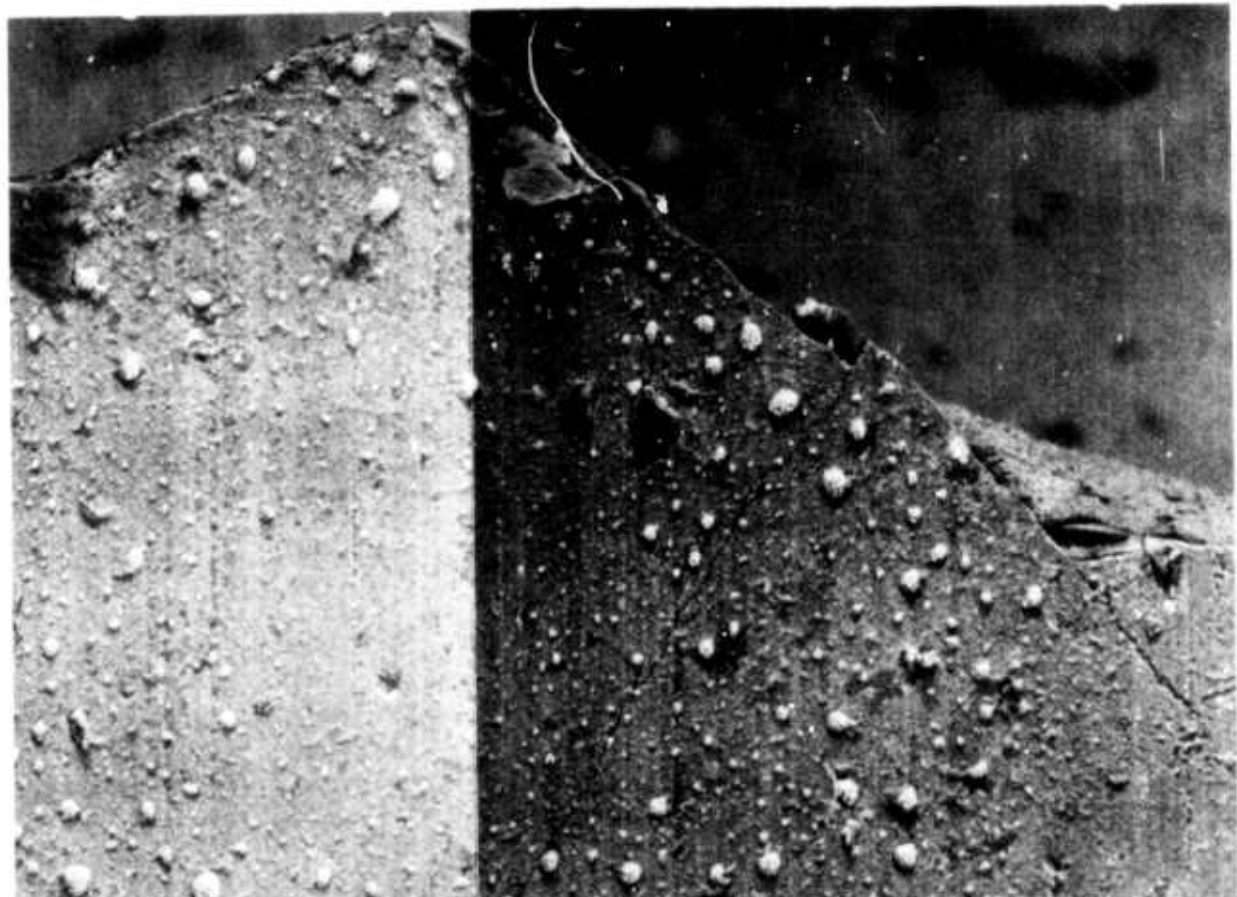
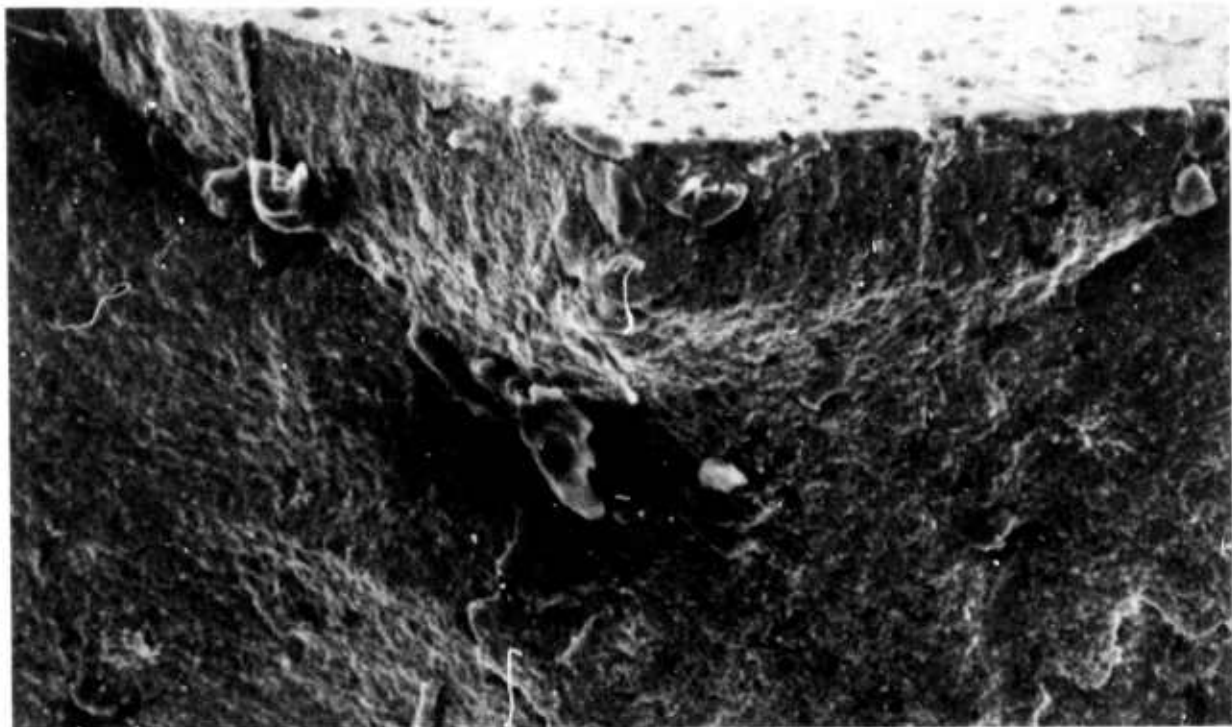


Figure 5.71 Scanning Electron Micrographs of Fractured Flexure Test Ford Dense Silicon Nitride: A) View of Laser Shocked and Final Fracture Surfaces, (135X), B) View of Laser Induced Cracks and Final Fracture on Tensile Surface. (225X)

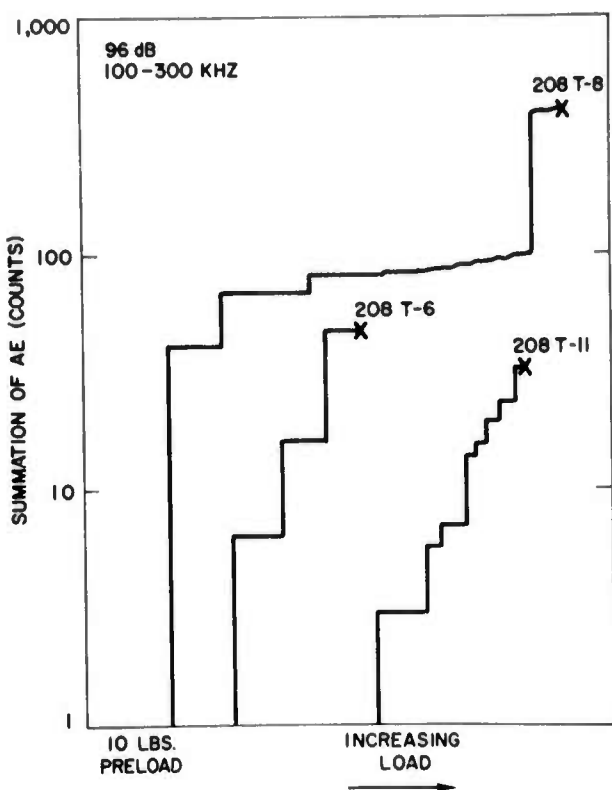


Figure 5.72 Crack Extension of Ford Hot-Pressed Silicon Nitride During Flexure Testing Shown as an Increase in AE Prior to Final Fracture.

#### Detection of Flaws

Test specimens representing various levels of surface cracks induced by the laser were subjected to reduced laser power densities to utilize the available thermal energy as a crack propagation force. Proper positioning of the test specimen within the diverging portion of the beam and the selection of specific scanning rates resulted in controlling the applied surface thermal stress. The minimum energy level necessary to slightly propagate existing cracks was then determined and when reached, displayed on a X-Y plotter as a sudden occurrence in AE events. This procedure is shown in Figure 5.73.

It was possible to visually correlate the AE events with the laser-induced cracks during scanning. The heat-affected material appeared cherry red and therefore, the actual laser path could be observed. Changes in absorption when the laser beam passed over the surface cracks also served as a visual indicator of beam position and correlated with the occurrence of AE events displayed on the S-Y plotter. The AE response of flaws to the applied thermal stress is shown in Table 5.14. Various levels of damage, as indicated by the AE response during laser shocking, are shown to respond to an increasing thermal stress in a uniform manner. The reciprocal of the defocus distance ( $D$  factor) serves as a measure of the power density, and therefore, the level of thermal stress and the flaw AE response increases as this parameter increases. The series of multiple scans on test specimen 196B-13 indicates the incremental extension of pre-existing cracks. Holding the  $D$  factor constant initially increases crack length as shown by an increasing AE response through scan number 3. Subsequent scans, however, revealed a diminishing AE flaw response until such time that further crack extension required a stress level exceeding that associated with the available power density. At this time (scan number 8), no further AE events are detected.

### Acoustic Emission During Bend Testing of Silicon Nitride

The general view of the equipment used for this work is shown in Figure 5.74. Samples were stressed under four point loading using an Instron machine. Load was recorded as a function of time on a strip chart recorder. The dowel pins (1/8" diameter), used for knife edges, were covered with layers of Teflon tape to insure acoustic isolation of the sample from the knife edges and the rest of the fixture.

The sensor was fastened to the sample with a layer of electrical insulation tape and rubber bands. The system operated at the maximum available gain of  $10^4$  with a discriminator setting of 180 mv for all tests.

Specimens, 1/8" x 1/4" x 4" were diamond cut from billet material, rough ground, and final finished with a 320 grit diamond wheel which removed at least 0.005 in. from the rough ground surface. Multiple breaks were made. Inner and outer span distances of 3/8" and 3/4", respectively were employed.

Figure 5.75 shows the total count vs load curve for a  $\text{Si}_3\text{N}_4$  sample which exhibited a flexural strength of 115,900 psi. No significant acoustic emission was observed for this specimen except at the failure point. This observation appeared typical of high flexural strength specimens. Figure 5.76 represents data from another portion of the same sample tested subsequently. Here, acoustic emission occurred initially at 64% of the failure load. The signal persisted at constant load (385 lb.) for 100 seconds. A slight change was recorded as loading was resumed. A sharp increase in acoustic emission was observed at failure. The ultimate failure stress was only 105,900 psi. These data suggest time-dependent crack propagation in  $\text{Si}_3\text{N}_4$  at room temperature. The crack initiation seems to be accompanied by an acoustic emission signal. Furthermore, there is a finite time interval between the appearance of the signal and the final failure.

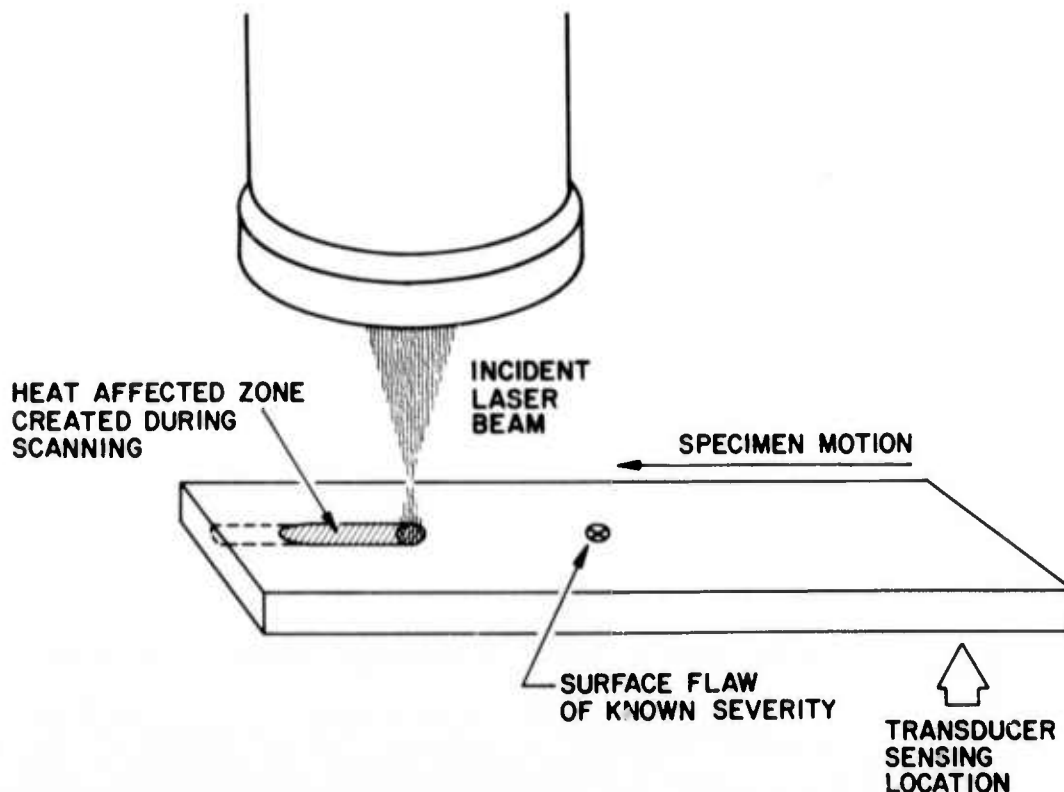


Figure 5.73 Laser Scanning to Detect Surface Flaws.

Table 5.14

Spec. No.	Scan No.	$\Sigma AE$ While Inducing Flaw	D-Reciprocal Of Defocus Distance (in)	Flaw Response While Scanning * ( $\Sigma AE$ )
208T-10	1	106	0.55	12
196B	1	172	.50	0
	2	172	.55	10
	3	182	.57	85
196B-13A	1	283	.53	36
196B-8	1	606	.55	25
196B-12	1	890	.50	320
96B-13	1	583	.44	22
	2	605	.44	39
	3	644	.44	72
	4	716	.44	33
	5	749	.44	36
	6	785	.44	26
	7	811	.44	9
	8	820	.44	0
HS-130 (Billet)	1	737	.42	0(a)
	2	737	.44	15
	3	752	.45	44
	4	796	.46	61
HS-130 (Billet)	1	311	.44	21(a)
	1	582	.44	24(a)
HS-130 (Billet)	1	1444	.44	10(b)
	2	1454	.46	441
	3	1895	.47	506
	4	2401	.48	865
HS-110 (1/2 inch disk)	1	1099	.40	24

\* Scanning Rate Equals 0.2 in/sec. Unless noted otherwise

(a) Scanning Rate Equals 0.3 in/sec.

(b) Scanning Rate Equals 0.4 in/sec.

TABLE 5.14 Scanning Data in Terms of Detected Acoustic Emission

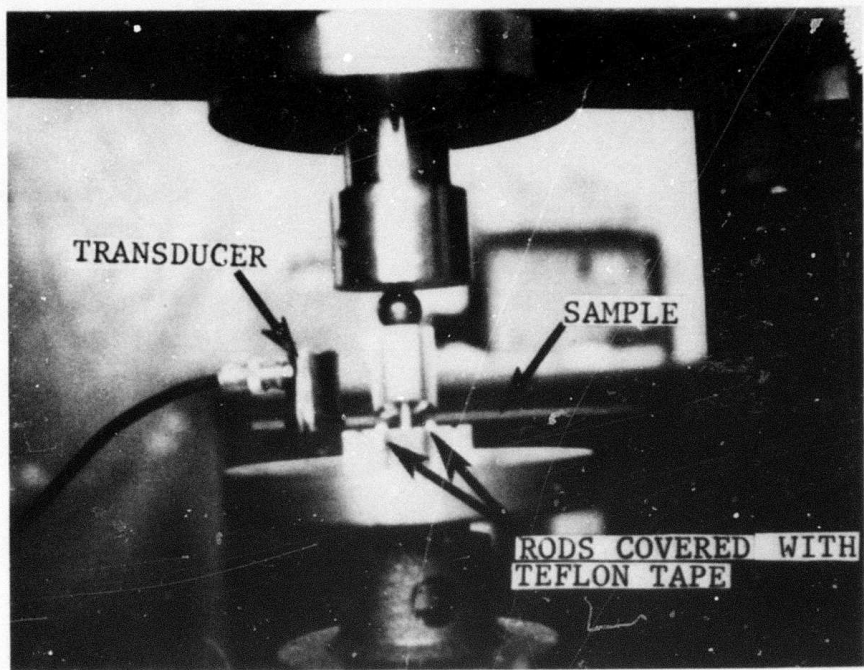


Figure 5.74 Experimental Setup Used For Study of Acoustic Emission From Samples Under Four-Point Bend Test.

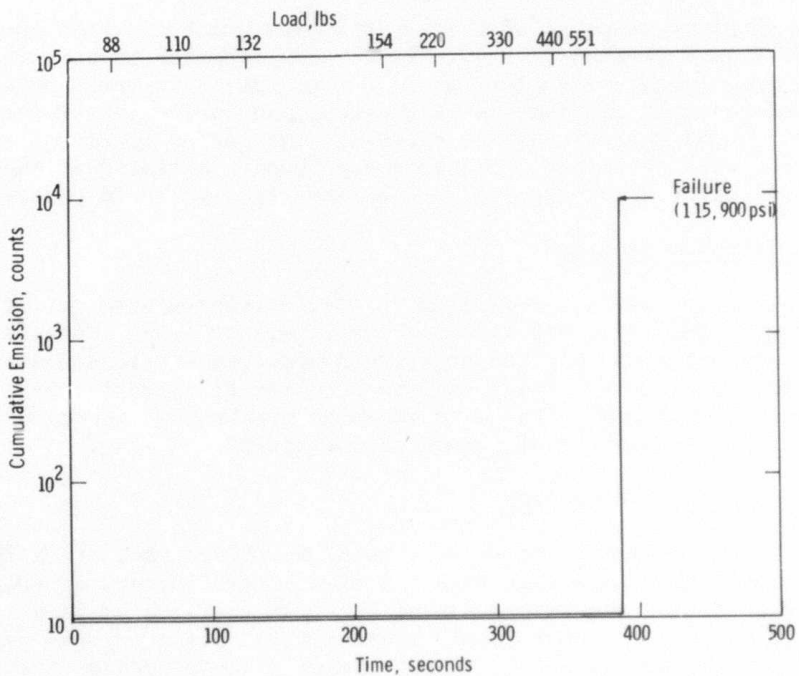


Figure 5.75 Total Count vs Load For a  $\text{Si}_3\text{N}_4$  Sample

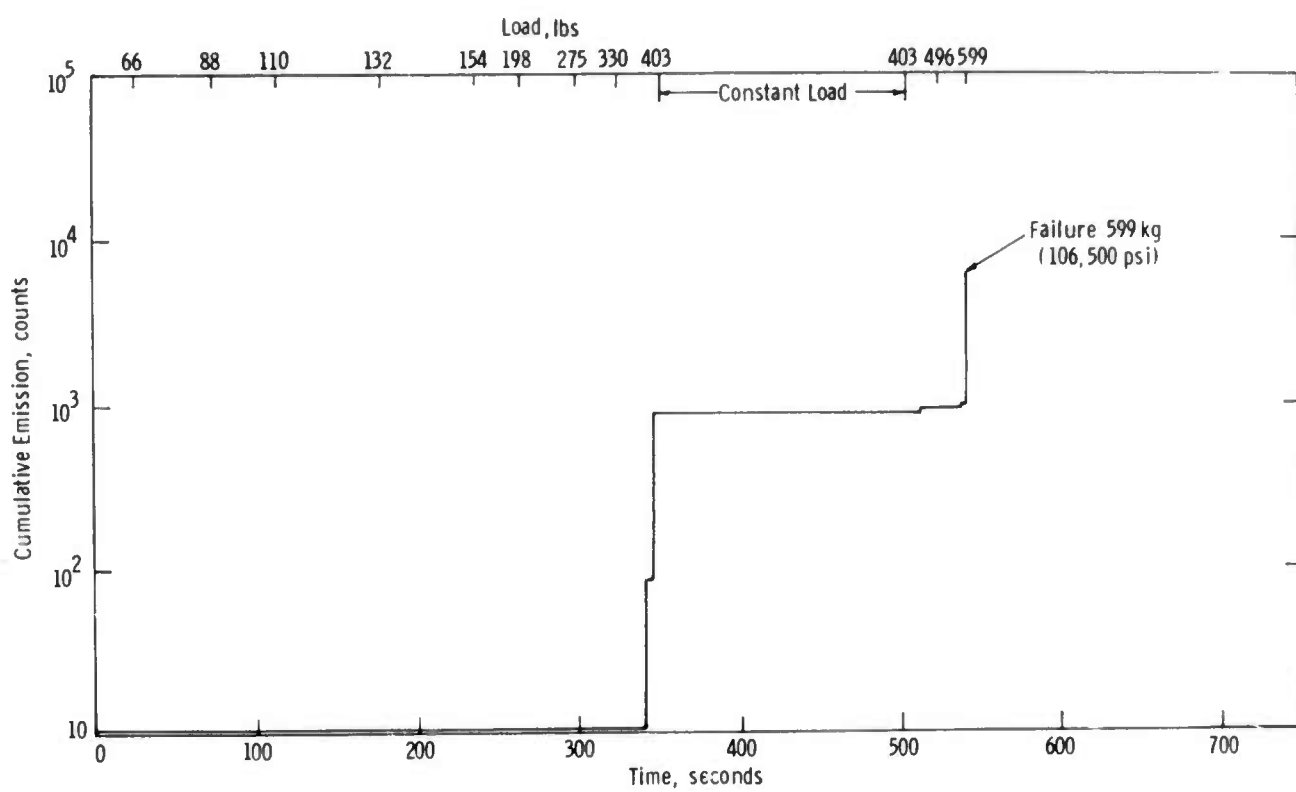


Figure 5.76 Total Count vs Load For Another Portion of  $\text{Si}_3\text{N}_4$  Sample Shown in Figure 5.82

The acoustic response of a  $\text{Si}_3\text{N}_4$  specimen which had been quenched in air from  $2552^{\circ}\text{F}$  is described in Figure 5.77. The increase in acoustic emission with load and premature failure at 54,000 psi stress suggest a damaged specimen. Since a microscopic examination of the specimen surface after thermal shock failed to reveal any evidence of cracking, the source of damage could not be established with certainty. Fracture apparently initiated at the two crack origins illustrated in Figure 5.78. Further testing is in progress.

#### Acoustic Emission from SiC

SiC samples, air quenched from  $2552^{\circ}\text{F}$ , exhibited some acoustic emission activity at a load of  $\sim 880$  lb. as shown in Figure 5.79. Considerable acoustic emission was recorded when the unquenched specimen was loaded statically to 990 lb. for 10 minutes. Final failure occurred at a 110 lb. load (64,000 psi) as shown in Figure 5.80. As noted above no cracks were observed microscopically, and therefore, the source of damage is uncertain.

#### Hertzian Cone Crack Detection

Since the foregoing experiments on  $\text{Si}_3\text{N}_4$  showed that crack initiation is accompanied by an acoustic emission signal, preliminary experiments were performed to detect the initiation of Hertzian cone cracks in silicon nitride and silicon carbide. A steel ball bearing ( $1/8"$  diameter) was pressed into the polished surface of a silicon nitride or silicon carbide test specimen to which the sensor transducer was attached. Acoustic emission was monitored as load was applied to the ball bearing.

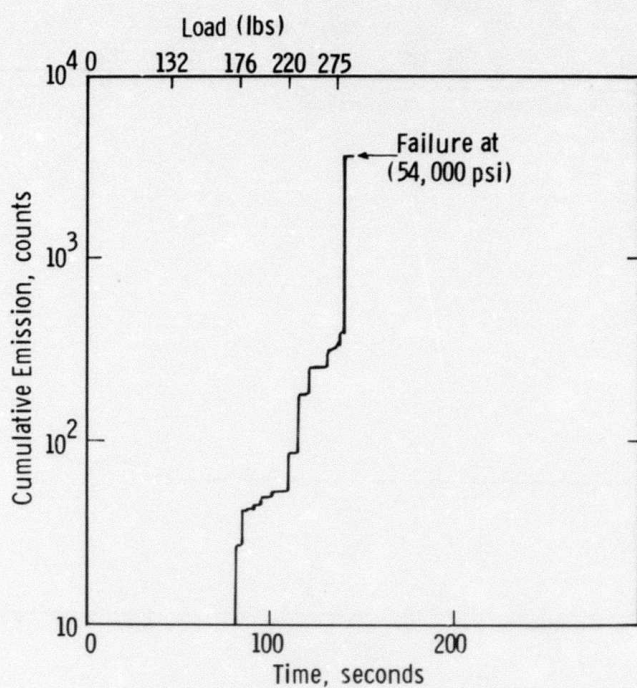


Figure 5.77 Total Count vs Load For a  $\text{Si}_3\text{N}_4$  Sample Pre-quenched in Air From  $2552^\circ\text{F}$ .

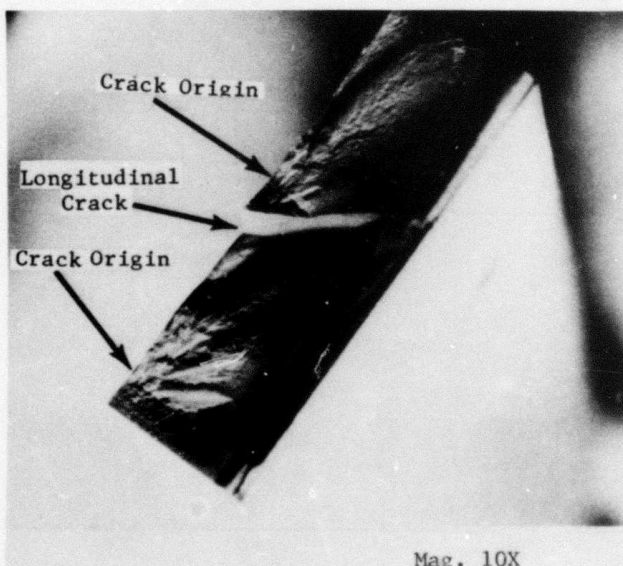


Figure 5.78 Fractured Surface of The  $\text{Si}_3\text{N}_4$  Sample For Which The Acoustic Emission Data is Shown in Figure 3a. (10X)

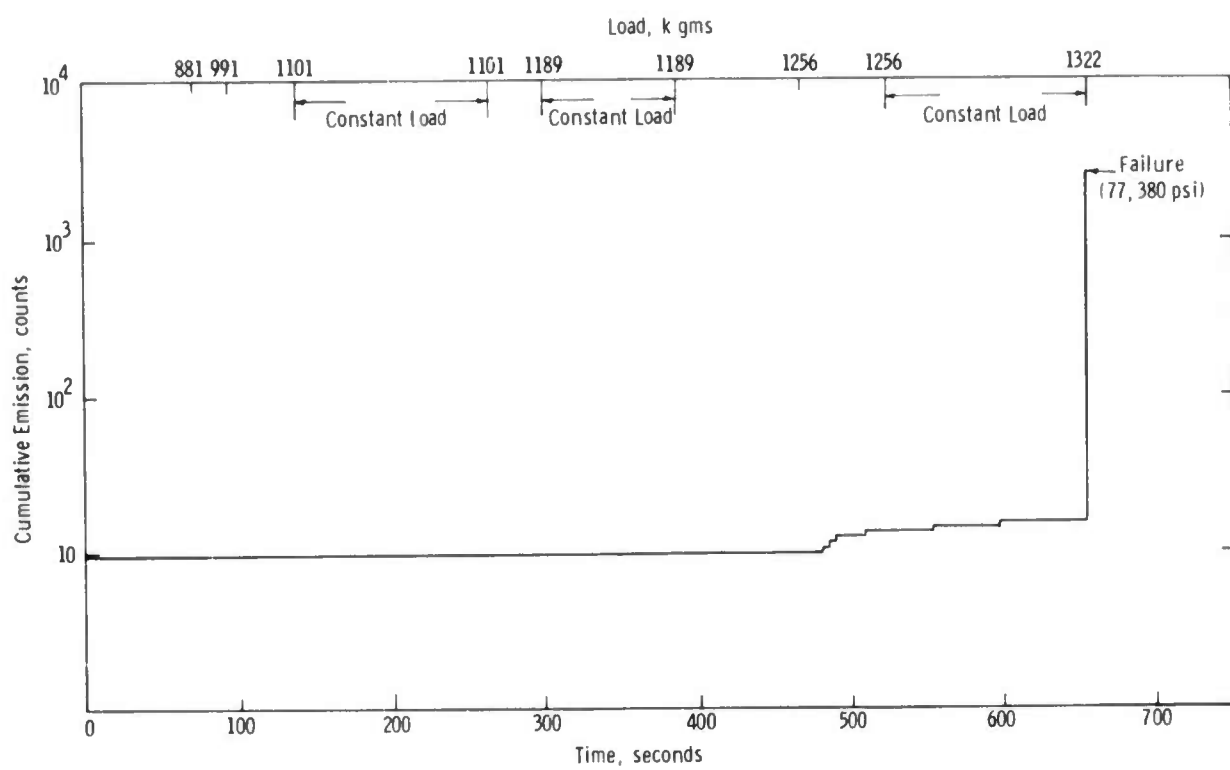


Figure 5.79 Total Count vs Load For SiC Sample Pre-quenched in Air From 2552° F (1400° C)

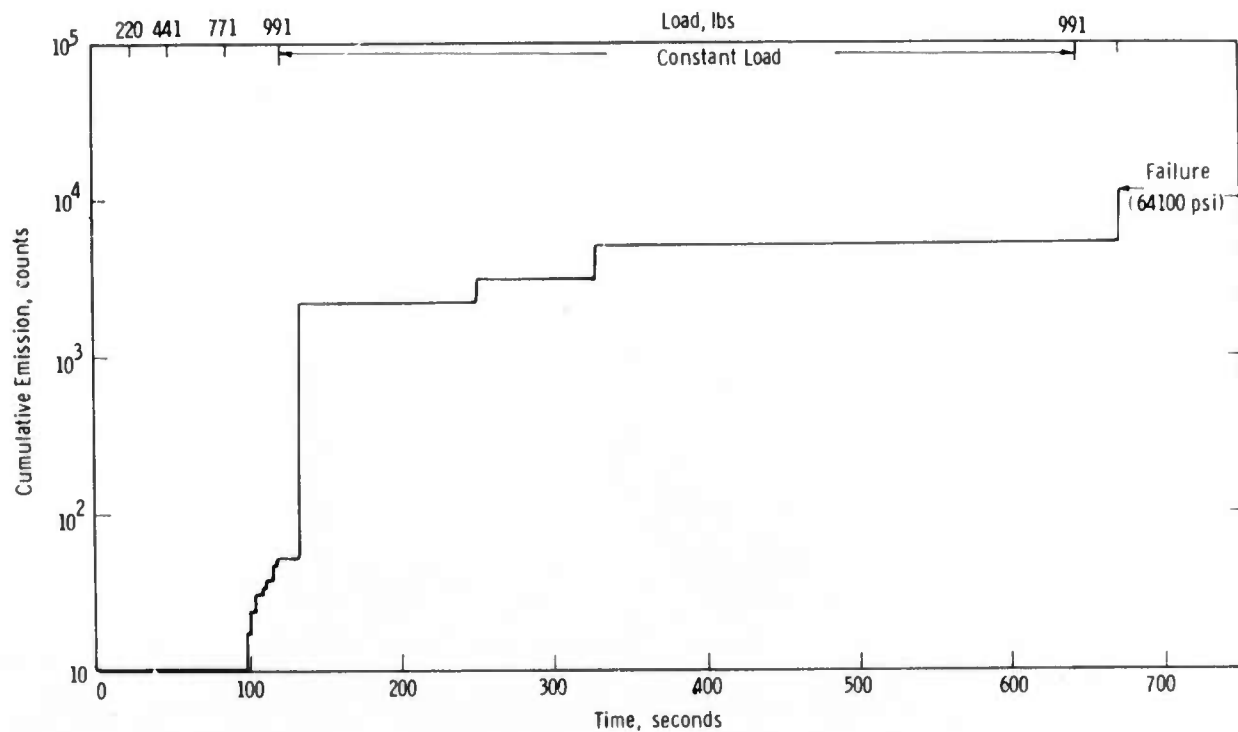


Figure 5.80 Total Count vs Load For a SiC Sample Not Subjected to Thermal Shock.

When an acoustic signal was recorded, loading was terminated and the specimen surface was examined under the microscope. In all cases, Hertzian cone cracks developed as a result of the contact stress. Examination of the contact surface prior to acoustic emission failed to disclose any evidence of cracking. Cracks were observed in all instances after acoustic emission had been recorded. The stress at which cracking occurred was relatively constant within samples of the same thickness. However, the stress required to initiate cracking decreased with specimen thickness.

The data taken so far suggest that a correlation may exist between the mechanical strength of  $\text{Si}_3\text{N}_4$  and the stress level at which significant acoustic emission starts. However, at this stage of the investigation, this observation lacks statistical confirmation. More data are needed before the existence of such a correlation between the mechanical strength and the stress level for start of significant acoustic emission can be determined. On occasion, acoustic emission was observed at low stresses from specimens which turned out to be of high strength.

The work so far has been performed using samples of simple shape. However, the ultimate objective is the proof-test of actual turbine components. This may require that parts be subjected to complicated mechanical and thermal stresses and monitored for acoustic emission as evidence of damage.

### 5.3.3 X-RAY RADIOGRAPHY

The x-ray standard previously fabricated <sup>(1)</sup> from a billet of Norton HS-130 silicon nitride was used to compare the quality of conventional x-ray radiography with that obtained by a dry process called xeroradiography (Xerox Corporation). The step block standard, while not intended as a means to determine size or to establish acceptance limits of discontinuities, does measure the ability of a specific technique to show contrast and definition. In this manner the overall x-ray image may be evaluated to determine the radiographic quality level or sensitivity. The specific objective of this study was to investigate the reported increase in accentuation of variations in density. The process is amenable to material systems that are conventionally evaluated by x-ray techniques up to 200 kV. Since the ceramic systems utilized in the gas turbine program fall well within this range, it would be extremely advantageous to be able to detect subtle changes in density due to segregated porosity, impurity inclusions with somewhat coherent interfaces with the matrix, and tight cracks which are not oriented properly for optimum detection.

The results of this comparison are shown in Table 5.15. The quality levels, as indicated by the ability of each process to show contrast (2% of step thickness) and definition (the actual penetrometer hole diameter imaged and visually apparent on the radiograph) are documented with respect to each step thickness of the radiographic standard. The outlined regions shown in the table encompass the penetrometer hole diameters readily imaged during a single exposure. It is apparent that a wider range of material thickness may be evaluated by the xeroradiographic process with no apparent loss in radiographic quality. For instance, a single exposure by the conventional x-ray method was capable of imaging a 2T hole for step thicknesses of 0.75, 1.000 and 1.250 in. However, the xeroradiographic process was able to image, in a single exposure, the 2T holes for a step thickness range of 0.500 to 1.500 in. These results warrant continued future investigation to optimize the xeroradiographic process on ceramic materials.

Step Thickness (in.)	Quality Levels						
	Conventional X-Ray Radiography			Xeroradiography		Penetrometer Hole Dia. (in.)	
	2% Step Thick.-T(in.)	1T	2T	4T	2% Step Thick.-T(in.)	1T	2T
0.125	0.0025	-	-	-	0.0025	0.020	0.020
.250	.005	-	0.011	0.020	.005	.016	.029
.375	.0075	-	.016	.029	.0075	.026	.039
.500	.010	.011	.026	.039	.010	.030	.062
.750	.015	.015	.030	.062	.015	.041	.081
1.000	.020	.022	.041	.081	.020	.050	.102
1.250	.025	.026	.050	.102	.025	.061	.123
1.500	.030	.031	.061	.123	.030	.061	.123

Table 5.15 Comparison of Quality Levels Obtained on the Hot-Pressed Silicon Nitride Radiographic Standard

## 6. REFERENCES

1. McLean, A. F., Fisher, E. A., Bratton, R. J., "Brittle Materials Design, High Temperature Gas Turbine," AMMRC CTR 73-9, Interim Report, July 1, 1972 to December 31, 1972.
2. McLean, A. F., Fisher, E. A., Bratton, R. J., "Brittle Materials Design, High Temperature Gas Turbine," AMMRC CTR 72-19, Interim Report, January 1, 1972 to June 30, 1972.
3. McLean, A. F., Fisher, E. A., and Harrison, D. E., "Brittle Materials Design, High Temperature Gas Turbine, "AMMRC CTR 72-3, Interim Report, July 1, 1971 to December 31, 1971.
4. Singh, Krishna Pal, "Contact Stresses in Elastic Bodies with Arbitrary Profiles", Ph.D. Dissertation at the Graduate School of Arts and Sciences of the University of Pennsylvania under the supervision of Dr. Burton Paul (1972) 296 pages.
5. Meyer, A. J. Jr., Kaufman, A., and Caywood, C., "The Design of Brittle-Material Blade Roots Based on Theory and Rupture Tests of Plastic Models", NACA TN 3773, September, 1956.
6. Deutsch, G. C., Meyer, A. J. Jr., and Morgan, W. C., "Preliminary Investigation in J33 Turbojet Engine on Several Root Designs for Ceramal Turbine Blades", NACA RM E52K13, January 26, 1953.
7. Meyer, A. J., Deutsch, G. C., and Morgan, W. C., "Preliminary Investigation of Several Root Designs for Cermet Turbine Blades in Turbojet Engine, II - Root Design Alterations", NACA RM E53602, October 13, 1953.
8. Pinkel, B., Deutsch, G. C., and Morgan, W. C., "Preliminary Investigation of Several Root Designs for Cermet Turbine Blades in Turbojet Engine, III - Curved Root Design", NACA RM E55J04, Dec. 28, 1955.
9. Morgan, W. C., Deutsch, G. C., "Experimental Investigation of Cermet Turbine Blades in an Axial-Flow Turbojet Engine", NACA TN 4030, October, 1957.
10. Peterson, R. E., "Stress Concentration Design Factors" John Wiley and Sons, Inc., New York.
11. Timoshenko, S., "Theory of Elasticity", McGraw-Hill Book Co., Inc. (1934) p. 66-70.
12. Evans, A. G. and Davidge, R. W., "The Strength and Oxidation of Reaction-Sintered Silicon Nitride", Journal of Material Science, 5 (1970) p. 314-325.
13. Messier, D. R. and Wong, P., "Dependence of Mechanical and Dielectric Properties of  $\text{Si}_3\text{N}_4$  on Fabrication Conditions", Presented at 75th Annual Meeting of the American Ceramic Society, Cincinnati, Ohio, April, 1973.
14. Seydel, J. A., "Computerized Enhancement of Ultrasonic Non-Destructive Testing Data," Ph.D. Thesis, The University of Michigan, 1972.

Army Materials and Mechanic Research Center,  
Watertown, Massachusetts 02172

ARMY MATERIALS AND MECHANIC RESEARCH CENTER,  
Watertown, Massachusetts 02172

AD

Key Words

BRITTLE MATERIALS DESIGN  
HIGH TEMPERATURE GAS TURBINE

The "Brittle Materials Design, High Temperature Gas Turbine" program is to demonstrate successful use of brittle materials in demanding high temperature structural applications. A small vehicular gas turbine and a large stationary gas turbine, each utilizing uncoupled ceramic components, will be used in this iterative design and materials development program. Both the contractor, Ford Motor Company, and the subcontractor, Westinghouse Electric Corporation, have had in-house research programs in this area prior to this contract.

In the vehicular turbine project, a more refined heat transfer and stress analysis was performed for the monolithic hot-pressed silicon nitride rotor. Methods of fabricating duo-density silicon nitride rotors were evaluated with several rotors being made; the best of these failed at 50,500 rpm during spin testing. Revised design stators demonstrated improved durability, although cracking has not been completely eliminated. Creep resistance of reaction-sintered silicon nitride has been considerably improved by decreasing calcium-containing impurities. The strength of reaction-sintered silicon nitride has been increased by the use of small amounts of hydrogen added to the nitrogen atmosphere.

In the stationary turbine project, stress and heat transfer analyses were completed for the stator vane assembly system. The three dimensional stress analysis program has been expanded to steady state and transient heat transfer capability. Installation of the static test rig for evaluating stator-vanes under turbine conditions has been completed. Additional information about the properties of hot-pressed silicon nitride and silicon carbide has been determined, and the microstructure of hot-pressed silicon carbide was studied in detail.

Army Materials and Mechanic Research Center,  
Watertown, Massachusetts 02172

ARMY MATERIALS AND MECHANIC RESEARCH CENTER,  
Watertown, Massachusetts 02172

AD

Key Words

BRITTLE MATERIALS DESIGN  
HIGH TEMPERATURE GAS TURBINE

The "Brittle Materials Design, High Temperature Gas Turbine" program is to demonstrate successful use of brittle materials in demanding high temperature structural applications. A small vehicular gas turbine and a large stationary gas turbine, each utilizing uncoupled ceramic components, will be used in this iterative design and materials development program. Both the contractor, Ford Motor Company, and the subcontractor, Westinghouse Electric Corporation, have had in-house research programs in this area prior to this contract.

In the vehicular turbine project, a more refined heat transfer and stress analysis was performed for the monolithic hot-pressed silicon nitride rotor. Methods of fabricating duo-density silicon nitride rotors were evaluated with several rotors being made; the best of these failed at 50,500 rpm during spin testing. Revised design stators demonstrated improved durability, although cracking has not been completely eliminated. Creep resistance of reaction-sintered silicon nitride has been considerably improved by decreasing calcium-containing impurities. The strength of reaction-sintered silicon nitride has been increased by the use of small amounts of hydrogen added to the nitrogen atmosphere.

In the stationary turbine project, stress and heat transfer analyses were completed for the stator vane assembly system. The three dimensional stress analysis program has been expanded to steady state and transient heat transfer capability. Installation of the static test rig for evaluating stator-vanes under turbine conditions has been completed. Additional information about the properties of hot-pressed silicon nitride and silicon carbide has been determined, and the microstructure of hot-pressed silicon carbide was studied in detail.

Army Materials and Mechanic Research Center,  
Watertown, Massachusetts 02172

ARMY MATERIALS AND MECHANIC RESEARCH CENTER,  
Watertown, Massachusetts 02172

AD

Key Words

BRITTLE MATERIALS DESIGN  
HIGH TEMPERATURE GAS TURBINE

The "Brittle Materials Design, High Temperature Gas Turbine" program is to demonstrate successful use of brittle materials in demanding high temperature structural applications. A small vehicular gas turbine and a large stationary gas turbine, each utilizing uncoupled ceramic components, will be used in this iterative design and materials development program. Both the contractor, Ford Motor Company, and the subcontractor, Westinghouse Electric Corporation, have had in-house research programs in this area prior to this contract.

The "Brittle Materials Design, High Temperature Gas Turbine" program is to demonstrate successful use of brittle materials in demanding high temperature structural applications. A small vehicular gas turbine and a large stationary gas turbine, each utilizing uncoupled ceramic components, will be used in this iterative design and materials development program. Both the contractor, Ford Motor Company, and the subcontractor, Westinghouse Electric Corporation, have had in-house research programs in this area prior to this contract.

In the vehicular turbine project, a more refined heat transfer and stress analysis was performed for the monolithic hot-pressed silicon nitride rotor. Methods of fabricating duo-density silicon nitride rotors were evaluated with several rotors being made; the best of these failed at 50,500 rpm during spin testing. Revised design stators demonstrated improved durability, although cracking has not been completely eliminated. Creep resistance of reaction-sintered silicon nitride has been considerably improved by decreasing calcium-containing impurities. The strength of reaction-sintered silicon nitride has been increased by the use of small amounts of hydrogen added to the nitrogen atmosphere.

In the stationary turbine project, stress and heat transfer analyses were completed for the stator vane assembly system. The three dimensional stress analysis program has been expanded to steady state and transient heat transfer capability. Installation of the static test rig for evaluating stator-vanes under turbine conditions has been completed. Additional information about the properties of hot-pressed silicon nitride and silicon carbide has been determined, and the microstructure of hot-pressed silicon carbide was studied in detail.

Army Materials and Mechanic Research Center,  
Watertown, Massachusetts 02172

ARMY MATERIALS AND MECHANIC RESEARCH CENTER,  
Watertown, Massachusetts 02172

AD

Key Words

BRITTLE MATERIALS DESIGN  
HIGH TEMPERATURE GAS TURBINE

The "Brittle Materials Design, High Temperature Gas Turbine" program is to demonstrate successful use of brittle materials in demanding high temperature structural applications. A small vehicular gas turbine and a large stationary gas turbine, each utilizing uncoupled ceramic components, will be used in this iterative design and materials development program. Both the contractor, Ford Motor Company, and the subcontractor, Westinghouse Electric Corporation, have had in-house research programs in this area prior to this contract.

In the vehicular turbine project, a more refined heat transfer and stress analysis was performed for the monolithic hot-pressed silicon nitride rotor. Methods of fabricating duo-density silicon nitride rotors were evaluated with several rotors being made; the best of these failed at 50,500 rpm during spin testing. Revised design stators demonstrated improved durability, although cracking has not been completely eliminated. Creep resistance of reaction-sintered silicon nitride has been considerably improved by decreasing calcium-containing impurities. The strength of reaction-sintered silicon nitride has been increased by the use of small amounts of hydrogen added to the nitrogen atmosphere.

In the stationary turbine project, stress and heat transfer analyses were completed for the stator vane assembly system. The three dimensional stress analysis program has been expanded to steady state and transient heat transfer capability. Installation of the static test rig for evaluating stator-vanes under turbine conditions has been completed. Additional information about the properties of hot-pressed silicon nitride and silicon carbide has been determined, and the microstructure of hot-pressed silicon carbide was studied in detail.

## UNCLASSIFIED

Security Classification

## DOCUMENT CONTROL DATA - R &amp; D

(Security classification of title, body of abstract and indexing annotation must be entered when the overall report is classified)

1. ORIGINATING ACTIVITY (Corporate author)  Ford Motor Company Dearborn, Michigan 48121		2a. REPORT SECURITY CLASSIFICATION  Unclassified
2b. GROUP		
3. REPORT TITLE  Brittle Materials Design, High Temperature Gas Turbine		
4. DESCRIPTIVE NOTES (Type of report and inclusive dates) Interim Report, January 1, 1973 to June 30, 1973		
5. AUTHOR(S) (First name, middle initial, last name) Arthur F. McLean Eugene A. Fisher Raymond J. Bratton		
6. REPORT DATE September, 1973	7a. TOTAL NO. OF PAGES 225	7b. NO. OF REFS 14
8a. CONTRACT OR GRANT NO. DAAG 46-71-C-0162	9a. ORIGINATOR'S REPORT NUMBER(S)  AMMRC-CTR 73-32	
b. PROJECT NO. ARPA Order No. 1849	9b. OTHER REPORT NO(S) (Any other numbers that may be assigned this report)	
c. Project Code No. 1D10 d. Agency Accession No. DA OD 4733		
10. DISTRIBUTION STATEMENT Distribution limited to U.S. Government agencies only; Test and Evaluation data; September, 1973. Other requests for this document must be referred to the Director, Army Materials & Mechanics Research Center, ATTN: AMXMR-PL, Watertown, Massachusetts 02172		
11. SUPPLEMENTARY NOTES		12. SPONSORING MILITARY ACTIVITY Army Materials and Mechanics Research Center, Watertown, Massachusetts 02172
13. ABSTRACT  ABSTRACT  The "Brittle Materials Design, High Temperature Gas Turbine" program is to demonstrate successful use of brittle materials in demanding high temperature structural applications. A small vehicular gas turbine and a large stationary gas turbine, each utilizing uncooled ceramic components, will be used in this iterative design and materials development program. Both the contractor, Ford Motor Company, and the subcontractor, Westinghouse Electric Corporation, have had in-house research programs in this area prior to this contract.  In the vehicular turbine project, a more refined heat transfer and stress analysis was performed for the monolithic hot-pressed silicon nitride rotor. Methods of fabricating duo-density silicon nitride rotors were evaluated, with several rotors being made; the best of these failed at 50,500 rpm during spin testing. Revised design stators demonstrated improved durability, although cracking has not been completely eliminated. Creep resistance of reaction-sintered silicon nitride has been considerably improved by decreasing calcium-containing impurities. The strength of reaction-sintered silicon nitride has been increased by the use of small amounts of hydrogen added to the nitrogen atmosphere.  In the stationary turbine project, stress and heat transfer analyses were completed for the stator vane assembly system. The three dimensional stress analysis program has been expanded to steady state and transient heat transfer capability. Installation of the static test rig for evaluating stator-vanes under turbine conditions has been completed. Additional information about the properties of hot-pressed silicon nitride and silicon carbide has been determined and the microstructure of hot-pressed silicon carbide was studied in detail.		

DD FORM 1 NOV 68 1473

REPLACES DD FORM 1473, 1 JAN 64, WHICH IS  
OBSOLETE FOR ARMY USE.

UNCLASSIFIED

Security Classification

**UNCLASSIFIED**

Security Classification

14 KEY WORDS	LINK A		LINK B		LINK C	
	ROLE	WT	ROLE	WT	ROLE	WT
Gas turbine engine						
Brittle design						
Ceramics						
High-temperature materials						
Silicon nitride						
Silicon carbide						
Non-destructive tests						
Mechanical properties						

**UNCLASSIFIED**

Security Classification